

Aerodynamic development of Le Mans prototype cars using CFD tools



Grado en Ingeniería Mecánica

Trabajo Fin de Grado

Christian Gallués Urrutia

Vanesa Estremera Carrera

Pamplona, 16/01/2023

upna

Universidad Pública de Navarra
Nafarroako Unibertsitate Publikoa

Acknowledgements

I would like to thank my parents for their unconditional support throughout my years as an engineering student that has helped so much in both the good and bad times. I would also like to express my gratitude towards my father for passing me on his passion for cars and dirt bikes since I was a kid.

To Vanesa for her support and patience during the development of this thesis, as I could not have finished this project without all the things related to automobiles that she's taught me, that will, for sure, be of high value in the future.

Abstract

This thesis covers the development phase of the aerodynamic package of a Le Mans prototype car based on a base geometry, aimed at achieving an aerodynamic performance similar to any LMP1 Prototype currently competing. The development of the different aerodynamic elements is conducted using general concepts from fluid dynamics that are validated and quantified using advanced Computer Fluid Dynamics software CFD.

The design is improved based on the results from the previous CFD simulation results. These improvements are designed with the help of CAD software to be analysed in another CFD simulation.

The result only is only meaningful as a concept, as the work done in this thesis only covers the general attributes of a complete aerodynamic package.

Keywords

- CFD: Computational Fluid Dynamics
- CAD: Computer Aided Design
- FIA: Federation Internationale de l'Automobile
- LMP1: Homologation rules for endurance race cars
- STAR-CCM+
- Development
- Aerodynamic
- Downforce
- Drag
- Air foil
- Diffuser
- Splitter
- Balance
- Flow
- Velocity
- Pressure

Index

List of Figures	7
List of Tables	11
1 Introduction	12
1.1 General objectives	12
1.2 Performance objectives	12
1.3 Background	13
2 CFD and Fluid Dynamics concepts	14
2.1 Basic concepts of CFD analysis	14
2.2 Understanding how CFD analysis works	14
2.3 Strengths and Limitations of CFD analysis	14
2.4 Governing equations	16
2.5 Concepts of interest in fluid dynamics and CFD	18
2.5.1 non-Dimensional numbers	18
2.5.2 Turbulence models	19
2.5.3 Boundary layer management	21
2.6 Bernoulli's principle and Venturi effect	28
2.7.1 Lift force and coefficient	30
2.7.2 Drag force and coefficient	31
2.8 CFD software: Siemens STAR CCM+	32
3 Geometry	33
3.1 Important aerodynamic structures in the car	35
3.1.1 Floor and rake angle	35
3.1.2 Rear wing	36
3.1.3 Rear diffuser	38
4 Base geometry analysis	39
4.1 Control volume	40
4.2 Pre-Processing	43
4.2.1 Pre-process: geometry import	43
4.2.3 Boundary conditions	45
4.2.4 Physics continuum	47
4.2.5 Mesh operation	49

4.2.6	Reports and graphic plots	54
4.3	Post-processing.....	58
4.3.1	Simulation and Residuals.	58
4.3.2	Data analysis, data plotting and visual analysis.	61
4.4	Aerodynamic improvements	66
5	Geometry Iteration 1	69
5.1	Desired results overview	69
5.1.1	Floor and rake angle	69
5.1.2	Frontal Area	73
5.1.3	Rear diffuser.....	77
5.1.4	Rear wing.....	78
5.1.5	Front wings	88
5.1.6	Other modifications.....	97
5.2	Simulation.....	98
5.2.1	Visual analysis	106
6	Geometry Iteration 2	119
6.1	Geometry improvements.....	119
6.1.1	Rear wing.....	119
6.1.2	Front wing	121
6.1.3	Front splitter	122
6.1.4	Rear diffuser and rake angle	123
6.1.5	Engine air intake	124
6.2	Simulation 3.....	125
6.3	Visual analysis and possible improvements	131
7	Geometry iteration 3. Final design.....	136
7.1	Geometry changes	136
7.1.1	Front splitter	136
7.1.2	Front wing	137
7.1.3	Engine air intake	138
7.1.4	Front splitter wake management	138
7.1.6	Other modifications.....	139
7.2	Simulation 4.....	140
7.3	Visual analysis.....	145

8	Conclusions	150
8.1	Technical review	150
8.2	Final conclusions.....	151
8.3	Future improvements.....	152

List of Figures

FIGURE 1: MERCEDES T80 LAND SPEED CAR FROM 1939.	13
FIGURE 2: RESIDUALS PLOTTED IN STAR CCM+ SOFTWARE.	15
FIGURE 3: COMPARISON OF BOUNDARY LAYERS IN LAMINAR AND TURBULENT FLOW.	21
FIGURE 4: PRISM LAYER IN THE REGIONS CLOSE TO THE CAR'S SURFACE. NOT TO SCALE.	22
FIGURE 5: THIN MESH CELLS CAPTURING THE VISCOUS REGION OF THE BOUNDARY LAYER. SOURCE: SIMSCALE.	23
FIGURE 6: BOUNDARY LAYER SECTIONS BASED ON THE NORMALIZED SPEED U	24
FIGURE 7: Y^+ VALUES GRAPH. SOURCE: SIMSCALE.	24
FIGURE 8: EXAMPLE OF FULL BOUNDARY LAYER CALCULATION PRISM MESH. NOTICE THE HIGH CELL COUNT NEEDED.	25
FIGURE 9: DIFFERENCE BETWEEN WALL FUNCTIONS AND FULL BOUNDARY LAYER CALCULATIONS.	26
FIGURE 10: COMMONLY USED PIPE TO EXPLAIN BERNOULLI'S PRINCIPLE.	28
FIGURE 11: VENTURI EFFECT GENERATING A LOWER PRESSURE REGION UNDER A CAR.	29
FIGURE 12: LOTUS 79 GROUND EFFECT CAR. NOTICE THE INVERTED WING PROFILE.	29
FIGURE 13: AERODYNAMIC FORCE COMPONENTS ACTING ON THE CENTER OF GRAVITY.	30
FIGURE 14: STAR CCM+ FEATURE TREE AND TOOLBARS.	32
FIGURE 15: TYPICAL LMP CAR.	33
FIGURE 16: FRONT $\frac{3}{4}$ VIEW OF THE BASE GEOMETRY.	34
FIGURE 17: BASE CAD UNDERFLOOR HIGHLIGHTED IN ORANGE.	34
FIGURE 18: LMP BASE MODEL SIDE VIEW AND DIMENSIONS.	35
FIGURE 19: LMP BASE MODEL FRONT VIEW AND DIMENSIONS.	35
FIGURE 20: RAKE ANGLE IN A TOYOTA ENDURANCE RACE CAR.	36
FIGURE 21: PRESSURE AND VELOCITY IN AN AIRFOIL.	36
FIGURE 22: TWO ELEMENT REAR WING. FIGURE 23: THREE ELEMENT REAR WING.	37
FIGURE 24: GURNEY FLAP PERPENDICULAR TO THE UPPER ELEMENT SURFACE.	37
FIGURE 25: BOUNDARY LAYER SEPARATION IN AN AIRFOIL AT HIGH ANGLES OF ATTACK. NOTICE THE SEPARATION BUBBLES.	38
FIGURE 26: EFFECT OF THE GURNEY FLAP IN THE AIRFOIL OF FIGURE 21. NOTICE THE NOW COUPLED FLOW.	38
FIGURE 27: CONTROL VOLUME AND THE CAR'S POSITION.	39
FIGURE 28: HOLLOW CAVITY INSIDE THE CONTROL VOLUME.	40
FIGURE 29: AUTOMOTIVE WIND TUNNEL FOR 1:1 SIZED CAR.	40
FIGURE 30: TOP PLANE IS THE REAL CONTACT PLANE. LOWER PLANE IS THE GROUND PLANE.	41
FIGURE 31: TOP VIEW OF THE CONTROL VOLUME SET-UP AND DIMENSIONS.	41
FIGURE 32: EXTRUDE OPERATION.	42
FIGURE 33: CONTROL VOLUME READY FOR CFD ANALYSIS.	42
FIGURE 34: GEOMETRY IMPORTED INTO STAR-CCM+.	43
FIGURE 35: SELECTION AND NAMING OF THE SELECTED FACE.	44
FIGURE 36: ALL THE SURFACES HAVE BEEN GROUPED EITHER BY BOUNDARY SURFACE OR AERODYNAMIC SURFACE.	44
FIGURE 37: BOUNDARY SURFACE CREATION COMMAND.	46
FIGURE 38: LIST OF ALL THE BOUNDARY CONDITIONS AND TYPES.	46
FIGURE 39: AVAILABLE PHYSICS MODELS IN STAR-CCM+.	47
FIGURE 40: PHYSICS MODEL.	48
FIGURE 41: INITIAL VELOCITY IN ALL THE DOMAIN CELLS. 10 [m/s] POSITIVE IN THE X AXIS.	48
FIGURE 42: FLOW VELOCITY AT THE INLET BOUNDARY. 75 [m/s] OR 270 [km/h] IN THE POSITIVE X AXIS DIRECTION.	49
FIGURE 43: MOVING GROUND UNDER THE VEHICLE USING RELATIVE VELOCITY ON THE GROUND BOUNDARY.	49
FIGURE 44: ABSOLUTE PRESSURE.	49
FIGURE 45: AUTOMATED MESH CREATION.	50
FIGURE 46: MESHES TO BE USED IN THIS SIMULATION.	51
FIGURE 47: MAIN MESH VARIABLES IN STAR-CCM+.	51
FIGURE 48: OUTER VIEW OF THE MESH VOLUME.	53
FIGURE 49: SURFACE MESH AROUND THE CAR AND WAKE AREA. NOTICE THE FINER MESH SIZE.	54
FIGURE 50: CELL SIZE DIFFERENCE BETWEEN THE WAKE AREA AND REST OF THE VOLUME REGION.	54
FIGURE 51: AVAILABLE REPORTS.	55

FIGURE 52: LIST OF ALL FORCES TO BE CALCULATED.	55
FIGURE 53: CoP COORDINATES CARTESIAN REFERENCE SYSTEM HIGHLIGHTED IN PINK.	56
FIGURE 54: K – EPSILON SIMULATION RESIDUALS.	59
FIGURE 55: WALL Y+ VALUES FRONT ¾ VIEW OF THE CAR. WHITE IS Y+>30 AND BLACK IS Y+<30. SIMULATION 1.	59
FIGURE 56: Y+ VALUES ON THE FLOOR PAN. COLOUR RANGE ADJUSTED FOR 5<Y+<30. SIMULATION 1.	60
FIGURE 57: STREAMLINES UNDER THE FLOOR. NOTICE THE WAKE THAT STALLS THE FLOOR RIGHT BEHIND THE FRONT WHEELS. SIMULATION 1.	60
FIGURE 58: AERODYNAMIC LOAD DISTRIBUTION ON EACH AXLE. SIMULATION 1.	62
FIGURE 59: FRONTAL AREA CONTOUR. FRONTAL AREA CONTOURS HIGHLIGHTED IN PINK.	62
FIGURE 60: MEASURE OPERATION FOR THE FRONTAL AREA.	63
FIGURE 61: AUDI R18 TDI 2011.	64
FIGURE 62: PRESSURE COLOUR FIELD ON THE UPPER SURFACES OF THE CAR. SIMULATION 1.	66
FIGURE 63: FRONT WHEEL WAKE TURBULENCE GENERATED INSIDE THE WHEEL FENDER. SIMULATION 1.	67
FIGURE 64: UPPER VENT FOR THE WHEEL WAKE. NOTICE THE POOR EXTRACTION. SIMULATION 1.	67
FIGURE 65: REAR DIFFUSER STREAMLINES. NOTICE THE LACK OF AIR FLOW ON THE OUTER SECTIONS.	68
FIGURE 66: FRONT SPLITTER ON THE FIRST DESIGN ITERATION. NOTICE THE RAISED FLOOR LIP.	69
FIGURE 67: SECTION VIEW OF THE FRONT SPLITTER. IN ORANGE, THE LONGITUDINAL PROFILE.	70
FIGURE 68: DIFFERENCE BETWEEN THE FRONT SPLITTER (LEFT) AND THE ORIGINAL FLOOR PROFILE (RIGHT).	70
FIGURE 69: BEAM WINGS CONNECTING THE SPLITTER TO THE CHASSIS.	70
FIGURE 70: SEALED FLOOR ON THE FRONT WHEEL WAKE AREA (LEFT) AND ORIGINAL WAKE VENT CUT (RIGHT).	71
FIGURE 71: VORTEX GENERATOR HIGHLIGHTED IN RED. THE VORTEX CREATED FLOWS ALONG THE FLOOR EDGE TO SEAL IT.	72
FIGURE 72: RAKE ANGLE SKETCH. THIS SKETCH ALLOWS FOR A QUICK AND EASY CHANGE OF RAKE ANGLE AND RIDE HEIGHT.	72
FIGURE 73: RAKE ANGLE. THE BLUE LINE IS THE GROUND PLANE.	73
FIGURE 74: FRONT CANARDS HIGHLIGHTED IN RED.	73
FIGURE 75: PRESSURE DISTRIBUTION ON THE ORIGINAL GEOMETRY WHEEL FENDERS.	74
FIGURE 76: WHEEL FENDER GEOMETRY COMPARISON. LEFT IS THE REVISED GEOMETRY AND RIGHT IS THE ORIGINAL GEOMETRY.	74
FIGURE 77: HIGH PRESSURE LEADING EDGES.	75
FIGURE 78: NOTICE THE DIFFERENCE BETWEEN THE ORIGINAL FRONTAL SECTION (RIGHT) AND THE REVISED FRONTAL AREA (RIGHT).	75
FIGURE 79: MIRROR HIGHLIGHTED IN RED.	76
FIGURE 80: REAR DIFFUSER PROFILE SKETCH HIGHLIGHTED IN ORANGE.	77
FIGURE 81: BASE GEOMETRY DIFFUSER (LEFT) AND MODIFIED GEOMETRY DIFFUSER (RIGHT).	77
FIGURE 82: DIFFUSER EXIT HEIGHT. LEFT IS BASE GEOMETRY AND RIGHT IS MODIFIED GEOMETRY.	78
FIGURE 83: MODIFIED REAR WING PROFILE.	79
FIGURE 84: CONTROL VOLUME WITH THE WING PROFILE.	80
FIGURE 85: 2D MESH OPERATION FOR THE FIRST WING PROFILE DESIGN. AROUND 1E5 CELLS.	80
FIGURE 86: RESIDUALS OF THE FIRST 2D SIMULATION OF THE WING PROFILE.	81
FIGURE 87: DRAG AND DOWNFORCE REPORT FOR THE FIRST 2D SIMULATION OF THE WING PROFILE.	81
FIGURE 88: PRESSURE DISTRIBUTION ON THE FIRST REAR WING PROFILE.	82
FIGURE 89: PRESSURE DISTRIBUTION WITH VELOCITY FIELD STREAMLINES.	82
FIGURE 90: REVISED REAR WING PROFILE.	83
FIGURE 91: RESIDUALS OF THE SECOND REAR WING PROFILE SIMULATION. NOTICE THE LOWER RESIDUALS COMPARED TO THOSE OF THE PREVIOUS SIMULATION.	83
FIGURE 92: DRAG AND DOWNFORCE REPORT OF THE SECOND REAR WING PROFILE.	84
FIGURE 93: PRESSURE DISTRIBUTION ALONG THE REVISED REAR WING PROFILE.	84
FIGURE 94: IMPROVED REAR WING PROFILE. PRESSURE DISTRIBUTION.	85
FIGURE 95: ORIGINAL REAR WING PROFILE. PRESSURE DISTRIBUTION.	85
FIGURE 96: STREAMLINES AROUND THE REVISED WING PROFILE.	85
FIGURE 97: GURNEY FLAP ON THE UPPER WING ELEMENT.	86
FIGURE 98: RESIDUALS PLOT OF THE REVISED REAR WING PROFILE WITH THE GURNEY FLAP INSTALLED.	87
FIGURE 99: FORCE REPORTS PLOT OF THE REVISED REAR WING PROFILE WITH THE GURNEY FLAP INSTALLED.	87
FIGURE 100: PRESSURE DISTRIBUTION WITH THE GURNEY FLAP INSTALLED.	88
FIGURE 101: PRESSURE DISTRIBUTION WITHOUT THE GURNEY FLAP INSTALLED.	88
FIGURE 102: REAR WING PLACEMENT RELATIVE TO THE CAR.	88

FIGURE 103: FRONT WINGS HIGHLIGHTED IN RED.	89
FIGURE 104: FRONT WING PROFILE IMPORTED INTO STAR-CCM+.	90
FIGURE 105: FRONT WING PROFILE 2D SIMULATION RESIDUALS.	90
FIGURE 106: DRAG AND DOWNFORCE REPORT OF THE FRONT WINGS PROFILE 2D SIMULATION.	91
FIGURE 107: PRESSURE FIELD OF THE FRONT WING PROFILE.	92
FIGURE 108: STREAMLINES FLOWING ALONG THE FRONT WING PROFILE.	92
FIGURE 109: GURNEY FLAP ON THE FRONT WING PROFILE.	93
FIGURE 110: 2D SIMULATION RESIDUALS OF THE FRONT WING PROFILE WITH THE GURNEY FLAP INSTALLED.	93
FIGURE 111: DRAG AND DOWNFORCE REPORT OF THE FRONT WINGS PROFILE FITTED WITH THE GURNEY FLAP.	94
FIGURE 112: PRESSURE FIELD OF THE FRONT WING PROFILE FITTED WITH THE GURNEY FLAP.	95
FIGURE 113: PRESSURE FIELD ON THE FRONT WING FITTED WITH THE GURNEY FLAP.	95
FIGURE 114: PRESSURE FIELD W/ GURNEY FLAP.	96
FIGURE 115: PRESSURE FIELD WO/ GURNEY FLAP.	96
FIGURE 116: VENT LOUVRES ON THE BACKSIDE OF EACH WHEEL FENDER.	97
FIGURE 117: LOW PRESSURE REGION ON THE REAR WHEEL FENDERS.	98
FIGURE 118: IMPROVED CAR GEOMETRY IMPORTED INTO STAR-CCM+.	98
FIGURE 119: SURFACE MESH. SECOND CFD SIMULATION.	99
FIGURE 120: INITIAL VELOCITY CONDITIONS. SECOND CFD SIMULATION.	100
FIGURE 121: RESIDUALS OF THE SECOND 3D SIMULATION.	100
FIGURE 122: DRAG AND DOWNFORCE GLOBAL VALUES OF THE REVISED CAR GEOMETRY.	100
FIGURE 123: DOWNFORCE VALUES BY AERODYNAMIC SURFACE.	101
FIGURE 124: DRAG VALUES BY AERODYNAMIC SURFACES.	101
FIGURE 125: FRONTAL AREA MEASUREMENT. SIMULATION 2.	103
FIGURE 126: AERODYNAMIC LOAD DISTRIBUTION. SIMULATION 2.	103
FIGURE 127: LOW PRESSURE ON THE COCKPIT CANOPY. SIMULATION 2.	105
FIGURE 128: LOW PRESSURE REGION BETWEEN THE SPLITTER AND THE FLOOR. SIMULATION 2.	106
FIGURE 129: STREAMLINES FLOWING THROUGH THE SPLITTER TUNNEL. SIMULATION 2.	107
FIGURE 130: TURBULENT AIR EXITING THE INSIDE OF THE FRONT WHEEL FENDER. SIMULATION 2.	107
FIGURE 131: PRESSURE FIELD ON THE DIFFUSER REGION. NOTICE THE SMALL LOW-PRESSURE REGION. SIMULATION 2.	108
FIGURE 132: STREAMLINES ON THE DIFFUSER. NOTICE THE LACK OF VELOCITY DECELERATION ON THE FLOW. SIMULATION 2.	108
FIGURE 133: STREAMLINES VELOCITY PROFILE ON THE REAR DIFFUSER REGION. SIMULATION 2.	109
FIGURE 134: STREAMLINES FLOWING ABOVE THE CAR. NOTICE THE DOWNWARDS DIRECTION OF THE FLOW NEAR THE MIDDLE SECTION OF THE REAR WING. SIMULATION 2.	111
FIGURE 135: PRESSURE FIELD UNDER THE 2D PROFILE OF THE REAR WING. NOTICE THE LONGER LOW-PRESSURE REGION UNDER THE PROFILE, SIMILAR TO THE OUTER PART OF THE 3D REAR WING PRESSURE FIELD.	111
FIGURE 136: PRESSURE FIELD UNDER THE REAR WING. NOTICE THE INCREASED LOW-PRESSURE REGION ON THE OUTER PART OF THE WING.	111
FIGURE 137: RELATIVE ANGLE OF ATTACK ON THE CENTRE SECTION OF THE REAR WING. SIMULATION 2.	112
FIGURE 138: FLOW DETACHMENT UNDER THE MIDDLE SECTION OF THE REAR WING. SIMULATION 2.	112
FIGURE 139: RELATIVE ANGLE OF ATTACK OF THE REAR WING ON THE OUTER SECTION. SIMULATION 2.	113
FIGURE 140: FLOW UNDER THE OUTER PART OF THE REAR WING. SIMULATION 2.	113
FIGURE 141: DETACHED FLOW UNDER THE CENTRE SECTION OF THE REAR WING. SIMULATION 2.	114
FIGURE 142: HIGH PRESSURE REGION ON THE UPPER REAR WING SURFACES. SIMULATION 2.	114
FIGURE 143: INCREASED HIGH PRESSURE ON THE REAR WING SIDE SUPPORTS. SIMULATION 2.	115
FIGURE 144: HIGH-ENERGY VORTICES ON THE REAR WING. SIMULATION 2.	115
FIGURE 145: VORTICITY PLANE ON THE WAKE OF THE CAR. SIMULATION 2.	116
FIGURE 146: PRESSURE FIELD ON THE UNDERSIDE OF THE FRONT WING. SIMULATION 2.	117
FIGURE 147: LOW-PRESSURE REGION IN BLACK/DARK BLUE. SIMULATION 2.	117
FIGURE 148: PRESSURE DECREASES AND VELOCITY INCREASES AS A RESULT OF SECTION AREA REDUCTION AFTER THE FRONT WINGS. SIMULATION 2.	118
FIGURE 149: SWEPT REAR WING. GEOMETRY ITERATION 2.	119
FIGURE 150: FRONTAL VIEW OF THE TWISTED REAR WING. NOTICE THE INCREASED UNDERSIDE SECTION NEAR THE MIDDLE (HIGHLIGHTED IN GREEN). GEOMETRY ITERATION 2.	120

FIGURE 151: REAR WING VENT LOUVRES ON THE SUPPORT BEAMS. GEOMETRY ITERATION 2.	120
FIGURE 152: SIDE VIEW OF THE REAR WING VENT LOUVRES. GEOMETRY ITERATION 2.	120
FIGURE 153: REVISED FRONT WING HIGHLIGHTED IN GREEN. GEOMETRY ITERATION 2.	121
FIGURE 154: ENDPLATE AND OUTWASH ELEMENTS ON THE FRONT WING HIGHLIGHTED IN GREEN. GEOMETRY ITERATION 2.	122
FIGURE 155: LONGER FRONT SPLITTER (LEFT) COMPARED TO THE FRONT SPLITTER DESIGNED IN THE FIRST DESIGN ITERATION (RIGHT).	122
FIGURE 156: REAR DIFFUSER WITH VERTICAL STRAKES. GEOMETRY ITERATION 2.	123
FIGURE 157: MODIFIED ENGINE AIR INTAKES. GEOMETRY ITERATION 2.	124
FIGURE 158: RESIDUALS OF THE THIRD 3D CFD SIMULATION. SIMULATION 3.	125
FIGURE 159: GLOBAL FORCE VALUES. SIMULATION 3.	126
FIGURE 160: DRAG VALUES OF THE DIFFERENT AERODYNAMIC SURFACES. SIMULATION 3.	126
FIGURE 161: DOWNFORCE VALUES OF THE DIFFERENT AERODYNAMIC SURFACES. SIMULATION 3.	127
FIGURE 162: FRONTAL AREA. GEOMETRY ITERATION 2.	129
FIGURE 163: FRONT-REAR AERODYNAMIC LOAD DISTRIBUTION. SIMULATION 3.	130
FIGURE 164: PRESSURE FIELD UNDER THE REAR WING. SIMULATION 3.	131
FIGURE 165: WAKE VORTEX GENERATED BEHIND THE REAR WING.	132
FIGURE 166: PRESSURE FIELD UNDER THE CAR. NOTICE THE HIGH-PRESSURE ZONE ON THE FRONT SECTION OF THE SPLITTER.	132
FIGURE 167: PRESSURE FIELD ON THE REAR DIFFUSER.	133
FIGURE 168: FLOW UNDER THE REAR DIFFUSER. NOTICE THE FLOW BEING DIRECTED TOWARDS THE MIDDLE SECTION.	134
FIGURE 169: PRESSURE FIELD UNDER THE FRONT WING. NOTICE THE LOWEST PRESSURE CREATED NEAR THE MIDDLE SECTION.	134
FIGURE 170: LOW PRESSURE ON THE FRONT WHEEL FENDER'S SURFACE.	135
FIGURE 171: REDESIGNED FRONT SPLITTER HIGHLIGHTED IN PINK.	136
FIGURE 172: FRONT SPLITTER PROFILE.	137
FIGURE 173: LARGER FRONT WING AREA NEAR THE MIDDLE SECTION OF THE CAR.	137
FIGURE 174: ENGINE AIR DUCT FOR THE FINAL GEOMETRY ITERATION HIGHLIGHTED IN PINK.	138
FIGURE 175: SIDE PANELS.	138
FIGURE 176: AIR DUCT HIGHLIGHTED IN PINK.	139
FIGURE 177: FILLETED FLOOR EDGE HIGHLIGHTED IN PINK.	139
FIGURE 178: RESIDUALS PLOT. SIMULATION 4.	140
FIGURE 179: GLOBAL FORCE REPORT. SIMULATION 4.	140
FIGURE 180: INDIVIDUAL DOWNFORCE REPORT. SIMULATION 4.	141
FIGURE 181: INDIVIDUAL DRAG REPORT. SIMULATION 4.	141
FIGURE 182: CoP COORDINATES. SIMULATION 4.	141
FIGURE 183: AERODYNAMIC LOAD DISTRIBUTION ON EACH AXLE. SIMULATION 4.	143
FIGURE 184: EXAMPLE OF HOW THE AERODYNAMIC LOADS CAN BE EVENED.	143
FIGURE 185: FRONTAL AREA. GEOMETRY ITERATION 3.	143
FIGURE 186: LOW PRESSURE REGION ON THE FRONT SPLITTER. SIMULATION 4.	145
FIGURE 187: STREAMLINES AROUND THE FRONT SPLITTER. NOTICE THE FLOW SEPARATION NEAR THE EXIT. SIMULATION 4.	146
FIGURE 188: AIR FLOW EXITING THE FRONT SPLITTER REGION. SIMULATION 4.	146
FIGURE 189: STAGNATION REGION NEAR THE COOLING DUCTS. SIMULATION 4.	147
FIGURE 190: TURBULENT FLOW EXTRACTION. SIMULATION 4.	147
FIGURE 191: AIR FLOW EXITING THE SIDE PANELS THROUGH THE VENT LOUVRES. SIMULATION 4.	148
FIGURE 192: LOW PRESSURE REGION UNDER THE REAR WING. NOTICE THE CONSTANT LOW-PRESSURE AREA ALONG THE WING. SIMULATION 4.	148
FIGURE 193: FLOW AROUND THE REAR WING MIDDLE SECTION. SIMULATION 4.	149
FIGURE 194: EXHAUST EXIT TO INCREASE THE FLOW ENERGY ON THE REAR DIFFUSER . MCLAREN MP4/15.	152

List of Tables

TABLE 1: CONTROL VOLUME DIMENSIONS.	41
TABLE 2: MESH VALUES.	52
TABLE 3: SURFACE MESH REFINEMENT OPTIONS.	52
TABLE 4: WAKE REFINEMENT VALUES.	52
TABLE 5: PC HARDWARE.	53
TABLE 6: LEVELS OF CONVERGENCE BASED ON RESIDUAL VALUES.	58
TABLE 7: AERODYNAMIC FORCES. SIMULATION 1.	61
TABLE 8: CoP COORDINATES. SIMULATION 1.	61
TABLE 9: FRONTAL REFERENCE AREA FOR THE DRAG AND LIFT COEFFICIENTS. SIMULATION 1.	63
TABLE 10: LIFT AND DRAG COEFFICIENTS. SIMULATION 1.	63
TABLE 11: ORIGINAL AUDI R18 GENERAL AERODYNAMIC DATA [11].	64
TABLE 12: ADJUSTED AUDI R18 AERODYNAMIC DATA. IN GREEN, THE VELOCITY ADJUSTED FORCES.	64
TABLE 13: AERODYNAMIC DATA COMPARISON BETWEEN THE AUDI R18 AND THE BASE GEOMETRY.	65
TABLE 14: RIDE HEIGHTS OF THE MODIFIED GEOMETRY.	72
TABLE 15: INDIVIDUAL REAR WING SIMULATION FORCES.	81
TABLE 16: FORCES GENERATED BY THE SECOND REAR WING PROFILE.	84
TABLE 17: AERODYNAMIC IMPROVEMENTS OF THE REVISED REAR WING GEOMETRY COMPARED TO THE ORIGINAL PROFILE.	85
TABLE 18: DRAG AND DOWNFORCE VALUES OF THE REVISED WING PROFILE WITH THE GURNEY FLAP INSTALLED.	88
TABLE 19: AERODYNAMIC FORCES AND COEFFICIENTS OF THE FRONT WING PROFILE.	91
TABLE 20: AERODYNAMIC DATA OF THE FRONT WING FITTED WITH THE GURNEY FLAP.	94
TABLE 21: MESH VALUES FOR THE SECOND CFD SIMULATION.	99
TABLE 22: WAKE REFINEMENT FOR THE SECOND CFD SIMULATION.	99
TABLE 23: AERODYNAMIC FORCES ON HALF OF THE CAR. SIMULATION 2.	102
TABLE 24: AERODYNAMIC FORCES ON THE WHOLE CAR. SIMULATION 2.	102
TABLE 25: FRONTAL AREA OF THE REVISED GEOMETRY V1.	103
TABLE 26: DRAG AND LIFT COEFFICIENTS OF THE REVISED GEOMETRY V1.	103
TABLE 27: CoP COORDINATES. SIMULATION 2.	103
TABLE 28: GENERAL AERODYNAMIC DATA OF THE REVISED GEOMETRY V1. SIMULATION 2.	104
TABLE 29: COMPARISON BETWEEN THE REVISED GEOMETRY CAR AND THE AUDI R18. SIMULATION 2.	104
TABLE 30: DIFFERENCE IN AERODYNAMIC FORCES BETWEEN THE ORIGINAL AND REVISED GEOMETRY DIFFUSERS.	109
TABLE 31: COMPARISON BETWEEN THE ORIGINAL REAR WING AND THE REVISED REAR WING V1. SIMULATION 2.	110
TABLE 32: DATA DIFFERENCES BETWEEN THE 2D AND 3D SIMULATIONS OF THE REVISED REAR WING PROFILE.	110
TABLE 33: RIDE HEIGHT COMPARISON (0,0° AND 0,5°)	123
TABLE 34: AERODYNAMIC FORCES OF HALF THE CAR. SIMULATION 3.	128
TABLE 35: AERODYNAMIC FORCES OF THE WHOLE CAR. SIMULATION 3.	128
TABLE 36: MEASURED FRONTAL AREA. GEOMETRY ITERATION 2.	129
TABLE 37: DRAG AND LIFT COEFFICIENTS. SIMULATION 3.	129
TABLE 38: CoP COORDINATES. SIMULATION 3.	129
TABLE 39: GENERAL AERODYNAMIC DATA. SIMULATION 3.	130
TABLE 40: AERODYNAMIC FORCES COMPARISON BETWEEN THE LINEAR AND CURVED REAR WING.	131
TABLE 41: AERODYNAMIC FORCES OF HALF THE CAR. SIMULATION 4.	142
TABLE 42: AERODYNAMIC FORCES ACTING ON THE WHOLE CAR. SIMULATION 4.	142
TABLE 43: CoP COORDINATES. SIMULATION 4.	142
TABLE 44: MEASURED FRONTAL AREA. GEOMETRY ITERATION 3.	144
TABLE 45: LIFT AND DRAG COEFFICIENTS. SIMULATION 4.	144
TABLE 46: GENERAL AERODYNAMIC DATA. SIMULATION 4.	144
TABLE 47: COMPARISON BETWEEN THE AUDI R18 AND THE LMP ITERATION 3 AERODYNAMIC DATA. SIMULATION 4.	145
TABLE 48: COMPARISON BETWEEN THE INITIAL CAR GEOMETRY, FINAL CAR GEOMETRY AND AUDI R18.	151

1 Introduction

1.1 General objectives

The objective of this thesis consists in the Computational Fluid Analysis (CFD) of an Le Mans prototype car, focusing on the possible improvements that can be implemented into the vehicle's geometry to achieve the desired aerodynamic performance. Apart from the objective cited above, there are other secondary objectives:

- Validation of the different aerodynamic packages using CFD software tools
- Learn how to develop a full aerodynamic concept
- Learn how to use complex CFD tools applying concepts from fluid dynamics and general physics
- Use CAD design to create complex aerodynamic surfaces
- Use Python code scripts to solve engineering problems

1.2 Performance objectives

Apart from the general objectives explained above, there are a number of objectives regarding the aerodynamic performance of the different concepts and design iterations simulated in this thesis:

- Obtain similar downforce and drag values compared to a LMP car
- Independent validation of minor aerodynamic elements
- Analysis of the load distribution between the front and rear axles
- Reduce drag
- Increase downforce

1.3 Background

Since the beginning of car racing back in the early 20th century, aerodynamics has played a vital role on the design of most race cars. The first wide spread design of cars with aerodynamic performance in mind took place during the 1930's, a time when land speed record cars saw a huge interest, pushing the boundaries of what was established in terms of vehicle performance, and especially aerodynamics. These cars were designed with top speed as the only objective that required high horsepower combined with very low amounts of aerodynamic drag, resulting in futuristic-looking shapes that had its roots in the aircraft design trends of the time:

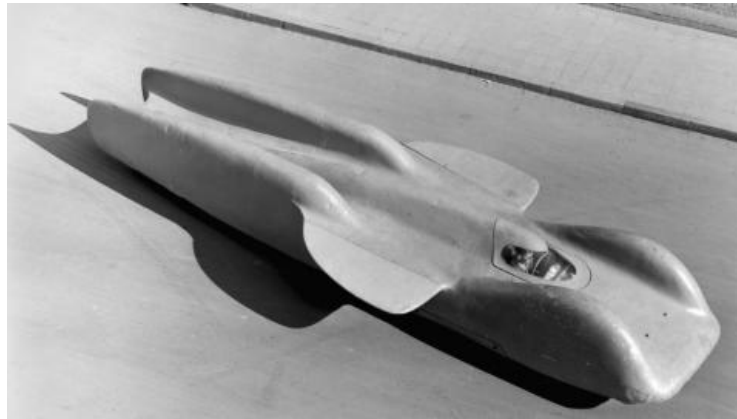


Figure 1: Mercedes T80 land speed car from 1939.

The aerodynamic development of race cars was mainly conducted in wind tunnels designed for aircraft that made it difficult to imitate the real conditions that the car would experiment in a circuit. This pushed the development of modern wind tunnels that were specifically designed for cars and, as a natural progression, engineers realized that by implementing the same basic principles that make airplanes fly could be applied to race cars as a way to generate downforce that increases the car's stability and cornering speeds. This new approach to aerodynamic development took place during the early 1970's, the time that computers were also starting to become a usable tool to solve complex problems that otherwise would require extremely long time to be solved by hand.

Computer technology evolved, and reached a point where the computer power available was enough to run primitive CFD programs. The first use of CFD on motorsport came in the early 1990's, when Formula 1 teams used primitive 2D models to validate rear wing profiles, that later evolved to extremely complex 3D models that require dozens of engineers to set up and run each simulation.

As usual, Formula 1 (F1) represents the pinnacle of motorsport in terms of performance and engineering development, especially in the aerodynamic side of vehicle design, but other high end racing regulations like the World Endurance Championship (WEC) also require similar levels of aerodynamic design compared to F1. Although not as demanding as in Formula 1, the aerodynamic development needed to make a competitive car for the WEC requires a dedicated team of engineers to develop the aerodynamic package.

2 CFD and Fluid Dynamics concepts

2.1 Basic concepts of CFD analysis

CFD stands for “*Computational Fluid Dynamics*”. It is a branch of fluid mechanics that uses numerical methods to solve complex fluid flow problems, such as free flow, internal flow, supersonic, hypersonic, etc. Modern Computational fluid mechanics programs also can solve fluid problems combined with heat transfer, aeroacoustics, combustion, etc.

CFD flourished during the 1980’s due to the exponential increase in computing power of modern pc’s during this decade. This transformed the way in which engineers developed new ideas due to the whole new approach to, what used to be, extremely difficult fluid flow problems. Many of the early CFD programs were developed as a proprietary software of many aerospace industries, such as NASA, Lockheed-Martin, Macdonell-Douglas, etc. Such different projects resulted in multiple software packages, many of them still being sold and developed nowadays (ex: NASTRAN).

Nowadays, CFD is a vital part of many engineering branches, especially aeronautical and mechanical.

2.2 Understanding how CFD analysis works

This method works by dividing the region of analysis in nodes and elements, that discretize the volume of interest in a finite number of elements that will be solved by the computer using numerical models and fluid dynamics equations. This discretized region of interest is commonly known in CFD as “Mesh”. The equations that need to be solved are derived from these elements after setting the boundary conditions and initial physical conditions.

These equations have their roots in the models for conventional fluid dynamics, such as the Conservation Laws, Navier-Stokes Equations, Euler Equations, etc. Although most modern CFD programs have the possibility of setting the solving method and physical conditions, all of them follow the same hierarchy in terms of equations importance, with the Conservation Laws being the most important ones, followed by the different variations of the Navier-Stokes Equations.

2.3 Strengths and Limitations of CFD analysis

Being a discrete analysis method, CFD will always present an error in the solutions for the model compared to the real-life model of the same geometry. Ideally, an infinitely small discretization would perfectly predict the real behavior of a fluid. Obviously, this is impossible, but with growing computational power, more refined and finer models are being analyzed.

One of the most important aspects of CFD modelling is the selection of the correct meshing and physical parameters of the model, in search of a solution that closely resembles the data gathered

from a real-life model or a correct numerical model. This makes comparing solution data a basic task during the completion of a CFD model.

In CFD, very accurate models and results can be easily achieved, solving complex engineering problems that, otherwise, couldn't be solved with manual methods. However, numerical methods are far from perfect, and if simulations are not set-up correctly, numerically generated data may not match that of the empirical experiments.

Due to its numerical approach to solving equations, CFD always presents certain inherent errors, that must be addressed in the pre-processing phase of the analysis. The most common of errors are the following:

- **Simulation residuals:** CFD solvers iterate set equations starting with the previous iteration's result, expecting an ever-decreasing difference between the current equation solution and the previous iteration results. If set properly, these differences tend to dilute as iterations progress, but this may not be the case if the geometrical or physical model haven't been set properly. In most CFD programs, these errors are plotted and continuously updated as the iteration progresses, so that the user can evaluate the validity of the obtained equation solutions.

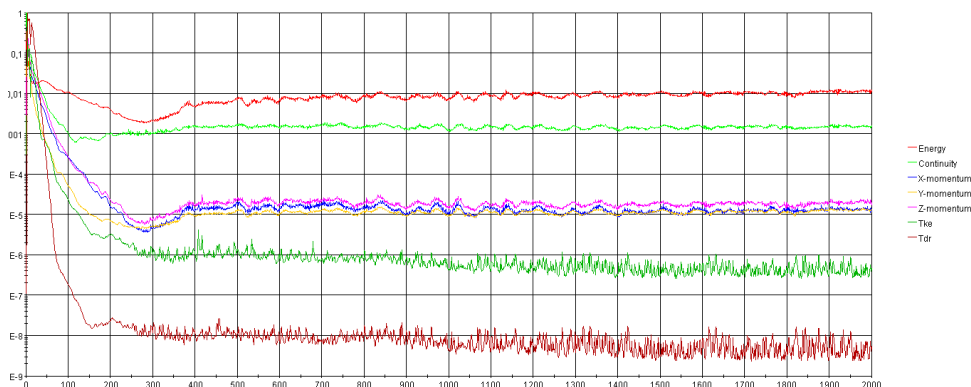


Figure 2: Residuals plotted in STAR CCM+ software.

These residuals must be studied after the simulation in search of possible anomalies with the solver or convergence.

- **Numerical diffusion:** This error occurs when the flow direction is not aligned with the mesh lines that connect the different nodes, generating an error in the equation convergence [1]. The discrepancy is maximized when the flow's local direction and the mesh line conform a 45° angle, and can be reduced by mesh refinements.

This error results in divergent simulation solutions most of the time as cause of bad cell meshing. Most modern CFD software packages include dedicated mesh refinement modules that reduce the probability of numerical diffusivity once all the mesh has been constructed.

2.4 Governing equations

The governing equations establish all the interactions between both the particles and its surroundings, considering the forces (internal and external), pressure, temperature, enthalpy, density, etc. With these equations, the fluid's behavior is fully defined.

Navier-Stokes partial differential equations [1] are the base to all fluid dynamics models, even though these equations have no general solution. These equations are usually simplified by deleting certain parts that have very little influence in the final solution of these equations, thus simplifying the numerical analysis and computing power.

These equations consist of two parts:

- **Continuity Equation:** Establishes the Conservation of Matter principle and, in this application, controls the mass flow inside the control volume (assuming constant density in the flow).

$$\nabla \cdot \vec{V} = 0$$

- **Momentum Equation:** This part of the equation is a particular application of Newton's Second Law.

$$\rho \left(\frac{\partial \vec{V}}{\partial t} + (\vec{V} \cdot \nabla) \vec{V} \right) = -\nabla p + \rho \vec{g} + \mu \nabla^2 \vec{V}$$

Where:

- $\rho \left(\frac{\partial \vec{V}}{\partial t} + (\vec{V} \cdot \nabla) \vec{V} \right)$:

Is the total derivative. This term accounts for the change in velocity inside the fluid and the convective aspect of it.

Terms:

- ρ is the fluid's density.
- $\frac{\partial \vec{V}}{\partial t}$ is the change of velocity with time.
- $(\vec{V} \cdot \nabla) \vec{V}$ is the convection inside the fluid.

- $-\nabla p$:
Is the pressure gradient. Makes the fluid flow in the direction of largest pressure differential.
- $\rho \vec{g}$:
Adds all the external forces that actuate on the fluid (gravitational, electromagnetic, etc). Usually, these forces are so small that are depreciated.
- $\mu \nabla^2 \vec{V}$:

These are the forces derived from the intrinsic viscosity of the fluid. This equation term is extremely important due to the effect of the viscosity value has in the overall behavior of the flow. In cases where the viscosity is very low, like in gas mediums, this term will affect the vorticity throughout the flow. The effects of this equation part will be further explained in the CFD physics model section.

Terms:

- μ is the fluid's viscosity.
- $\nabla^2 \vec{V}$ is the diffusion of momentum

2.5 Concepts of interest in fluid dynamics and CFD

There are certain concepts in fluid dynamics that need to be understood prior to setting the conditions in the numerical analysis, such as non-dimensional numbers, turbulence models, boundary layer management.

2.5.1 non-Dimensional numbers

In fluid dynamics, these numbers determine a relation between different physical attributes, that result in the cancellation of the different numbers' dimensions. These numbers have great importance in fluid dynamics due to the meaningful information implicit in these expressions.

- **Reynold's Number [2]:**

One of the most important dimensionless numbers in fluid dynamics. Determines the turbulent nature within a fluid, depending on its viscosity and velocity in the control volume. It is a relation between the inertia forces and viscous forces of a fluid.

$$Re = \frac{\rho u L}{\mu} = \frac{\text{inertia forces}}{\text{viscous forces}}$$

Where:

- ρ is the fluid's density.
- u is the flow speed.
- L is a characteristic linear dimension.
- μ is the dynamic viscosity of the fluid.

This number's magnitude determines whether the flow is laminar, transient, or turbulent. For air, these are the commonly used Reynold's numbers (Re):

- $Re < 2300$: Laminar flow
- $2300 < Re < 5000$: Transient flow.
- $Re > 5000$: Fully turbulent flow.

For the models used in the CFD analysis, fully turbulent flow is assumed.

- **Mach's Number:**

This number defines the flow speed as a proportion of the fluid's sound speed.

$$Ma = \frac{v}{c}$$

Where:

- v is the flow speed.
- c is the fluid's sound speed. For air, 343 [m/s]

2.5.2 Turbulence models

Most of free flow problems have turbulent nature, meaning that the Reynold's Number throughout most of the control volume is greater than a certain value, in this case over 5000. Prior to running the simulation in CFD, is extremely important to select the correct kind of flow, laminar, transient or turbulent, and the respective mathematical model to obtain good results. For the case being, only turbulent mathematical methods will be considered.

When it comes to CFD, most software relies on four main approaches to modelling turbulent flow in a control volume:

- **Large Eddy Simulation (LES):** This model simplifies the turbulence equation by dismissing the turbulent eddies that occur at small scale, which are the hardest turbulences to solve computationally. This feature makes the LES numerical model not suitable for small scale free flow simulations, like a car.
- **Detached Eddy Simulation (DES):** Combines features from both the Reynolds-averaged Navier-Stokes Equations (RANS) and Large Eddy Simulation (LES) models. Optimizes the model used depending on the flow region: near surface boundaries where eddy size is smaller than the mesh size, RANS is used, and LES is used in the regions where eddy size is greater than the mesh size. This model reduces significantly computing cost but is not widely used in generic CFD simulation because of the increased mesh complexity derived from having two different numerical models.
- **Direct Numerical Simulation (DNS):** Numerically solves the Navier-Stokes Equations without any additional turbulence model. Not used in CFD analysis due to the high computational power needed for this model, although DNS is used in research to improve and develop new turbulence models.
- **Reynolds Averaged Navier-Stokes Equations (RANS):** These equations are obtained from the original Navier-Stokes Equations by averaging them based on the Reynold's decomposition [3]:

$$u(t) = U + u'(t)$$

Of all four main approaches cited here, this is the least computationally expensive method, therefore being the preferred turbulent flow model in CFD analysis. It's important to note that RANS turbulence models are derived from empirical observations, therefore having some degree of discrepancy depending on the flow application. These are the three main RANS variations:

- ***K-Epsilon Standard***: Suitable for pressure changes in regions far away from the boundary walls of the model. As in the K-Omega model, K-Epsilon's main variable is the turbulence kinetic energy (k), with Epsilon being the rate of dissipation of turbulent kinetic energy. This model is used for measuring flow characteristics in regions far away from the complex parts of the model, but is also used to conduct full size external and internal flow simulations.
- ***K-Omega Standard* [5]**: This is a two-equation based RANS model that considers the turbulences generated closed the boundary walls using the wall functions Y^+ based on the turbulence kinetic energy (k) and the specific dissipation value (ω). This model is suitable for high pressure gradients or sudden flow changes.
- ***K-Omega SST (Sear Stress Transport)* [5]**: This K-Omega derived model combines characteristics from the K-Epsilon model depending on the distance relative to the model, using the K-Omega model in the regions closer to the geometry and the K-Epsilon model in the regions far away. This RANS model is widely used because of its versatility, sitting in between the K-Omega and K-Epsilon standard models in terms of computing power.

These three RANS models produce similar results in most situations, although in certain cases, like complex flow and sudden pressure changes, differing results may be obtained. For this simulation, only the K-Epsilon Standard model is used due to the good qualities for external aerodynamic studies combined with the simplicity on computation side.

2.5.3 Boundary layer management

The boundary layer is a region of lower flow speeds generated on the proximity of the walls containing the flow and are intrinsic to all types of fluids with a velocity greater than zero. This reduction in speeds takes place as a result of the interaction between the fluid containing walls and the viscous nature of any fluid.

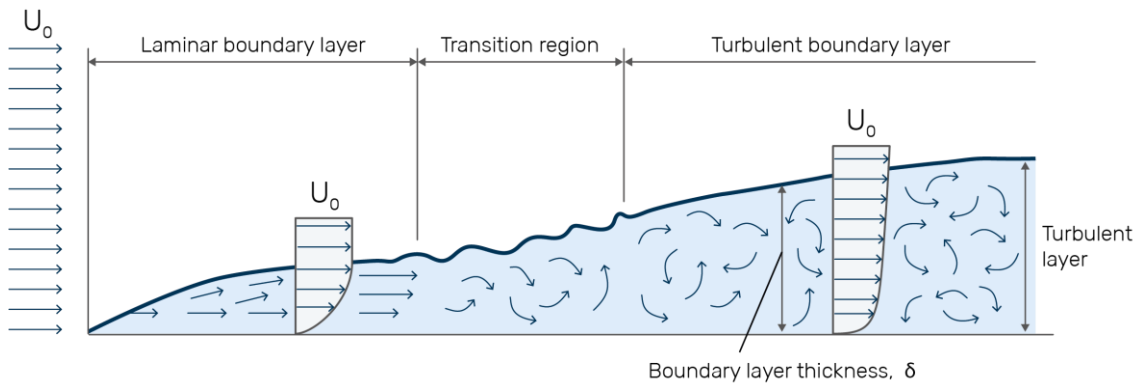


Figure 3: Comparison of boundary layers in laminar and turbulent flow

In *Figure 4* there is a comparison of the different velocity profiles for the boundary layers of both laminar and turbulent flow. For the laminar profile, the flow speed in the layer immediately above the boundary has a speed equal to zero, with flow layers experimenting a parabolic growth in speed with separation from this boundary.

For turbulent boundary layers, this velocity profile has a steeper growth rate because of the flow's chaotic nature, making it difficult to measure the velocity profile accurately, although usually this profile resembles a logarithmic curve. A non-controlled turbulent layer can cause several problems, such as instability at high speeds, unstable downforce values, aerodynamic chatter, and high levels of noise.

In CFD, boundary layer management is critical to perform a simulation with meaningful and representative solutions, and therefore, shall be addressed properly to achieve relevant results. There are multiple ways of simulating the boundary layer in CFD, depending on the model complexity and flow properties. For aerodynamic analysis, these are the main solutions to boundary layer simulation:

- **Prism Layer meshing:** This meshing strategy refines the mesh size in the near proximity of the boundary walls, shaping these cells with a longitudinal pattern parallel to the air flow. Usually, a 4-10 prism layers are created, with a decreasing size from the outermost layer. The common minimum layer thickness is around 2-4mm with a growth factor of 1.2-1.3

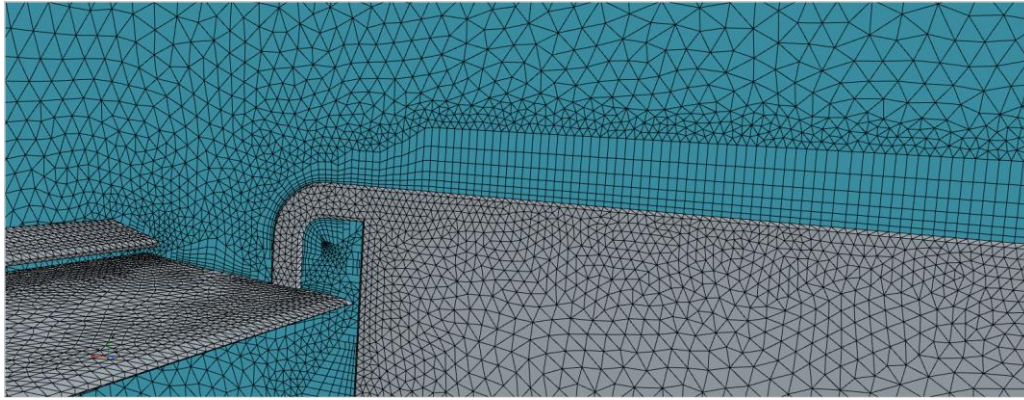


Figure 4: Prism layer in the regions close to the car's surface. Not to scale.

- **Ground relative velocity:** STAR-CCM+ has the ability to set the boundary walls with a non-zero velocity. This is very useful to properly simulate the effect of the boundary layer propagation under the car by setting the groundspeed with a linear velocity vector. This results in a realistic way of simulating the velocity conditions in a real-life situation.

The wheel rotation can also be simulated in STAR-CCM+, but implies high computational power and added complexity, because of the rotating vector is applied to all the nodes and cells in the wheel's proximity. Compared the ground velocity, this rotating boundary condition involves a higher number of calculations for each iteration, so for this analysis, only the ground velocity will be used.

In boundary layer management, layer separation is the most important aspect in terms of derived effects. STAR-CCM+ includes post-processing tools to analyze, locate and quantify the boundary layer separation throughout the whole car's geometry. This comes in handy in iteration-based design workflow, as in this thesis, to improve the geometry regions where the boundary layer separates in future CAD model iterations. The main tool for boundary layer separation is the Extract Separation command.

Turbulent flows are the norm in most of the CFD analysis performed, however, these turbulent flows are highly affected by the boundary walls of the control volume due to the inherent viscous properties of the simulated fluid. Some of the RANS models, like K – Epsilon, are only valid in the region where the turbulence is fully developed [7], thus generating invalid results in regions where the desired solution data, like forces and moments, are generated by boundary walls.

One way to solve this issue is to integrate the turbulence to the wall by creating a layer of thin mesh cells to capture the boundary layer properties:

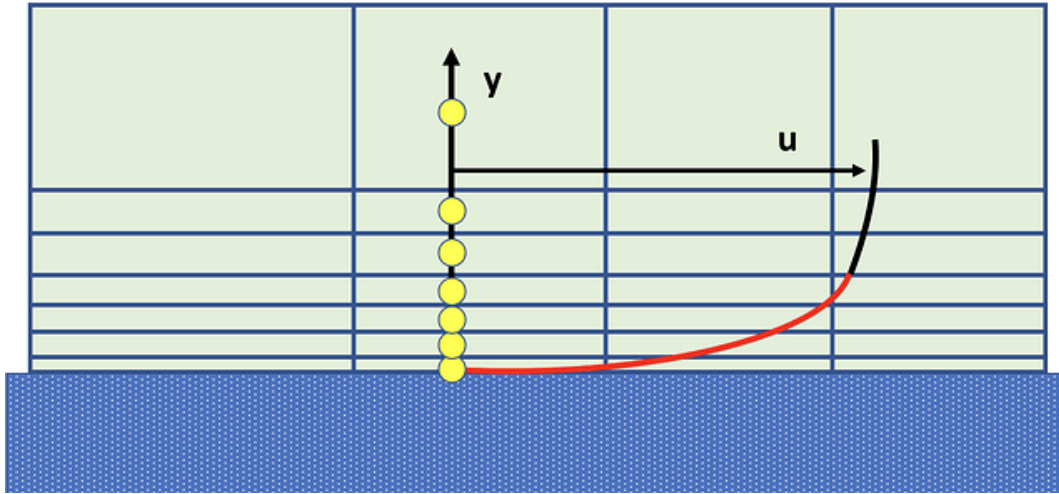


Figure 5: Thin mesh cells capturing the viscous region of the boundary layer. Source: SIMSCALE.

This wall function is suitable for models which require the simulation of forces in aerodynamic surfaces and is usually used with low – Re models like K – Omega. The quality of the first mesh cells in the viscous subregion is determined by the y^+ number, based on the universal law of the wall [7]:

$$y^+ = \frac{y \cdot u_t}{\nu}$$

Where:

- y is the absolute distance from the wall [m].
- u_t is the friction velocity.
- ν is the kinematic viscosity. For air: $1.48E-5$ [m²/s].

The wall y^+ values represent how much of the boundary layer is captured by the mesh in the proximity of a wall boundary. There are different y^+ intervals that determine the section of the boundary layer captured by the solver:

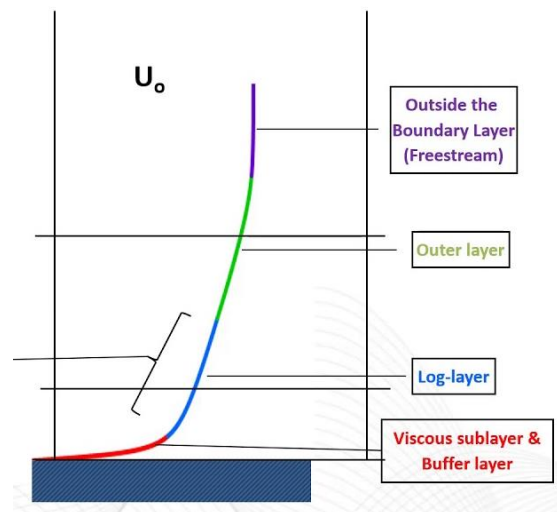


Figure 6: Boundary layer sections based on the normalized speed U .

The Y^+ values increase based on the distance from the computed boundary layer section to the wall. The following graph shows which boundary layer section is captured based on the surface Y^+ value:

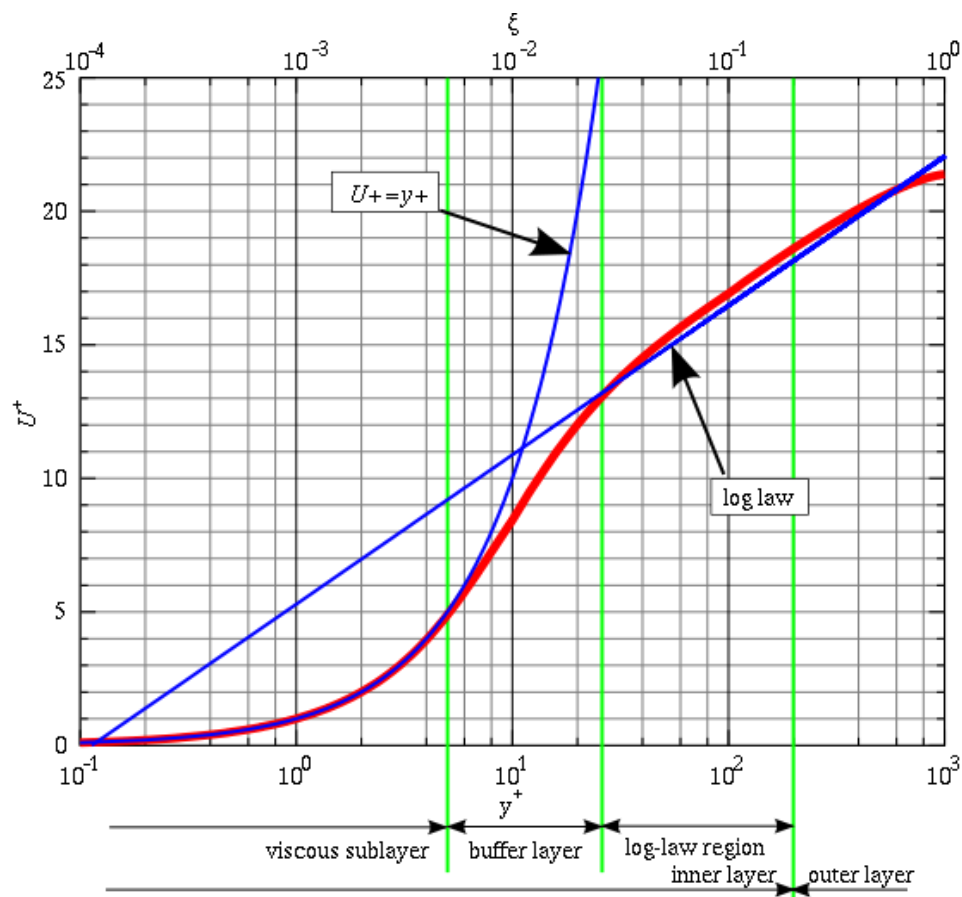


Figure 7: Y^+ values graph. Source: SIMSCALE.

These values determine the wall models needed to capture the boundary layer properties based on the initial target for the Y^+ value. Usually, a base Y^+ value is calculated beforehand to estimate

the thickness value for the prism mesh in contact with the boundary wall of the 3D model. The Y^+ values are only calculated in these initial prism layer cells because of the direct contact with the model.

Most modern CFD programs have two main approaches to wall function computation:

- **Full boundary layer calculation:** This method needs direct implication from the user at the mesh creation stage, as a fully calculated prism mesh is needed. This procedure needs all the initial prism layer cells to have a Y^+ value under 1 throughout the whole first mesh layer to capture all the boundary layer regions (viscous sublayer, buffer layer, log-law region and the outer region) by creating a velocity profile for all the boundary layer. Having a $Y^+ < 1$ in all the initial cells means the whole boundary layer is captured and computed. The mesh sizing can be calculated using the equations cited further in this section, usually resulting in very high number of prism layers near the surface geometry. This usually results in high computational power needed, with the full boundary layer calculation usually reserved for 2D or simple 3D simulations.

It is important to remember that the full boundary layer calculation strategy is incapable of simulating boundary layer separation, thus making this approach unsuitable for external aerodynamic analysis.

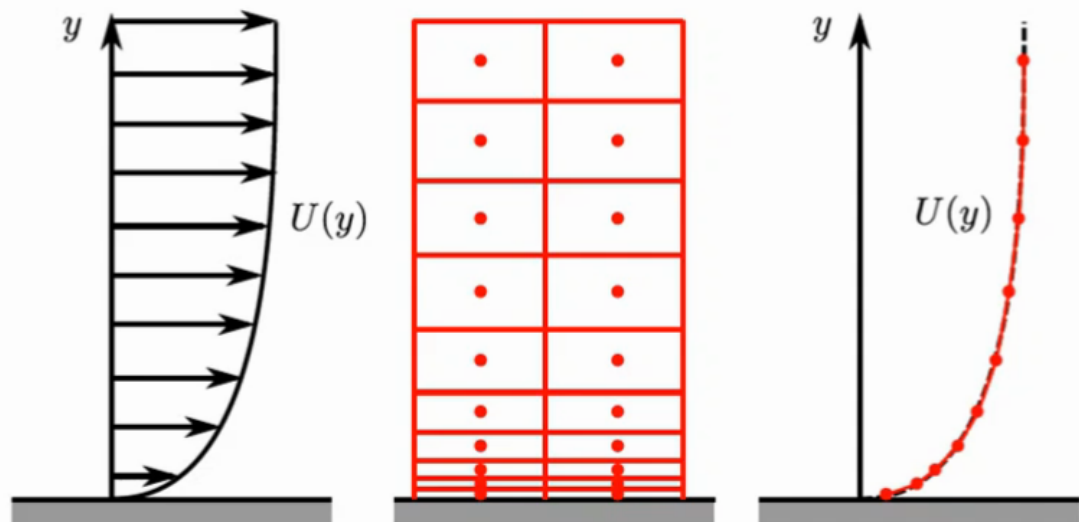


Figure 8: Example of full boundary layer calculation prism mesh. Notice the high cell count needed.

This approach is only used in relatively simple geometry simulations or in cases when high performance computers are available.

- **All-Wall Y+ Treatment (wall functions):** This approach is native to STAR-CCM+, although many other CFD packages also have similar wall function approaches. The All-Wall Y+ Treatment applies the best Y+ strategies based on the flow and boundary layer mesh conditions, either the minimum Y+ value is below 1 or above 30. In each case, the full boundary layer is calculated using a combination of prism layer mesh and approximating functions.

For the All-Wall Y+ Treatment the minimum surface Y+ value is usually kept above 30 to avoid the “Buffer section” ($5 < Y^+ < 30$). This section of the boundary layer usually creates instability in the solution convergence. Instead, the prism layer mesh is constructed by keeping the minimum cell size in the region of the boundary layer where $Y^+ > 30$ for most of the geometry surface. The sections where the Y+ values of the boundary layer are lower than 30 are computed using the so called “Wall Functions”. This software integrated functions approximate the properties of the low Y+ sections of the boundary layer by mathematically approaching the velocity and physics values of this region of the boundary layer. This strategy results in much lower computing power and time needed to obtain a fully converged solution. This is also the preferred approach to complex aerodynamic simulations like the ones to be performed in this thesis.

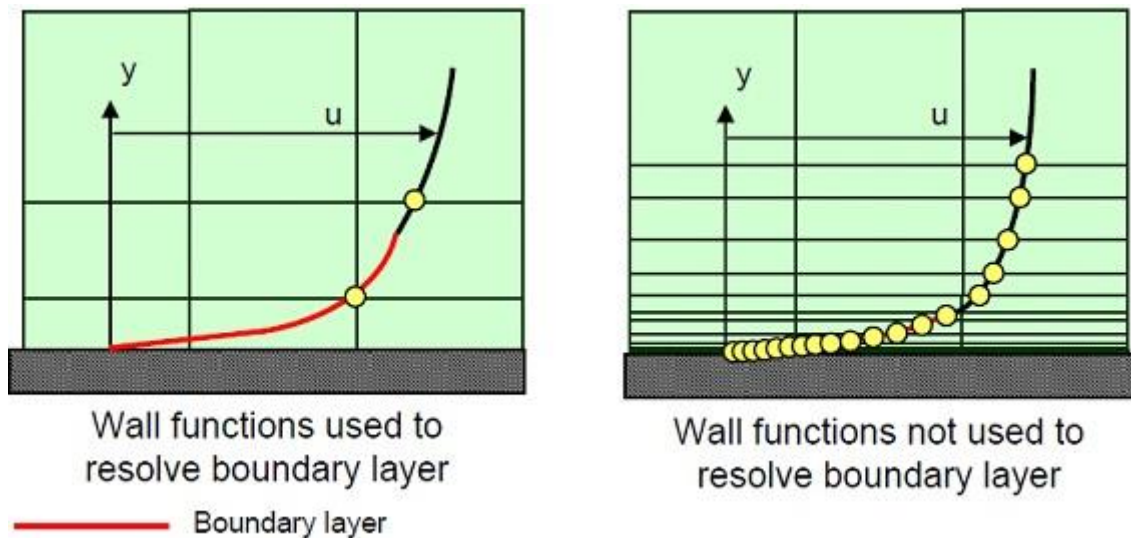


Figure 9: Difference between wall functions and full boundary layer calculations.

To calculate the thickness (y) of the mesh cells, these are the following needed equations [7]:

$$y = \frac{y^+ \cdot \nu}{u_t}$$

u_t is the friction velocity, determined by the following equation:

$$u_t = \sqrt{\frac{\tau_w}{\rho}}$$

Where:

- τ_w is the wall shear stress.
- ρ is the fluid's density (Air: 1.125 [Kg·m⁻³]).

The wall shear stress follows this equation:

$$\tau_w = \frac{1}{2} C_f \rho U_\infty^2$$

Where:

- C_f is the skin friction coefficient.
- U_∞^2 is the square of the free-stream velocity [m/s].

The friction coefficient is defined by [8]:

$$C_f = \frac{\tau_w}{\frac{1}{2} \rho U^2} \sim \frac{2}{\sqrt{Re}}$$

The Reynolds Number (Re) can be estimated by the free-stream flow speed:

$$Re = \frac{\rho U_\infty L}{\mu}$$

Where:

- ρ is the fluid's density.
- u is the flow speed.
- L is the length of the boundary layer. In this case, the boundary layer length is assumed as the car's length (4.5 [m]).
- μ is the dynamic viscosity of the fluid. For air: 1.983E-5 [Nsm⁻²]

2.6 Bernoulli's principle and Venturi effect

Bernoulli's principle dictates how a flow's pressure decreases as its speed and/or potential energy increases.

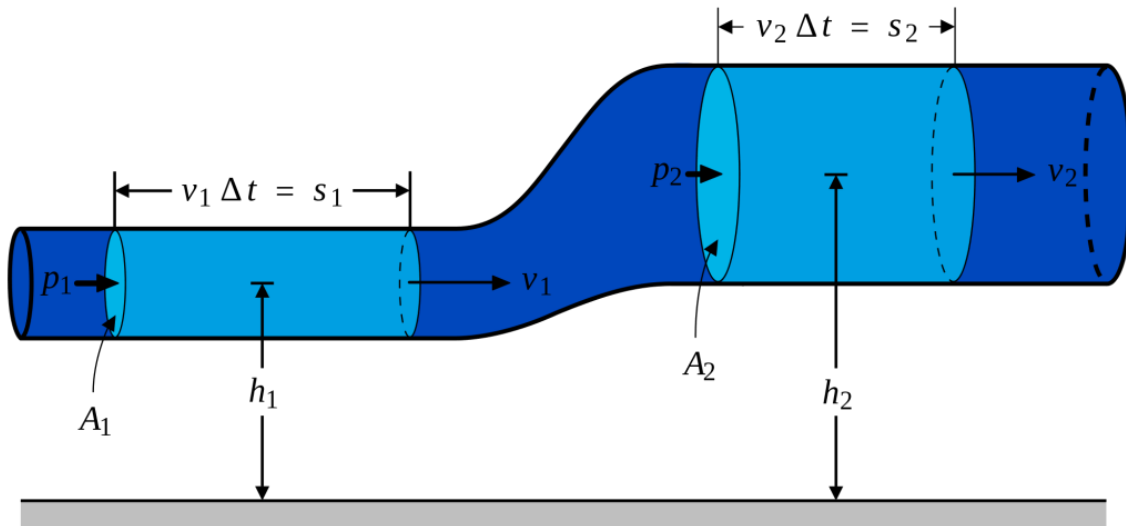


Figure 10: Commonly used pipe to explain Bernoulli's Principle

For a closed region whose inlet and outlet have the same potential energy ($h_1=h_2$), mass flow is equal through the inlet and outlet. Considering the section change, the following equation is derived:

$$A_1 v_1 = A_2 v_2$$

Where:

- A_1 is the inlet surface
- V_1 is the flow speed in the section A_1
- A_2 is the outlet surface
- V_2 is the flow speed in the section A_2

This variation in flow speed is translated into a pressure increase in the second region, where the section surface of the pipe is bigger than the first section. This is a simplified explanation of the principle, but the equation for this phenomenon considers the possible change in potential energy as well:

$$\frac{P_1}{\rho g} + \frac{v_1^2}{2g} + z_1 = \frac{P_2}{\rho g} + \frac{v_2^2}{2g} + z_2$$

Where:

- p_i is the pressure in any point of the fluid
- v_i is the flow speed in any point of the fluid
- z_i is the height of a point inside the fluid

In race cars, Bernoulli's principle is widely used to generate downforce through a particular application of this principle: the Venturi effect. This phenomenon was first described by Venturi, as a particular case of Bernoulli's principle, reserved for the reduction in pressure as a cause of flow section reduction.

This effect occurs as the incoming air flow is conducted into a smaller section area, resulting in an increased air speed, and by Bernoulli's Principle, in a reduction in pressure as well:

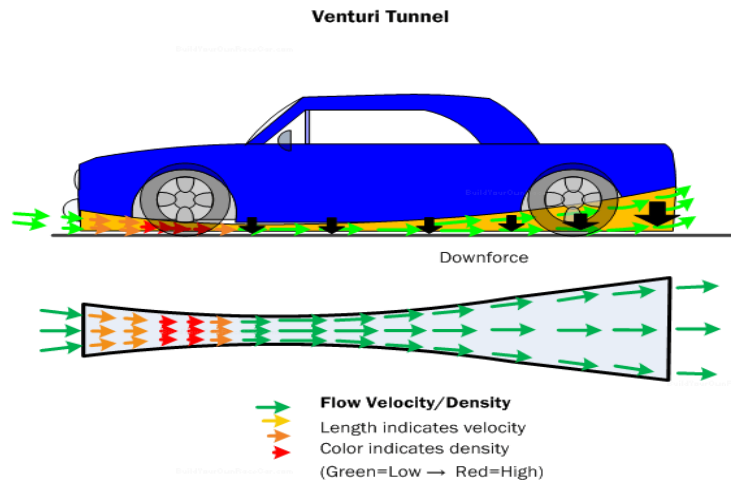


Figure 11: Venturi Effect generating a lower pressure region under a car

The Venturi Effect is achieved in race cars by shaping the underfloor in a wing-like shape. This architecture was first developed in the mid 70's in Formula 1, and created extremely high levels of downforce with very little drag in exchange

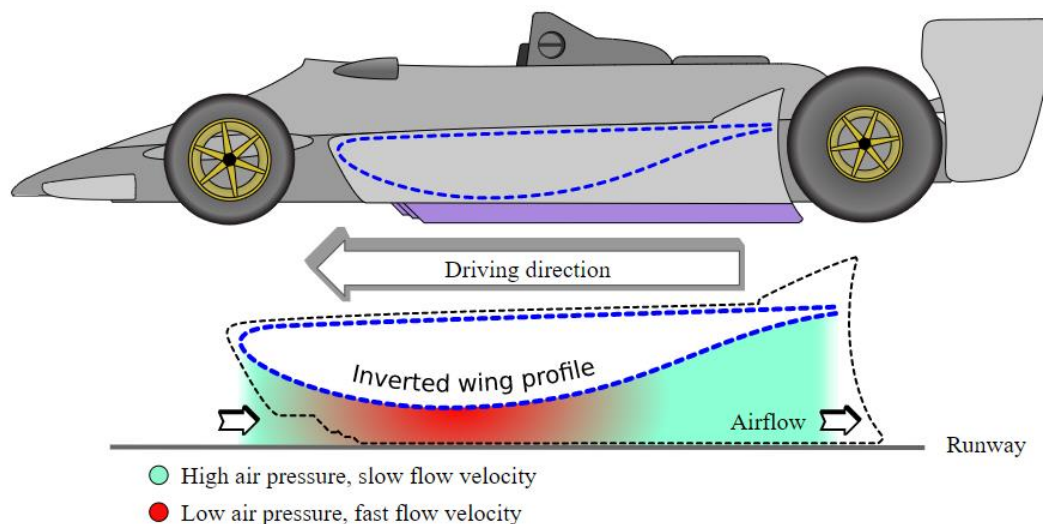


Figure 12: Lotus 79 ground effect car. Notice the inverted wing profile.

A sealed flow under the car was critical to achieve the desired Venturi Effect, with side skirts needed to seal the inverted wing region. These skirts do a great job of sealing the airflow under

the car but pose many secondary problems like accused ride height sensibility and mechanical reliability issues.

Nowadays, the underfloor sealing is achieved by creating high power vortices in the frontmost part of the car. By properly directing these vortices a sealing airflow can be achieved without the previously mentioned problems.

In endurance race cars, this vortex generated sealing effect isn't as pronounced as in Formula 1 cars but must be taken into account while developing the aerodynamic architecture of the car, nonetheless. Also, it is important to mention that the current Venturi Effect underfloor in LMP cars are nowhere near as pronounced as the ones in ground effect Formula 1 cars, being mostly flat except for the front splitter and rear diffuser. The effect of the floor profile is further explained in the geometry section.

2.7 Lift and Drag

In aerodynamics, these two forces are commonly studied to quantify the major forces actuating in a body placed inside an air stream. Instead of expressing these forces in magnitude, a dimensionless approach is preferred, making comparisons between geometries easier, although in race cars, both approaches are equally used.

These forces are automatically calculated on each iteration of the CFD solver, but it is a good practice to understand the fundamentals behind these calculations, in case a discrepancy between the expected and numerical results is found.

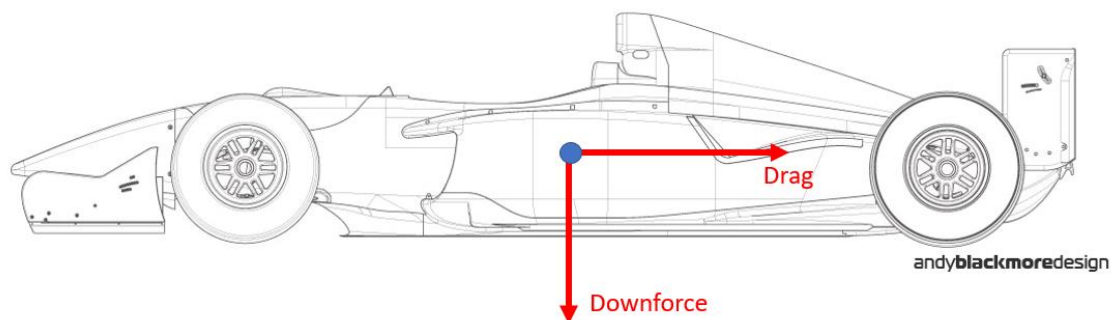


Figure 13: Aerodynamic force components acting on the center of gravity.

2.7.1 Lift force and coefficient

Lift is the aerodynamic force that has a perpendicular direction to the flow. This force is generated by the geometry inside the flow. In race cars, lift actuates downwards, pushing the car into the ground and loading the tires, increasing the friction force in the tires, and resulting in higher cornering speeds as the car experiments high levels of negative lift. In motorsport, this negative lift is commonly referred as "*Downforce*" and is the most important aerodynamic force in race car dynamics.

In race cars, high levels of downforce are ideal, although high levels of negative lift usually come with an increase in drag forces, limiting top speed and increasing fuel consumption (drag forces are opposed to the car's moving direction). A compromise is usually achieved through different aerodynamic packages depending on the car and circuit characteristics but a base lift and drag values must be calculated during the car's development phase, to avoid structural and powertrain issues later in the car's life.

As previously stated, lift is usually expressed as a coefficient of force and fluid properties:

$$C_L = \frac{L}{\frac{1}{2} \rho u^2 S}$$

Where:

- C_L : Lift coefficient
- L : Lift force
- u^2 : flow speed
- S : relevant surface area

In LMP cars, the lift coefficient has a very high low value (negative) compared to road cars because of the downforce generating architecture, although not as high as a formula car. For an endurance car, the Lift coefficient usually takes a value between

2.7.2 Drag force and coefficient

Drag force is the resistance of a body in a fluid environment, with the resulting force component opposing the velocity direction of the car. Two main factors influence the overall drag force: skin friction and form drag.

The fundamental formula of the drag coefficient is very similar to that of the lift coefficient:

$$C_D = \frac{F_D}{\frac{1}{2} \rho u^2 A}$$

Where:

- C_D : Drag coefficient
- F_D : Drag force
- u^2 : flow speed
- A : Reference area

2.8 CFD software: Siemens STAR CCM+

For this thesis, Siemens STAR CCM+ is the chosen CFD software. This program is the engineering industry standard regarding computational fluid dynamics, thanks to its collection of tools, including a built-in CAD module, surface repair tool, automesher, etc. Another great feature of this software is the ease of use and progressive hierarchy feature tree, allowing the user to quickly change the model's characteristics.

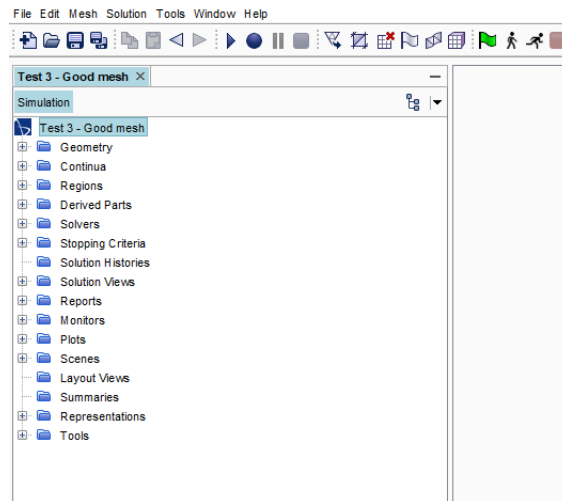


Figure 14: STAR CCM+ Feature tree and toolbars

Apart from the available online tutorials, this program includes over one thousand pages of official documentation provided by the Siemens corporation, covering, and thoroughly explaining all the different options of this software.

The geometry can be imported as a native file from the supported CAD formats (NX and CATIA) or as a neutral 3D file such as Parasolid, STL or STEP. In this thesis, all geometry has been imported from Solidworks as a Parasolid (.X_T) file.

Many of the features included in STAR-CCM+ are explained in future chapters of this thesis.

3 Geometry

Le Mans Prototype (LMP) is a racing car homologation rulebook developed for endurance racing and used in many championships, the most known being the 24 Hours of Le Mans, FIA World Endurance Championship, IMSA Endurance Series and European Le Mans Series [5]. Compared to a Formula 1 car, these cars are not as fast round a circuit, mainly due to higher weight and less aerodynamic downforce, resulting in slower cornering speeds. From all the closed-wheel homologation rules, the LMP cars are the fastest in terms of lap times, rivaling with open wheel cars in some circuits and even achieving a higher top speed than the latter in most configurations due to the overall smaller drag coefficient.

These cars have a very distinctive outer shape as a result of the regulations imposed by the FIA and the low drag requirements of most circuits, with the most important features being:

- Closed wheel arches
- Rectangular view from the top
- “Sharkfin” element between the air intake ram and the rear wing
- Full width rear wing



Figure 15: Typical LMP car

For the base geometry, an LMP style generic car has been selected, containing all the characteristic features of an endurance car, like covered wheels, closed cockpit and a “shark fin” between the engine intake duct and the rear wing. The 3D model meets the legal dimensions of a LMP car imposed by the FIA, making the analysis relevant compared to the experimental aerodynamic data available for this type of cars.

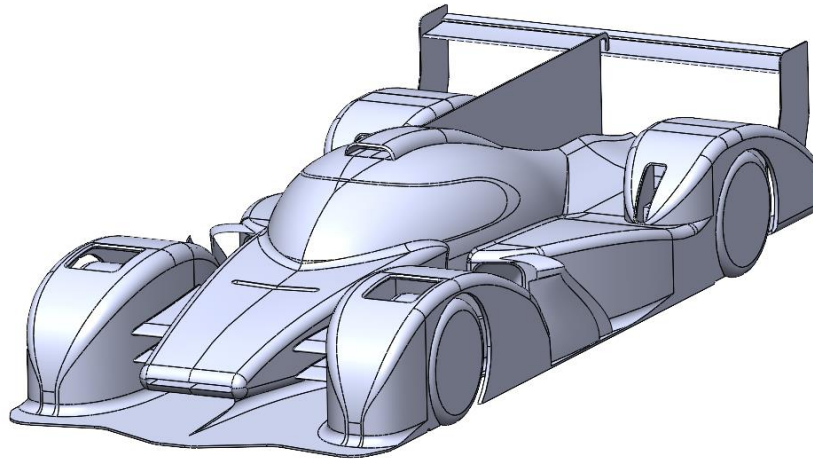


Figure 16: Front $\frac{3}{4}$ view of the base geometry

Although STAR CCM+ has a built-in CAD module, the geometry has been modified using Solidworks due to the more extensive collection of tools, special in surface modelling. This is not a problem, because the geometry produced with Solidworks can easily be exported as a .X_T file into STAR CCM+, without losing geometrical features and resolution.

On the underside of the car, the LMP cars usually have a flat plank of carbon fiber as a low pressure generating aerodynamic structure, resulting in a constant pressure distribution along the whole plank. This characteristic is further explained in the first CFD analysis.

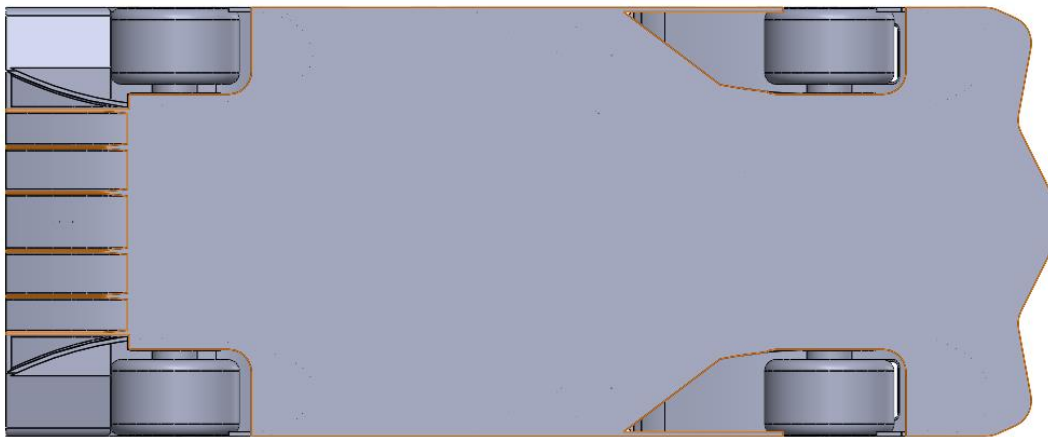


Figure 17: Base CAD underfloor highlighted in orange

The outer dimensions of the CAD model are of the utmost importance, as they will dictate the base mesh size and therefore, highly influencing the precision of the simulation and results. The outer dimensions also dictate the size of the control volume in the CFD simulation, needing enough volume to properly calculate

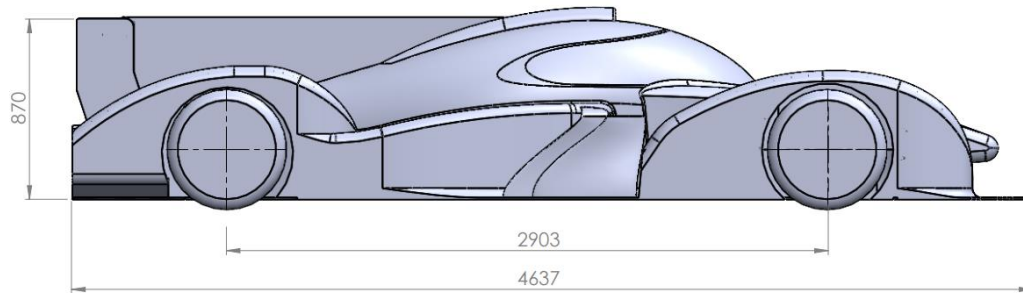


Figure 18: LMP base model side view and dimensions

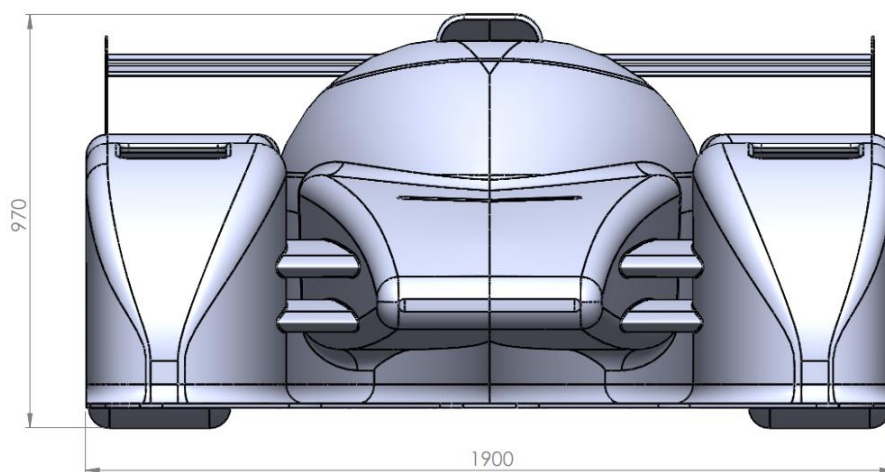


Figure 19: LMP base model front view and dimensions

3.1 Important aerodynamic structures in the car

Even though all aerodynamic surfaces in the car are important, some of them have a critical effect on the overall performance and drivability and can make a huge difference on the aerodynamic efficiency by just making slight changes. There are two main aerodynamic structures in the car:

3.1.1 Floor and rake angle

As previously said, the floor is the most important aerodynamic region in an endurance car due to the highly efficient way in which downforce is generated. This region is very susceptible to ride height changes and must be properly designed to work with the final height values of the car in race conditions.

Boundary layer effects are critical in the floor plank due to its proximity to the ground and having a constant height throughout the whole floor may cause flow stagnation on the rear of the car due to the boundary layer growing and stalling the flow speed in the rear floor and diffuser region. To mitigate this problem, a 0 to 1 degree rake is usually adopted. This angle countereffects the

increasing boundary layer thickness with a longitudinally increasing floor to track surface distance, creating a continuous and homogenous flow under the car.



Figure 20: Rake angle in a Toyota endurance race car.

In the CFD analysis of a car, this angle must be accounted for, as it makes a huge difference in the overall aerodynamic performance and handling of the car. If this angle is not properly set, may cause handling instability, especially when the car drives over a kerb or a bumpy section of the track due to the suddenly decreasing Venturi Effect in the part most separated from the track surface.

3.1.2 Rear wing

Wings and airfoil profiles were first developed in the aircraft industry to create lift by using the incoming air flow and the derived pressure difference in the upper and lower faces of the airfoil. During the mid-1960's, Formula 1 teams started exploring the benefits of fitting inverted aero foil profile wings to the cars in search of faster cornering speeds. This development race between the teams resulted in advanced understanding of car aerodynamics, that ultimately had influence in all motorsport branches, as well as in road cars.

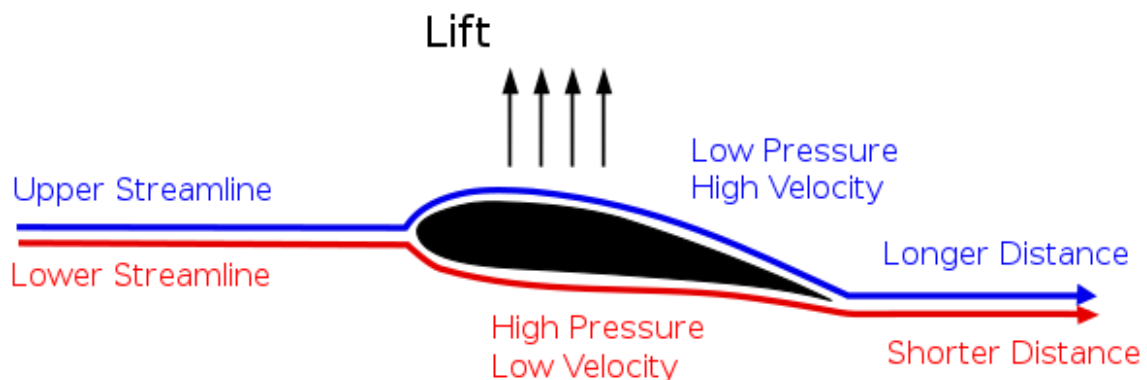


Figure 21: Pressure and velocity in an airfoil

This specific aerodynamic shape generates lift by creating a low-pressure region in the upper half of the airfoil. The low pressure is generated due to the longer tangent distance in the upper part of the airfoil and because the air mass flow must be constant, the flow velocity increases. This flow velocity increase results in a lower pressure (Bernoulli Principle).

In motorsport, these aerodynamic profiles are inverted to generate downforce in multiple parts of the car by placing these airfoils upside down. Depending on the aerodynamic function and purpose, multiple airfoils can be used together to increase the negative lift, this being the case of the rear wing. Usually, two element rear wings are the norm in most forms of motorsport, although three element wings are also used in some motorsport homologations.

For this specific case, FIA rules regarding endurance car homologation rules are followed, stating that only two element rear wings must be used.

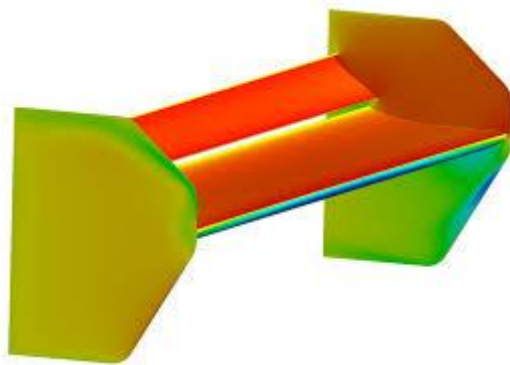


Figure 22: Two element rear wing.

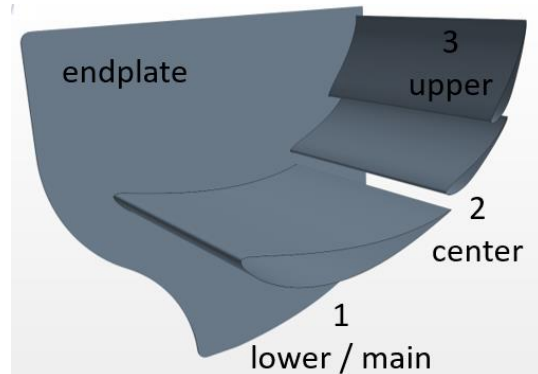


Figure 23: Three element rear wing.

Another important geometrical feature in rear wing is the “*Gurney Flap*”, a small tab perpendicular to the upper element surface that sharpens the exit angle of the airflow, generating a low-pressure region that prevents the flow separation in the lower side of the wing at high attack angles. This small longitudinal flap generates reasonable amounts of downforce with very little drag, thus improving the overall efficiency of the rear wing.



Figure 24: Gurney flap perpendicular to the upper element surface.

At first, fitting this small tab perpendicular to the airflow and creating may seem counter intuitive, but the obtained results speak for themselves. Due to the low-pressure region created immediately behind the Gurney flap, the boundary layer doesn't separate from the suction side of the airfoil, therefore reducing the overall rear wing generated drag that was previously caused by the boundary layer separating at high angles of attack.

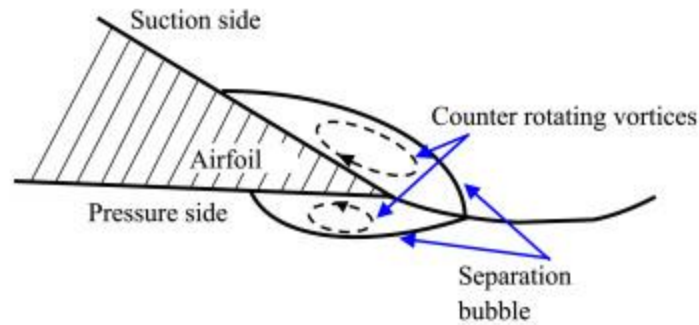


Figure 25: Boundary layer separation in an airfoil at high angles of attack. Notice the separation bubbles

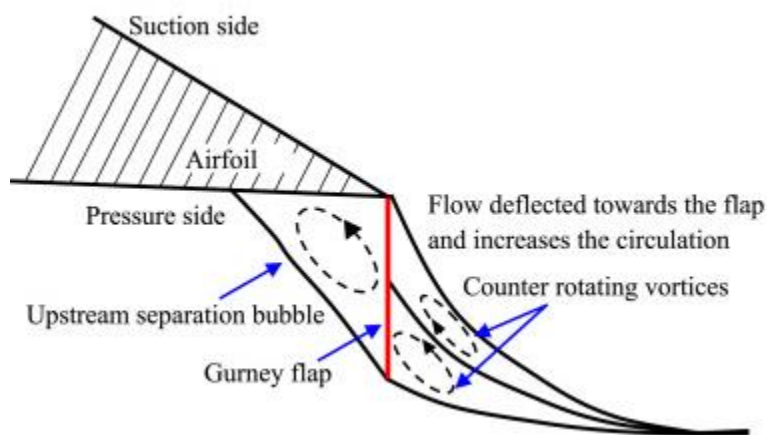


Figure 26: Effect of the Gurney flap in the airfoil of Figure 21. Notice the now coupled flow.

3.1.3 Rear diffuser

This part is critical in the overall aerodynamic behavior of the car, creating a large part of the total downforce in the car. A diffuser works by providing a smooth flow transition between the underside and the free stream air behind the car (wake). This is achieved by increasing the section area in a controlled way to avoid boundary layer separation. In this process, the flow is accelerated in the initial part of the diffuser, creating an additional low-pressure region.

The rear diffuser creates a smooth transition between the high velocity air stream under the car and the low velocity wake stream, assuming constant air density (suitable for low velocity flow studies like the one conducted in this thesis)

4 Base geometry analysis

During this chapter, the CFD analysis is conducted together with the explanation on how STAR CCM+ performs the simulation. Also, the different options for pre- and post-processing are explored.

For the geometry, the base model is analyzed using only one half of the car using a symmetry boundary wall in the CFD program. This reduces the computational power needed for a fully converged simulation. Also, better results are achieved because of the finer mesh.

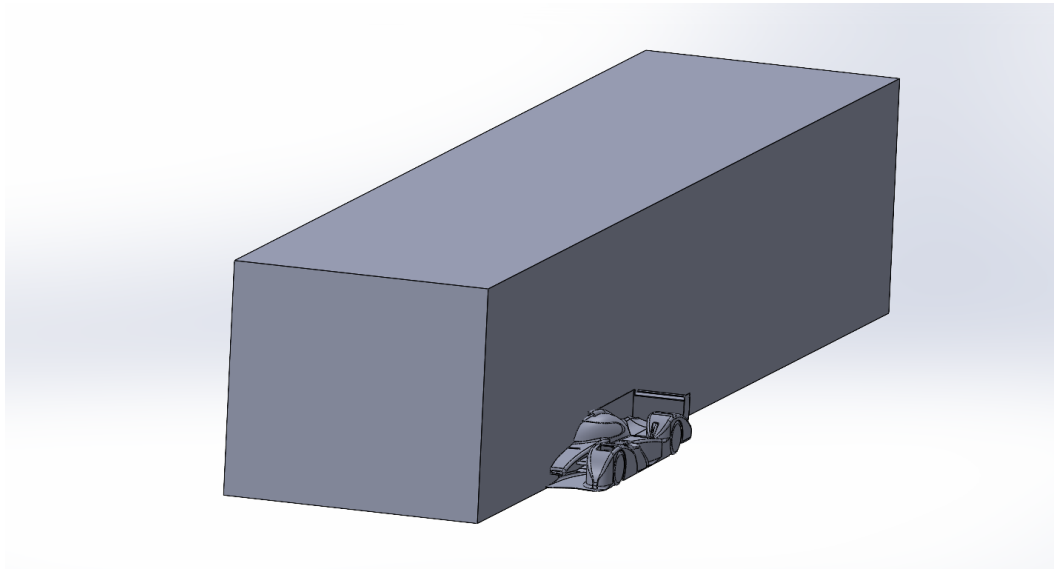


Figure 27: Control volume and the car's position.

The control volume is generated in Solidworks due to the native file compatibility, making the Boolean subtract operation cleaner. This could also be done natively in STAR-CCM+ but part files are imported to this program as a mesh, usually resulting in more complex Boolean operations. The final control volume is imported to STAR-CCM+ as a Parasolid (.x_t) file.

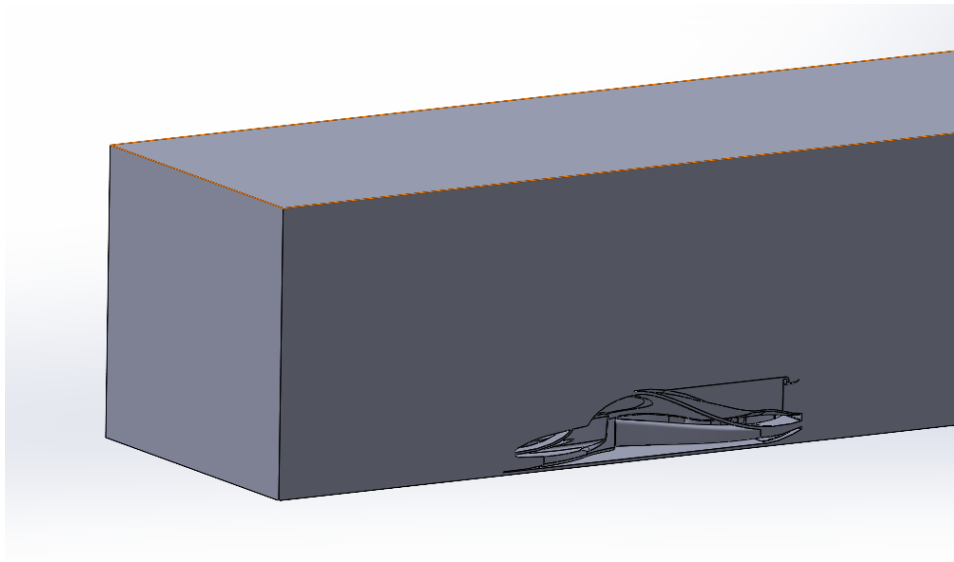


Figure 28: Hollow cavity inside the control volume.

4.1 Control volume

To avoid differences between simulations, the control volume has fixed dimensions for all three simulations. This volume must have sufficient distance to the car model, specially behind the model, to properly calculate the turbulences generated by the model. Having a small control volume may result in bad results and poor convergence, even divergent results if the turbulent flow energy near the control volume boundaries is too high. Usually, the common practice when designing a control volume for CFD is to replicate the distribution and proportions of an automotive wind tunnel.



Figure 29: Automotive wind tunnel for 1:1 sized car.

For these simulations, only the right half of the car is analyzed due to the longitudinal symmetry.

These are the final dimensions of the control volume:

Direction	Value [mm]
Length (X)	21000
Height (Y)	4000
Width (Z)	4500
Distance from Inlet to front of the car (X)	3500

Table 1: Control volume dimensions.

It is important to model the tire-ground contact patch, as this section greatly influences the aerodynamic behavior under the car. For this geometry, a tangent plane to all four wheels has been created, used as a ground reference. From this reference plane, another parallel plane is created with a vertical separation of 12 mm. This simulates the tire contact patch under load.

Also, this method of setting the ground clearance allows for quick ride height changes as both planes are automatically updated once the desired dimension has been changed. This is useful in the incoming models with variable ride height and rake angle.

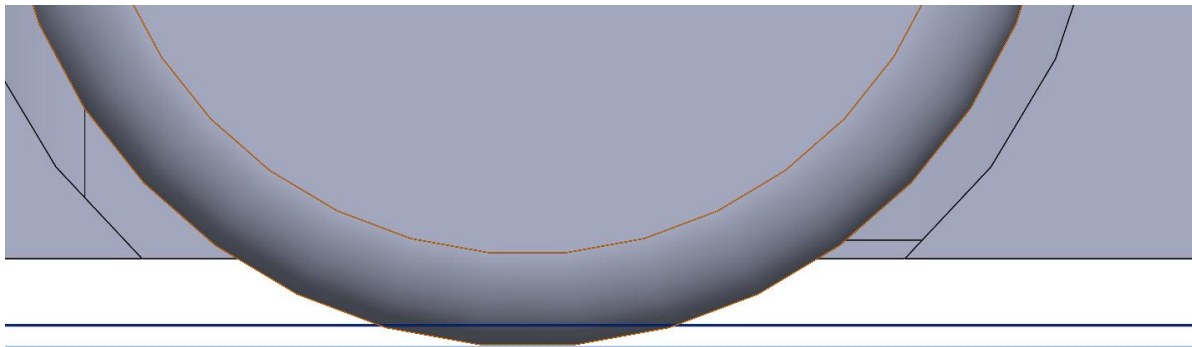


Figure 30: Top plane is the real contact plane. Lower plane is the ground plane.

Once both planes have been created, the car geometry is imported into a new part file to create the control volume:

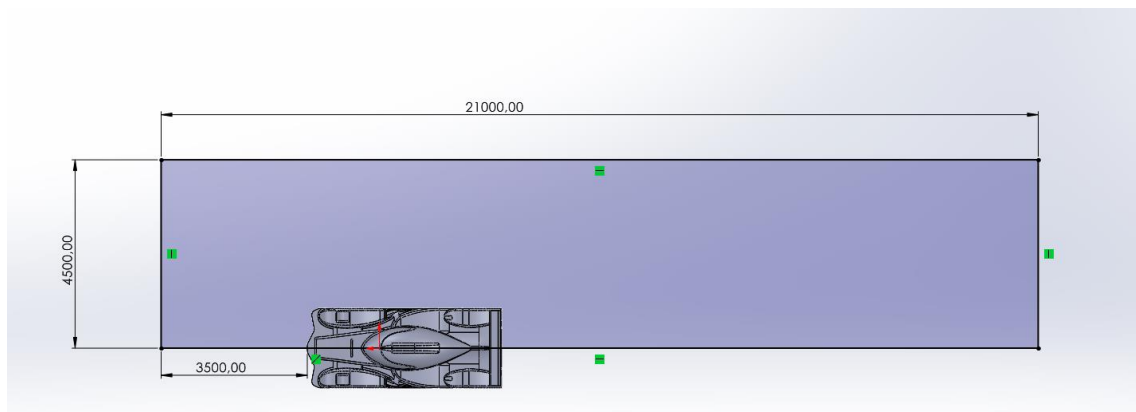


Figure 31: Top view of the control volume set-up and dimensions.

This profile is extruded using a non-combine option. This generates two bodies, one for the car and another one for the control volume:

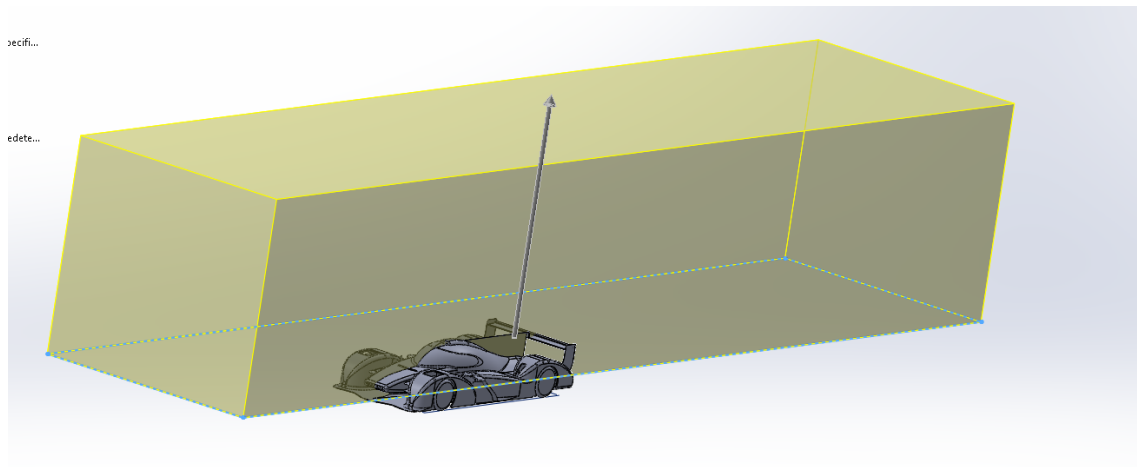


Figure 32: Extrude operation.

The last step to generate the complete control volume is to perform a Boolean subtract operation. This consists of subtracting the part of the car inside the control volume from this new body. This is the final geometry for the control volume:

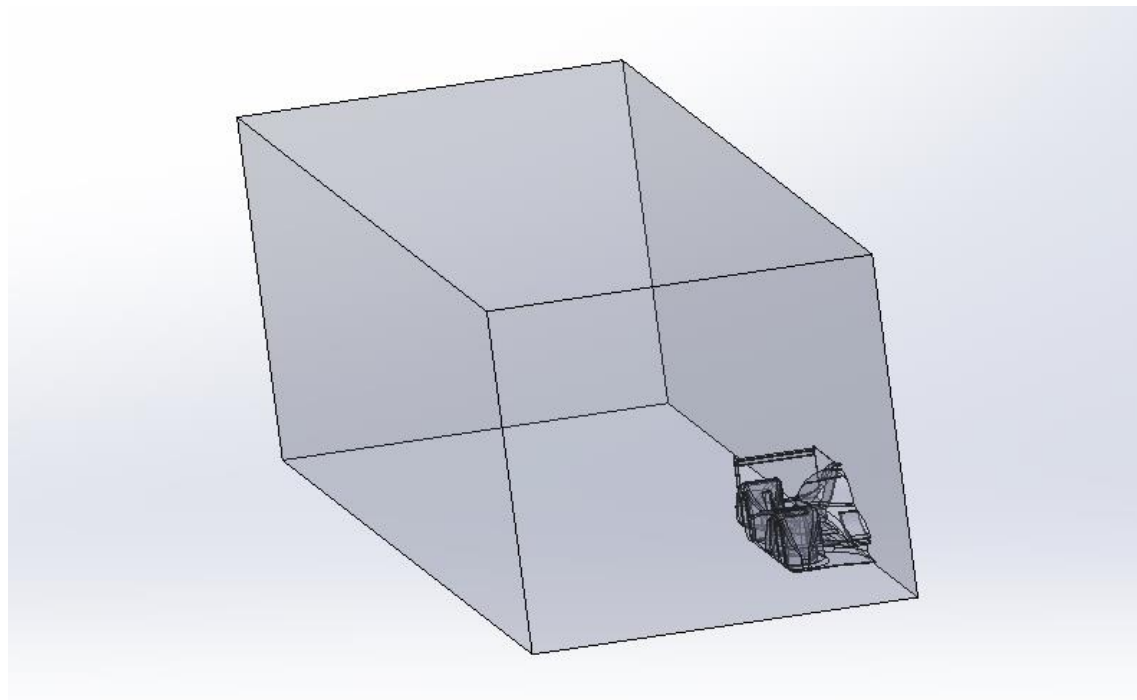


Figure 33: Control volume ready for CFD analysis.

This model is saved as a Parasolid (.x_t), ready to be imported into STAR-CCM+.

4.2 Pre-Processing

In the pre-process stage, all the steps prior to running the simulation are set. This is the most important stage in the CFD analysis workflow because of the importance of proper initial conditions, that will later condition the final quality of the results. These are the pre-processing steps:

1. Import the car geometry and surface management.
2. Create the boundary conditions for the control volume.
3. Create the physical model.
4. Perform the mesh operation.
5. Create reports and plots with the necessary data (drag, downforce, etc.).

Of all these stages, meshing is the most critical due to the important effect on the simulation results. A fine and coherent mesh must be created to avoid convergence issues. This meshing process usually requires multiple iterations until a mesh that captures the geometry features without being too fine is achieved.

These stages are further explained in the following pre-processing chapters.

4.2.1 Pre-process: geometry import

As explained in the previous chapter, the CAD geometry is imported into STAR-CCM+ as a Parasolid file. The geometry can be imported as many different file formats, but Parasolid is preferred due to its mesh simplicity compared to STEP and STL files. These files import the geometry as a mesh, not as a complete and native 3D CAD file.

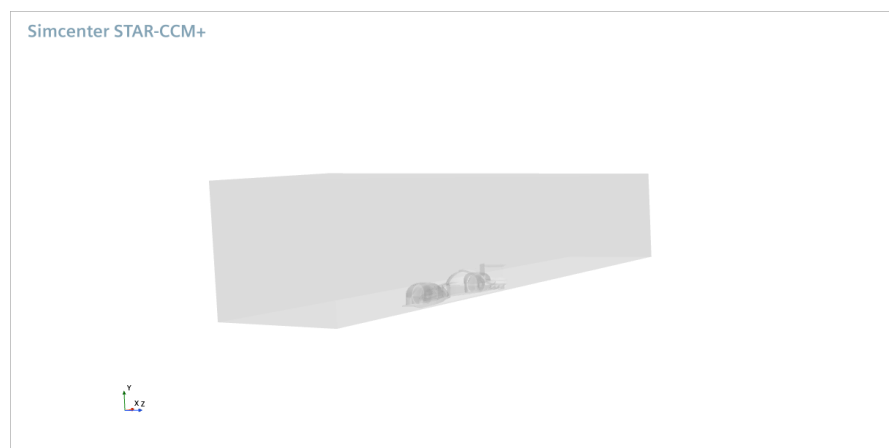


Figure 34: Geometry imported into STAR-CCM+

It is a good practice to run the “Repair Surface” command after importing the geometry, in case there are duplicated faces or non-manifold surfaces in the imported file. For this case there are any issues with the surface quality of the geometry mesh.

After checking the quality, the surfaces that compose the whole geometry must be separated and organized into groups or individual surfaces. This allows for an easy creation of the boundary conditions in further steps of the pre-processing workflow. It is also important to group each important aerodynamic surfaces into a single group each, in order to calculate independent aerodynamic values for each aerodynamic part.

For these simulations, these are the aerodynamic parts that are analyzed separately:

- Rear diffuser
- Rear wing
- Underfloor
- Front part of the floor pan (top side)

These surface groups are creating using the “*Split by Patch*” command inside the Parts dialog tree:

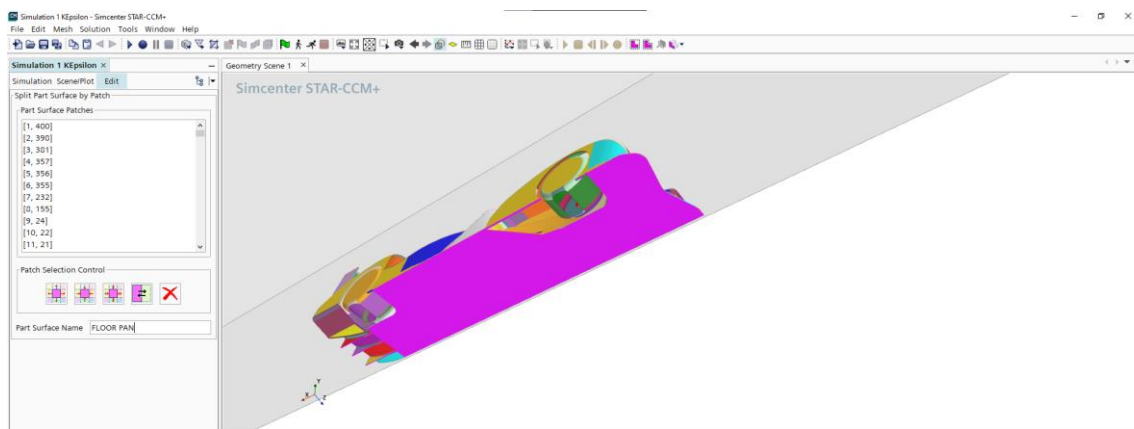


Figure 35: Selection and naming of the selected face.

Once all the surfaces have been grouped. This is the result:

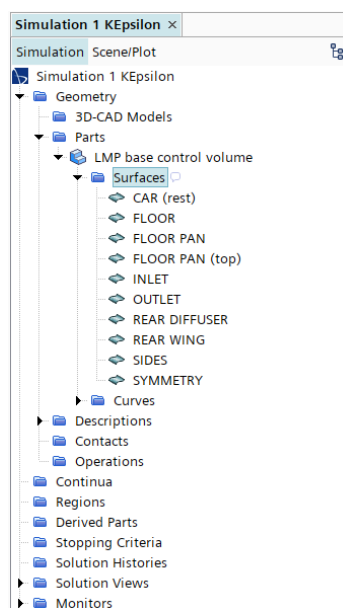


Figure 36: All the surfaces have been grouped either by boundary surface or aerodynamic surface.

4.2.3 Boundary conditions

The boundary conditions are the conditions imposed to the model before running the simulation. Usually, these conditions specify the initial or steady conditions in which the model is about to be simulated. For this case, these boundary conditions represent the environment condition and values in which the car would perform.

In STAR-CCM+, there are nine different boundary layer conditions depending on the required computation dynamics. For this simulation, only 4 are used:

- **Wall:** Represents an impermeable surface with friction and boundary layer interaction characteristics.
- **Symmetry Plane:** Similar to a Wall boundary, but has a no-Slip condition together with an imaginary symmetry plane. This boundary mirrors all the solution values as if the whole mesh domain was existing.
- **Velocity Inlet:** Represents the inlet of a duct at which the flow velocity is known. This is the CFD analogy of the air inlet duct of a wind tunnel
- **Pressure Outlet:** Is a flow outlet with a fixed specified pressure.

Once all the surfaces have been grouped, STAR-CCM+ automatically assigns each surface group to a new boundary surface by using the “Assign parts to Region” command in the Parts dialog tree:

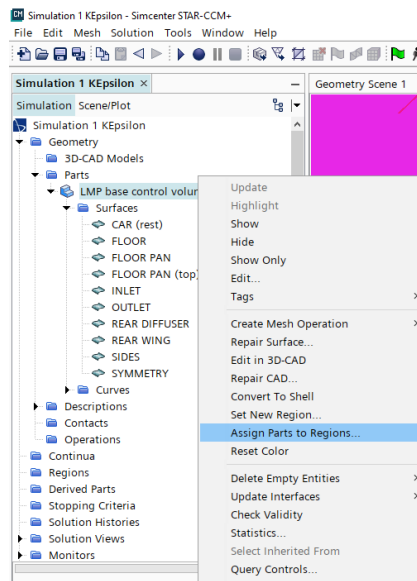


Figure 37: Boundary surface creation command.

This command generates one boundary condition for each surface group. By default, these boundaries are set to “Wall”, therefore some of them must be changed to the correct type. The boundaries have to be assigned before performing the mesh operation due to the mesh being influenced depending on the boundary type on each part surface.

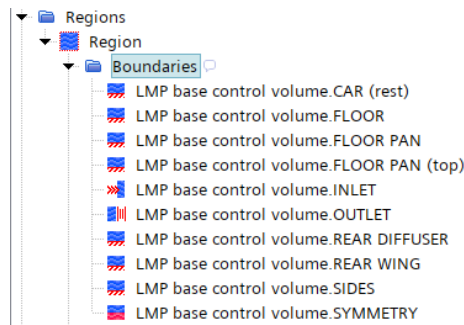


Figure 38: List of all the boundary conditions and types.

For now, the boundary conditions aren't assigned any physical values because there is no physical model existing. Once the physical model is set, the values for the boundary conditions have to be assigned. This is further explained in the physical model chapter.

4.2.4 Physics continuum

In CFD, the physical model dictates how the simulation is going to be performed and the physical magnitudes that are going to influence the final simulation results. In STAR-CCM+, the physical model is easily created using the “*New physics continuum*” command in the Continua section. A new physics model is created, with all the available physics models unselected.

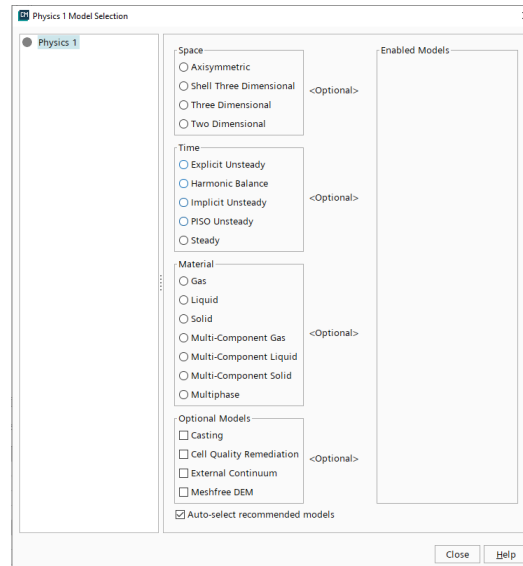


Figure 39: Available physics models in STAR-CCM+

For the simulations in this thesis, these are the physical models that are going to be used:

- Three dimensional
- Steady: Simulates the flow in a stationary flow situation
- Gas: Air by default
- Segregated flow: Suitable for low Mach number simulations. Less computational expensive than coupled flow
- Constant density
- Turbulent flow
- RANS equations

The final physics model has the following attributes:

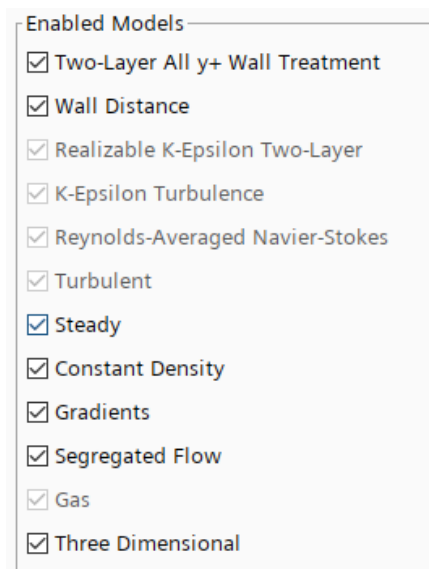


Figure 40: Physics model.

For the first simulation, all four RANS variations cited in “2.5.2 Turbulence models” will be explored in the first simulation. This allows for a direct comparison between the available RANS model and the computational resources needed for each simulation converge. From all the four available RANS models the one with the best compromise between accuracy and convergence time is selected.

Before performing the mesh operation, it is necessary to set the initial velocity and steady velocity values in both the physics continua and the boundary conditions. For the initial conditions, STAR-CCM+ allows to pre-set a fixed vectorial speed in all the cells inside the fluid domain. This allows for a faster convergence. The speed must be set according to the direction of the inlet velocity.

Velocity - Properties ×		—
▼ Properties		
Method	Constant	▼
Value	[10.0, 0.0, 0.0] m/s	...
Dimensions	Velocity	...
Coordinate System	Laboratory	▼

Figure 41: Initial velocity in all the domain cells. 10 [m/s] positive in the X axis.

For the boundary conditions, only the inlet velocity has to be specified, as the default pressure at the outlet boundary is set to 0.0 [Pa] relative pressure.

Velocity - Properties ×		—
▼ Properties		
Method	Constant	▼
Value	[75.0, 0.0, 0.0] m/s	+++
Dimensions	Velocity	+++
Coordinate System	Laboratory	▼

Figure 42: Flow velocity at the inlet boundary. 75 [m/s] or 270 [km/h] in the positive X axis direction.

To properly simulate real life conditions, the ground boundary is set to have a relative velocity to the car, simulating the moving ground under the car:

Relative Velocity - Properties ×		—
▼ Properties		
Method	Constant	▼
Value	[75.0, 0.0, 0.0] m/s	+++
Dimensions	Velocity	+++
Coordinate System	Laboratory	▼

Figure 43: Moving ground under the vehicle using relative velocity on the Ground boundary.

For the pressure, this program automatically sets the reference pressure to 101325 Pa absolute pressure, with rest of the pressure values now on being expressed in relative pressure to this absolute reference pressure.

Reference Pressure - Properties ×		—
▼ Properties		
Value	101325.0 Pa	+++

Figure 44: Absolute pressure.

For the turbulence reference and initial values, STAR-CCM+ automatically selects the base values according to the physics model selected. Unless the initial values of the turbulence model must be changed, these values shall not be changed, as a small change in the initial turbulence threshold may cause divergent or poor results.

4.2.5 Mesh operation

In CFD pre-processing this is the most important stage in the pre-processing workflow, dictating the quality of the obtained solution or even the its correct convergence. Usually, obtaining a good quality mesh is a trial-and-error procedure in which a compromise between a finer mesh and computational requirements is needed.

In STAR-CCM+ the mesh is constructed using a method known as “Per parts meshing” in which the mesh is generated inside the geometry dialog tree. This workflow allows the user test multiple geometry iterations inside the same file without creating separate meshing operations. For example, 2 or more parts can be imported into the simulation file for multiple simulation

iterations, but only one mesh operation is created, selecting the exact part that is going to be meshed. This method saves time and storage space by optimizing the mesh workflow.

To create a mesh operation, the *“Create Mesh Operation”* and *“Automated Mesh”* commands shall be selected from the part set to be meshed.

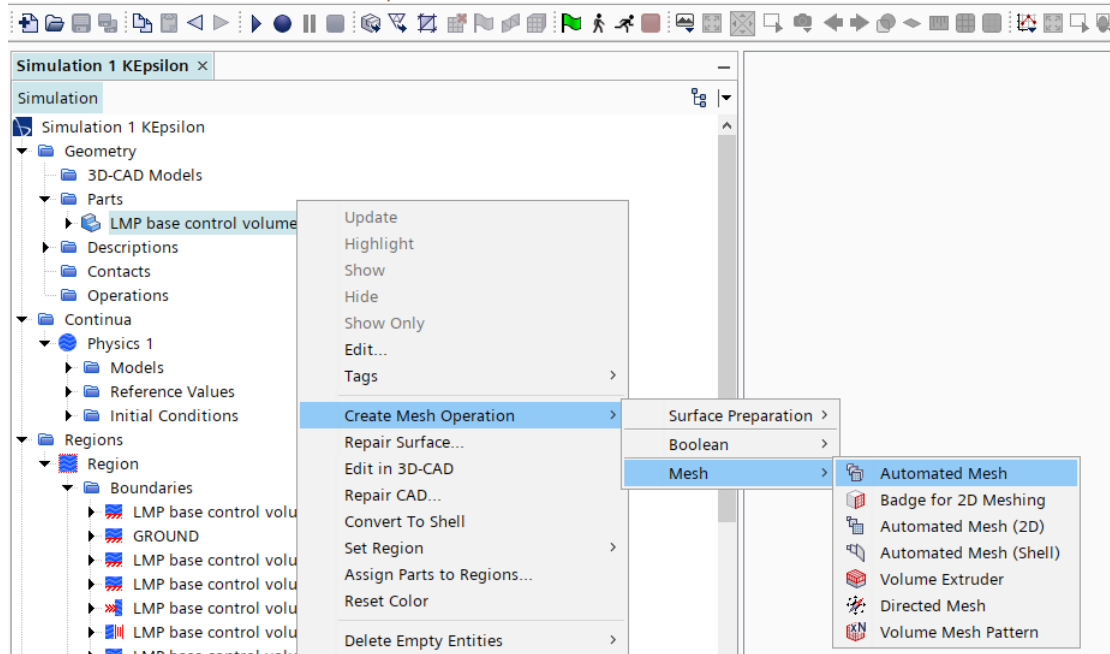


Figure 45: Automated mesh creation.

After creating this operation, the different mesh utilities are selected. For this case, these are the chosen meshers:

- **Surface Remesher:** This mesher uses the existing part mesh to create a surface mesh identical to it.
- **Automatic Surface repair:** Repairs the possible broken faces in the remeshed surface mesh.
- **Tetrahedral Mesh:** This volume mesh is composed of tetrahedral shaped cells. Combines good performance for aerodynamic simulation and low memory requirements.
- **Prism Layer Mesh:** Creates a layer of longitudinal thin cells to improve the boundary layer simulation.

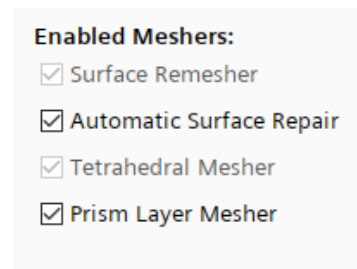


Figure 46: Meshers to be used in this Simulation.

Once the meshers have been selected, STAR-CCM+ requires the user to input the values that will determine the mesh cell count and final mesh quality. It is important to notice the exponential nature of the cell size reduction, where the cell count increases following a third-degree exponential function for a given cell size reduction compared to the previous cell size due to the volumetric mesh operation. This exponential growth in cell numbers must be taken into account at the time of introducing the base cell size values.

In STAR-CCM+ the mesh operation consists of many different variables, with the following being the most important:

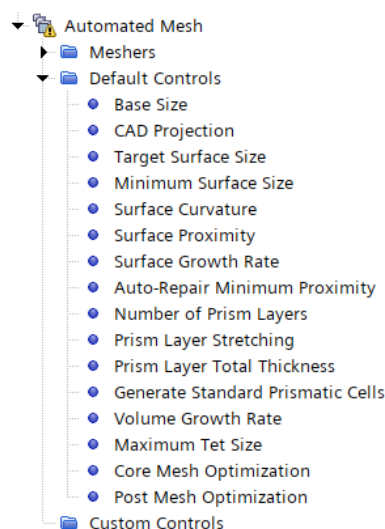


Figure 47: Main mesh variables in STAR-CCM+.

For this mesh operation multiple mesh models have been tested before finding the correct relation between cell size and computing power. These are the mesh size values that are going to be used on all mesh operation in this thesis:

Variable	Value
Base Size	220 [mm]
CAD Projection	yes
Target Surface Size	100.0 % of Base Size
Minimum Surface Size	7.5 [mm]
Surface Curvature	72 pts/circle, Max 360 pts/circle
Surface Growth Rate	Slow
Number of Prism Layers	4
Prism Layer Stretching	1.5
Prism Layer Total Thickness	15 [mm]
Volume Growth Rate	1.25
Maximum Tet Size	100.0 % of Base Size

Table 2: Mesh values.

In aerodynamic simulations a wake refinement operation is usually created to improve the results in the area right behind the car. This allows for a more precise analysis of the wake and turbulence characteristics of the car, giving the engineer valuable information. The mesh is refined using the “*Wake Refinement*” command under the surface control toggle window:

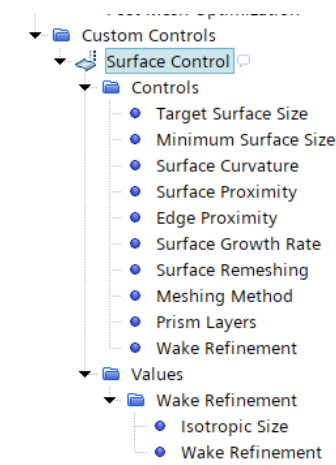


Table 3: Surface mesh refinement options.

These are the values for the wake refinement operation:

Variable	Value
Wake Distance	3.5 [m]
Direction	Vector (XYZ): [1, 0, 0]
Spread Angle	14 °
Isotropic Size	40 [mm]
Growth Rate	1.25

Table 4: Wake refinement values.

After introducing all the required values, the mesh operation is executed and the final mesh volume is computed. Usually, an aerodynamic study on a car has a minimum of $5E7$ cells forming an extremely fine mesh in order to obtain highly accurate results. This high cell count operations are performed with very powerful computing servers and normally take many hours, or even days, to complete a single simulation.

In this case, the mesh cell count has been reduced to around $5.9E6$ cells due to the limited computational power available. These are the computer's characteristics used on this thesis:

Hardware	Model
PC	Dell XPS 15 (9560)
Processor	Intel i7-7700HQ (4 core)
GPU	Nvidia GTX 1050 (4 Gb)
RAM	16 Gb, DDR4 2666Mhz

Table 5: PC hardware.

The full mesh operation takes about 18 minutes to complete, with the following results:

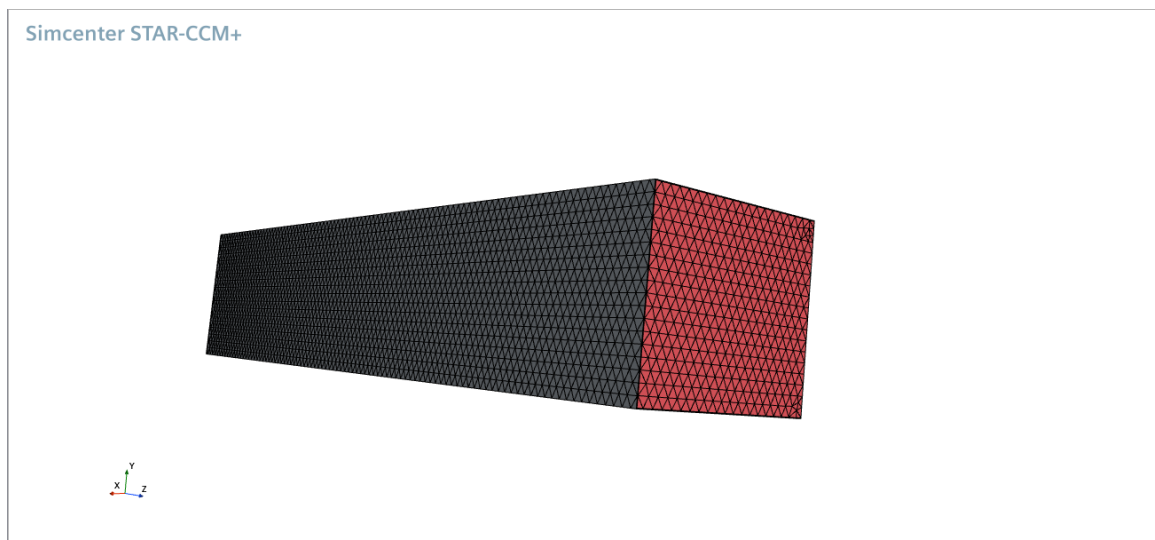


Figure 48: Outer view of the mesh volume.

The mesh operation creates a coarser mesh on the areas that are far away from the region of interest. This saves computational power that can be used in the important areas of the volume. The cell size in these coarse areas is 220 [mm].

On the inside of the volume, the mesh is refined around the car and wake areas. This helps obtain better results, and captures the turbulences in a more precise way:

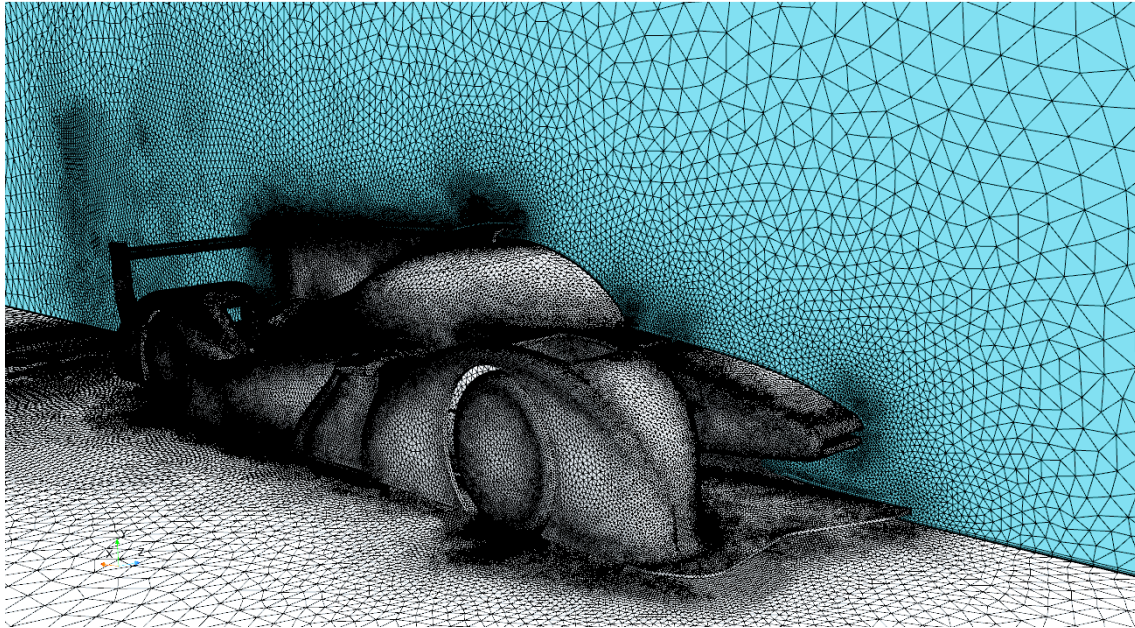


Figure 49: Surface mesh around the car and wake area. Notice the finer mesh size.

This finer mesh is extended 3.5 [m] behind the car to simulate the wake behind the car using the aforementioned “*Wake refinement*” command:

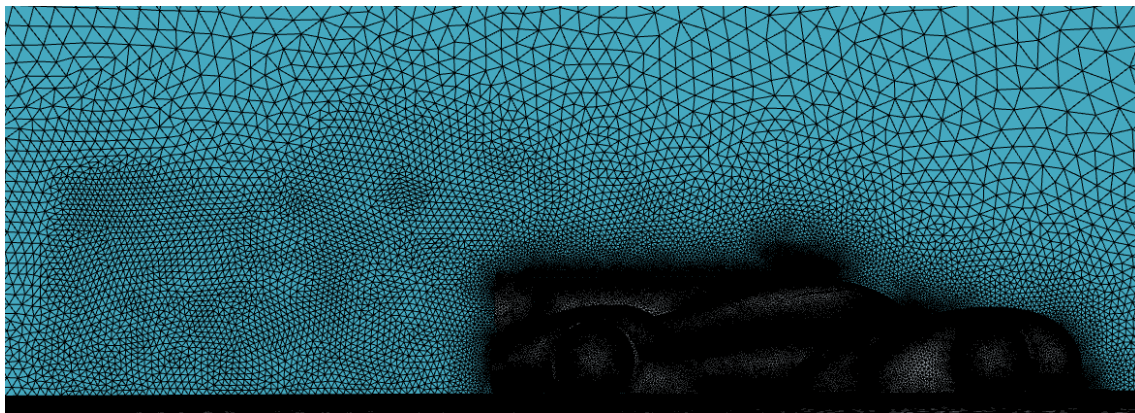


Figure 50: Cell size difference between the wake area and rest of the volume region.

4.2.6 Reports and graphic plots

In STAR-CCM+, and many other CFD programs, it is possible to create custom properties reports that calculate the value of many different physics magnitudes in each iteration. This feature is extremely useful to determine the aerodynamic forces acting on the car, or on some of its aerodynamic parts, and many other physics interactions between the car and the fluid continua.

The forces are automatically calculated by each force report created. In STAR-CCM+ the reports are created using the “*New Report*” command. There are many different reports type, but for this case, only the Flow and Energy reports are used.

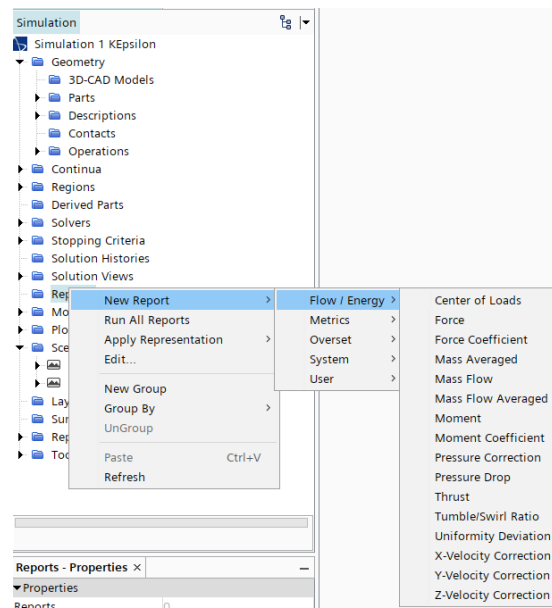


Figure 51: Available reports.

As explained in “2.7 Aerodynamic forces”, drag and downforce are the main acting forces on a race car. These two forces are calculated using an independent report for each important aerodynamic surface. By calculating the forces in this way, a better understanding of the aerodynamic effect of the different aerodynamic parts is obtained.

The global drag and downforce forces are also calculated using independent reports:

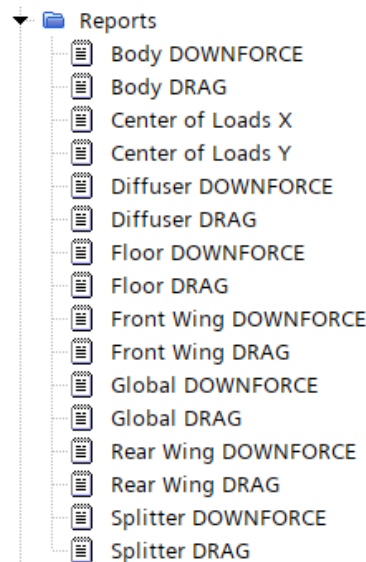


Figure 52: List of all forces to be calculated.

The Centre of Pressure (CoP) is an important geometric point in race car aerodynamics due to the effect in car handling. This force acting point dictates the evolution of the car handling (understeering or oversteering) as the downforce increases with the car's speed. If this point is located too far back or too far front may cause instability at high speeds and poor handling. STAR-CCM+ includes a specific command to calculate this point on each iteration of the solution. The CoP report integrates the forces acting on all the aerodynamic surfaces of the car and automatically calculates the moments generated by the said forces.

The CoP coordinates are expressed according to a cartesian reference system created explicitly to make the calculation of the load distribution easier. In this case, the front wheel contact patch is selected as the new cartesian origin. All three axis are parallel to their respective counterpart of the general cartesian reference system:

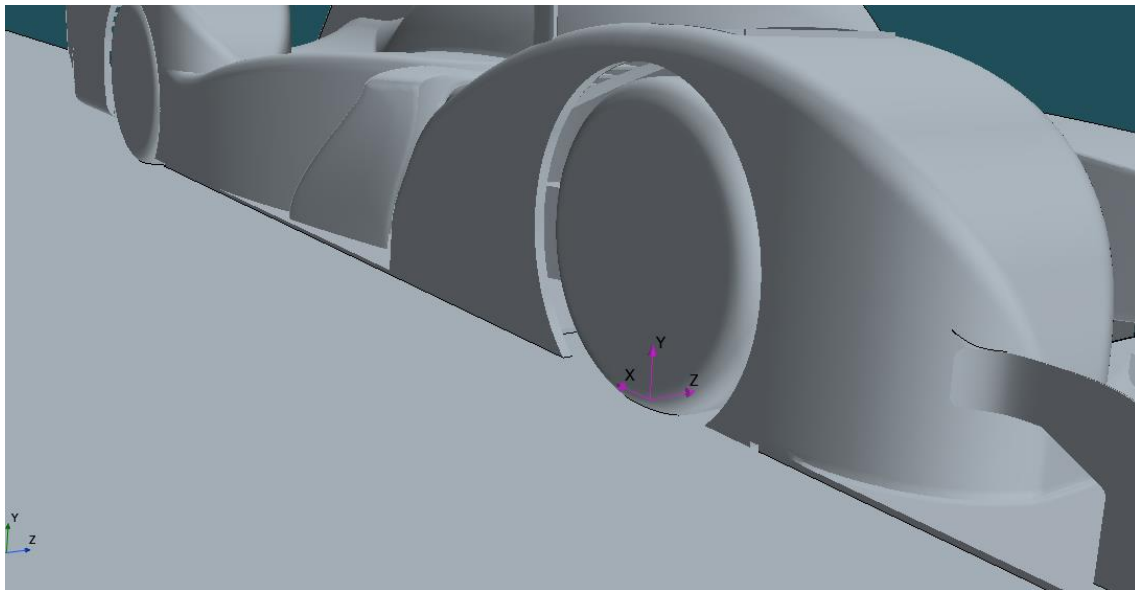


Figure 53: CoP coordinates cartesian reference system highlighted in pink.

To calculate the vertical loads and the respective distribution for each axle, the following equation is derived from the moments generated by the main aerodynamic forces on each axle:

$$L_{rear} = \frac{F_{dr} * Y - F_{df} * X}{WB}$$

$$L_{front} = \frac{-[F_{df} * (WB - X) + F_{dr} * Y]}{WB}$$

Where:

- L_{rear} and L_{front} are the loads on each axle of the car.
- F_{dr} and F_{df} are the global downforce and drag values.
- WB is the wheelbase, in this case 2.9 m.
- X and Y are the CoP coordinates on the specific cartesian reference frame.

Once the equations are solved, the process to calculate the loads and distribution is automated using a Python code script, which allow for quick calculations, and plotting if needed:

```
#DATA INPUT
WB=2.9
DOWNFORCE=float(input("Downforce value [N]: "))
DRAG=float(input("Drag value[N]: "))
X_Coordinate=float(input("COP X coordinate [m]: "))
Y_Coordinate=float(input("COP Y coordinate [m]: "))

#CHECK IF DOWNFORCE INPUT IS EXPRESSED AS A NEGATIVE FLOAT
if DOWNFORCE>=0:
    DOWNFORCE=-1*DOWNFORCE
else:
    DOWNFORCE=DOWNFORCE

#LOAD DISTRIBUTION
Load_Rear=(DRAG*Y_Coordinate-DOWNFORCE*X_Coordinate)/WB
Load_Front=- (DOWNFORCE*(WB-X_Coordinate)+DRAG*Y_Coordinate)/WB
Load_total=Load_Front+Load_Rear
Perc_front=100*(Load_Front/Load_total)
Perc_rear=100*(Load_Rear/Load_total)

#RESULTS
print("Rear axle aerodynamic load [N]: ", Load_Rear)
print("Front axle aerodynamic load [N]: ", Load_Front)
print("Front: ", Perc_front,"% Rear: ", Perc_rear,"%")
```

This code script returns the front and rear axle aerodynamic loads and the load percentage on both of them.

A common practice in aerodynamic development combines the CoP coordinates into the pressure coefficient plot . This plot gives the user a general understanding of the longitudinal aerodynamic behaviour, a very important aspect when it comes to car handling and stability.

4.3 Post-processing

This is the last step in CFD analysis, where the simulation is run and the data is analysed. This step includes the solvers that perform the multiple iterations needed to converge the solution. These are the main steps in post-processing:

1. Run the simulation and examine the residuals and simulation convergence.
2. Data analysis, data plotting and visual analysis.
3. Possible improvements based on the gathered data.

4.3.1 Simulation and Residuals.

This is the first step in the post-processing workflow, where all the data obtained from the simulation is checked to determine its validity and accuracy. The simulation starts by initializing the solution environment and introducing the boundary and physics initial conditions into the solver. In STAR-CCM+ this is done automatically by the *“Initialize solution”* command in the Simulation toolbar.

In most CFD programs, the solution starts by introducing a set of initial values. This is done automatically by the selected solvers depending on the initial values and conditions. From these initial values, the solver iterates solutions based on the previous obtained solution. If the boundary conditions and mesh are correct, the difference between the current and previous iteration solutions become smaller, finally converging to a set of continuous values.

The convergence of the solution overtime is visualized by a report plot containing the residuals for each iteration. Residuals are not the difference between the current and previous iteration, a very common misunderstanding in CFD. Instead, residuals measure the imbalance of a fluid-quantity in a finite volume (one for each cell in the control volume) [7].

For CFD, the residuals determine the convergence level of the whole simulation. Ideally, these residuals should be as small as possible, but in every simulation, there will always be a certain level of imbalance due to the numerical aspect of the calculations. These are the levels on convergence based on the residual values [7]:

Level of Convergence	Residual values
Loosely converged	1E-4
Well converged	1E-5
Tightly converged	1E-6

Table 6: Levels of convergence based on residual values.

The best possible scenario in CFD simulation is to obtain a solution whose residuals are as close to 1E-6 as possible, but this is not always possible, especially in simulations with high cell count or complex physics models, so these levels of convergence are only relevant as a guideline.

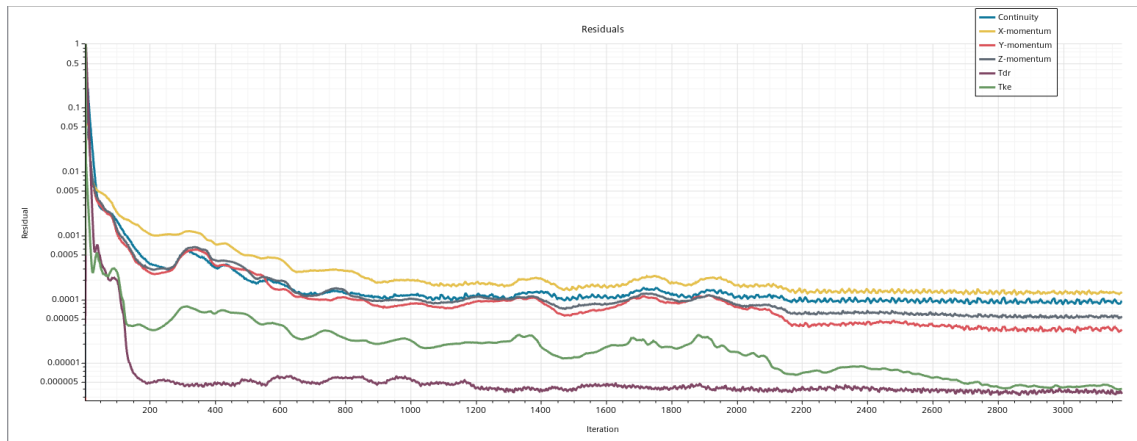


Figure 54: K – Epsilon simulation residuals.

The simulation is fully converged after 2300 iterations and 10 hours of computing time. The residuals oscillate around a fixed value, which means the solutions for the RANS equations are very close to the ideal value. The simulation runs for an additional 1000 iterations to make sure the solutions are fully converged. This can be seen in the left most part of the graph, where the residuals oscillate very little around a fixed value (horizontal graph lines). This means that the obtained results, such as forces and moments, are also converged as part of the computed solution.

As a form: of validating the accuracy of the results, it is usual to compare the Wall Y^+ values on the car surface. This scalar scene gives the user an estimation of how well the boundary layer has been captured. In this case the boundary layer has been calculated using wall functions, so most of the car's surface must be between $30 < Y^+ < 600$. This is the resulting Wall Y^+ surface values.

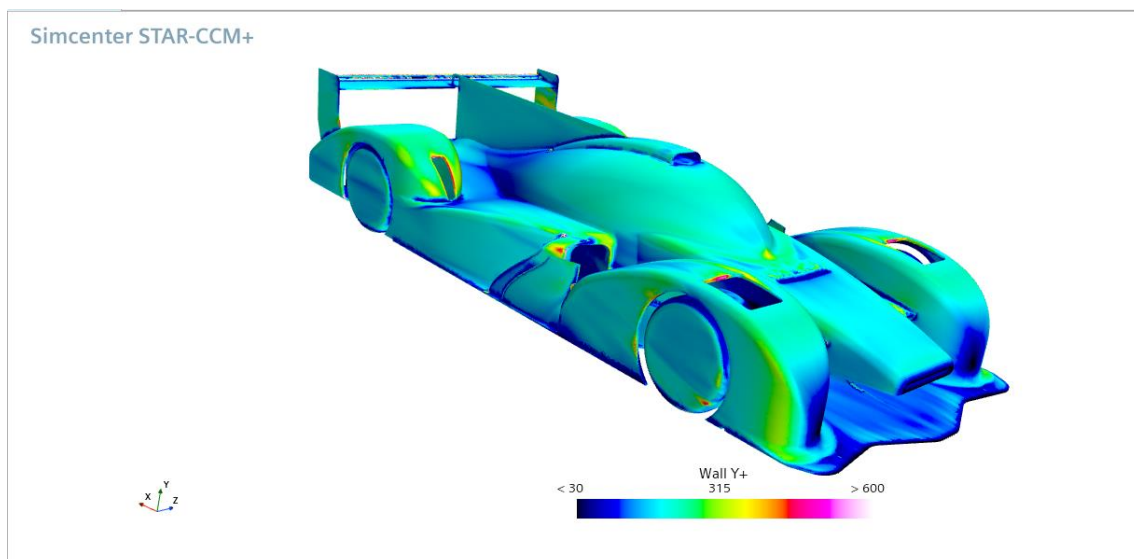


Figure 55: Wall Y^+ values front $\frac{3}{4}$ view of the car. White is $Y^+ > 30$ and black is $Y^+ < 30$. Simulation 1

5 On the upper surfaces of the car most of the Wall Y^+ values are kept between 30 and 600 therefore the log region of the boundary layer is captured. On the underside of the car, there are regions of the floor where the Y^+ value drops below 30:

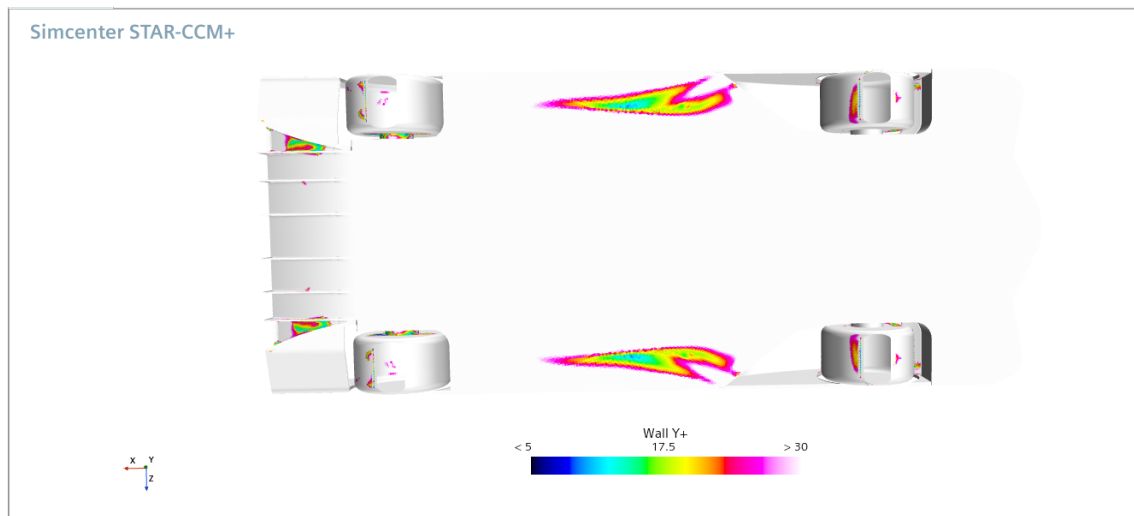


Figure 56: Y^+ values on the floor pan. Colour range adjusted for $5 < Y^+ < 30$. Simulation 1.

The Y^+ values drop below 30 in the floor regions affected by the front wheel wake. This is a small part and the overall result accuracy is not being affected, but this drops in the Y^+ values can also give the engineer valuable data about the aerodynamic performance. In this case, the buffer region of the boundary layer is computed, meaning that the wheel wake creates a low velocity region on the floor region immediately behind the front wheels. The effect can be seen by the following scalar and streamlines scene:

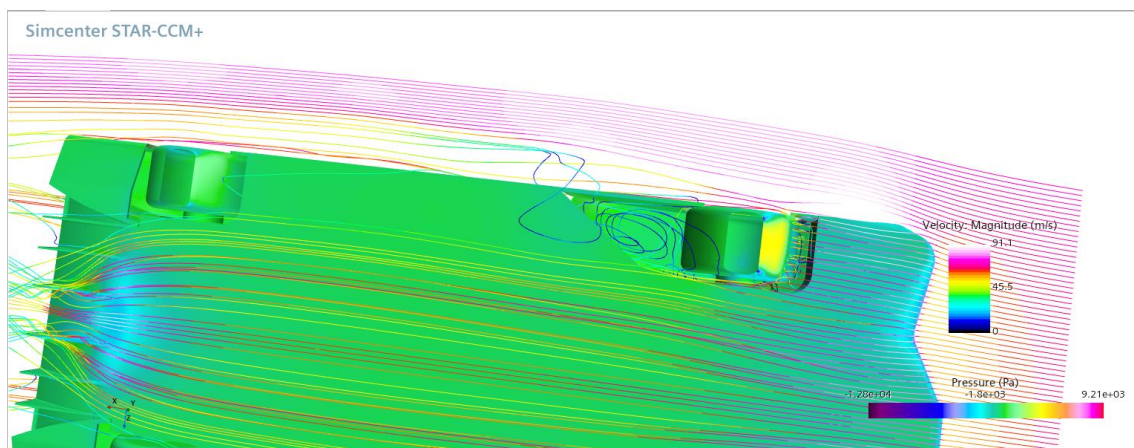


Figure 57: Streamlines under the floor. Notice the wake that stalls the floor right behind the front wheels. Simulation 1.

The surface colour field on the car represents the relative pressure (compared to 101325 Pa) and the streamlines colour field represents the velocity of the streamline on the specific point.

4.3.2 Data analysis, data plotting and visual analysis.

Once the simulation has converged, all the desired data is stored in the reports and plots that were set-up prior to running the simulation. In this case, these are the obtained aerodynamic values to assess the general aerodynamic behaviour and performance of the car:

- Drag and downforce in the diffuser.
- Drag and Downforce in the rear wing.
- Drag and downforce in upper part of the floor.
- Z Moment in the front and rear wheels.
- Drag and downforce of the whole car.

With these reports, it is possible to estimate the aerodynamic forces and how they interact with the car. It is important to note that the resulting forces are the result of only half of the car [11], even though a Symmetry plane boundary is being used. The forces shown below have been multiplied by a factor of 2, to show the total force magnitude acting on the car. All this data is imported into an Excel spreadsheet to perform the calculations needed:

Region / Part	Drag [N]	Downforce [N]
Front splitter	-	-
Diffuser	131,534	-554,88
Rear wing	203,72	-1844,4
Top Floor	9,52	-1460,94
Floor	45,36	-4117,18
Total	390,134	-7977,4
Global	2242,00	-1930,18

Table 7: Aerodynamic forces. Simulation 1.

The aerodynamic load distribution between both axles is calculated from the Centre of Pressure coordinates and the global drag and downforce values:

Coordinate direction	Value [m]
X axis	1,12
Y axis	0,465

Table 8: CoP coordinates. Simulation 1.

To calculate the distribution, the coordinates above and the global aerodynamic forces are processed using the Python script written for this purpose:

```
Downforce value [N]: -1930.18
Drag value[N]: 2242
COP X coordinate [m]: 1.12
COP Y coordinate [m]: 0.465
Rear axle aerodynamic load [N]: 1104.9419310344829
Front axle aerodynamic load [N]: 825.2380689655171
Front: 42.754461706447955 % Rear: 57.245538293552045 %
```

Figure 58: Aerodynamic load distribution on each axle. Simulation 1.

At first sight, the resulting forces are extremely low compared to a real LMP car, which usually generates between 12000 [N] and 14000 [N] of downforce at maximum speed. In this case, the simulation has been performed with 75 [m/s] or 270 [km/h] of air velocity, which is a more realistic wind speed when calculating the aerodynamic forces needed to estimate the cornering speeds.

Before calculating the rest of the data, it is necessary to calculate the frontal and reference areas. These areas are needed to calculate the drag and lift coefficient of the car. This is done by directly calculating the projection areas in Solidworks. Note that only the half area is measured:

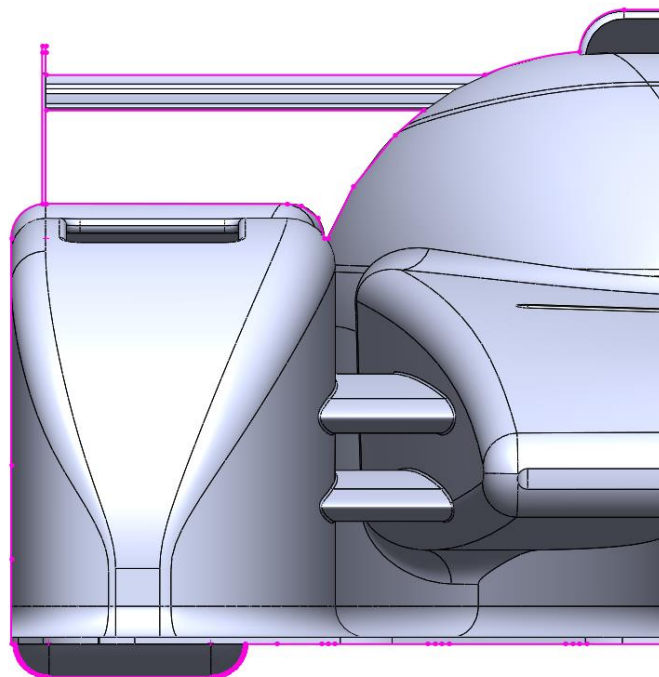


Figure 59: Frontal area contour. Frontal area contours highlighted in pink.

The contour highlighted in pink is the frontal area section. To calculate the surface area of this contour a extrude operation is performed:

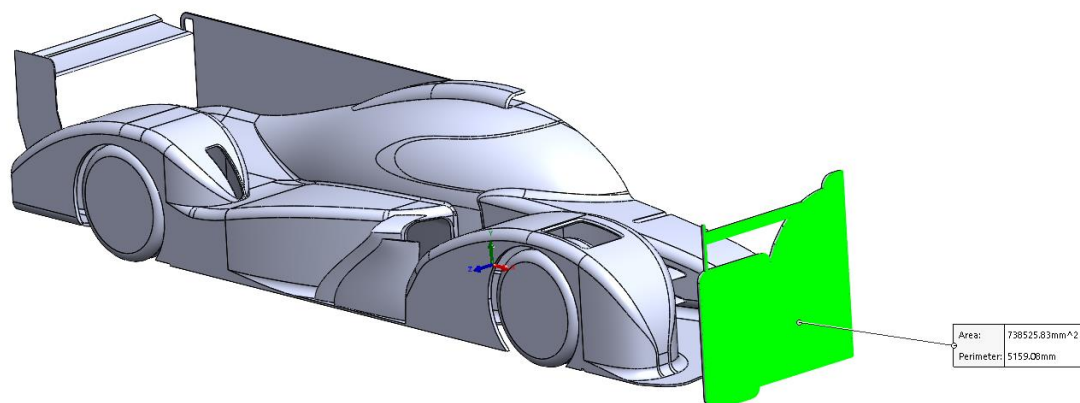


Figure 60: Measure operation for the frontal area.

These are the resulting areas:

Type	Measured [m ²] (half)	Total [m ²]
Frontal	0,7385	1,477

Table 9: Frontal reference area for the drag and lift coefficients. Simulation 1.

With these reference area values it is possible to calculate the drag and lift coefficient of the car using the equations explained in “2.7.1 Lift and drag coefficient” section:

Coefficient	Value
Drag (Cd)	0,455
Lift (Cl)	-0,39

Table 10: Lift and drag coefficients. Simulation 1.

These values are small compared to the coefficient that are to be expected in a real race car, especially for the lift coefficient (Cl). The main reason as to why these values are small compared to the expected values for a real car is the low accuracy in the measured data for these calculations. The forces calculated by the CFD software are converged but may not be fully accurate due to the coarser mesh used in the simulation to compromise computing time and resources. Also, the air velocity used in the previous calculations is the free stream air speed, which may not be equal to the air velocity in most of the surface cells of the 3D model.

Taking all this into account, it is a good practice to compare the manually calculated coefficient values with the coefficients calculated by the CFD software, due to the increased accuracy regarding the flow velocity in the different cells (more accurate result). In STAR-CCM+, the user must insert the area reference values manually, so in this case the areas from Table 11 are used. The simulation is performed using one half of the symmetric model.

The common aerodynamic coefficients for a LMP prototype car are usually in the region of 0,5 for the drag coefficient and 1,5-2 for the lift coefficient [11] (Audi R18 TDI 2010). This car is very similar to the model being simulated in this thesis:



Figure 61: Audi R18 TDI 2011.

The similarities between the Audi R18 and the model used for these simulations can give a reference of the aerodynamic data to be expected from a LMP car. These are the aerodynamic forces and coefficient of the Audi R18:

Audi R18 aerodynamic data	Value
Drag force	4154,64 [N]
Downforce	-16578,52 [N]
Cd	0,471
Cl	-1,8798
Downforce distribution	53% Front - 47% Rear
L/D	3.99:1
Frontal area	1,8 [m ²]
Original Flow velocity (estimated)	90,63 [m/s]

Table 11: Original Audi R18 general aerodynamic data [11].

These values are based on a free stream velocity of around 90 [m/s] or 324 [km/h], 15 [m/s] higher than the free stream velocity used in the simulations. This velocity difference can be adjusted by considering the lift and drag coefficients constant at high speeds. By doing this, it is possible to estimate the downforce and drag values of the Audi R18 at 75 [m/s] or 270 [km/h]. The velocity adjusted forces are obtained by solving the forces on each coefficient's formula:

Audi R18 aerodynamic data (adjusted)	Value
Drag force	2823,53 [N]
Downforce	-11268,95 [N]
Cd	0,471
Cl	-1,8798
Downforce distribution	53% Front - 47% Rear
L/D	3,99:1
Frontal area	1,8 [m ²]
Adjusted flow velocity	75 [m/s]

Table 12: Adjusted Audi R18 aerodynamic data. In green, the velocity adjusted forces.

Before analysing the aerodynamic behaviour of the model analysed in this thesis, the following table is constructed to directly compare the main aerodynamic properties of both the Audi R18 (velocity adjusted data) and the base model for the LMP car:

	Audi R18 (adjusted)	LMP base geometry
Drag force	2823,53 [N]	2242,00 [N]
Downforce	-11268,95 [N]	-1930,18 [N]
Cd	0,471	0,210
Cl	-1,8798	-0,181
Downforce distribution	53% Front - 47% Rear	42,75% Front – 57,25% Rear
L/D	3,99:1	0,86:1
Frontal area	1,8 [m ²]	1,6054 [m ²]
Flow velocity	75 [m/s]	75 [m/s]

Table 13: Aerodynamic data comparison between the Audi R18 and the base geometry.

At first sight, it is quite obvious that the model simulated in this thesis performs very poorly in terms of aerodynamic downforce compared to a real LMP car. The main reason for this poor aerodynamic performance is the general geometric construction of the car. Although the general shape of the car has potential to perform quite well, there are specific aerodynamic regions that are not developed enough to fully exploit the aerodynamic potential of the car. There are many different geometry alterations that need to be made in order to achieve similar aerodynamic performance compared to a regular LMP car like the Audi R18. These modifications are further explained in the next chapter.

4.4 Aerodynamic improvements

After extracting all the data from the simulation, the analyzed model shows very poor aerodynamic performance, especially in terms of overall downforce generated. The main objective of the future aerodynamic improvements is to exploit all the aerodynamic potential available in the car based on the original geometry. Creating a whole new geometry from scratch is the ideal path to take in order to achieve the desired aerodynamic performance, but usually this is not possible because of the extremely high costs of developing a whole new car. Usually, the car is developed from a base aerodynamic concept that has been proven prior to the CAD modelling of the car. The aerodynamic package of the car has to work in conjunction with the structural and drivetrain components, so creating a new aerodynamic concept once the mechanical side of the development project has already been developed is not possible.

Usually, most race car development teams iterate the aerodynamic design based on a general concept of how the main bodywork shape will be. In this particular case, the base geometry has the potential to achieve a high aerodynamic performance, mainly due to the low frontal area of the geometry. In terms of downforce generated, the base geometry performs very poorly and needs to be improved in future iterations.

Most of the aerodynamic issues can be seen using the scalar or vector scenes. The first and most important scalar field that should be inspected is the pressure on the car's surfaces. This scalar field gives a broad image of how the different aerodynamic surfaces are interacting with the air flow.

Simcenter STAR-CCM+

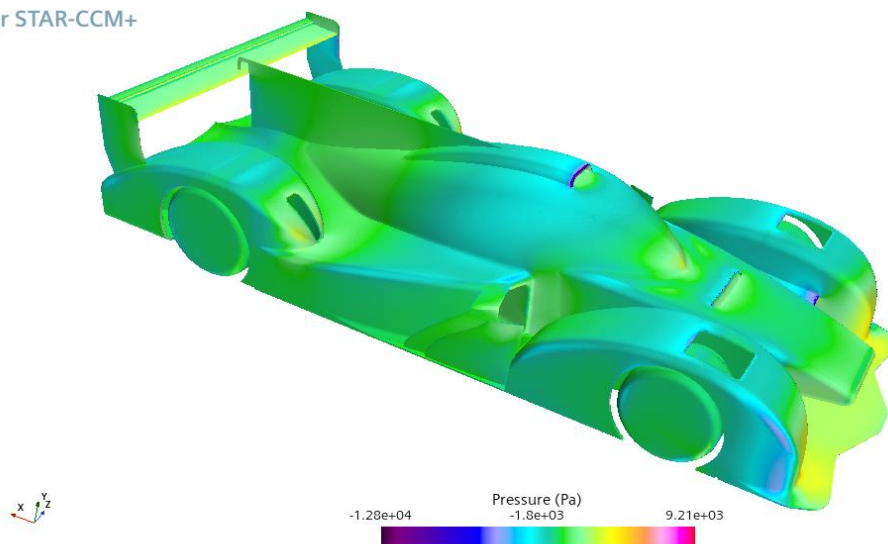


Figure 62: Pressure colour field on the upper surfaces of the car. Simulation 1.

From this scene alone it is possible to appreciate the low-pressure region (turquoise) above the cockpit area. This low-pressure area generates high amounts of positive lift, which is counterproductive to the desired downforce levels desired on a race car. In this case, there is little to be modified in order to mitigate the positive lift generated by this curved section, as this is usually part of the monocoque chassis and safety cell required by the sanctioning body, in this case the FIA.

One of the most concerning areas on this base geometry is the wheel wake management, with high levels of turbulence generating in the inner part of the wheel fender. This is caused by a poor turbulence exhaust geometry:

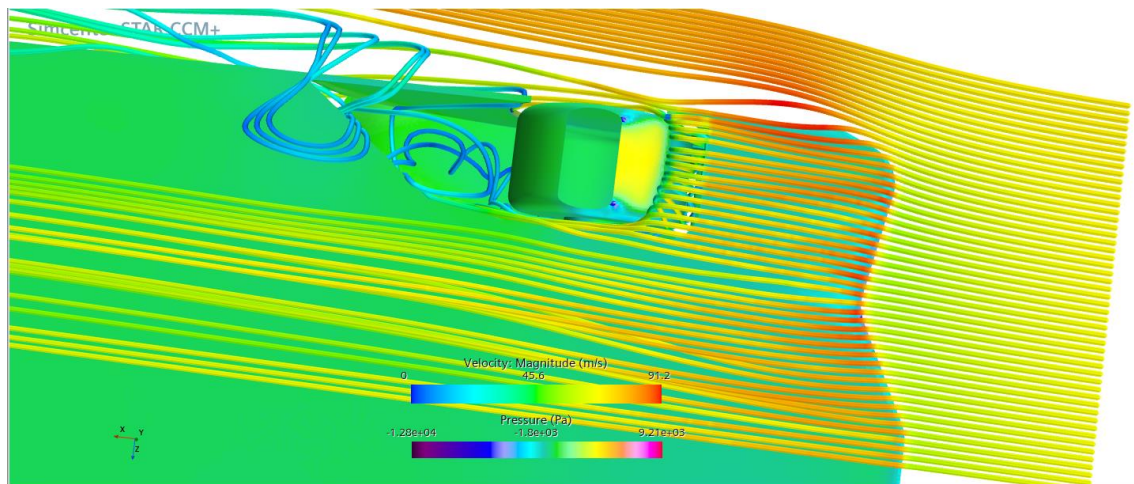


Figure 63: Front wheel wake turbulence generated inside the wheel fender. Simulation 1.

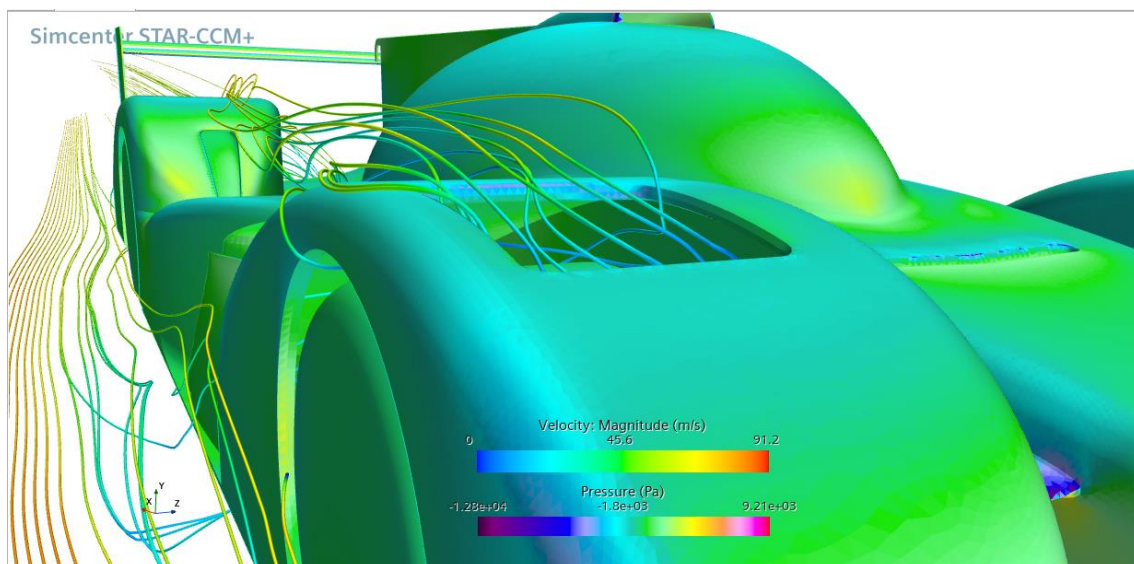


Figure 64: Upper vent for the wheel wake. Notice the poor extraction. Simulation 1.

This is a problem that must be addressed in the first design iteration due to the effects created in the floor and wheel fenders. This issue also happens on the rear wheels and should also be solved in the first design iteration.

On the rear diffuser, there are sections where the flow stalls and creates turbulence around the vertical strakes. This results in a reduction of efficiency and downforce:

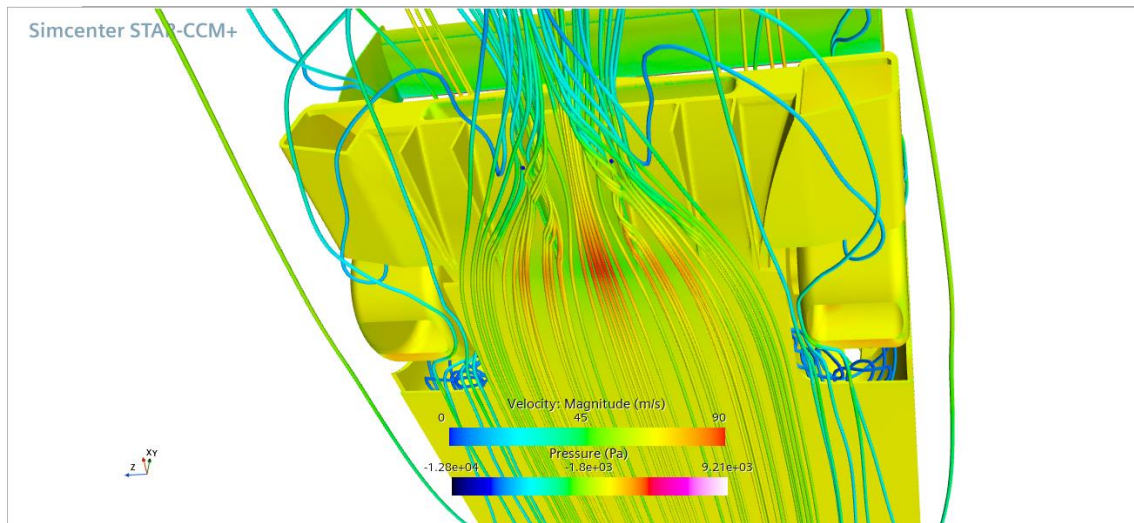


Figure 65: Rear diffuser streamlines. Notice the lack of air flow on the outer sections.

This can be improved by altering the diffuser geometry, especially by creating longer diffuser tunnels.

5 Geometry Iteration 1

In CFD it is very common to iterate the geometry design after analyzing the initial car design. It is almost impossible to achieve an aerodynamically useful geometry at the first try, therefore multiple design alterations and simulations are required. In this case, there are many changes needed to be made in order to achieve the desired aerodynamic results.

5.1 Desired results overview

From the data retrieved in the first simulation, there are a number of areas that need to be improved. The first iteration is focused on the major aerodynamic changes, with the second iteration focusing on the minor concept details. These are the main areas of development explored for the first design iteration.

5.1.1 Floor and rake angle

This is the most important region in terms of aerodynamic effect on the car. The floor generates most of the downforce with very little drag in exchange. The first design iteration tries to optimize the performance of this region by increasing the air mass flow that is introduced in this region, sealing the floor sides using high velocity vortices on both sides and increasing the rake angle.

The most important improvement to be made in the floor area is to increase the air mass flow that enters this region. This may seem an easy task as first, with an increased ride height solving this issue, but it is more complex than that. Increasing the overall ride height of the car raises the centre of gravity and reduces the Venturi effect on the floor region, decreasing the overall performance of the car. Instead, the increased air mass flow is achieved by creating a raised section on the frontmost part of the floor. This is called a front splitter:

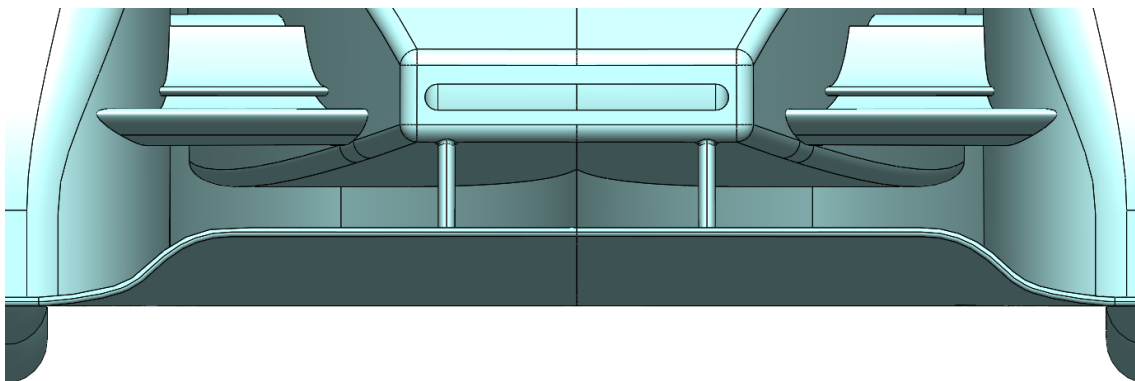


Figure 66: Front splitter on the first design iteration. Notice the raised floor lip.

This part serves two main purposes: increasing the air mass flow on the floor and creating a low-pressure area as a result of the increased flow velocity and reducing section area.

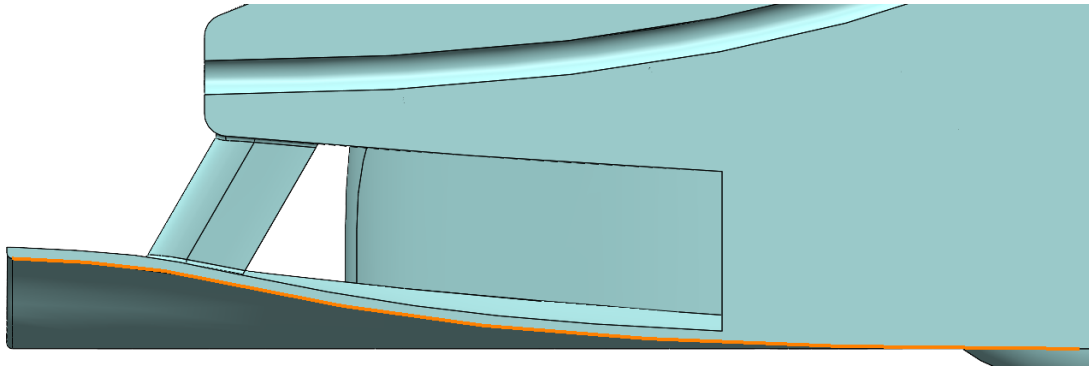


Figure 67: Section view of the front splitter. In orange, the longitudinal profile.

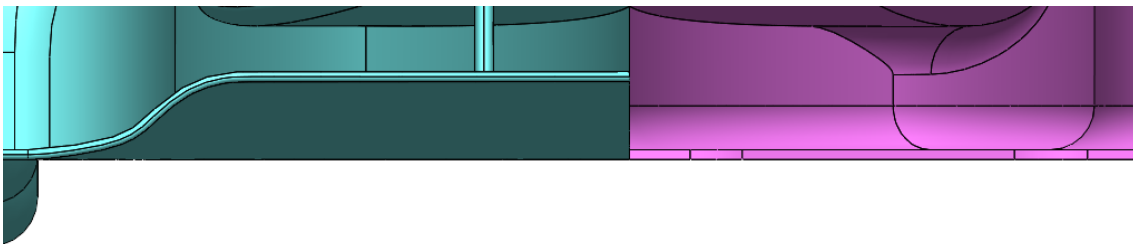


Figure 68: Difference between the front splitter (Left) and the original floor profile (Right).

The splitter is held to the chassis by a pair of vertical beam wings:

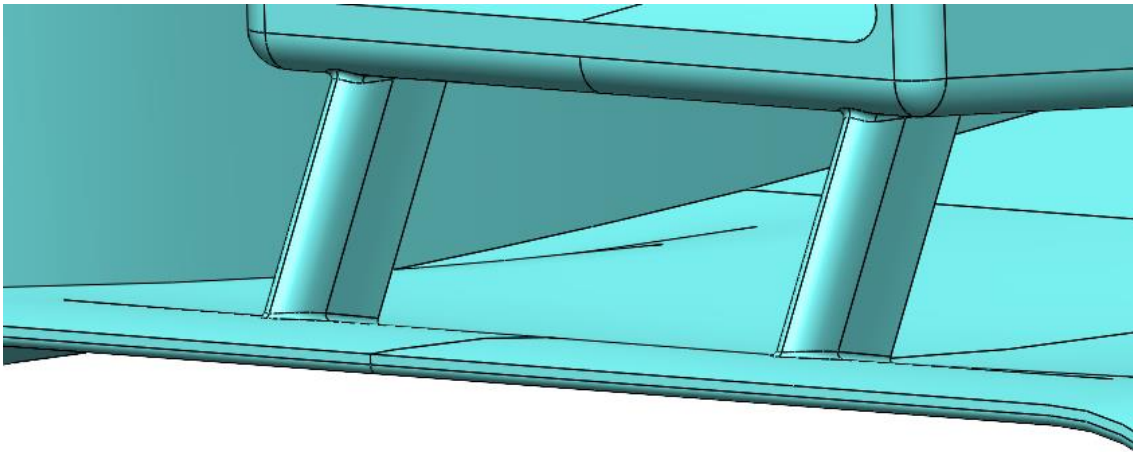


Figure 69: Beam wings connecting the splitter to the chassis.

As explained on the previous chapter, the front wheel wake caused problems on the floor, stalling the flow behind the front wheels. This issue has been addressed by modifying the wake vent present on the base geometry:

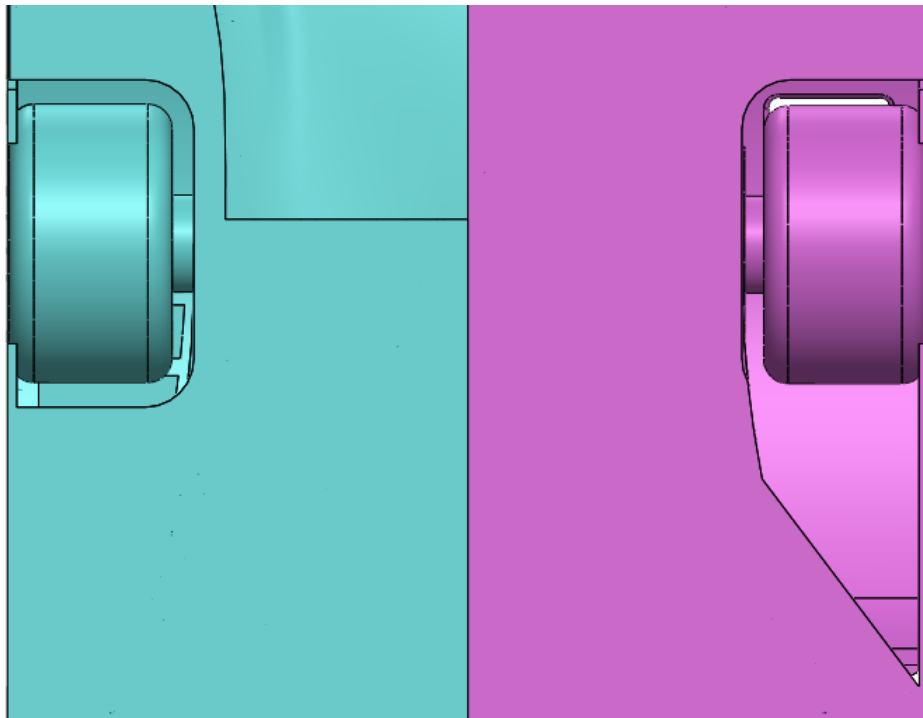


Figure 70: Sealed floor on the front wheel wake area (Left) and original wake vent cut (Right).

This closed floor area helps keeping the high energy air flow created by the wheels inside the floor area.

Sealing the floor is a critical task to maximize the aerodynamic downforce created in this region. This is achieved by placing high energy vortex generators on both sides of the floor:

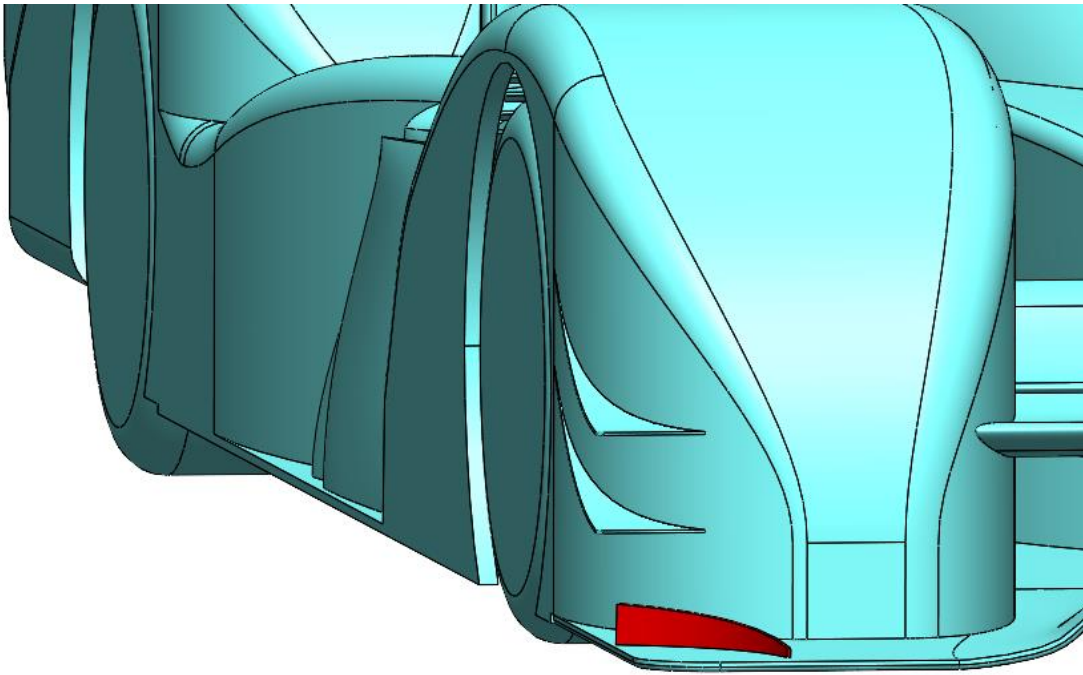


Figure 71: Vortex generator highlighted in red. The vortex created flows along the floor edge to seal it.

As explained in “3.1.1 Floor and rake angle”, rake is the angle formed between the floor and the ground and is a critical feature to the overall car performance, both for handling and aerodynamics. This angle generates a constant flow expansion due to the simulated diffuser effect all along the floor.

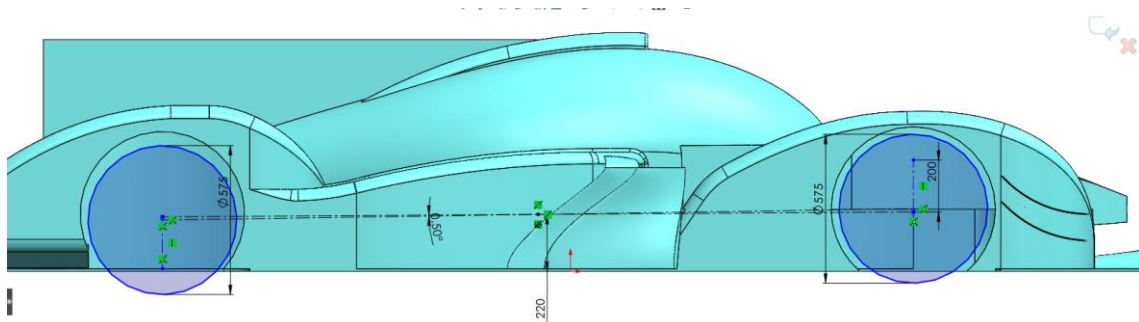


Figure 72: Rake angle sketch. This sketch allows for a quick and easy change of rake angle and ride height.

The result is a higher rear axle ride height compared to the front axle with a 0,5° rake angle:

Axle ride height	Distance [mm]
Front	29,91
Rear	80,59
Difference	+50,68 Rear

Table 14: Ride heights of the modified geometry.

This is the resulting floor profile after setting the rake angle:

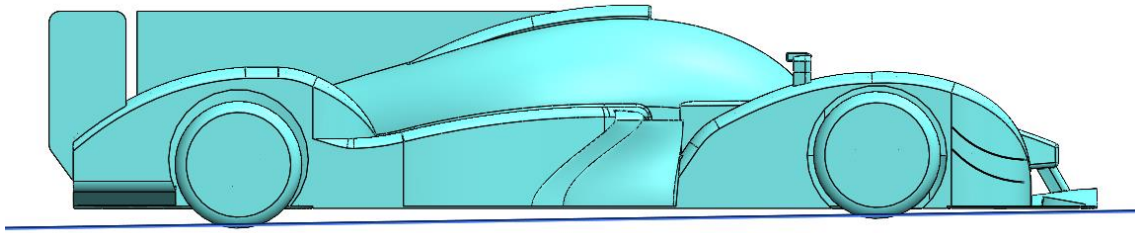


Figure 73: Rake angle. The blue line is the ground plane.

5.1.2 Frontal Area

The frontal area of the car has multiple modifications and geometry refinements to improve the aerodynamic performance. The front surfaces of the car are an efficient source of aerodynamic downforce due to the clean and direct air flow.

Most of modern closed wheel race cars, like the ones being studied here, have small winglets fitted to the external side of the front wheel fenders. These small winglets are commonly known as “Canards”:

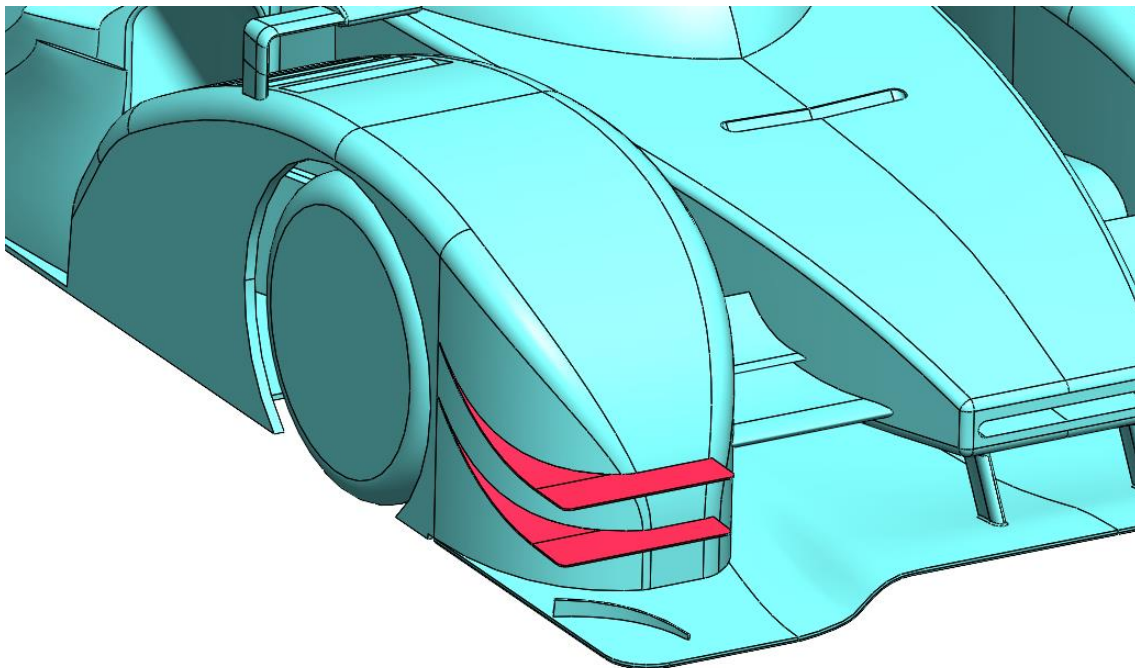


Figure 74: Front canards highlighted in red.

These small wings create downforce by creating a pressure difference between the top and lower sides of each winglet. The canards are located in regions where the surface pressure is high, like in the frontal surfaces of the car. These surfaces have high pressure due to the direct impact against the air flow:

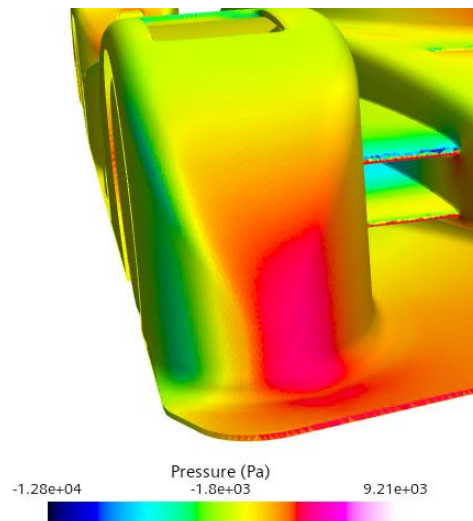


Figure 75: Pressure distribution on the original geometry wheel fenders.

On the base geometry, the wheel fenders have a high pressure region in the front/right side of the fender, redirecting the air towards the radiator intakes. On the outer part, there are even negative pressure regions.

The frontal area geometry of the wheel fenders has been modified to increase the total air mass flow impacting these canards, redirecting a higher amount of air mass flow outwards. The frontal surfaces have been moved inwards:

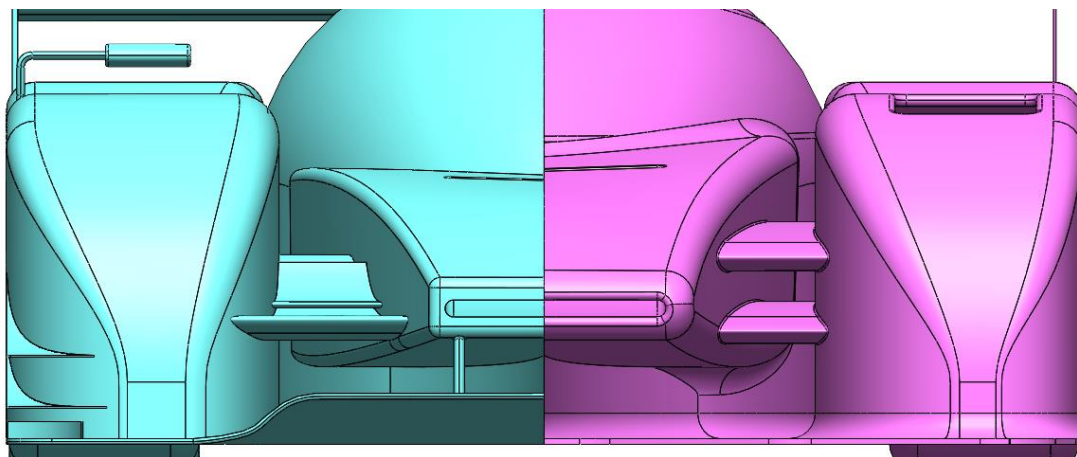


Figure 76: Wheel fender geometry comparison. Left is the revised geometry and right is the original geometry.

With this geometry revision, the canards have higher pressure difference to generate downforce.

The front chassis structure has also been modified to decrease the original frontal surface size. The base geometry of the chassis had a large frontal area that created high pressure zones, especially on the leading edge:

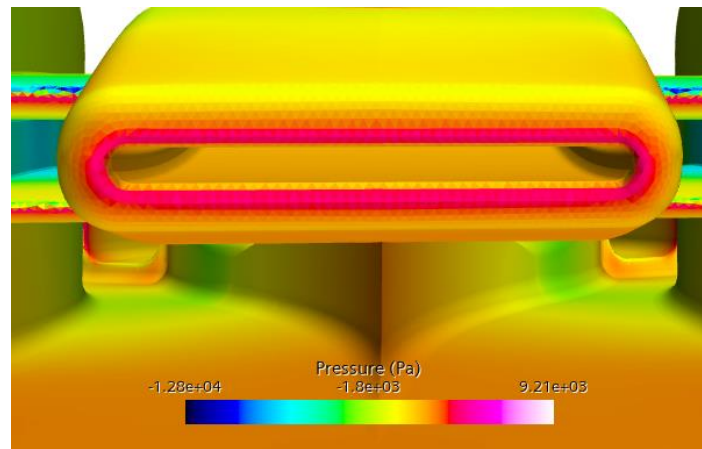


Figure 77: High pressure leading edges.

For the first design iteration, the front chassis section has been modified to decrease the total frontal area of this part and to provide a larger flow surface to the front wings on each side of the front chassis:

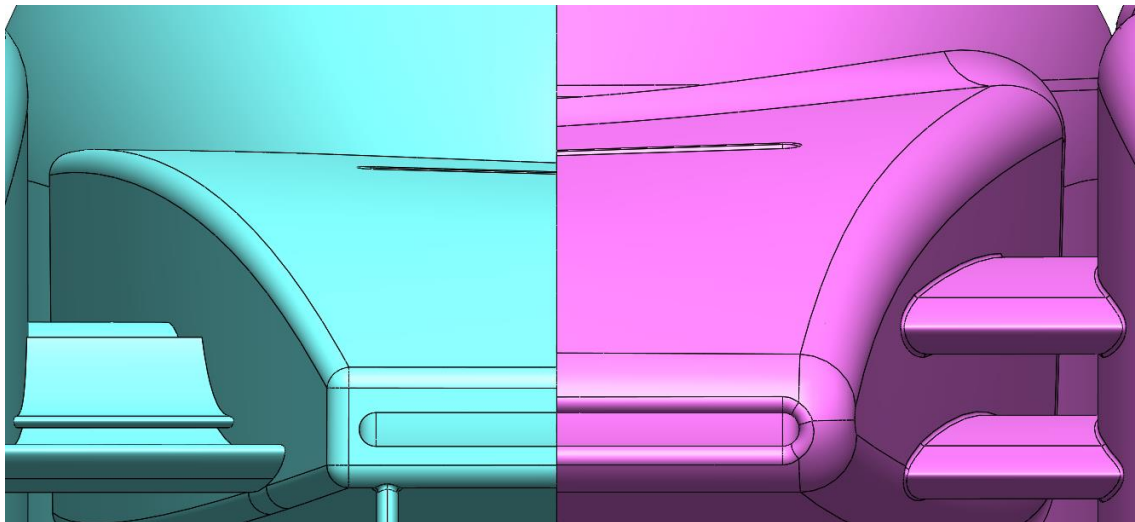


Figure 78: Notice the difference between the original frontal section (Right) and the revised frontal area (Right)

The base geometry was lacking the mirrors, which are mandatory for a homologated racecar. The mirrors have great influence on the overall drag value of the car because they are usually placed on free stream flow regions and have a rather large frontal area for an auxiliary bodywork part. In this case, the mirrors have been modelled to be similar to most of the current LMP cars:

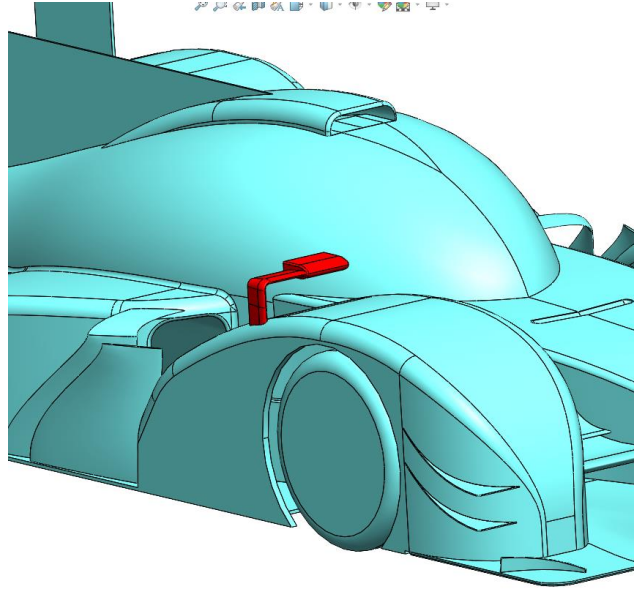


Figure 79: Mirror highlighted in red.

5.1.3 Rear diffuser

The rear diffuser is one of the most important aerodynamic regions in the whole car. On the base geometry, the diffuser was not optimized, with the outermost parts of the diffuser stalling the flow as explained in the previous chapter. The rear diffuser has been modified to maximize the performance.

Usually, most diffusers have a smooth longitudinal profile. The air flow is expanded in a constant manner, avoiding sudden changes in section area that may separate the flow from the diffuser's surface:

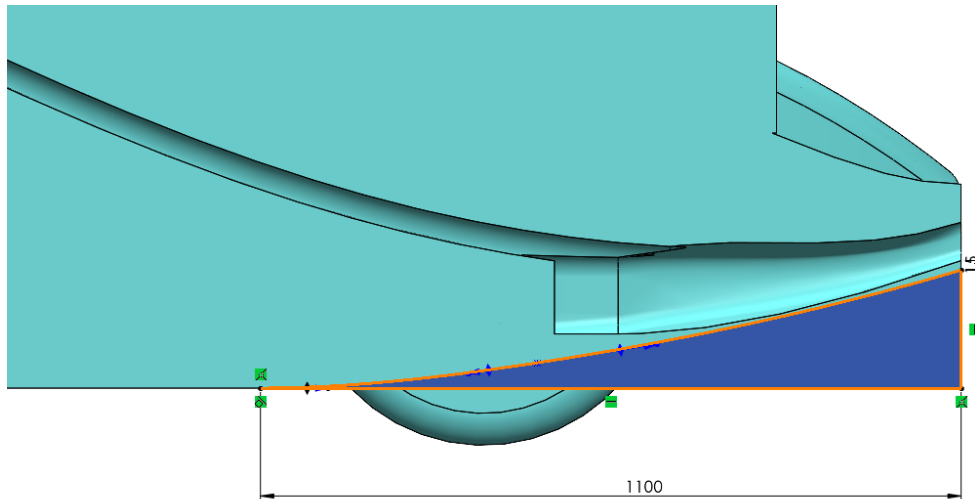


Figure 80: Rear diffuser profile sketch highlighted in orange.

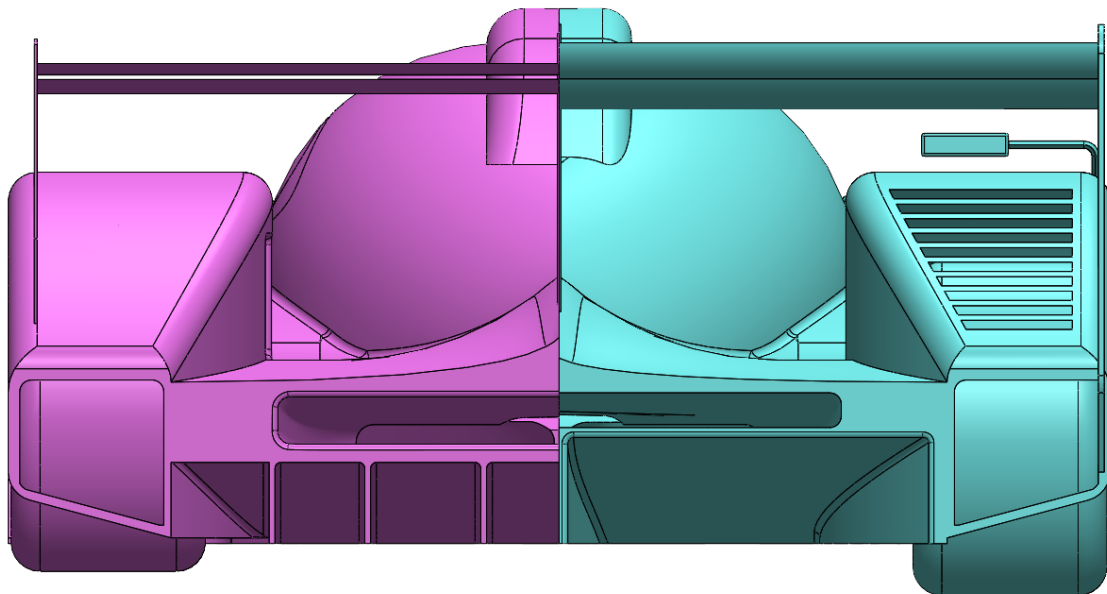


Figure 81: Base geometry diffuser (Left) and modified geometry diffuser (Right).

The revised geometry of the diffuser has a longer tunnel compared to the original geometry, which improves the flow transition from the floor to the wake flow region. Also, the total diffuser height has been increased by around 51 [mm]:

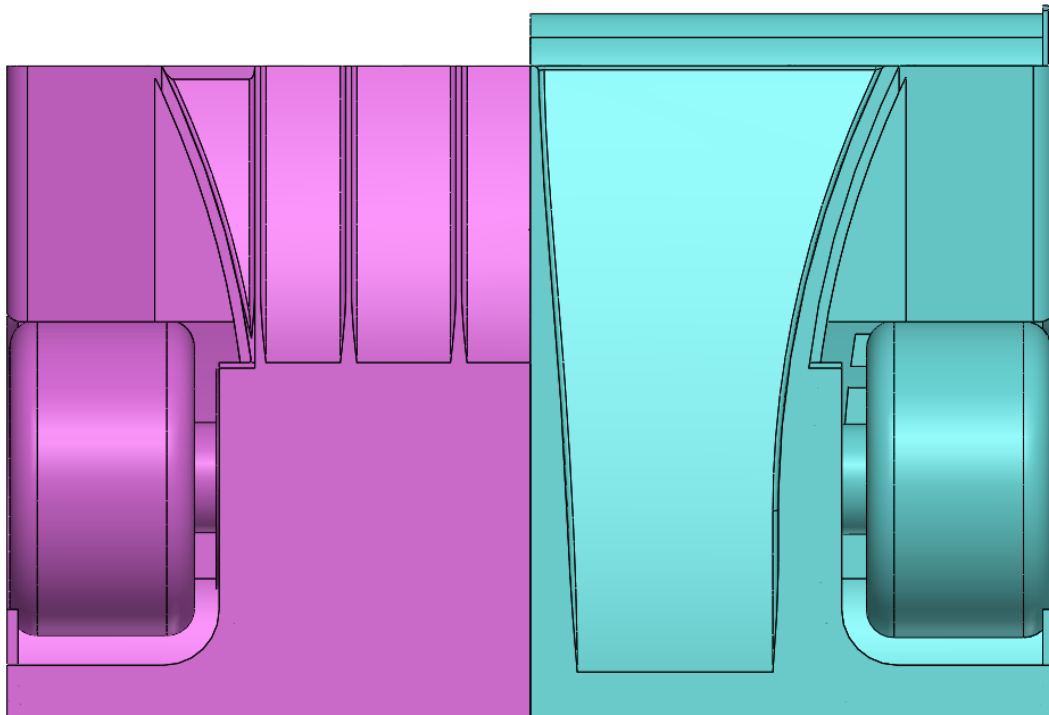


Figure 82: Diffuser exit height. Left is base geometry and right is modified geometry.

5.1.4 Rear wing

Most modern race cars rely on inverted air foil shaped wings to generate downforce. In the base geometry, the rear wing was not producing enough downforce. This issue has been solved in the revised geometry iteration by designing a new 2 element wing profile:

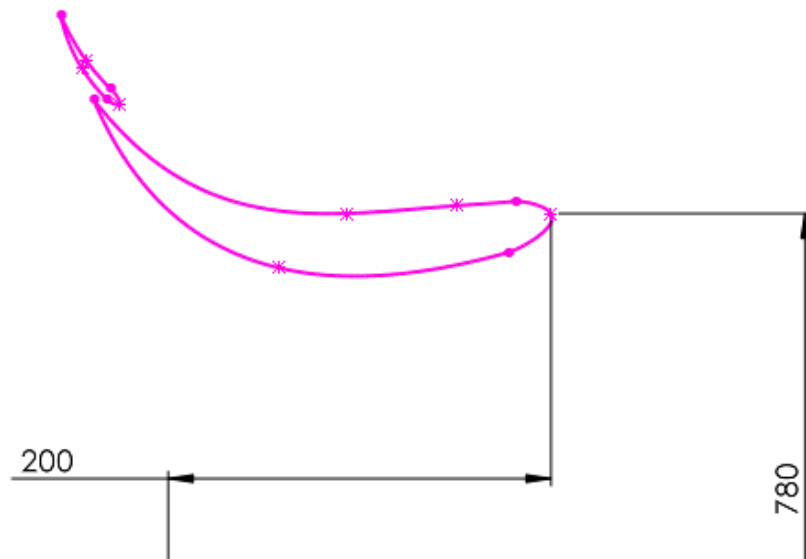


Figure 83: Modified rear wing profile.

It is a common practice in aerodynamic development to analyse the wing profiles independently from the car. Air foil profiles may not work properly, and if this is the case, lots of computing time in CFD is wasted if the engineer encounters this problem while performing a whole car simulation. Instead, it is usual to perform a 2D simulation of the designed wing profile to validate the air foil profile. This is not a completely accurate simulation compared to a full 3D wing simulation, but the 2D simulation can compute the stall and aerodynamic properties very accurately. This workflow was derived from the aerospace industry and is very common in many aerodynamic development projects.

As shown before, the initial 2D air foil profile is simulated in STAR-CCM+ using the profile simulation workflow. The wing profile is exported into the CFD program as a Parasolid (.x_t). Although this type of file is a 3D mesh, STAR-CCM+ allows the user to select the face in which the 2D analysis will be performed. In this case the control volume is a thin extruded operation containing the wing profile:

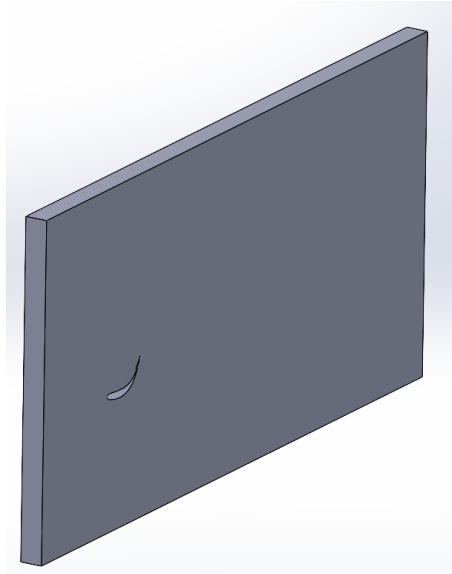


Figure 84: Control volume with the wing profile.

One of the side faces is selected as the 2D simulation plan and the mesh is performed in a very similar manner compared to the previously explained 3D mesh operation:

Simcenter STAR-CCM+

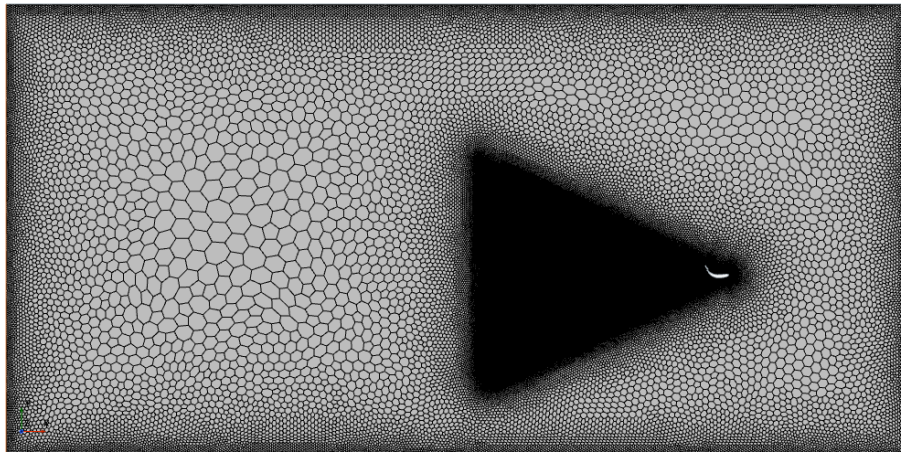


Figure 85: 2D mesh operation for the first wing profile design. Around 1E5 cells.

After the mesh operation, the procedure is the same as in the 3D simulation. The physics conditions are kept the same and drag and downforce reports are also generated. The simulation runs for around 1800 iterations to make sure the solution is fully converged:

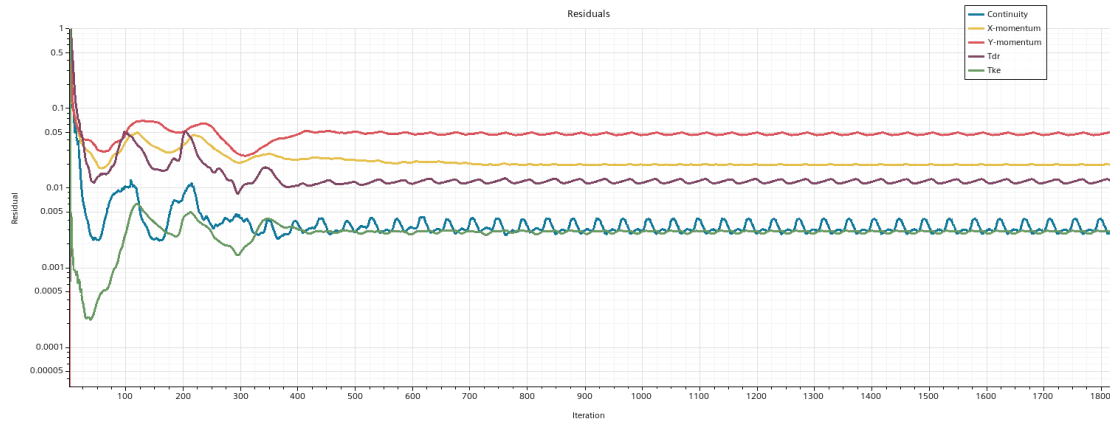


Figure 86: Residuals of the first 2D simulation of the wing profile.

As explained before, the 2D profile simulations require a lot less computational resources and time for a completely converged simulation, which helps save time on the design process. In this case, this simulation has taken under 8 minutes to run the 1800 iterations, even though the residuals indicate the simulation was converged after 600 iterations.

The force report plot is also converged:

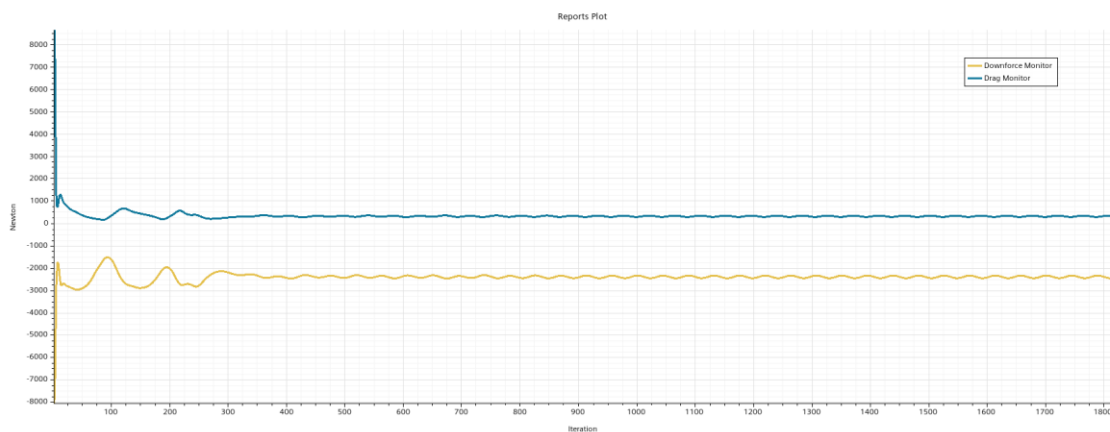


Figure 87: Drag and downforce report for the first 2D simulation of the wing profile.

The forces calculated above are based on a unitary length of wing profile, in this case the forces on 1 meter length wing:

Force / Coefficient at 75 [m/s]	Unitary length force	Wing (L=1860 [mm])
Drag	310,69 ± 31,71 [N/m]	577,88 ± 58,98 [N]
Downforce	-2400,11 ± 56,33 [N/m]	-4464,20 ± 104,77 [N]
Cd (A=0,25 [m²])	0,69	0,69
Cl (A=0,25 [m²])	-5,36	-5,36

Table 15: Individual rear wing simulation forces.

The residuals show oscillation due to the separated flow behind the rear wing. This shows that the physics models and solvers selected for this simulation are far from ideal. For separated flow, there

are better solvers that compute the pressure oscillations behind the wing in a dynamic manner by setting an unsteady time frame.

The air flow around the rear wing must follow the outer surfaces without detaching to avoid poor performance and boundary layer separation. There are many ways to visualize this in STAR-CCM+, but the most useful way is to use a source of streamlines and check the direction of these lines. If the lines do not follow the underside of the rear wing without detaching from the surface, this indicates a boundary layer separation. This is commonly known in the aeronautical industry as “*Wing stall*”.

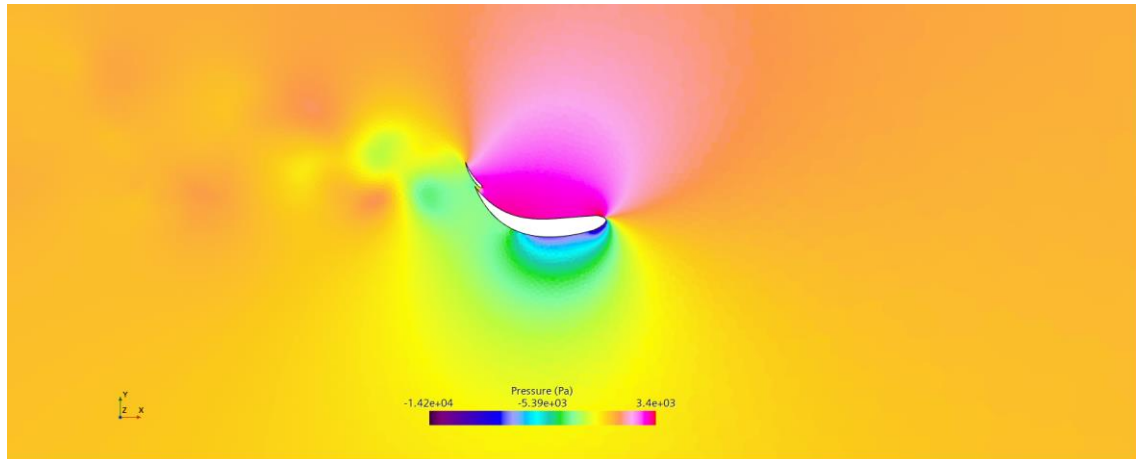


Figure 88: Pressure distribution on the first rear wing profile.

From this figure alone it is possible to tell that the underside of the rear wing does not have a constant pressure profile, indicating that the flow may be separating from the surface in this region.

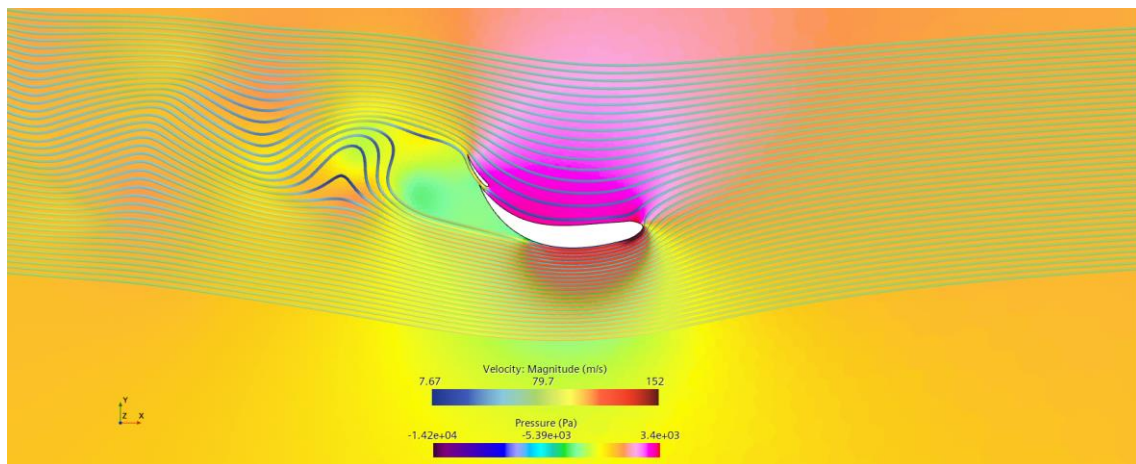


Figure 89: Pressure distribution with velocity field streamlines.

The streamlines separate from the underside of the first wing element. This is caused by a flow separation on the lower surface of the wing due to the lower element curvature being too steep on the exit region. Usually, the wing elements are compensated in size to distribute the pressure field more evenly along the underside.

Also, the small gap between the lower and upper elements is placed in a lower position to create an air flow that helps keeping the flow attached to the upper element.

The wing profile is modified considering all the tips explained in the previous paragraph:

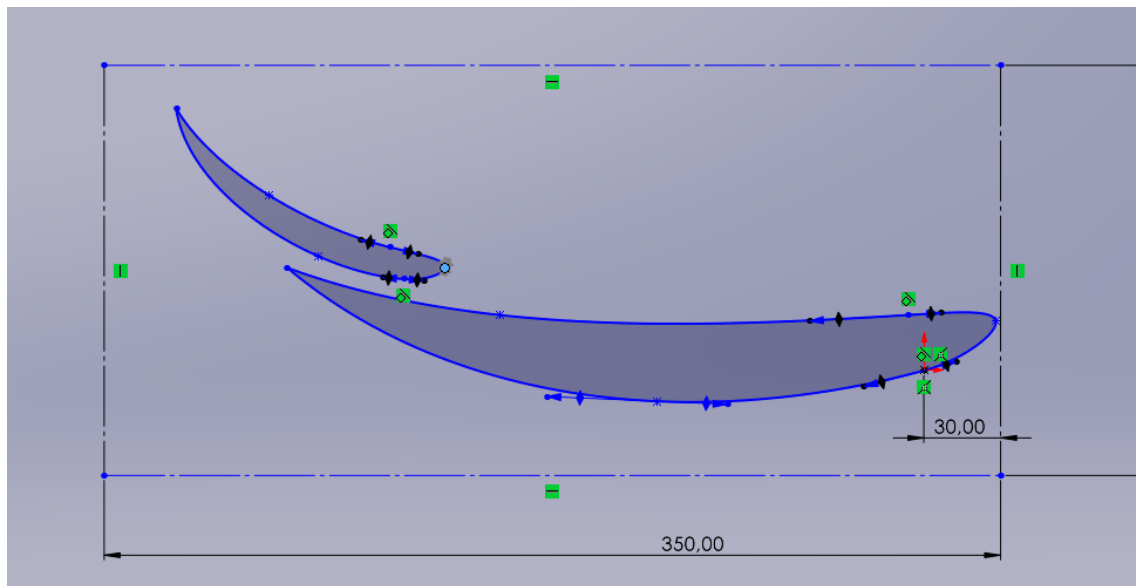


Figure 90: Revised rear wing profile.

This profile is imported into STAR-CCM+ to perform the simulation. The conditions are kept the same as in the first rear wing simulation:

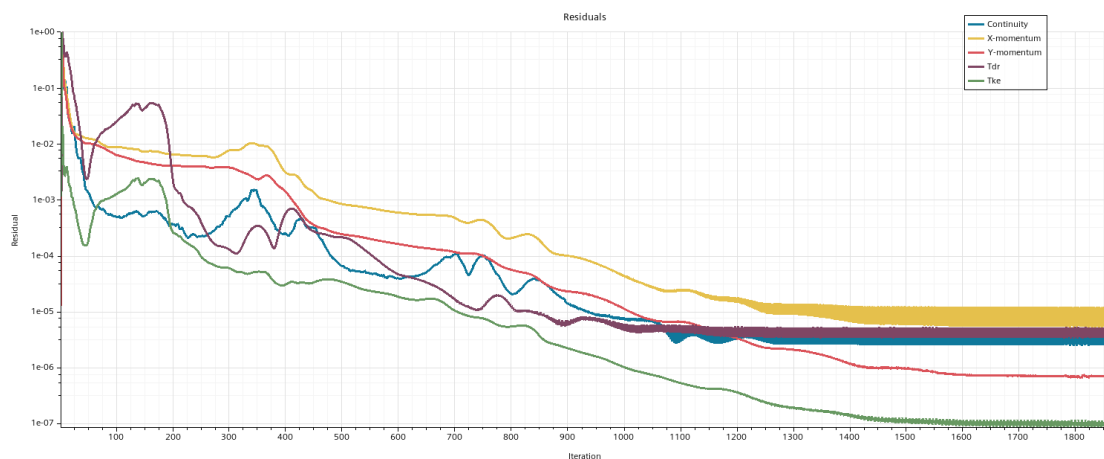


Figure 91: Residuals of the second rear wing profile simulation. Notice the lower residuals compared to those of the previous simulation.

The residuals oscillate after de simulation is converged, but the force results are fixed around a value. This indicates that the obtained solution is more accurate in this case compared to the first simulation, even though the residuals have a higher degree of oscillation:

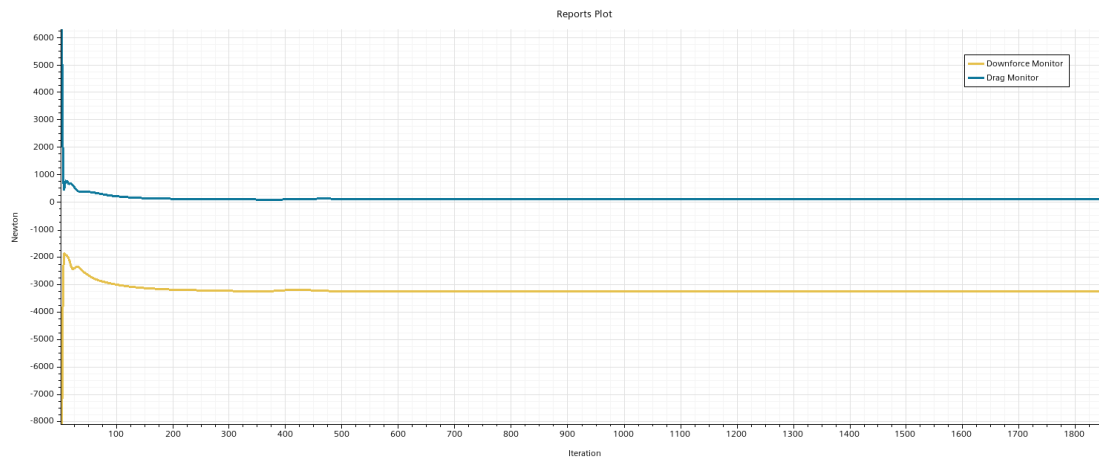


Figure 92: Drag and downforce report of the second rear wing profile.

From this force report alone, it is already known that the new profile has a better aerodynamic performance. The drag has decreased, while the downforce has increased, making the wing more efficient.

Force / Coefficient at 75 [m/s]	Unitary length force	Wing (L=1860 [mm])
Drag	99,40 [N/m]	184,88 [N]
Downforce	-3262,93 [N/m]	-6069,05 [N]
Cd (A=0,21 [m²])	0,260	0,260
Cl (A=0,21 [m²])	-48,55	-8,55

Table 16: Forces generated by the second rear wing profile.

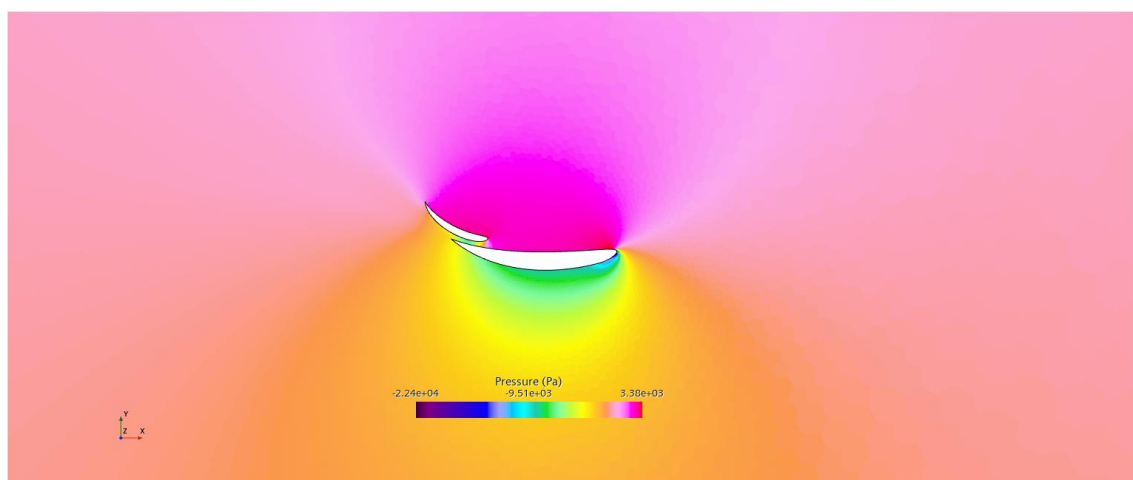


Figure 93: Pressure distribution along the revised rear wing profile.

The longitudinal pressure distribution is much better compared to the previous profile design, with a lower positive pressure on both the upper and lower sides of the wing profile. This means

that the new profile generates a higher amount of negative vertical force with less drag. This allows the car to have a higher top speed and a lower fuel consumption.

Below there is a comparison between the pressure profile of the original and revised rear wing profiles:

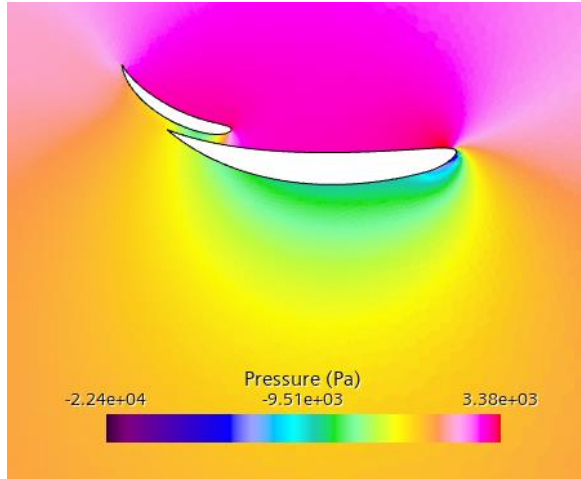


Figure 94: Improved rear wing profile. Pressure distribution.

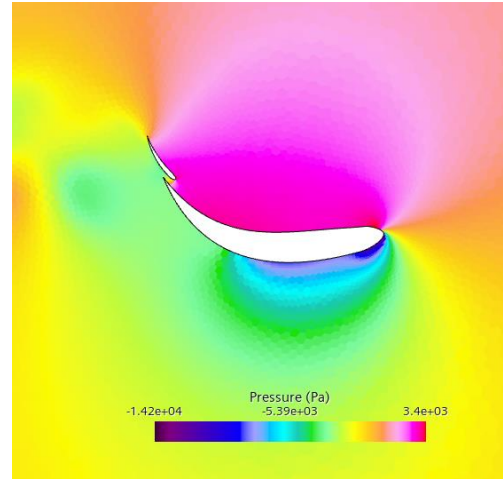


Figure 95: Original rear wing profile. Pressure distribution.

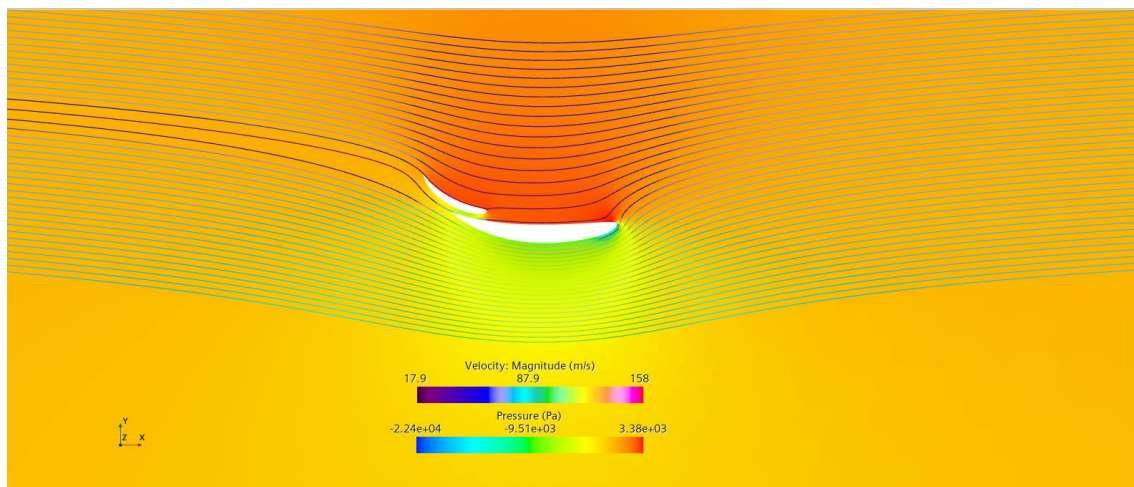


Figure 96: Streamlines around the revised wing profile.

On the revised geometry, the air flow under the rear wing does not detach from the lower surfaces like on the original geometry. This reduces the drag force to about a third of the drag force generated by the original wing profile.

Force at [75 m/s]	Original profile (unitary)	Revised profile (unitary)	Difference (%)
Drag	310,69 [N]	99,4 [N]	31,99 %
Downforce	-2400,11 [N]	-3262,93 [N]	135,95 %

Table 17: Aerodynamic improvements of the revised rear wing geometry compared to the original profile.

In motorsport, there are certain scenarios that require high amounts of downforce produced by the rear wing, resulting in high angles of attack that may stall the upper wing element. This is usually solved by installing a small perpendicular tab along the exit edge of the upper wing element. This tab is commonly known as a “*Gurney flap*” in the motorsport industry. In this case, the revised wing profile sketch is modified to add the perpendicular tab:

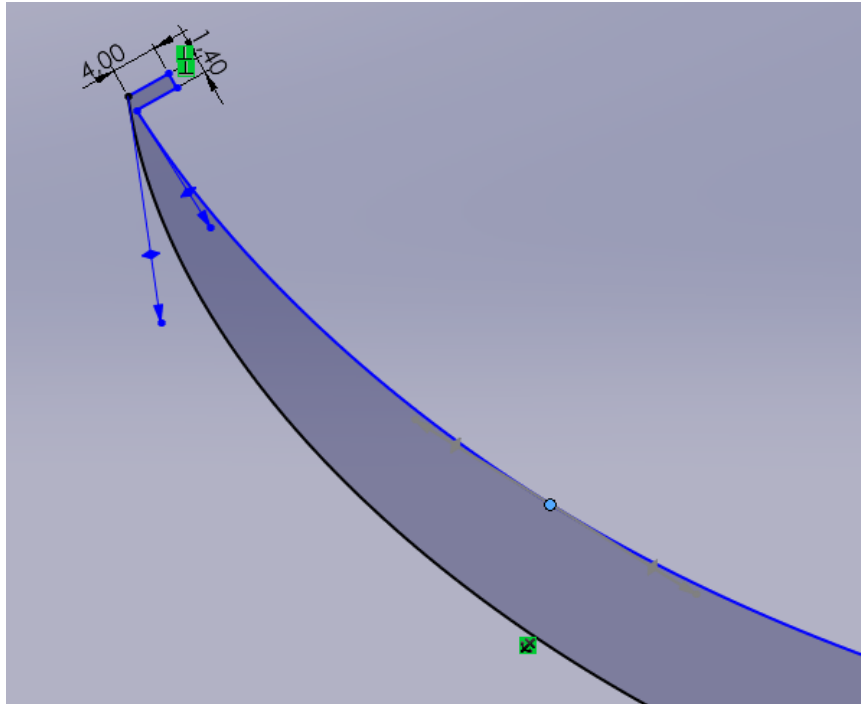


Figure 97: Gurney flap on the upper wing element.

In this case, this tab is not necessary because the flow on the revised rear wing profile does not detach from the underside of the rear wing, but it is interesting to compare the results of the revised profile with and without the Gurney flap installed. The following simulation has been computed using the same mesh and physics conditions as in the previous two:

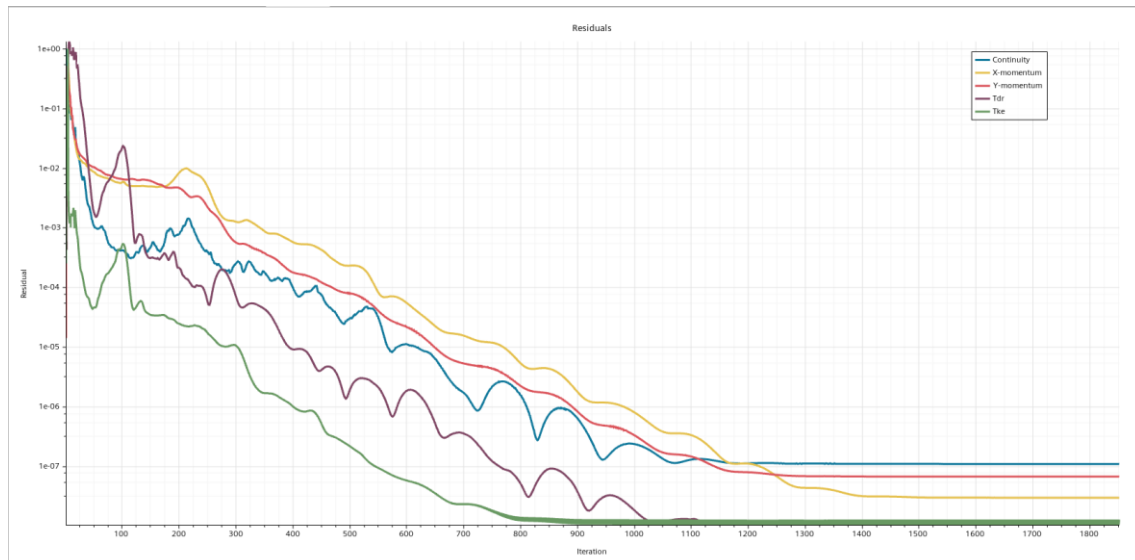


Figure 98: residuals plot of the revised rear wing profile with the Gurney flap installed.

The extremely low (around $1E-6$) residuals indicate that the simulation has converged with a very high level of accuracy. The drag and force reports have also converged with a high level of accuracy:

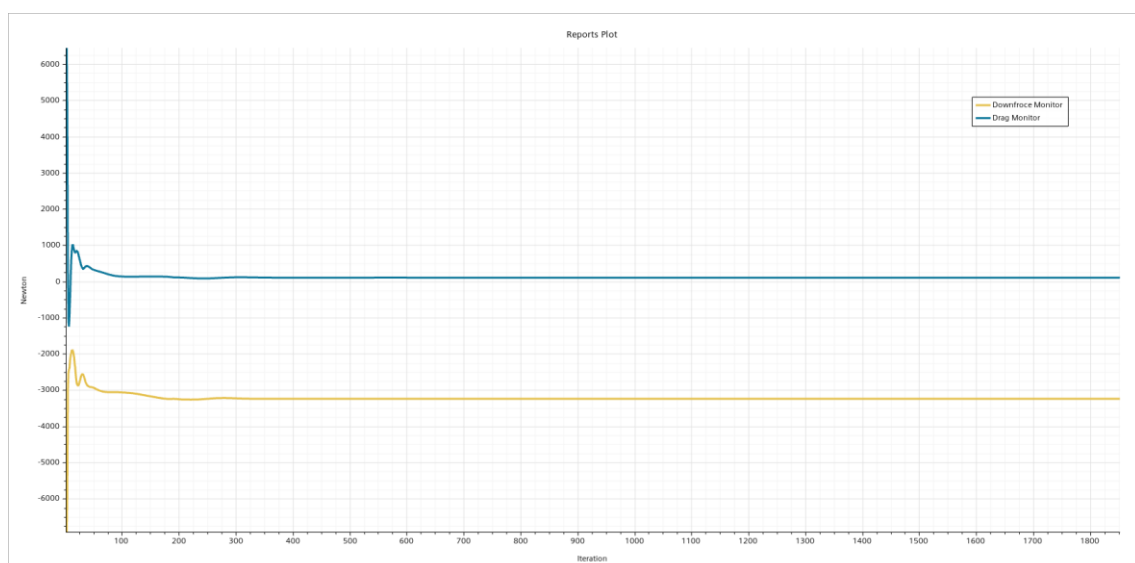


Figure 99: Force reports plot of the revised rear wing profile with the Gurney flap installed.

In this case the results are very similar to those obtained with revised rear wing profile. In this case, the Gurney flap does not have any effect of the flow separation under the rear wing:

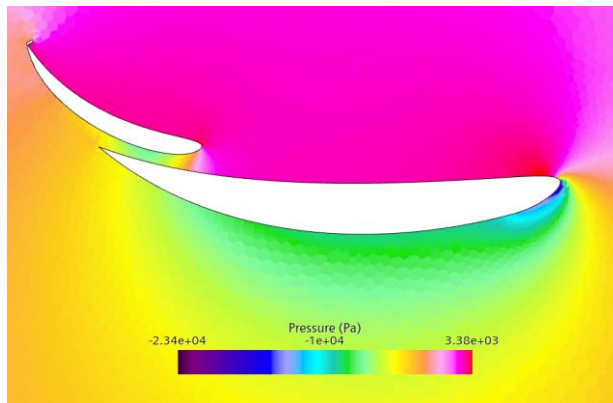


Figure 100: Pressure distribution with the Gurney flap installed.

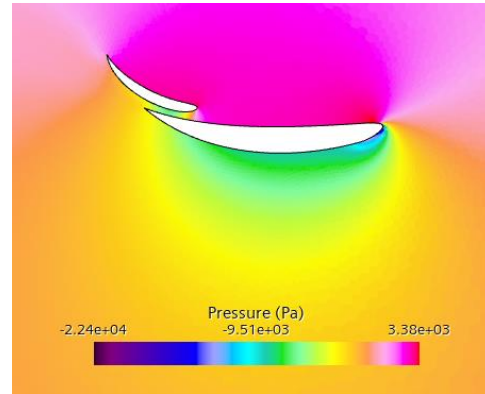


Figure 101: Pressure distribution without the Gurney flap installed.

The aerodynamic forces are very similar as well:

Force / Coefficient at 75 [m/s]	Unitary length force	Wing (L=1860 [mm])
Drag	103,54 [N/m]	192,58 [N]
Downforce	-3241,60 [N/m]	-6029,37 [N]
Cd (A=0,21 [m²])	0,27	0,27
Cl (A=0,21 [m²])	-8,49	-8,49

Table 18: Drag and downforce values of the revised wing profile with the Gurney flap Installed.

For the first design iteration, the Gurney flap is not installed due to the unnoticeable performance gains, although this aerodynamic element may be necessary when a high downforce rear wing is used. This case is further explored in the second design iteration.

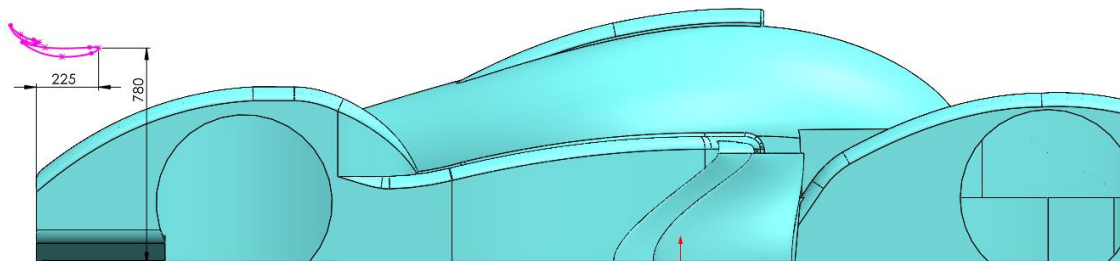


Figure 102: Rear wing placement relative to the car.

5.1.5 Front wings

The front wing works in a very similar way compared to the rear wing. In this case, the flow that is faced by the front wings is very clean, with very low level of turbulence. This increases the efficiency and effectiveness of these aerodynamic surfaces.

These wings are placed between the wheel fenders and the chassis crash structure:

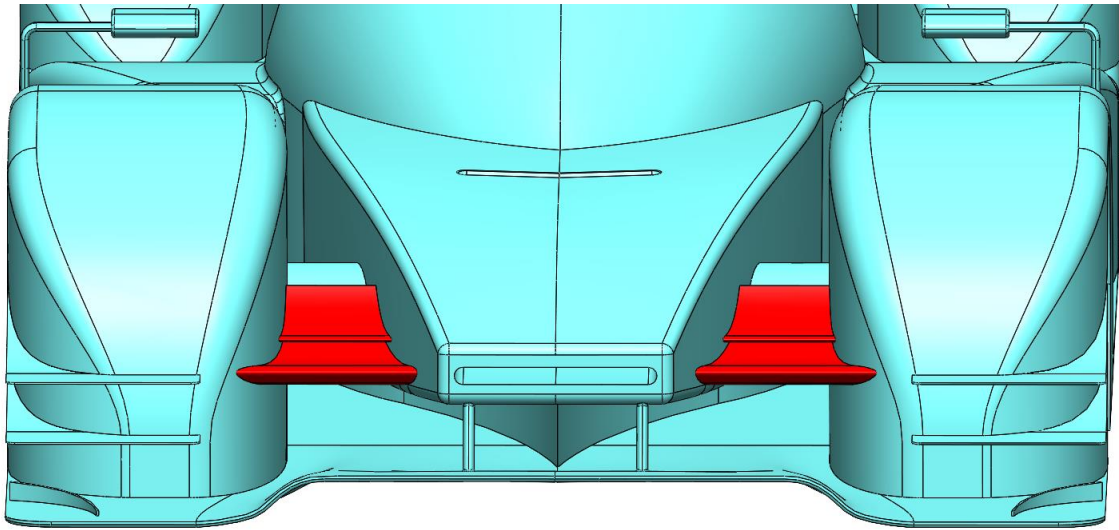


Figure 103: Front wings highlighted in red.

The wing profile is validated by performing a 2D simulation using STAR-CCM+ following the same workflow as in the rear wing profile validation study. The mesh and physics conditions are also kept the same as in the rear wing 2D simulations. The profile is imported into the CFD software as a Parasolid (.x_t) file:

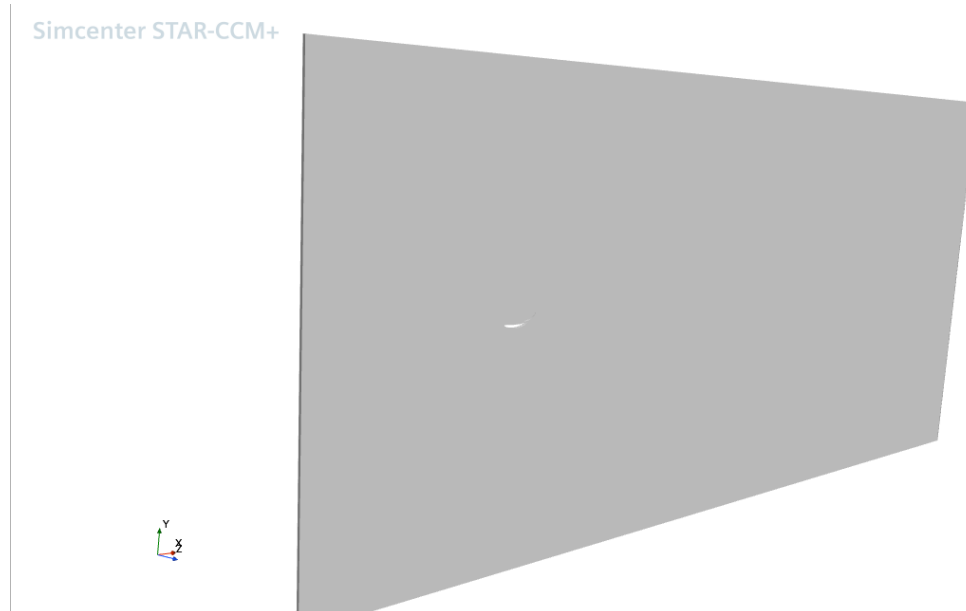


Figure 104: Front wing profile imported into STAR-CCM+.

The residuals are very good in this particular simulation. The simulation has converged after 1800 iterations with an average residual value of $1\text{E-}7$:

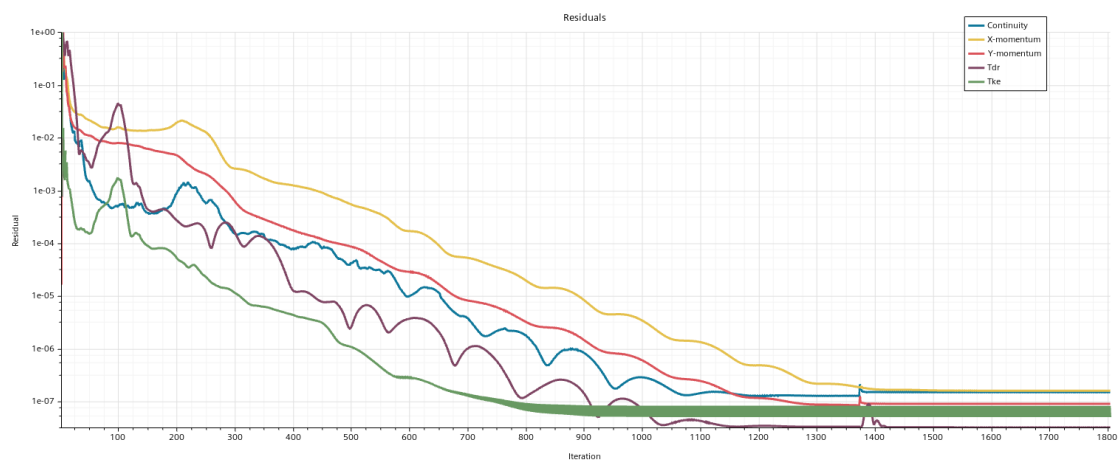


Figure 105: Front wing profile 2D simulation residuals.

The drag and downforce values are also converged as can be seen in the figure below:

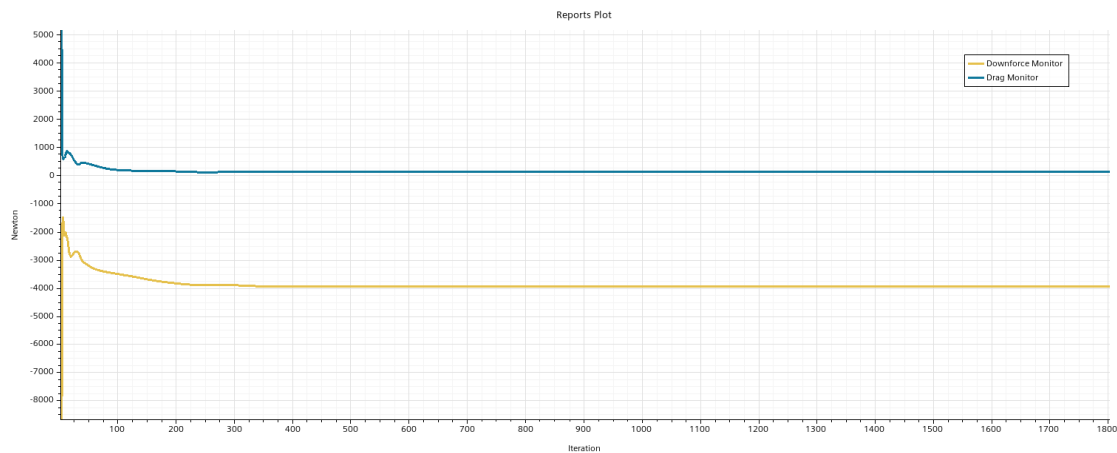


Figure 106: Drag and downforce report of the front wings profile 2D simulation.

The values for the drag and downforce values are converged after 600 iterations, but it is a good practice to assess the convergence level of the solution by checking the lack of solution oscillation of both the residuals and reports.

The force values of the front wings 2D simulation are only expressed as a unitary length force because the exact length of these wings is unknown due to the variable width:

Force / Coefficient at 75 [m/s]	Unitary length value
Drag	110,14 [N/m]
Downforce	-3956,98 [N/m]
Cd	0,24
Cl	-8,67

Table 19: Aerodynamic forces and coefficients of the front wing profile.

The first profile has a very good aerodynamic performance, even superior to that of the rear wing profile. From the data, this profile is unlikely to have flow separation or stagnation on the wake region, but this must shall be cross-examined with the visual scenes:

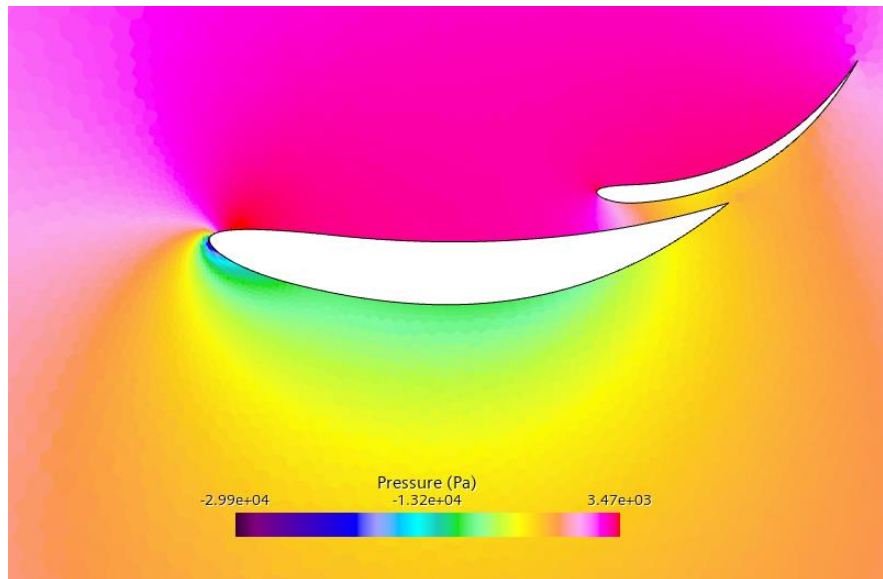


Figure 107: Pressure field of the front wing profile.

The pressure on the underside of this profile remains constant all along the profile length, with no sudden changes in pressure. This is the desired pressure field for any aerodynamic profile that needs to be efficient in maximizing low drag and high lift properties. There is not flow separation or flow stagnation on the underside of this profile as can be seen in the figure below:

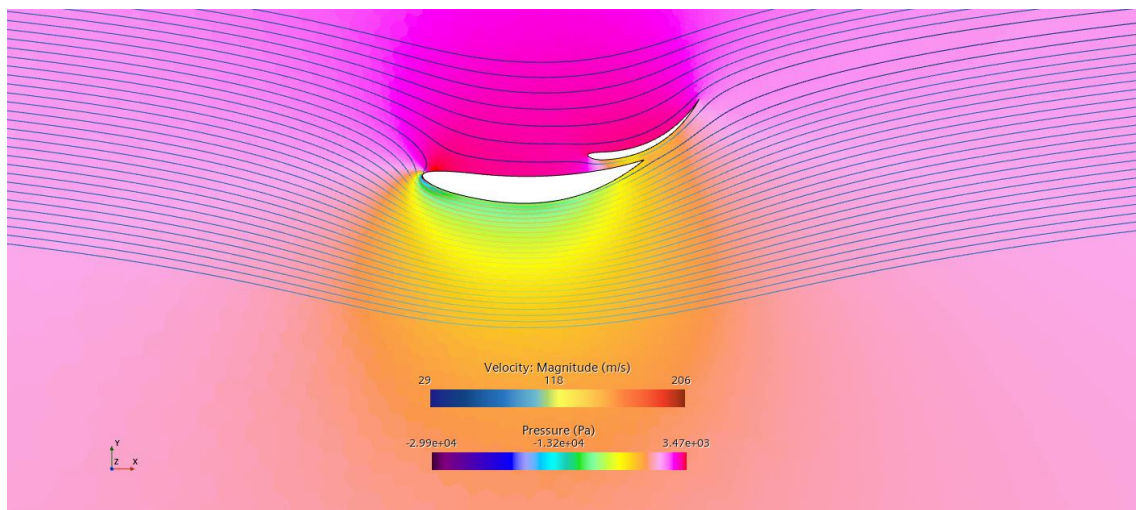


Figure 108: Streamlines flowing along the front wing profile.

The streamlines that flow under the front wing profile remain attach for most of the underside. There is a small amount of flow separation on the rightmost part of the upper element that indicates that the angle of attack of the upper element is on the critical flow separation angle. This can be optimized by installing a Gurney flap on the upper element, as explained in the rear wing optimization chapter of this thesis.

Usually, the Gurney flap should have a length of between the 2% and 5% of the cord length [13]. In this case, this wing profile has a combine cord length of 385 [mm]. For a percentage of 2.5% of the cord, the gurney flap should be 9.625 [mm] long:

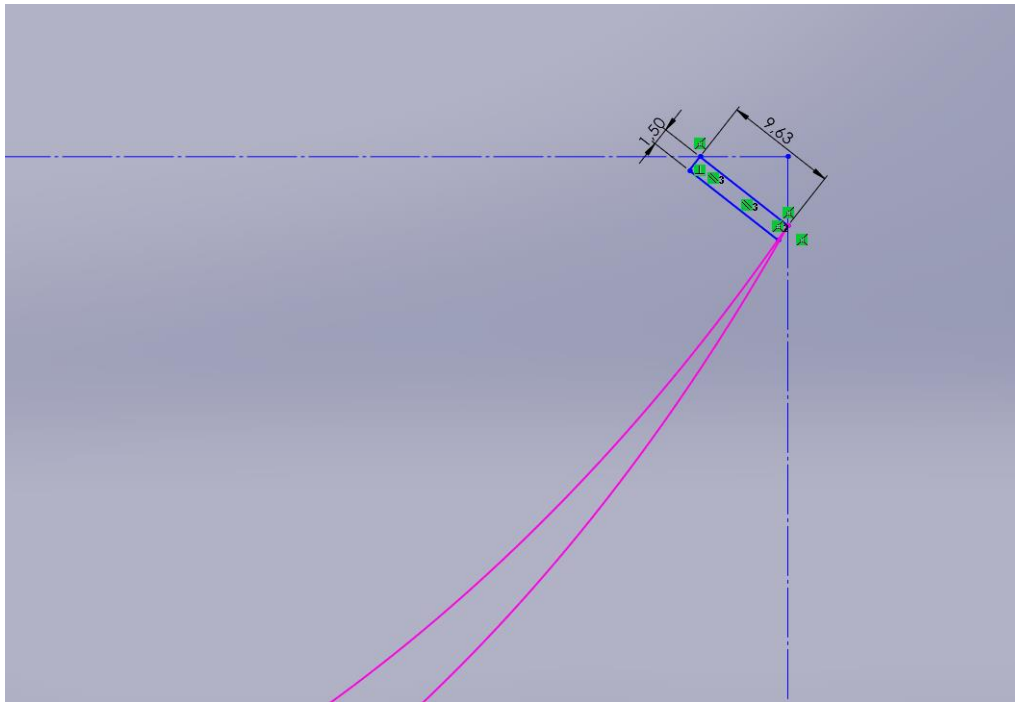


Figure 109: Gurney flap on the front wing profile.

The 2D simulation of the front wing profile with the Gurney flap installed is performed using the same mesh and physics conditions as in the previous 2D simulations. These are the residuals of the converged simulation:

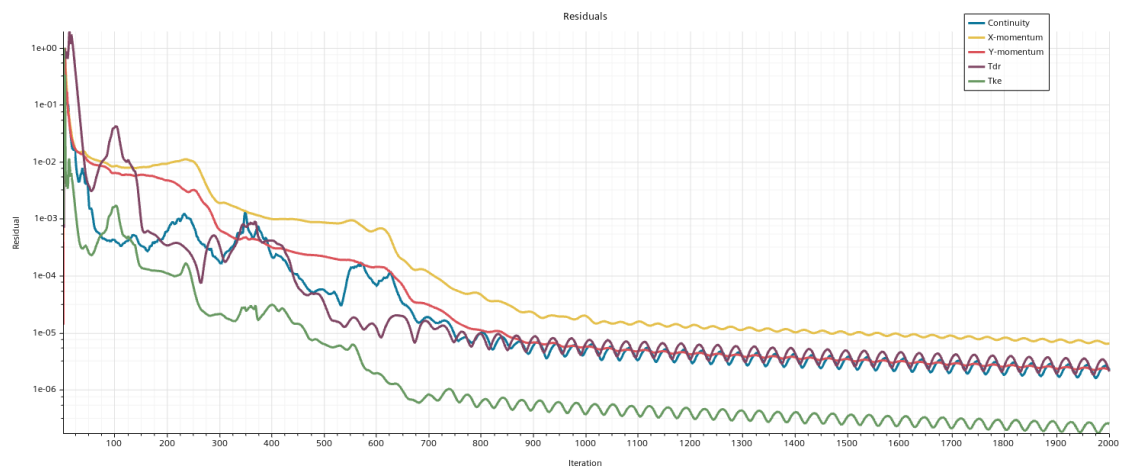


Figure 110: 2D Simulation residuals of the front wing profile with the Gurney flap installed.

Although the residuals fluctuate, the solution is fully converged after 2000 iterations as can be seen on the drag and downforce report plots:

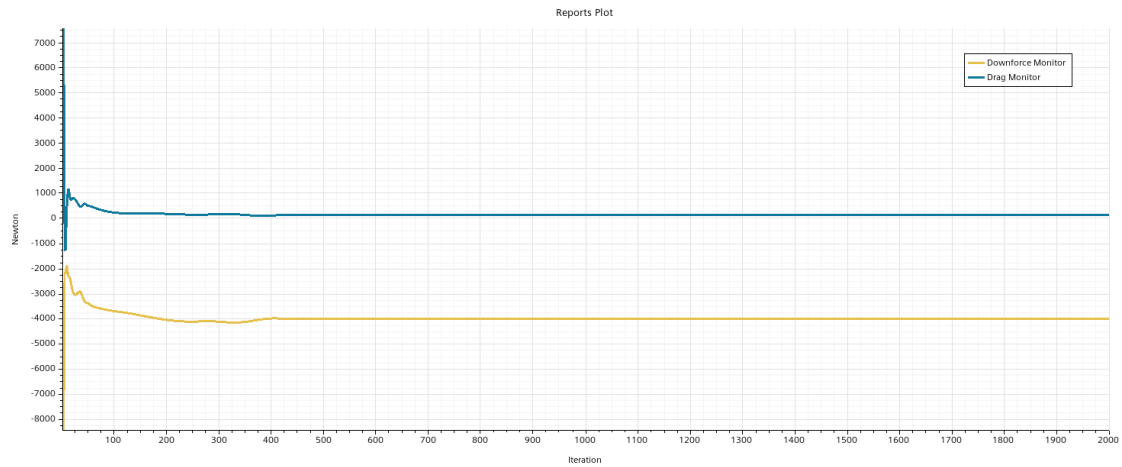


Figure 111: Drag and downforce report of the front wings profile fitted with the Gurney flap.

Force / Coefficient at 75 [m/s]	Unitary length value
Drag	133,02 [N/m]
Downforce	-4002,77 [N/m]
Cd	0,28
Cl	-8,40

Table 20: Aerodynamic data of the front wing fitted with the Gurney flap

The aerodynamic data of the front wing with the Gurney flap fitted indicates a reduction in performance, although this reduction is relatively small. This is caused by the frontal area added by the flap, which increases the drag produced by the front wing profile.

The pressure field is almost identical to that of the front wing without the gurney flap installed:

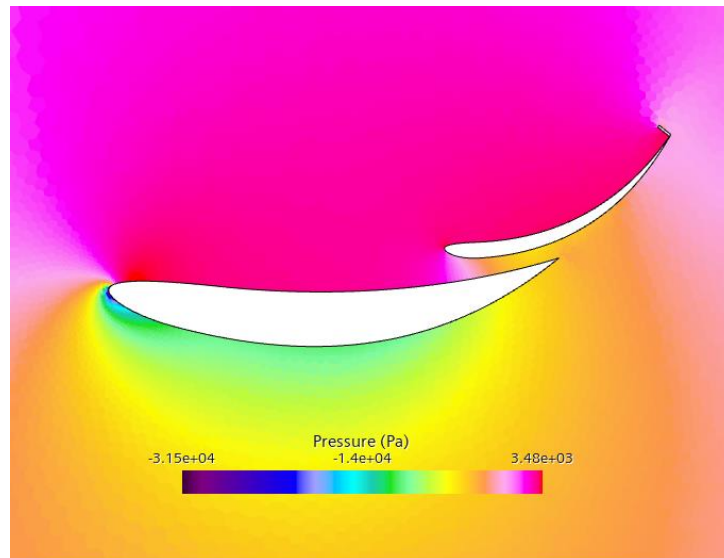


Figure 112: Pressure field of the front wing profile fitted with the Gurney flap.

On the wake region of the flap there is a low-pressure region that generates positive lift of the back face of the flap, resulting in lower overall downforce. The overall wing efficiency higher. The pressure is extended backwards compared to that of the front wing without the Gurney flap:

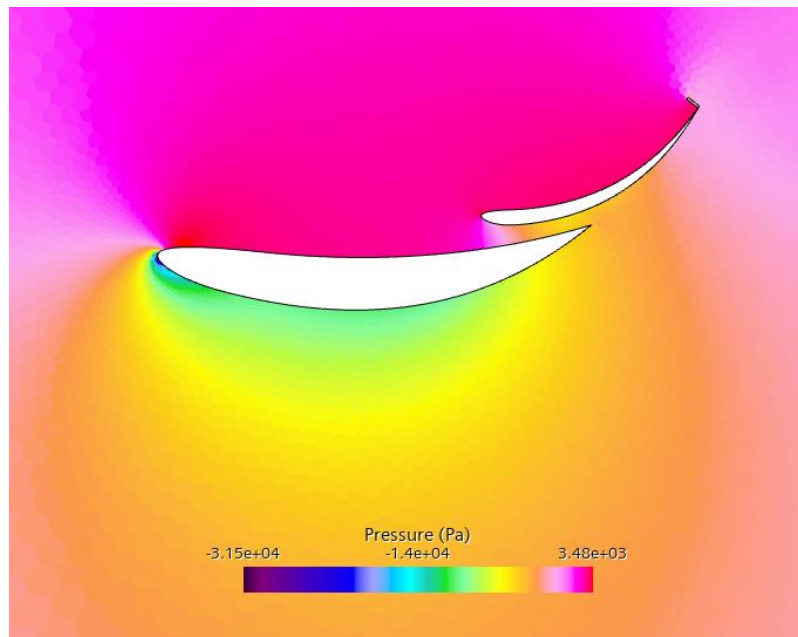


Figure 113: Pressure field on the front wing fitted with the Gurney flap.

The pressure field variation is better seen directly compared to that of the front wing without the gurney flap:

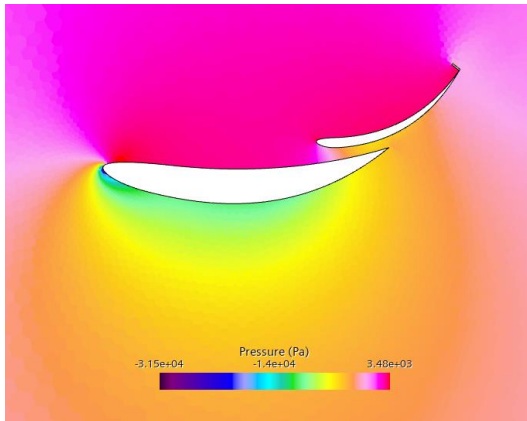


Figure 114: Pressure field w/ Gurney flap.

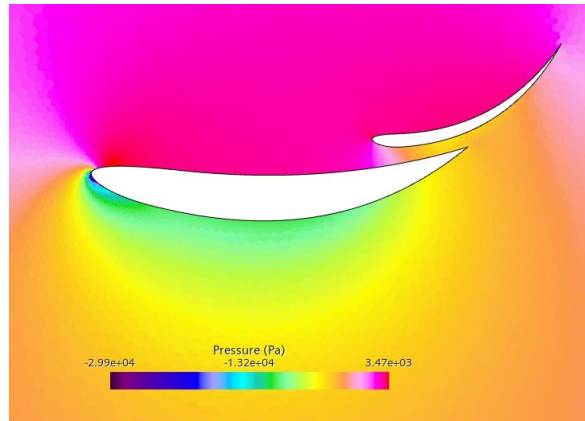


Figure 115: Pressure field wo/ Gurney flap.

Due to the overall lower efficiency of the front wing fitted with the Gurney flap, this tab is not included in the front wing of the car for the first design iteration CFD simulation.

5.1.6 Other modifications

The geometry has been modified in multiple places where the overall aerodynamic effect is not as big as the other major modifications such as floor, wings, diffuser, etc. The main objective of this modifications is to optimize secondary geometry features along the car's surface.

The first and most important of these secondary modifications are the wheel wake vent louvres. These cuts on the wheel fenders are a very common geometrical feature in most closed wheel racing cars. In this case, these louvres have been cut on the back side of both the front and rear wheel covers:

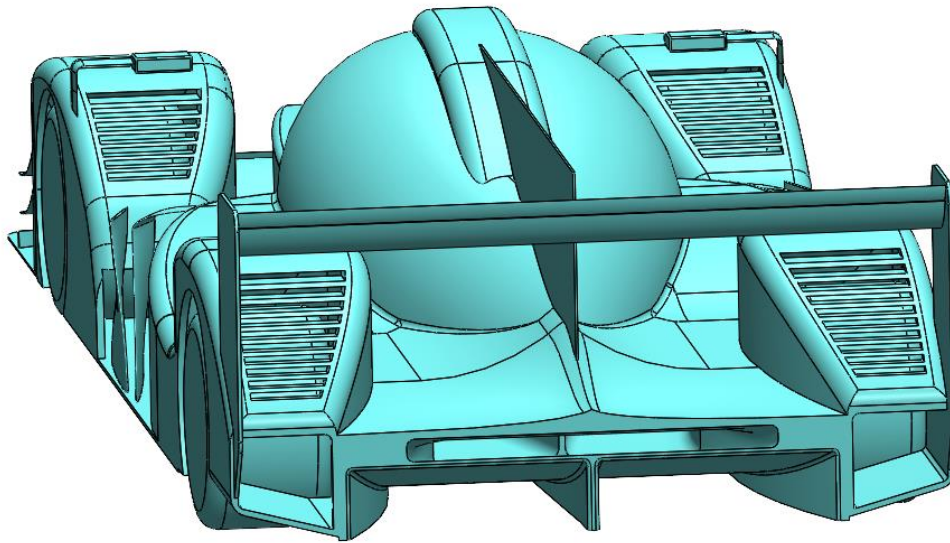


Figure 116: Vent louvres on the backside of each wheel fender.

These louvres have been cut in the region of the wheel fender where the incoming air flow generates a low-pressure zone. This strategy helps venting the trapped wheel wake turbulent flow inside the wheel fenders:

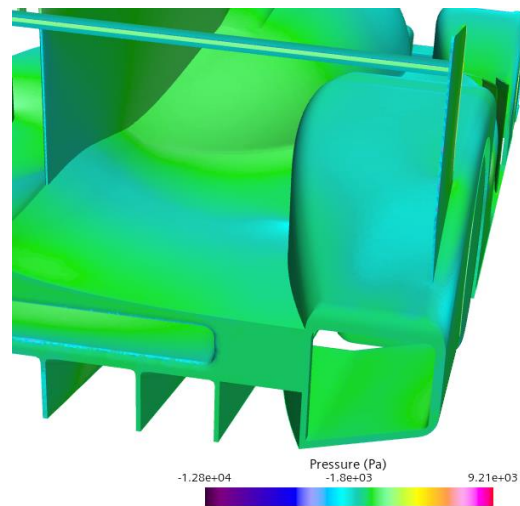


Figure 117: Low pressure region on the rear wheel fenders.

5.2 Simulation

After all the modifications have been included into the updated 3D model, the CFD simulation is prepared using the same parameters as in the first 3D model CFD simulation. By keeping all the mesh and physics parameters constant throughout all the simulations it is possible to accurately compare the resulting data between the simulations.

In this case, the 3D model is imported as a Parasolid (.x_t) into STAR-CCM+:

Simcenter STAR-CCM+

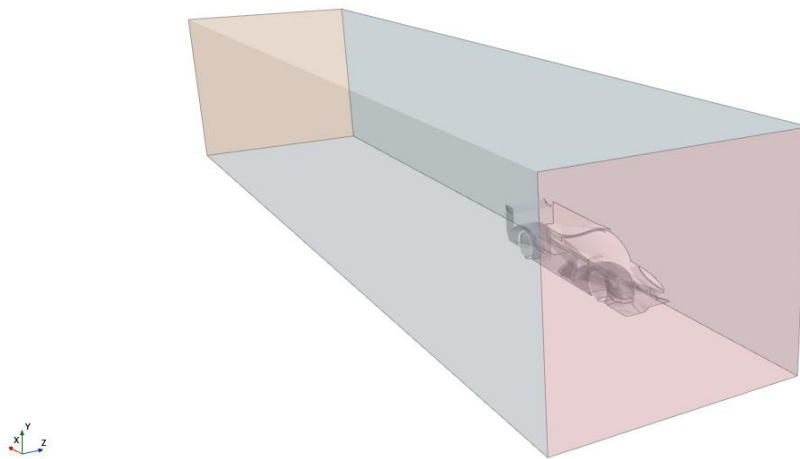


Figure 118: Improved car geometry imported into STAR-CCM+.

The meshing is performed using the same exact parameters as in the first 3D simulation. These are the mesh sizes used for this operation:

Variable	Value
Base Size	220 [mm]
CAD Projection	yes
Target Surface Size	100.0 % of Base Size
Minimum Surface Size	7.5 [mm]
Surface Curvature	72 pts/circle, Max 360 pts/circle
Surface Growth Rate	Slow
Number of Prism Layers	4
Prism Layer Stretching	1.5
Prism Layer Total Thickness	15 [mm]
Volume Growth Rate	1.25
Maximum Tet Size	100.0 % of Base Size

Table 21: Mesh values for the second CFD simulation.

Variable	Value
Wake Distance	3.5 [m]
Direction	Vector (XYZ): [1, 0, 0]
Spread Angle	14 °
Isotropic Size	40 [mm]
Growth Rate	1.25

Table 22: Wake refinement for the second CFD simulation.

Once all the mesh value shave been set, the mesh operation is executed, with the resulting mesh:

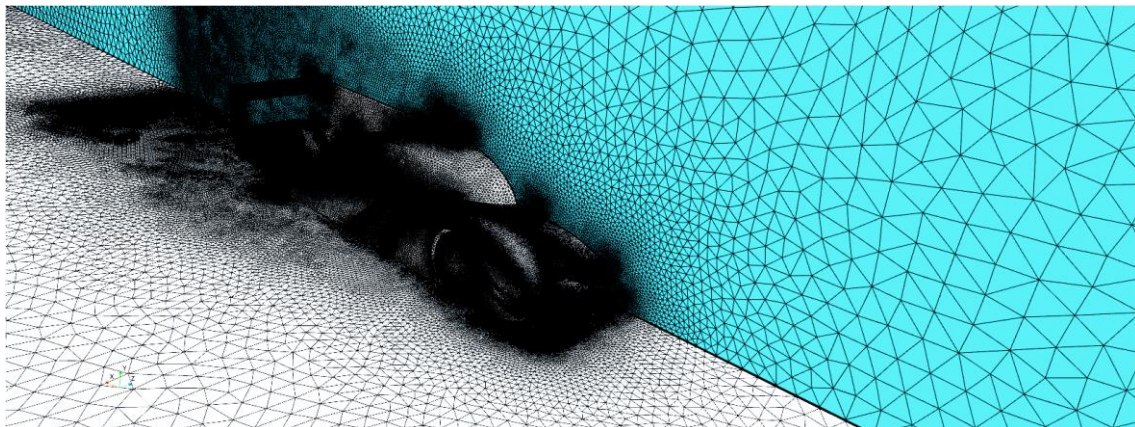


Figure 119: Surface mesh. Second CFD simulation.

The physics and boundary conditions are all kept the same except the initial velocity for the mesh cells. On the first 3D CFD simulation the initial velocity was set to 20 [m/s], a value much lower than the inlet flow velocity, which is 75 [m/s]. This can cause longer simulation time and bad convergence due to the increased iterations needed for a converged solution.

Instead, it is common to assign a slightly lower velocity as an initial velocity for all cells. This reduces the convergence time and the resulting solution has a higher level of accuracy. In this case, the initial flow velocity is set to 75 [m/s]:

Velocity - Properties ×	
▼ Properties	
Method	Constant ▼
Value	[75.0, 0.0, 0.0] m/s +++
Dimensions	Velocity +++
Coordinate System	Laboratory ▼

Figure 120: Initial velocity conditions. Second CFD simulation.

The simulation takes about 2200 iterations to fully converge. This is the residuals plot of the simulation:

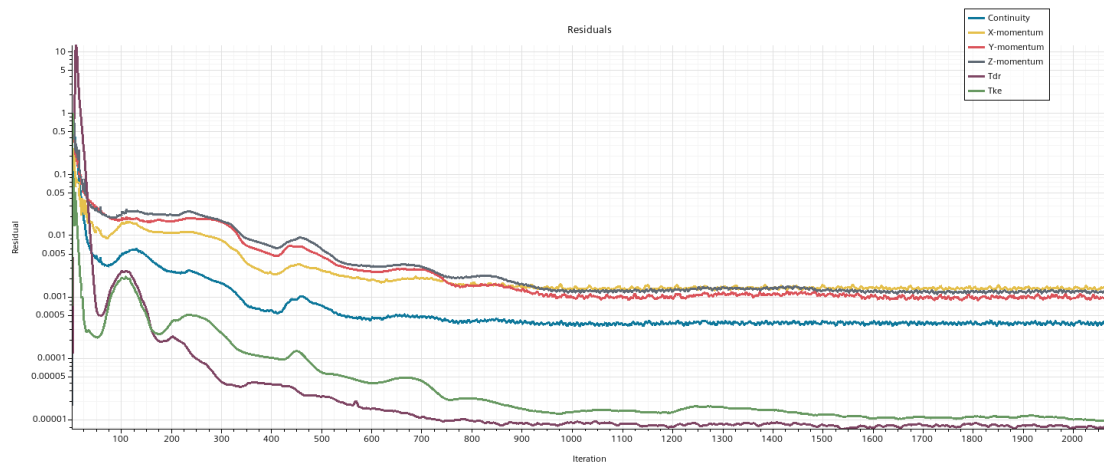


Figure 121: Residuals of the second 3D simulation.

In this case, the values of the residuals are higher compared to those of the first simulation, but the simulation is fully converged as can be seen in the force report plots:

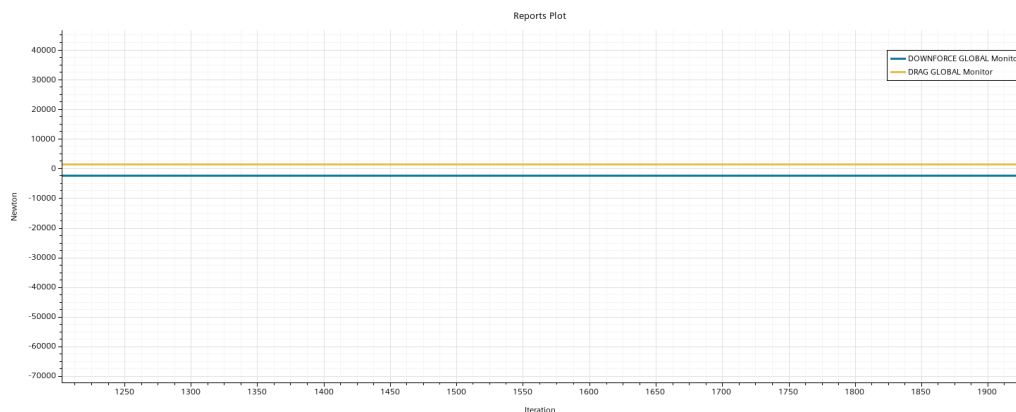


Figure 122: Drag and downforce global values of the revised car geometry.

The forces report of the different aerodynamic surfaces are also fully converged:

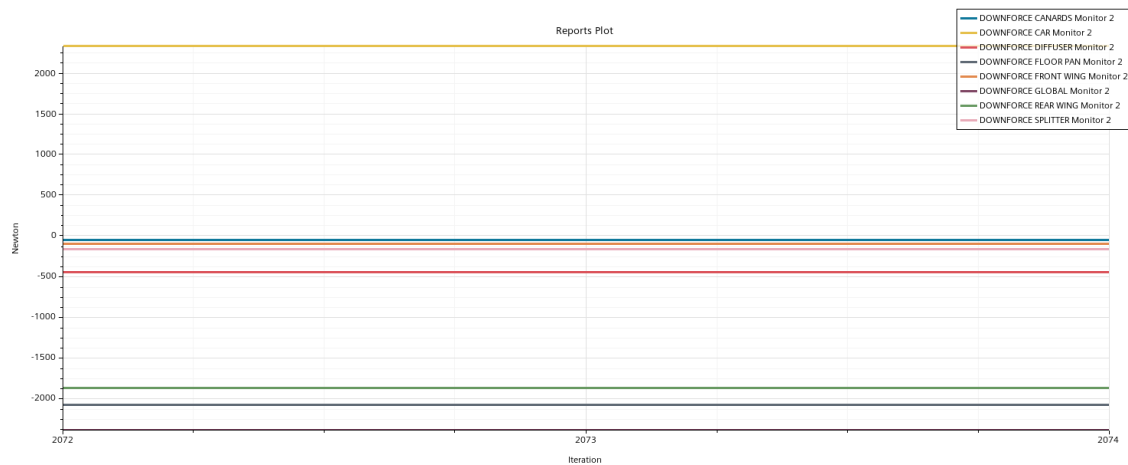


Figure 123: Downforce values by aerodynamic surface.

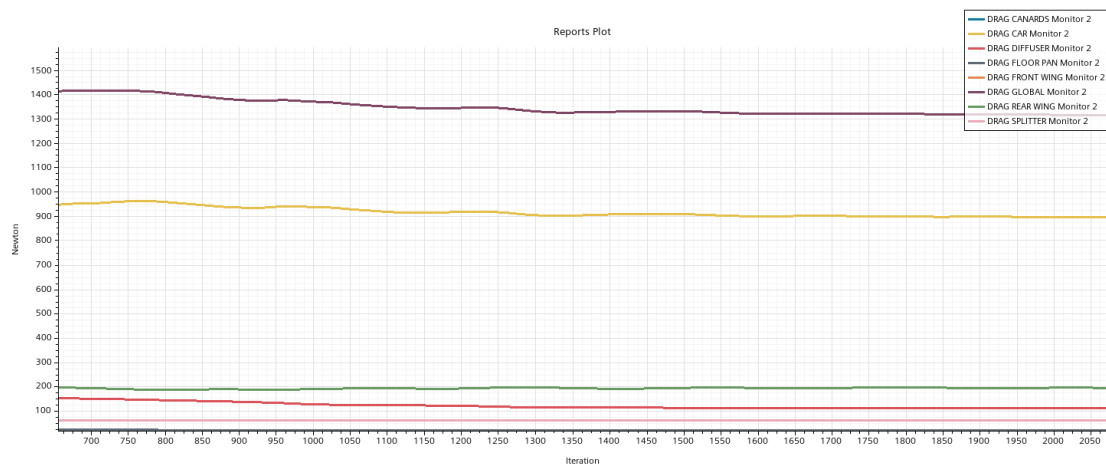


Figure 124: Drag values by aerodynamic surfaces.

The resulting forces are smaller than expected. Although the downforce and drag values of the different aerodynamic surfaces of the car are very similar to those of a LMP car, the body geometry still generates high levels of positive lift. Below, there is a table with all the aerodynamic forces of the car. By default, the CFD program outputs the forces acting on half of the car:

Region	Drag [N]	Downforce [N]
Canards	16,58	-56,38
Diffuser	110,07	-444,33
Floor	18,212	-2080,41
Front wing	109,97	-99,05
Rear wing	194,27	-1868,64
Splitter	59,67	-169,76
Sum	508,77	-4718,57
Car	894,09	2330,68
Global	1402,862	-2387,89

Table 23: Aerodynamic forces on half of the car. Simulation 2.

The values need to be multiplied by two to obtain the whole car aerodynamic forces:

Region	Drag [N]	Downforce [N]
Canards	33,16	-112,76
Diffuser	220,14	-888,66
Floor	36,424	-4160,82
Front wing	219,94	-198,1
Rear wing	388,54	-3737,28
Splitter	119,34	-339,52
Sum	1017,54	-9437,14
Car	1788,18	4661,36
Global	2805,72	-4775,78

Table 24: Aerodynamic forces on the whole car. Simulation 2.

The frontal area is measured following the same procedure as in previous cases:

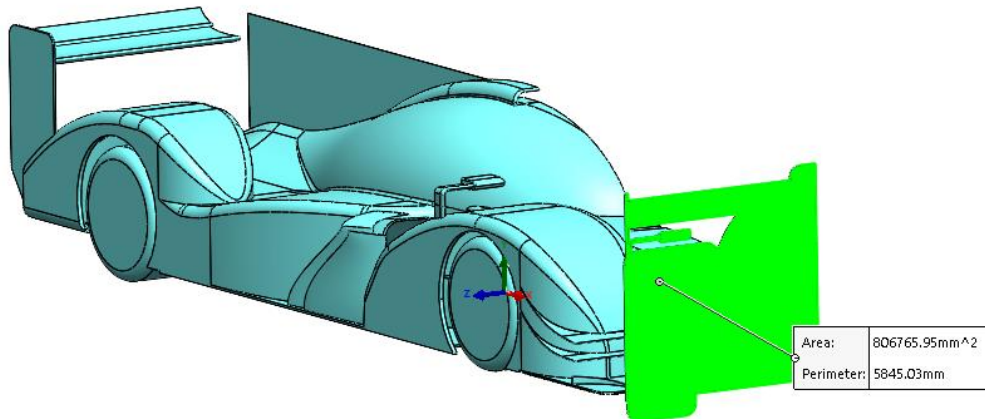


Figure 125: Frontal area measurement. Simulation 2.

Type	Half [m ²]	Total [m ²]
Frontal Area	0,8067	1,6135

Table 25: Frontal area of the revise geometry V1.

With this frontal area it is possible to calculate the drag and lift coefficients of the revised car geometry:

Coefficient	Value
Cd	0,52
Cl	-0,88

Table 26: Drag and lift coefficients of the revised geometry V1.

As in the first simulation, the Centre of Pressure coordinates are calculated using a dedicated metrics report in STAR-CCM+:

Coordinate direction	Value [m]
X axis	2,16
Y axis	0,37

Table 27: CoP Coordinates. Simulation 2.

These are the results after running the Python script:

```
Downforce value [N]: -4775.78
Drag value[N]: 2805.72
COP X coordinate [m]: 2.16
COP Y coordinate [m]: 0.37
Rear axle aerodynamic load [N]: 3915.103862068966
Front axle aerodynamic load [N]: 860.6761379310342
Front: 18.02168730408507 % Rear: 81.97831269591492 %
```

Figure 126: Aerodynamic load distribution. Simulation 2.

Below, there is a compilation of all the data gathered from the simulation. These are the most important values regarding the aerodynamic performance of the car:

Revised geometry	Value
Drag force	2805,72 [N]
Downforce	-4775,78 [N]
Cd	0,52
Cl	0,88
Downforce distribution	18,02% Front – 81,98% Rear
L/D	-1,7:1
Frontal area	1,6135 [m ²]
Flow velocity	75 [m/s]

Table 28: General aerodynamic data of the revised geometry V1. Simulation 2.

With this data, it is possible to directly compare the aerodynamic performance of the revised geometry car with the aerodynamic data of the Audi R18:

	Audi R18 (adjusted)	LMP revised geometry V1
Drag force	2823,53 [N]	2805,72 [N]
Downforce	-11268,95 [N]	-4775,78 [N]
Cd	0,471	0,52
Cl	-1,8798	0,88
Downforce distribution	53% Front - 47% Rear	18,02% Front – 81,98% Rear
L/D	-3,99:1	-1,7:1
Frontal area	1,8 [m ²]	1,6135 [m ²]
Flow velocity	75 [m/s]	75 [m/s]

Table 29: Comparison between the revised geometry car and the Audi R18. Simulation 2.

The negative lift forces on the whole car are still much lower compared to the expected downforce values generated by a LMP car. The main cause of these low downforce values is the outer shape of the monocoque, more specific, the rounded shape around the driver's cockpit. The outer shape of this surface acts as an air foil, generating a low-pressure region:

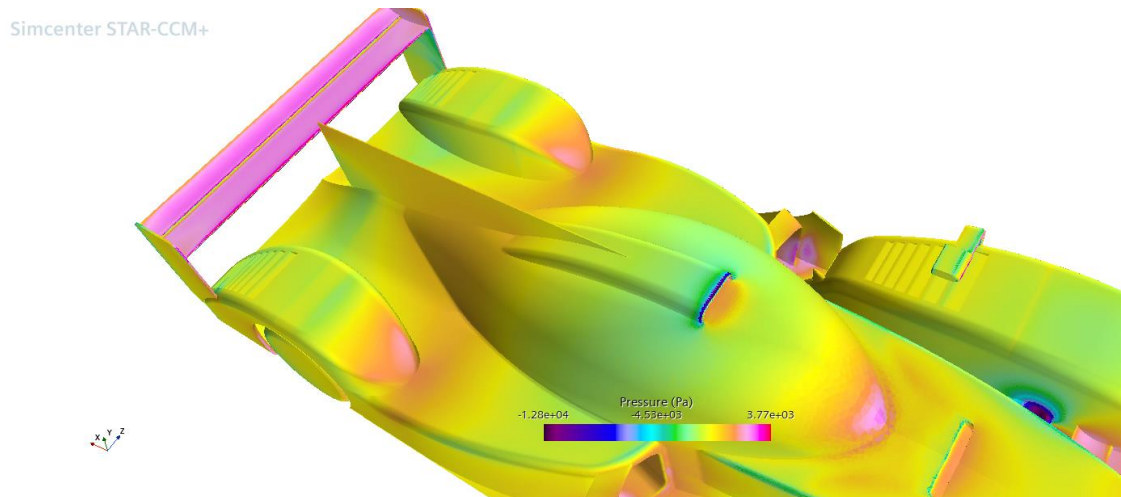


Figure 127: Low pressure on the cockpit canopy. Simulation 2.

This problem is carried over from the first 3D simulation, as the cockpit geometry has not been changed. This is a critical problem that counter effects all the aerodynamic efficiency of the car. The geometry of the canopy is very difficult to modify due to it being part of the monocoque chassis. Usually, the outer shape is designed in the early stages of the development phase and it is almost impossible to change the outer profile of the chassis. For the case being, the outer shape is modified in the second design iteration of this thesis.

Overall, the aerodynamic performance of the car has improved, especially in terms of generated downforce. The improvements have performed as expected, although there are certain aerodynamic surfaces that still need to be improved to perform at the desired level.

5.2.1 Visual analysis

After retrieving all the aerodynamic data from the simulation, it is necessary to visually analyse the aerodynamic behaviour of the different surfaces in case there are certain areas where the flow does not attach to the surface or causes other problems that may reduce the overall aerodynamic performance.

Starting with the underside floor, the revised geometry in this region improves the generated downforce along the underside of the car. The main reason as to why the floor works more efficiently as before is the added front splitter that introduces a higher amount of air mass floor under the car. This results in a low-pressure region near the transition section of the splitter:

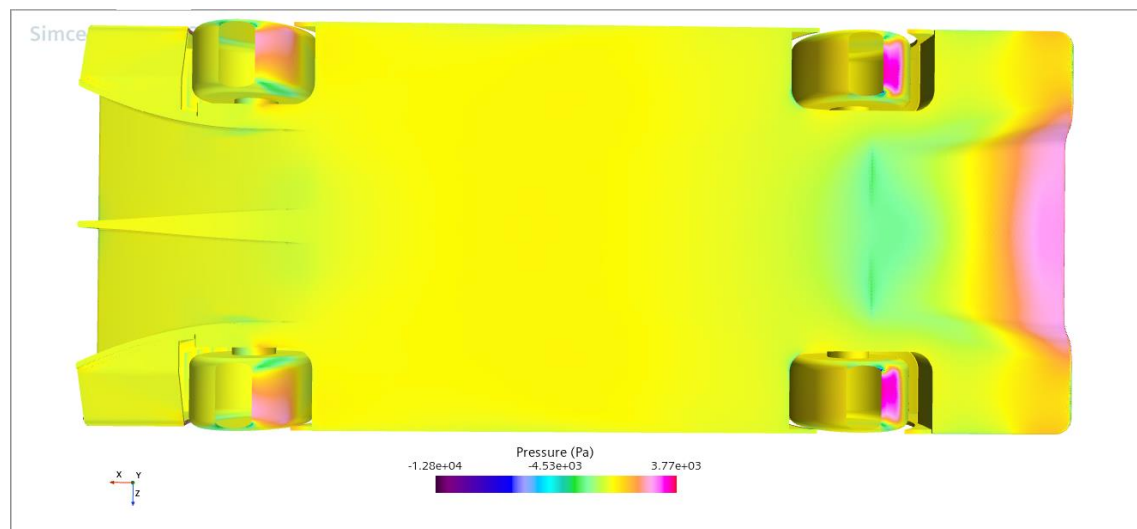


Figure 128: Low pressure region between the splitter and the floor. Simulation 2.

This low-pressure region generates negative pressure between the front wheels, meaning that the aerodynamic balance of the car is not affected by this force. Only the front wheels are loaded, helping reduce understeer at high cornering speeds.

Even though the splitter performs as expected, the shape creates an air flow management problem on the proximity of the front wheels. This happens because the air flow exits the splitter tunnel as the section area decreases:

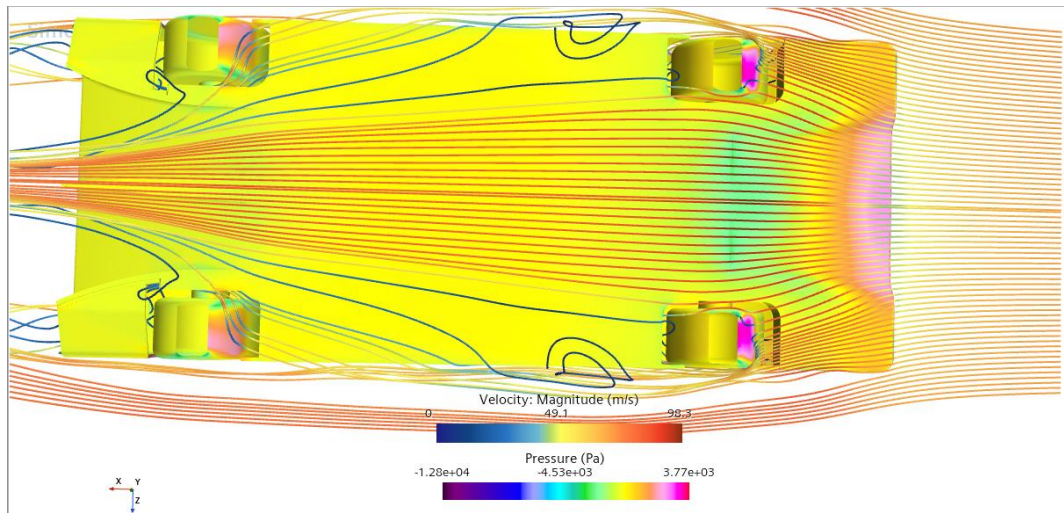


Figure 129: Streamlines flowing through the splitter tunnel. Simulation 2.

The streamlines flowing through the splitter tunnel show that the air flow is derived towards the front wheels, creating turbulences inside the wheel fenders and reducing the air flow mass that flows through the floor up to the rear diffuser:

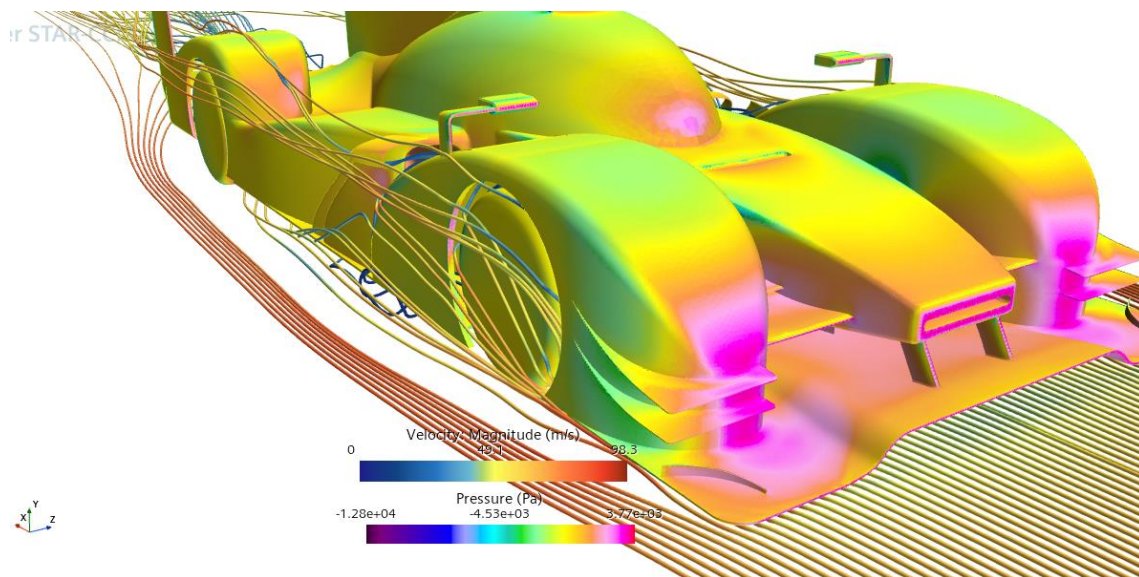


Figure 130: Turbulent air exiting the inside of the front wheel fender. Simulation 2.

Although the overall performance of the underside has been improved, the splitter tunnel geometry shall be improved in future design iterations to mitigate this effect.

The rear diffuser with the new geometry (longer and higher expansion tunnel) does not perform as expected. There is flow separation on the majority of the diffuser:

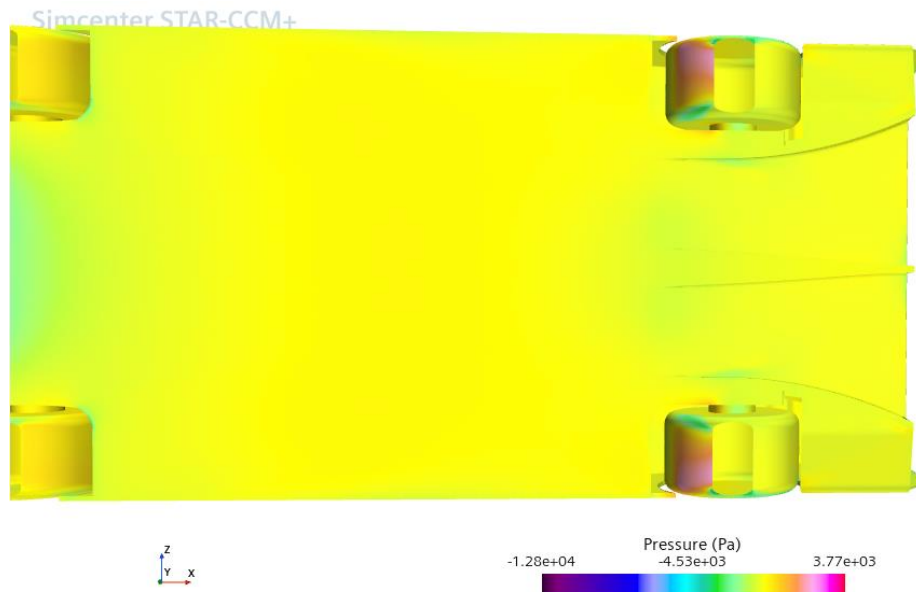


Figure 131: Pressure field on the diffuser region. Notice the small low-pressure region.
Simulation 2.

The diffuser does not expand the flow smoothly as intended. Instead, the flow continues backwards without a change in direction or velocity, meaning that the diffuser is not working as intended. This can be seen by the streamlines flowing through the diffuser:

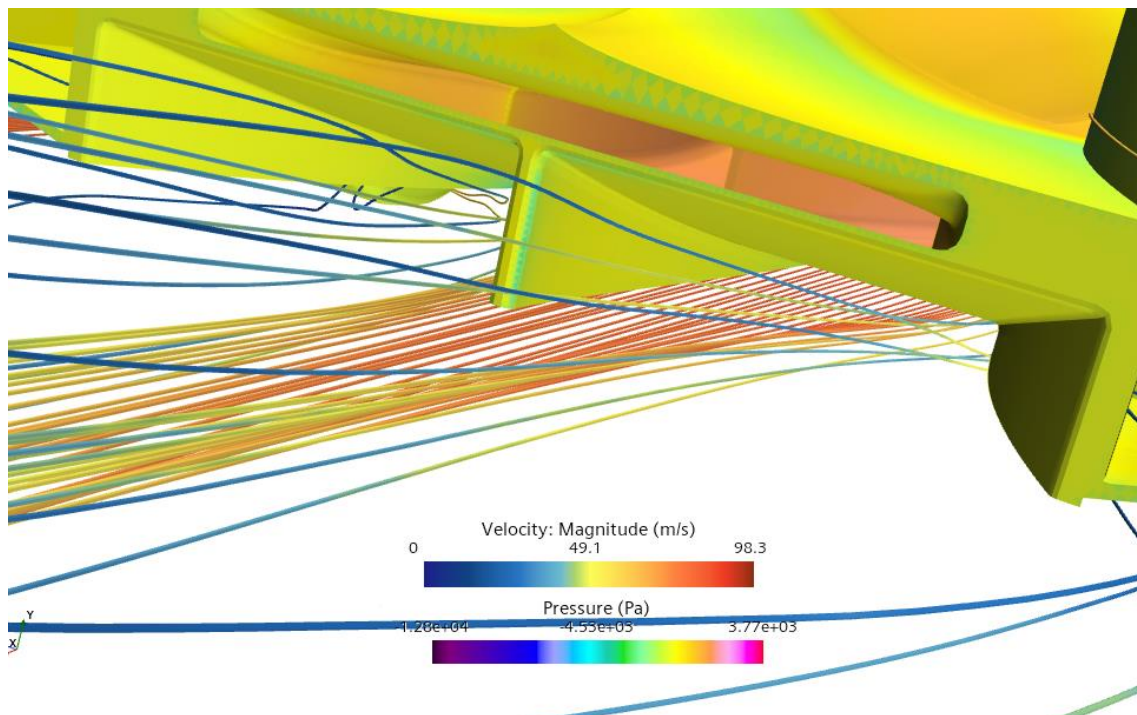


Figure 132: Streamlines on the diffuser. Notice the lack of velocity deceleration on the flow.
Simulation 2.

The velocity of the streamlines is not reduced on the diffuser. This means that the flow detaches from the diffuser's surface at the beginning of it. This problem is exaggerated by the vertical strake in the middle of the diffuser that keeps the flow detached from the diffuser's surface. This is the difference in force between the original and revised geometry diffusers:

Force (Diffuser)	Original geometry [N]	Revised geometry V1 [N]	Difference %
Drag	131,53	220,14	+167,37
Downforce	-554,88	-888,66	-160,15
L/D	-4,21:1	-4,03:1	-4,27

Table 30: Difference in aerodynamic forces between the original and revised geometry diffusers.

Although the performance has been increased from the original geometry diffuser, the current performance is not what is expected from a geometry modification such as this. The revised geometry has longer tunnels and overall higher flow exit profile that should increase the downforce generated by almost 3 times.

Another factor influencing the flow separation on the diffuser region is the rake angle and rear ride height. In this case, the rake angle increases the rear ride height too much, separating the flow from the surface at the very beginning of the diffuser tunnel:

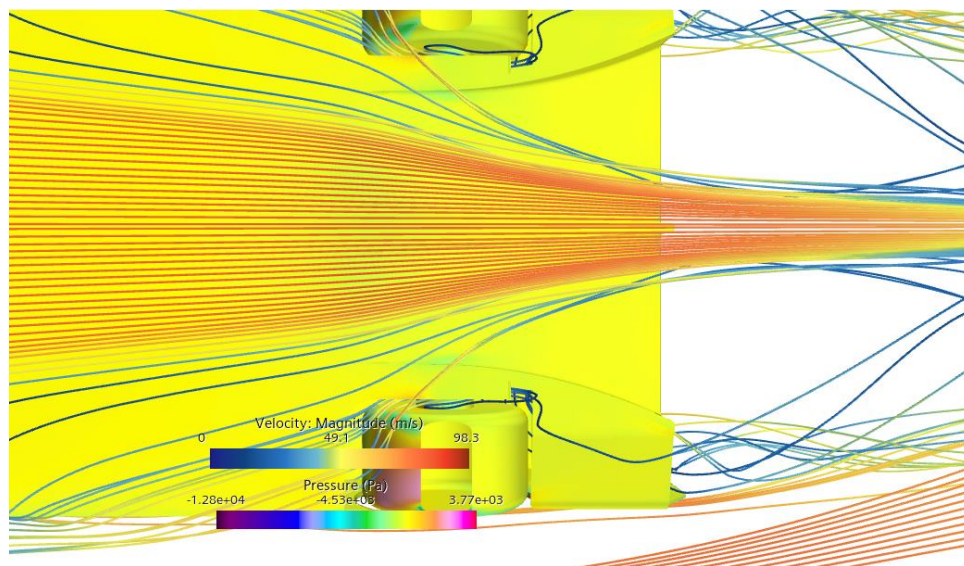


Figure 133: Streamlines velocity profile on the rear diffuser region. Simulation 2.

In future design iterations, the rake angle is reduced from 0,5° to 0,0° on the initial simulation to validate the overall underfloor design. Once the design has been validated, it is possible to simulate the aerodynamic performance of the underfloor in small rake angles increments.

The aerodynamic performance has been highly increased on the rear wing thanks to the upgraded air foil profile, especially in terms of downforce. Although the drag produced by the rear wing has been increased, the difference is minimal compared to the achieved improvement:

Force (Rear wing)	Original geometry [N]	Revised geometry V1 [N]	Difference [%]
Drag	203,72	388,54	+190,72
Downforce	-1844,40	-3737,28	-202,63
L/D	-9,05:1	-9,61:1	+6,18

Table 31: Comparison between the original rear wing and the revised rear wing V1. Simulation 2.

The overall downforce generated by the rear wing alone has been increased by two times just by altering the air foil profile. This improvement was validated by doing 2D simulations of the rear wing in the previous chapter of this thesis, but it is necessary to correlate the data of the 2D simulation of the rear wing profile with the data gathered from the 3D simulation. The values listed below are referred to the total length of the rear wing, which is 1860 [mm]:

Force	2D simulation [N]	3D simulation [N]	Error [%]
Drag	184,88	388,54	+210,16
Downforce	-6069,05	-3737,28	-162,39
L/D	-32,82:1	-9,62:1	-341,16

Table 32: Data differences between the 2D and 3D simulations of the revised rear wing profile.

At first, the correlation may seem very poor between the 2D and 3D simulations, but there are many reasons as to why the differences in force values are so high. The 2D simulation does not take into account the different flow deviation present in the 3D simulation of the whole car. One clear example of this issue can be seen in the next image:

Simcenter STAR-CCM+

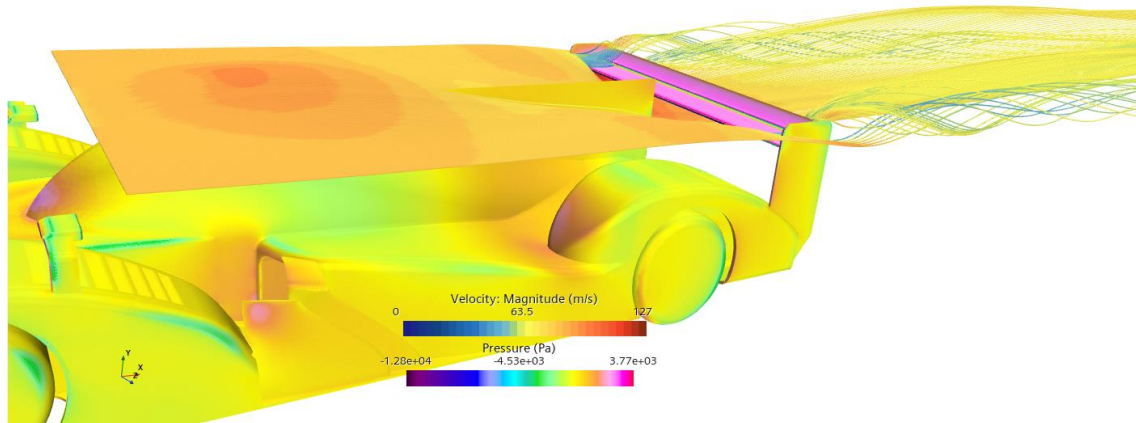


Figure 134: Streamlines flowing above the car. Notice the downwards direction of the flow near the middle section of the rear wing. Simulation 2.

The air flow is directed downwards, below the lower surface of the rear wing. This reduces the overall efficiency of the rear wing because there is less air mass flowing through the rear wing, reducing the potential downforce. This can be seen very clearly on the image below, where the pressure field under the rear wing only resembles that of the 2D simulation on the outermost parts of the wing, where the air flow has not been disturbed by any bodywork part:

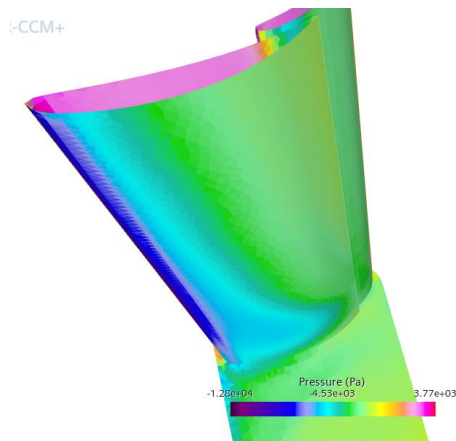


Figure 136: Pressure field under the rear wing. Notice the increased low-pressure region on the outer part of the wing.

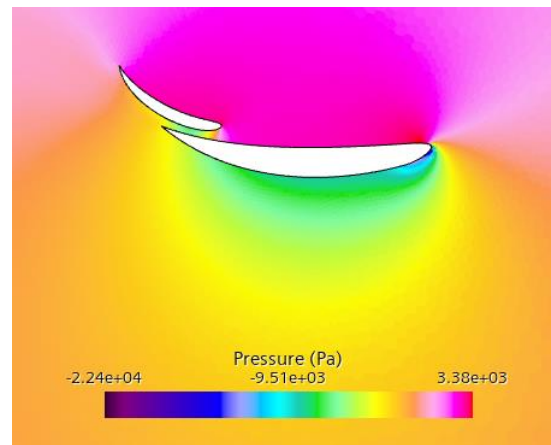


Figure 135: Pressure field under the 2D profile of the rear wing. Notice the longer low-pressure region under the profile, similar to the outer part of the 3D rear wing pressure field.

This reduced negative pressure under the rear wing is caused by the change in flow direction created by the cockpit, which directs the air flow downwards, as can be seen in the following figure:

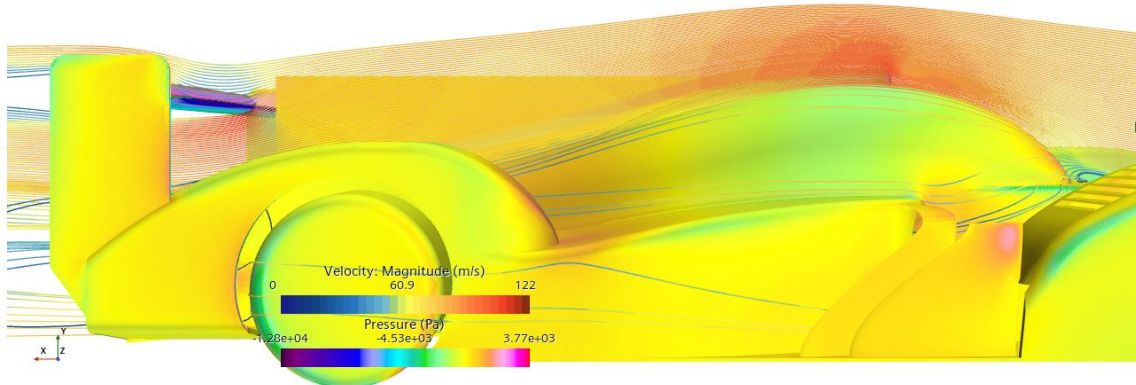


Figure 137: Relative angle of attack on the centre section of the rear wing. Simulation 2.

The change in direction results in a flow detachment on the underside of the rear wing, as if the angle of attack had been changed:

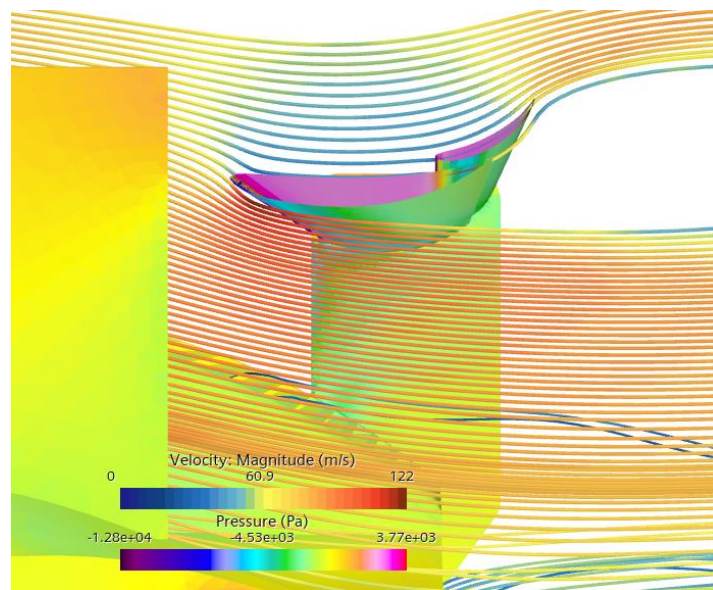


Figure 138: Flow detachment under the middle section of the rear wing. Simulation 2.

Even though the overall aerodynamic performance of the rear wing has improved, this flow detachment is causing a loss of downforce. This is the main reason for the data discrepancy between the 2D and 3D simulations. The 2D simulation accounts for an ideal situation where the flow remains attached throughout the whole rear wing.

The proper functioning of the rear wing can be seen on the outer sections, where the incoming flow remains horizontal compared to the rear wing profile:

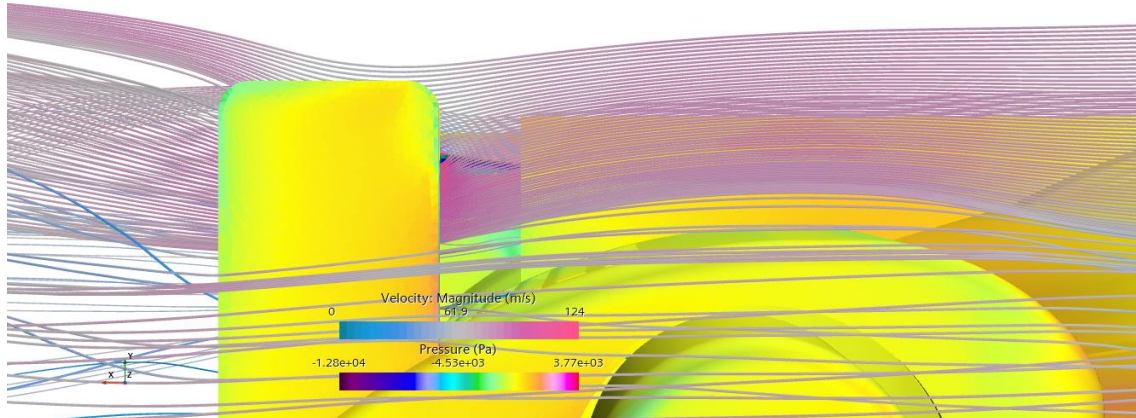


Figure 139: Relative angle of attack of the rear wing on the outer section. Simulation 2.

In this part of the rear wing, the relative angle of attack is smaller compare to the centre section. The flow remains attached on this section of the rear wing:

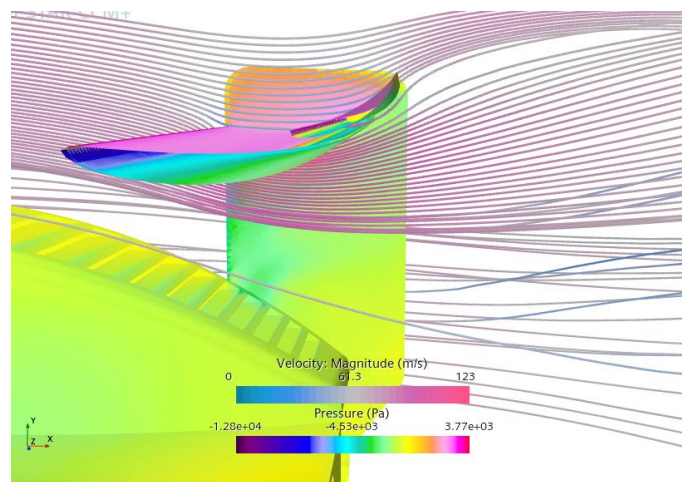


Figure 140: Flow under the outer part of the rear wing. Simulation 2.

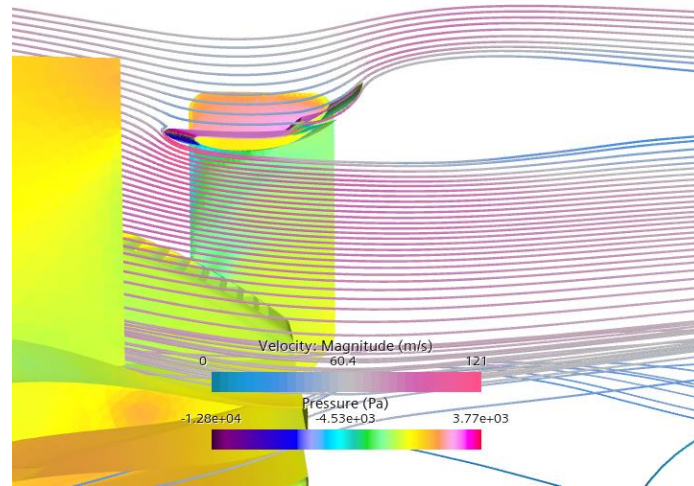


Figure 141: Detached flow under the centre section of the rear wing. Simulation 2.

The increased drag on the rear wing compared to the 2D model is created by the high-pressure region generated on the upper surfaces of the wing:

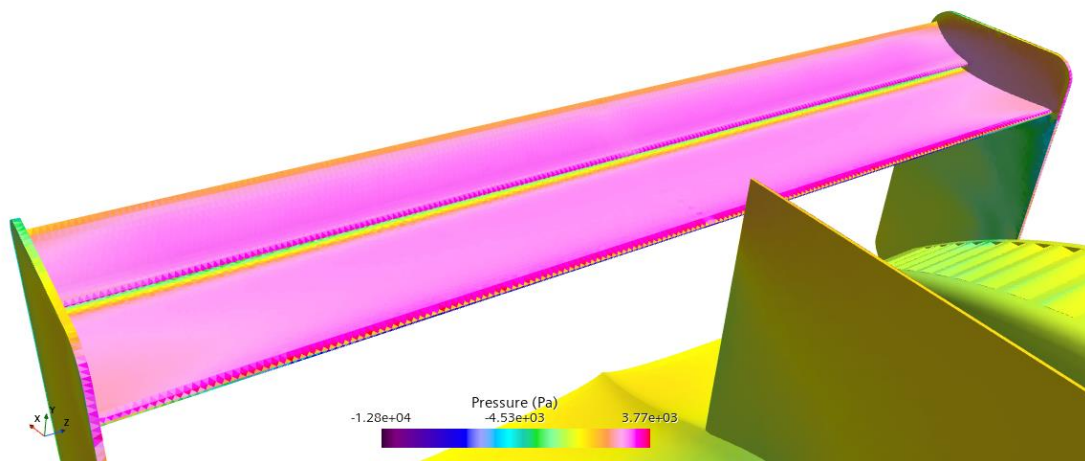


Figure 142: High pressure region on the upper rear wing surfaces. Simulation 2.

This high-pressure region causes increased drag due to the opposite force compared to the flow direction, an effect which is amplified by the support panels on each side of the rear wing:

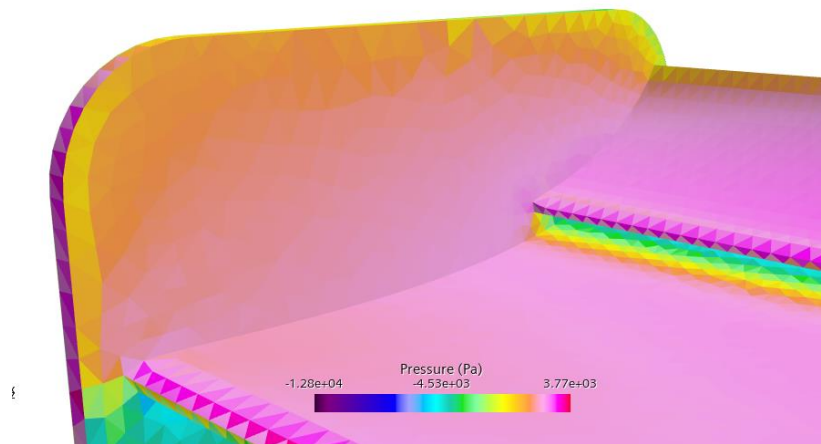


Figure 143: Increased high pressure on the rear wing side supports. Simulation 2.

These panels increase the pressure on the wing and help increase the high-power vortices generated on each side of the wing. Each vortex increases the drag on the rear wing due to the high energy required to generate. Although they can be reduced, these vortices are a natural occurrence on any air foil, and therefore should be managed as an intrinsic issue that will always be present.

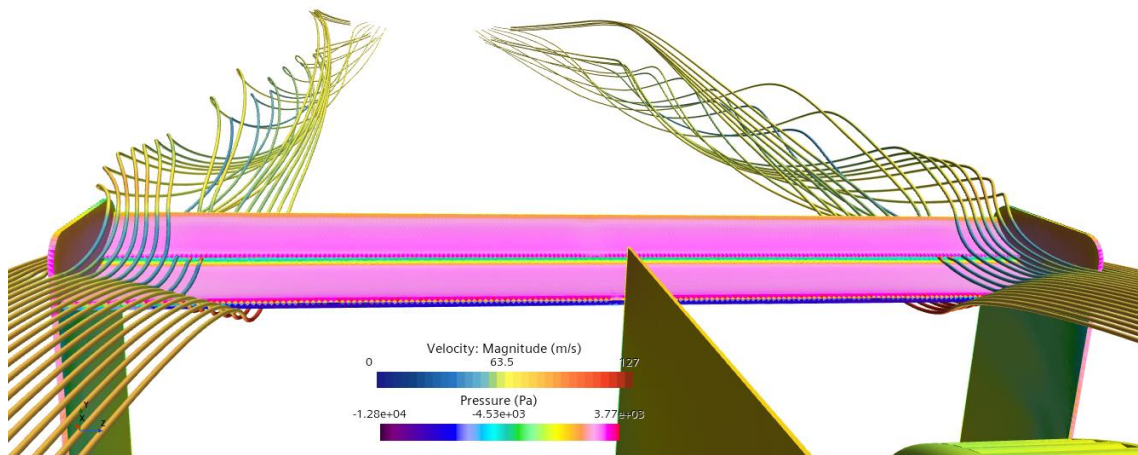


Figure 144: High-energy vortices on the rear wing. Simulation 2.

There are modifications that reduce both the energy of the vortices and the drag generated on the rear wing. These possible modifications are explained in further chapters. Even though the vortices produced by the rear wing are the most powerful, there are other vortices generated by the car that can be seen using a vorticity scene:

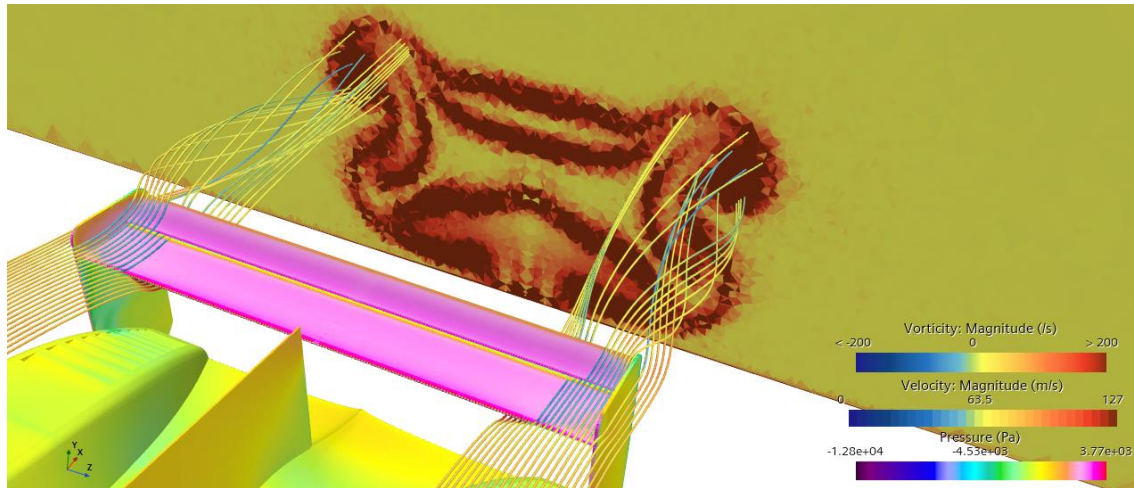


Figure 145: Vorticity plane on the wake of the car. Simulation 2.

The front wing does not perform as intended due to the intricate bodywork region where it has been placed. There is almost no low pressure on the underneath of the wing, caused by the high-pressure generated by the incoming air flow on all the frontal area of the car:

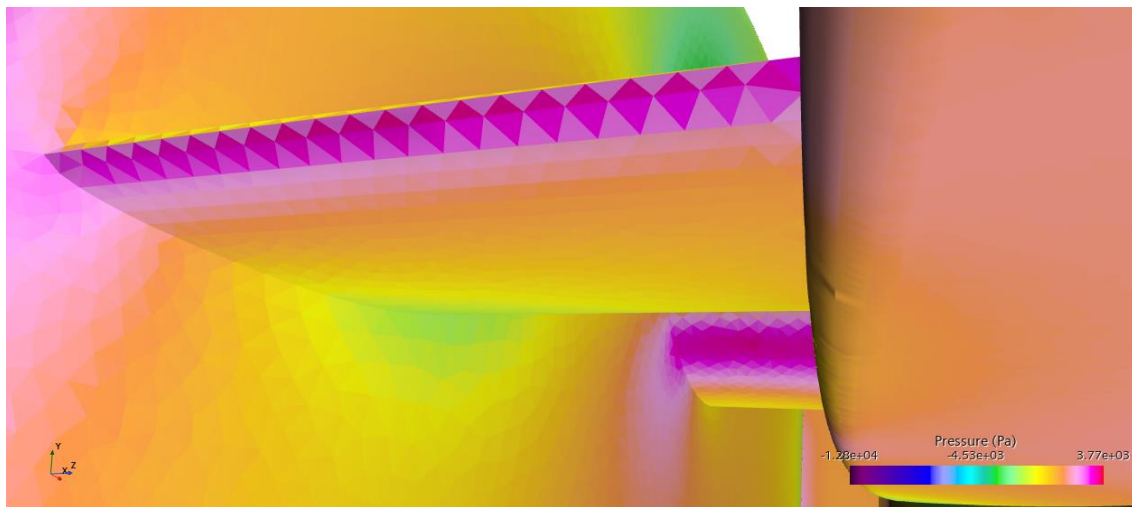


Figure 146: Pressure field on the underside of the front wing. Simulation 2.

The front wing changes the flow's direction and creates an extremely low-pressure region above the front suspension cowling, resulting in a high amount of positive lift that counter effects the overall downforce value in the car:

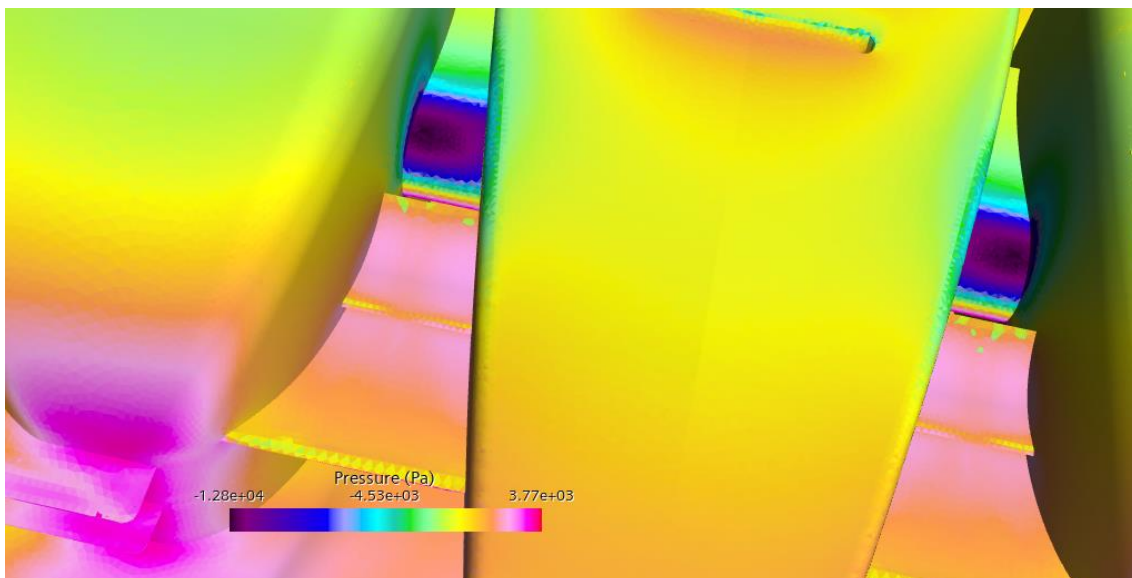


Figure 147: Low-pressure region in black/dark blue. Simulation 2.

This low-pressure is generated by the increased in velocity of the flow as the section are reduces near the wheel cover:

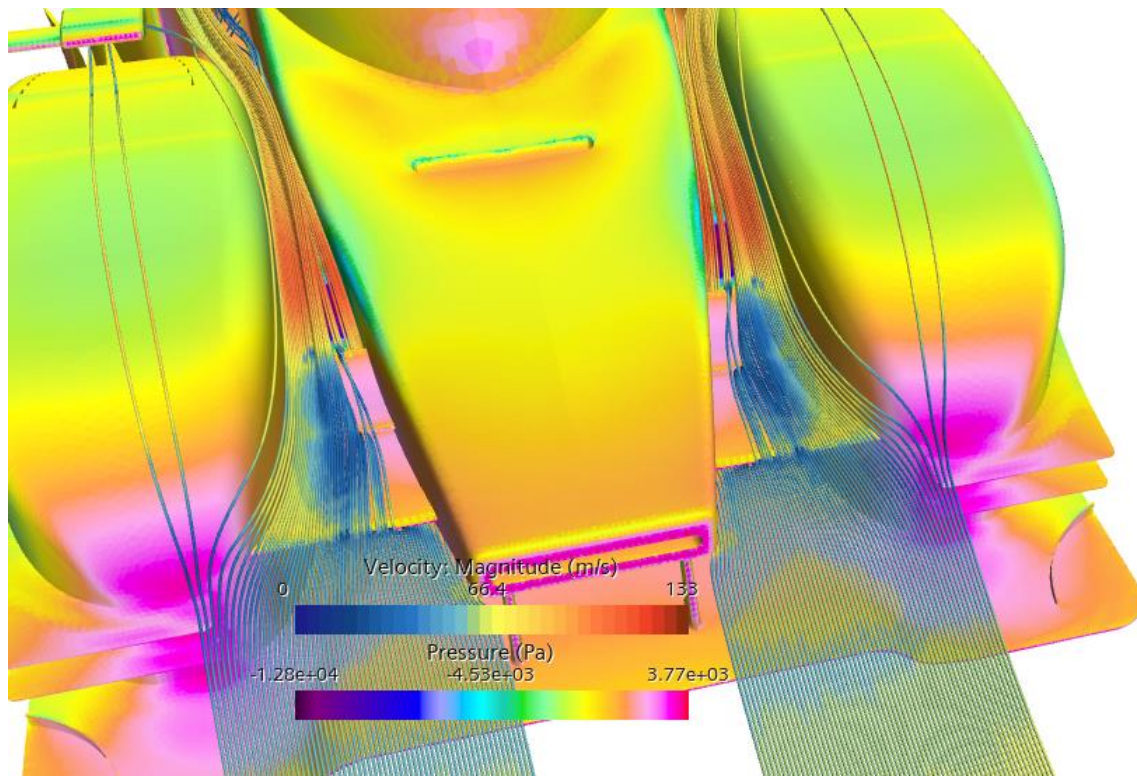


Figure 148: Pressure decreases and velocity increases as a result of section area reduction after the front wings. Simulation 2.

The geometry of the front section of the car shall be modified to solve the issues that take place as a result of the new geometry. Although the aerodynamic performance has improved, there are certain areas that create extremely low pressure above the suspension cowlings, reducing the overall downforce.

6 Geometry Iteration 2

As explained in the previous chapter, the revised geometry has better aerodynamic performance compared to the original car geometry, but still needs some improvements to perform at a level comparable to a LMP car.

6.1 Geometry improvements

On this geometry iteration, the main objective is to improve the aerodynamic performance by changing the multiple aerodynamic from the first geometry iteration that haven not performed as good as expected, focusing on the front part of the car.

6.1.1 Rear wing

The rear wing profile has been developed using 2D CFD simulations on the previous chapter. In this case, only the rear wing height is changed to exploit the downwards flow behind the canopy. Ideally, this increases the air mass flow through the rear wing, creating a higher amount of downforce without changing the profile design.

The wing is sept along a spline curve to decrease the height in the middle of the rear wing. This modification aims at placing the middle section of the rear wing in the region where the air mass flow is maximized:

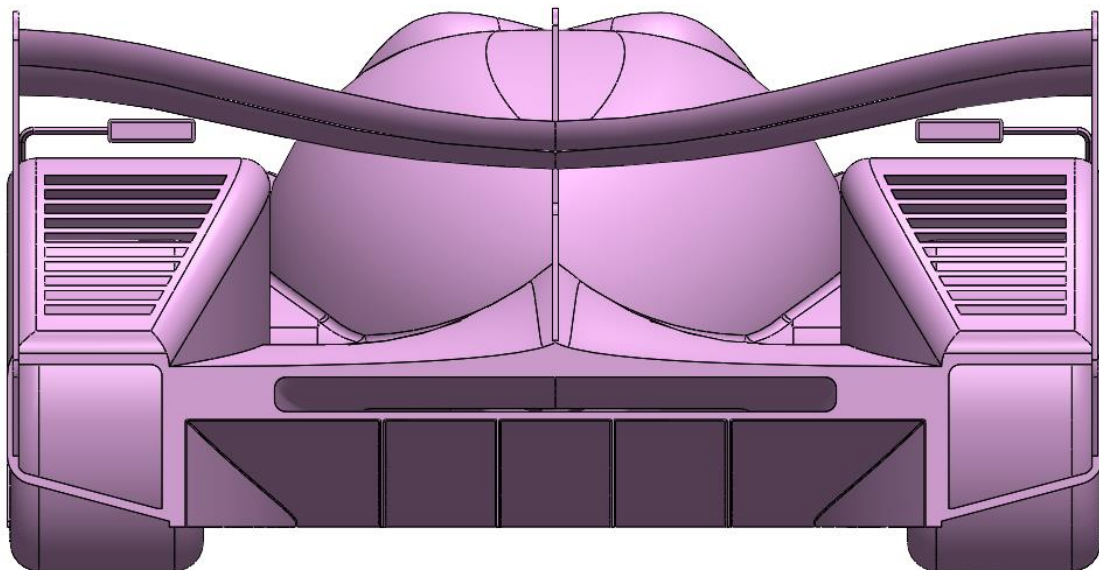


Figure 149: Swept rear wing. Geometry iteration 2.

The air foil profile remains the same as in the previous design iteration, but the middle section has been twisted 20° to compensate for the increase in relative angle of attack produced by the cockpit:

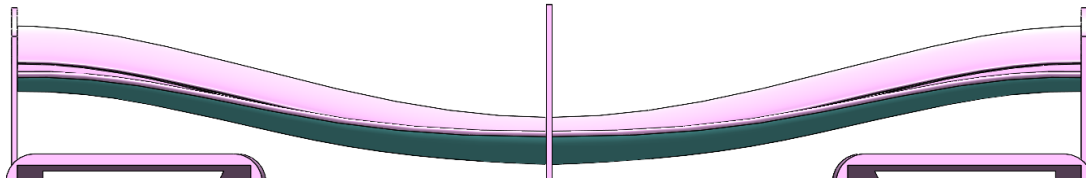


Figure 150: Frontal view of the twisted rear wing. Notice the increased underside section near the middle (highlighted in green). Geometry iteration 2.

To reduce the energy on the wake vortices of the rear wing, vent louvres have been cut into the support beams on each side of the wing. These vents help extract the high pressure that accumulates on the upper side of the rear wing:

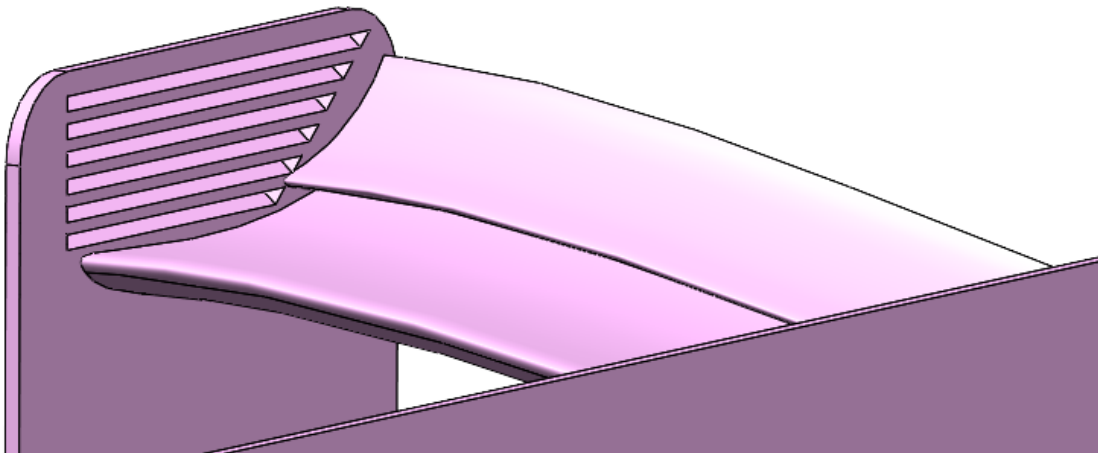


Figure 151: Rear wing vent louvres on the support beams. Geometry iteration 2.

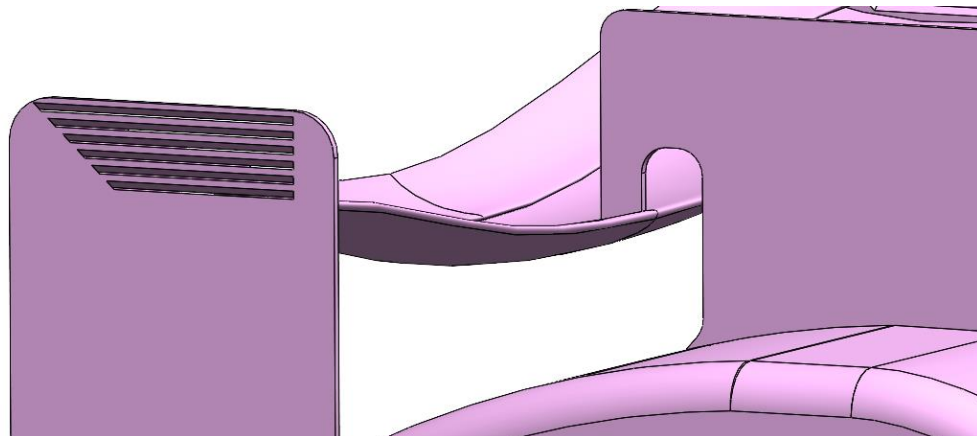


Figure 152: Side view of the rear wing vent louvres. Geometry iteration 2.

6.1.2 Front wing

As explained in the previous chapter, the front did not perform as expected due to the complex geometry around both front wings. To achieve proper front downforce levels, it is necessary to re-design the whole front section of the car, especially on the front wheel fenders area. The high pressure that accumulates in this region reduces the overall efficiency of the air foil profiles placed in this area.

The front wing has been re-designed to use the incoming air flow as efficiently as possible, with a longer two element wing being placed above the splitter:

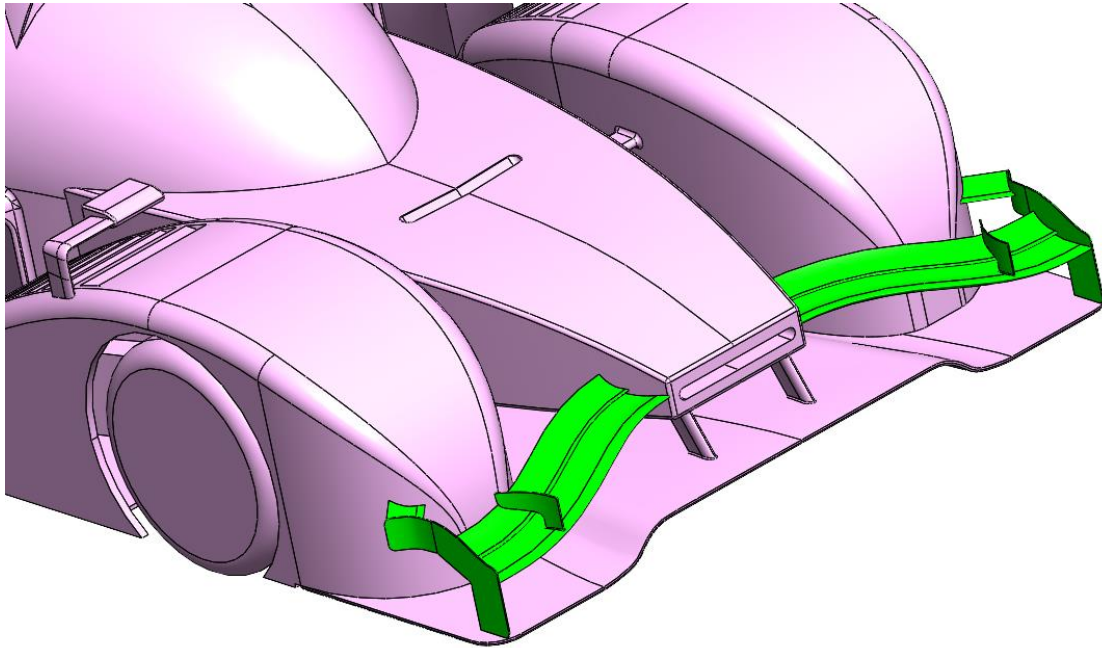


Figure 153: Revised front wing highlighted in green. Geometry iteration 2.

The new front wing has been designed using a 1:2 scaled down profile of the original front wing profile that was validated by 2D simulations in the first geometry iteration. Although the new front wing is much longer compared to that of the first geometry iteration, the air foil profiles are placed in a region where the incoming air flow is undisturbed, resulting in an overall higher aerodynamic efficiency of the wing.

The wing is supported on both sides by curved endplates that aim at diverting the high pressure created on the front wheel fenders. On the endplate, the exiting edge is curved outwards to create a low pressure on the inner face of the endplate. This low-pressure region relieves the high pressure generated in front of the wheel fenders, resulting in a flow stream. Additional downforce is created by placing a small inverted air foil wing between the endplate and wheel fender:

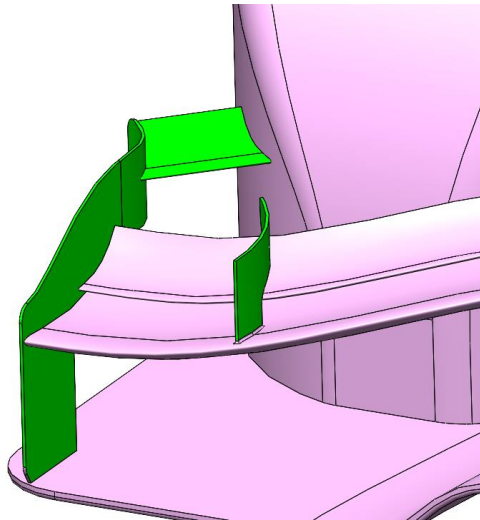


Figure 154: Endplate and outwash elements on the front wing highlighted in green. Geometry iteration 2.

6.1.3 Front splitter

On the first design iteration, the splitter created high amounts of downforce, but not without its consequences. The splitter works by accelerating the incoming flow into a smaller section area, which in this case, part of the high velocity air leaked into the wheel fenders, creating turbulent air and reducing the air mass flow under the floor. This flow leak can be reduced by extending the splitter backwards, where the high velocity flow that exits the tunnel does not leak into the wheel fenders, and remains inside the floor instead:

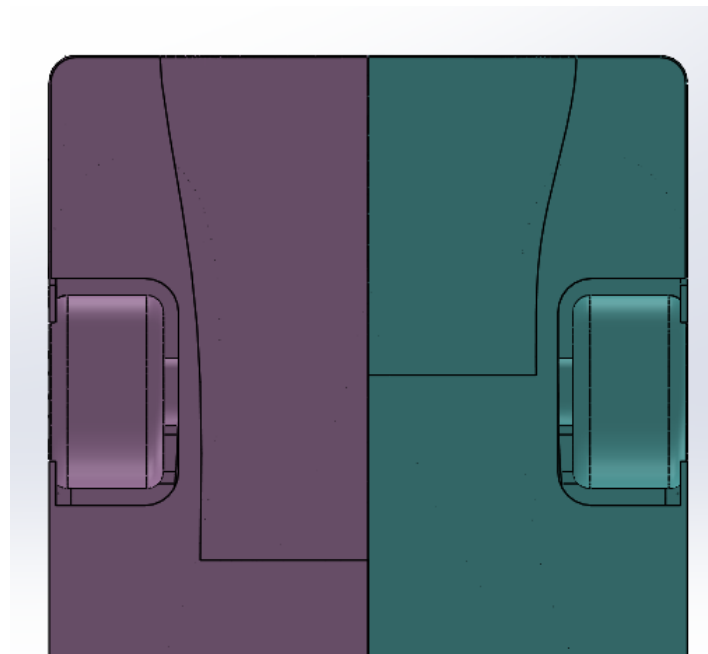


Figure 155: Longer front splitter (Left) compared to the front splitter designed in the first design iteration (Right).

Due to the longer splitter, the air leaks behind the front wheels, and therefore there is less air mass flow that exits the floor. The overall dimensions of the splitter, like intake height and width remain the same, except for the longitudinal length.

6.1.4 Rear diffuser and rake angle

The diffuser profile remains the same, but the center strake has been changed for 4 thinner vertical strakes:

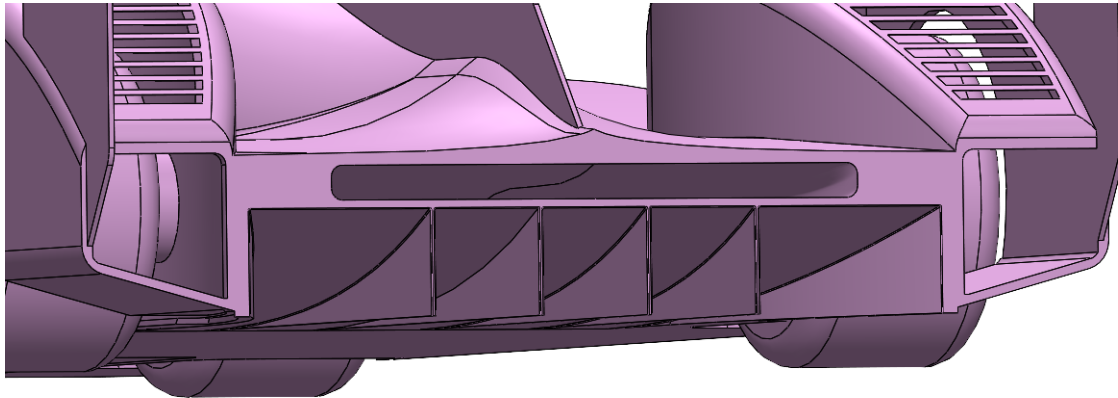


Figure 156: Rear diffuser with vertical strakes. Geometry iteration 2.

The main change in the underside region has been a reduction in the rake angle. On the geometry iteration 1, the car was given a $0,5^\circ$ rake angle, which caused flow separation on the diffuser due to the excessive change in ride height at the rear of the car. In this case, the rake angle has been set to 0° to validate the whole design of the underside.

The rake affects the ride height along the car, a critical dimension to the general behaviour and driveability of the car. These are the new ride heights:

Rake angle [°]	Front ride height [mm]	Rear ride height [mm]
0,50	29,91	80,59
0,00	47,68	66,16

Table 33: Ride height comparison ($0,0^\circ$ and $0,5^\circ$)

The rake angle can be easily adjusted by tweaking the suspension parameters such as push rod length, spring rate, sag and rocker arm configuration. Modern race cars' suspension is designed with suspension adjustability in mind, making it easier and quicker to tune the suspension to a driver's preferences.

6.1.5 Engine air intake

The main aerodynamic problem with this car has to do with the geometry of the bodywork. These smooth surfaces generate an excessive amount of positive lift that results in a lower total downforce. The main bodywork surface where this issue takes place is the cockpit due to the negative pressure generated, resulting in a positive air foil wing effect as has been explained in previous simulations.

To mitigate this effect, the engine air intake has been modified to disrupt the smooth flow over the cockpit. This aims at diverting the air that otherwise would flow attached to the cockpit and engine cover surfaces. The intake has been divided into two symmetrical curved inlets with an aggressive geometry:

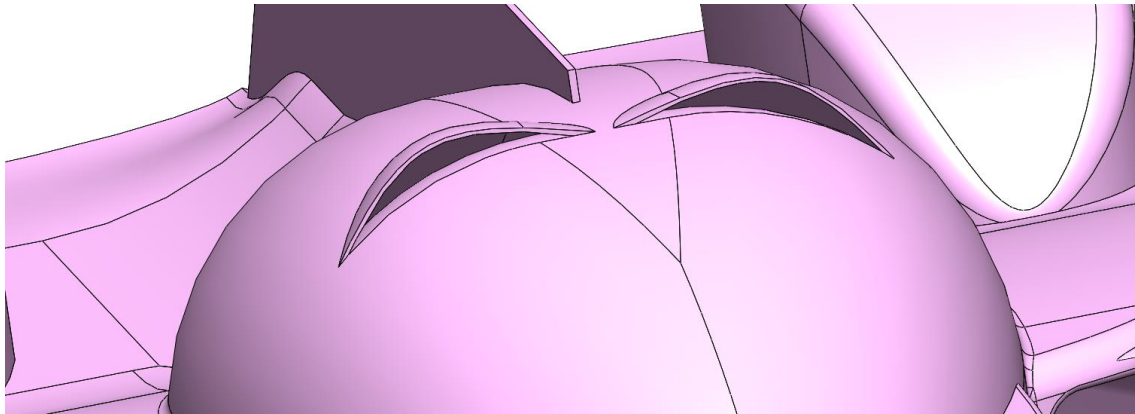


Figure 157: Modified engine air intakes. Geometry Iteration 2.

Although the intake area is greater than that of the original design, these intakes reduce the air mass flow around the upper surface of the cockpit. These new air intakes aim at reducing the air mass flow around the cockpit's upper surfaces, resulting in a lower positive lift in this area.

These new air intakes may cause flow disturbances on the middle section of the rear wing. This must be checked on the next CFD simulation in case the flow disturbances cause poor performance and stalling.

6.2 Simulation 3

After generating the geometry, the CFD simulation is created following the same steps as in previous simulations. All the mesh and physics values remain the same.

The simulation is fully converged after 2200 solver iterations, but in this case, the residuals present a high level of oscillation:

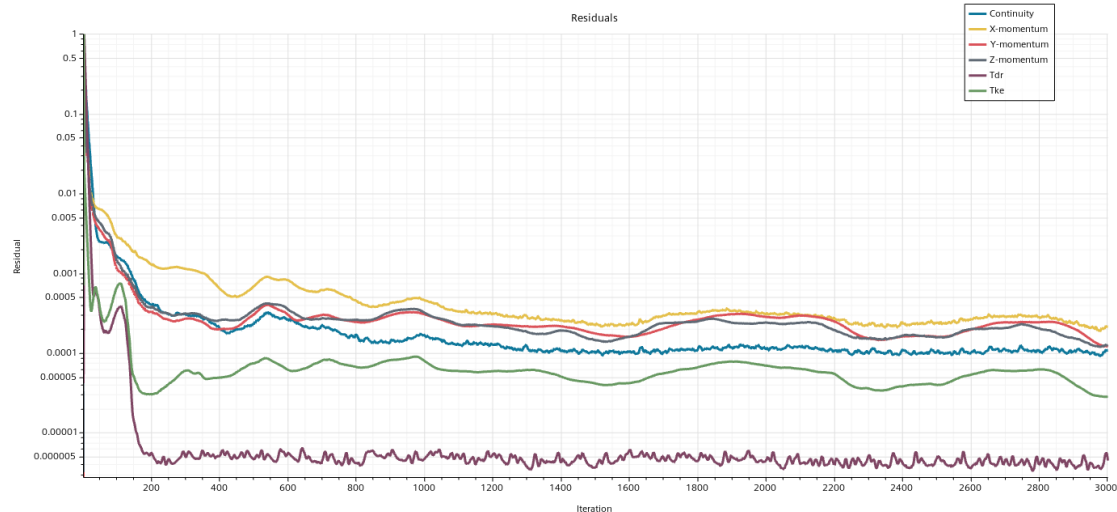


Figure 158: Residuals of the third 3D CFD simulation. Simulation 3.

These oscillations are usually caused by flow separation near the vehicle's surface, but it may be difficult to determine the exact area where there is a high level of turbulent flow separating from the surface. The data calculated from the simulation gives a great insight as how well the simulation has converged, as the forces and coordinates should stay constant even though the residuals are not completely constant.

In this case, the forces do oscillate, but the maximum and minimum force values are negligible compared to the overall force scale:

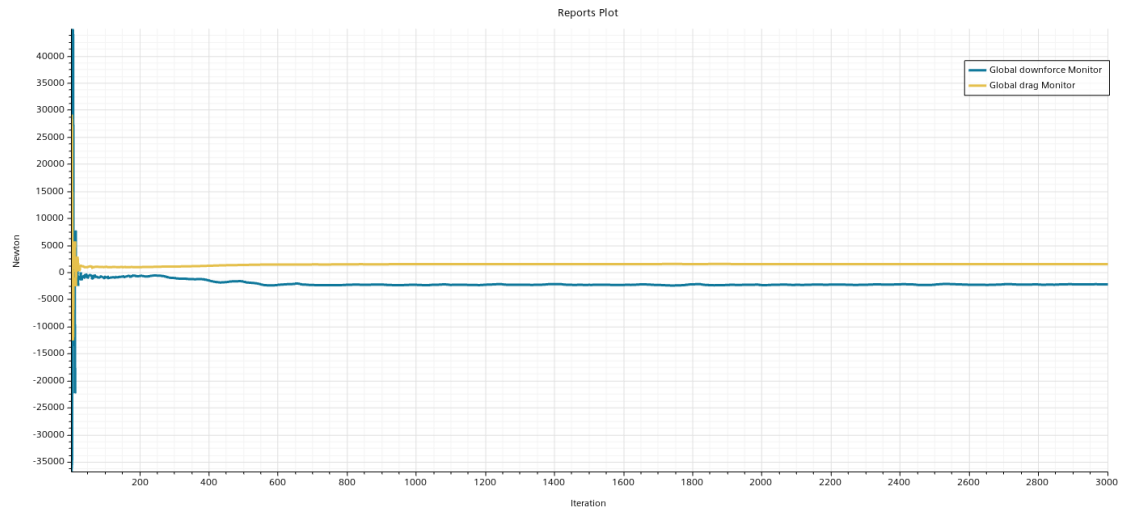


Figure 159: Global force values. Simulation 3.

The independent drag and downforce plots also show a high level of convergence based on the stability of the calculated data:

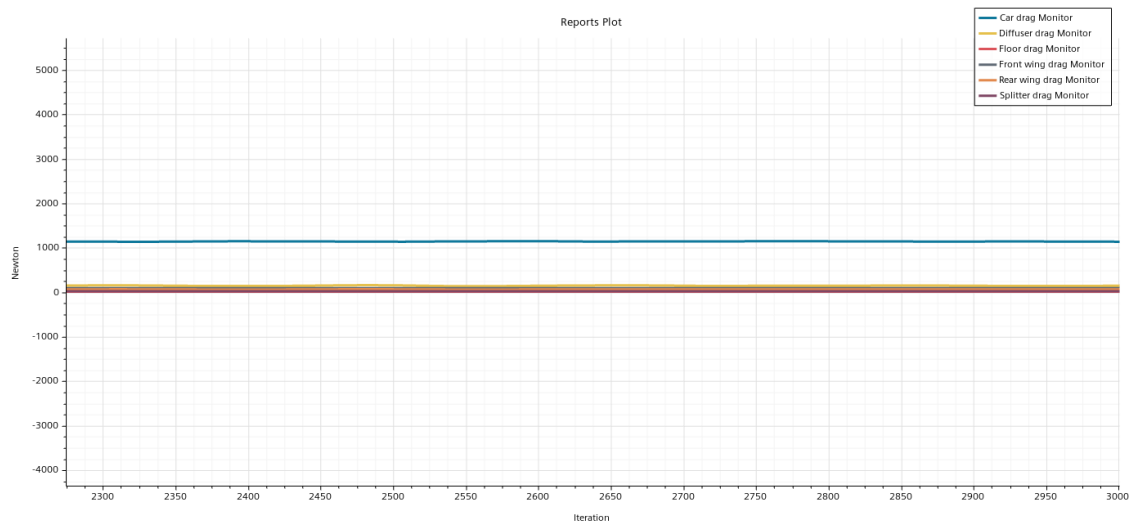


Figure 160: Drag values of the different aerodynamic surfaces. Simulation 3.

The same applies to the downforce values:

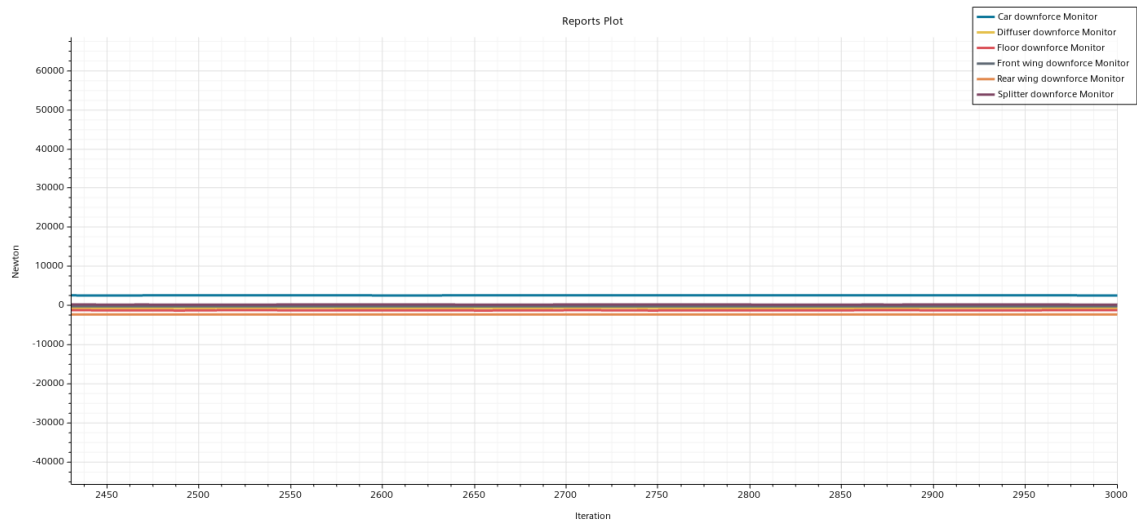


Figure 161: Downforce values of the different aerodynamic surfaces. Simulation 3.

Once the convergence of the simulation has been validated, the data gathered from the CFD simulation is retrieved and analysed. In this case, the downforce generated by the new geometric changes has improved by a noticeable amount compared to that of the second simulation:

Region	Drag [N]	Downforce [N]
Diffuser	149,61	-732,15
Floor	17,44	-1327,77
Front wing	93,38	-348,65
Rear wing	66,07	-2405,28
Splitter	24,99	-107,632
Sum	351,49	-4921,48
Body	1138,06	+2449,01
Global	1489,55	-2472,47

Table 34: Aerodynamic forces of half the car. Simulation 3.

These forces represent only half of the car, as they have been calculated based on the control volume that has been introduced into the CFD software. The table below shows the overall forces acting on the whole car:

Region	Drag [N]	Downforce [N]
Diffuser	299,22	-1464,30
Floor	34,88	-2655,54
Front wing	186,76	-697,30
Rear wing	132,14	-4810,56
Splitter	44,98	-215,26
Sum	702,98	-9842,96
Body	2276,12	+4898,02
Global	2997,10	-4944,94

Table 35: Aerodynamic forces of the whole car. Simulation 3.

The drag and lift coefficients are calculated based on the projected frontal area of the car:

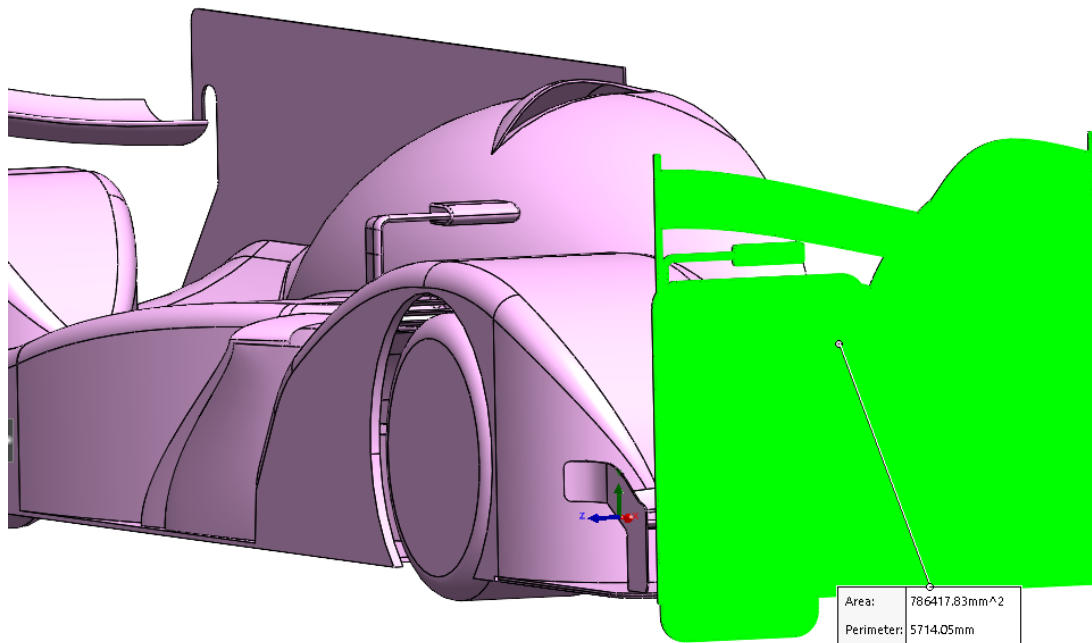


Figure 162: Frontal area. Geometry iteration 2.

Type	Half car [m ²]	Whole car [m ²]
Frontal area	0,786	1,572

Table 36: Measured frontal area. Geometry Iteration 2.

After measuring the frontal area of the car, the drag and lift coefficients are calculated:

Coefficient	Value
Cd	0,57
Cl	-0,94

Table 37: Drag and lift coefficients. Simulation 3

The centre of pressure is calculated using a pair of CoP reports. These are the CoP coordinates taking the front wheel as a cartesian origin:

Coordinate	Dimension [m]
Along X axis	2,03
Along Y axis	0,62

Table 38: CoP coordinates. Simulation 3.

It is possible to tell that the load distribution between the front and rear axle is extremely rear-biased by just looking at the CoP coordinates alone. This is confirmed by running the Python script to calculate the load distribution:

```
Downforce value [N]: -4944.94
Drag value[N]: 2997.10
COP X coordinate [m]: 2.03
COP Y coordinate [m]: 0.62
Rear axle aerodynamic load [N]: 4102.217310344827
Front axle aerodynamic load [N]: 842.7226896551725
Front: 17.042121636565312 % Rear: 82.95787836343469 %
```

Figure 163: Front-Rear aerodynamic load distribution. Simulation 3.

The CoP being too far back issue still persists from the previous simulations, and must be minimized for the final design iteration.

The following data gives a general understanding of the improvements and overall performance of the car, based on the computational data:

Revised geometry	Value
Drag force	2997,10 [N]
Downforce	-4944,94 [N]
Cd	0,57
Cl	-0,94
Downforce distribution	17,04 % Front, 82,96% Rear
L/D	-1,65:1
Frontal area	1,572 [m ²]
Flow velocity	75 [m/s]

Table 39: General aerodynamic data. Simulation 3.

6.3 Visual analysis and possible improvements

The overall aerodynamic performance still remains lower than what is expected from a LMP car, but the changes made on the second geometry iteration head on the right direction. In this case, the biggest improvements have been made on the rear of the car, which causes a very uneven load distribution between both axes.

The rear wing performs much better after changing the longitudinal profile to a curved one. The overall pressure distribution along the rear wing is much more even, without any flow separation on the middle section:

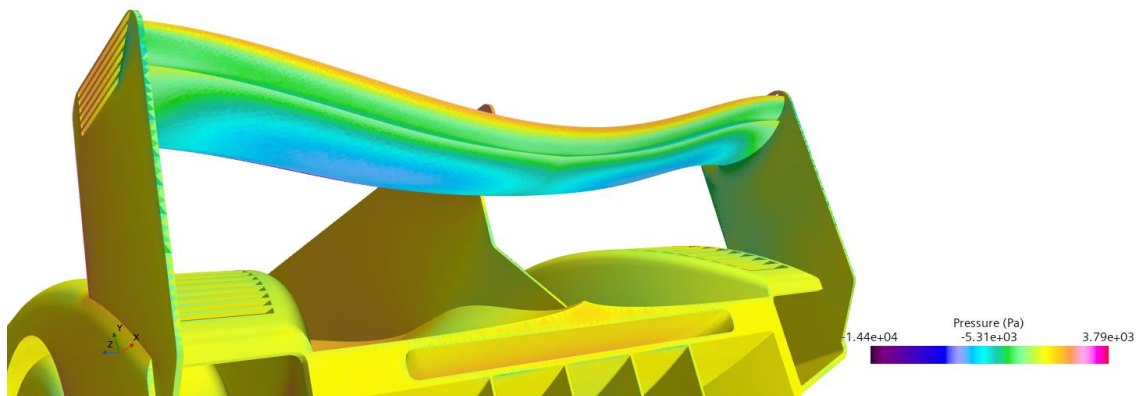


Figure 164: Pressure field under the rear wing. Simulation 3.

This pressure field results in a better performance of the rear wing, with higher amounts of downforce being generated whilst the drag values are also reduced:

Force	Linear rear wing [N]	Curved rear wing [N]	Difference [%]
Drag	388,54	132,14	-134,00
Downforce	-3737,28	-4810,56	+28,72

Table 40: Aerodynamic forces comparison between the linear and curved rear wing.

The side louvres on the rear wing endplates also help reducing the drag by extracting the high pressure generated on the upper side of the wing and by generating a much more coherent wake vortex behind the rear wing:

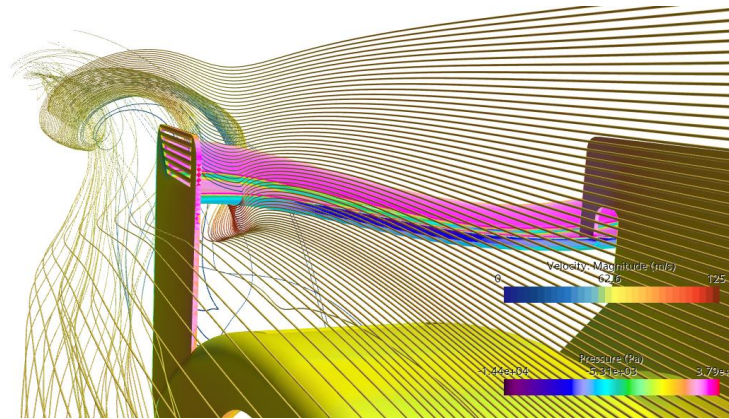


Figure 165: Wake vortex generated behind the rear wing.

Although these changes have improved the rear wing performance, this also contributes to the aerodynamic loads being too rear-biased. Instead of reducing the rear wing downforce, the overall load distribution can be shifted more towards the front axle by generating a higher amount of downforce on the front section of the car. These changes are further explained on the final design iteration.

The front splitter was redesigned on this geometry iteration, with a longer induction tunnel and a wider intake width. The aim was to introduce as much air as possible under the floor. In this case, the incoming air creates a high-pressure region on the front most part of the splitter that counter effects much of the generated downforce:

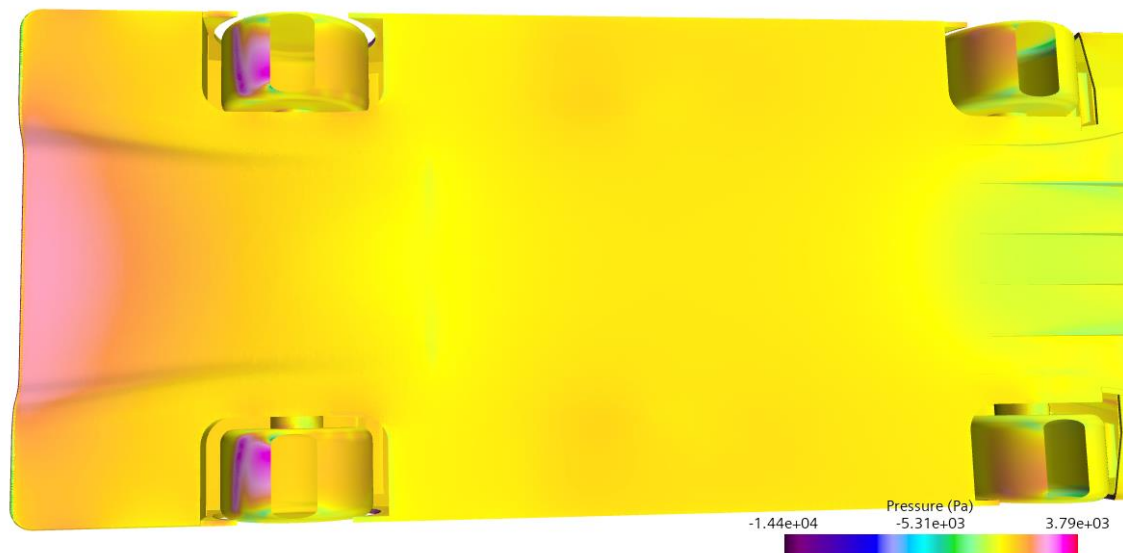


Figure 166: Pressure field under the car. Notice the high-pressure zone on the front section of the splitter.

Also, by making the floor section shorter, the downforce generated acts towards the rear axle, increasing the rear bias in terms of aerodynamic balance.

This splitter concept does not work as expected due to the inefficient nature of this front splitter and will be redesigned for the final design iteration based on a whole new splitter concept.

A noticeable change has been made on the rear diffuser, with a much bigger low-pressure region due to different concept applied for this geometry iteration. The air expands in a more controlled way, with the flow remaining attached for the entirety of the diffuser. The pressure field also remains constant throughout the diffuser's longitudinal axis, indicating that the flow does not detach from the surface.

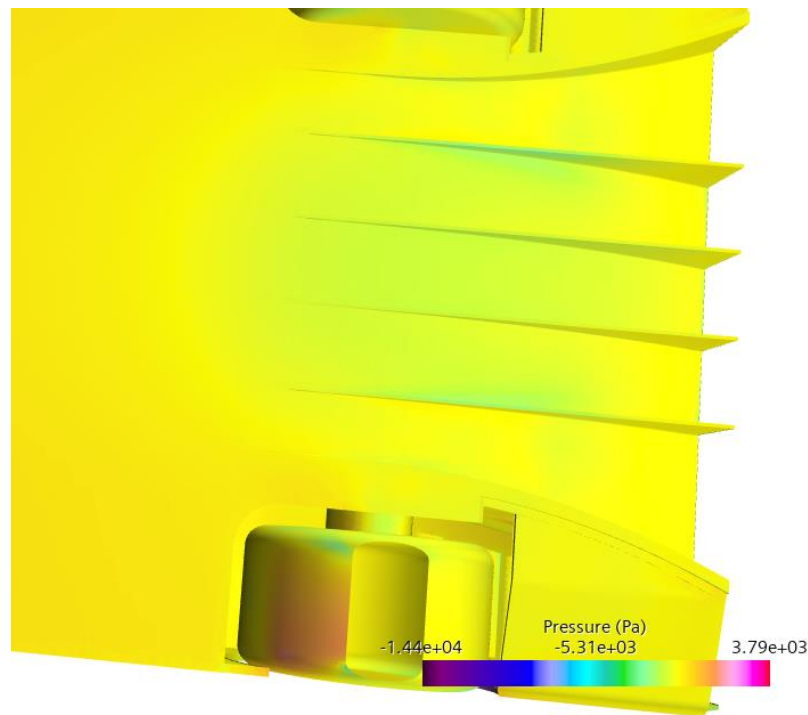


Figure 167: Pressure field on the rear diffuser.

The diffuser effect is maximized on the centre section, where the majority of the air mass flows, thus being the critical area where the most aerodynamic performance can be extracted from:

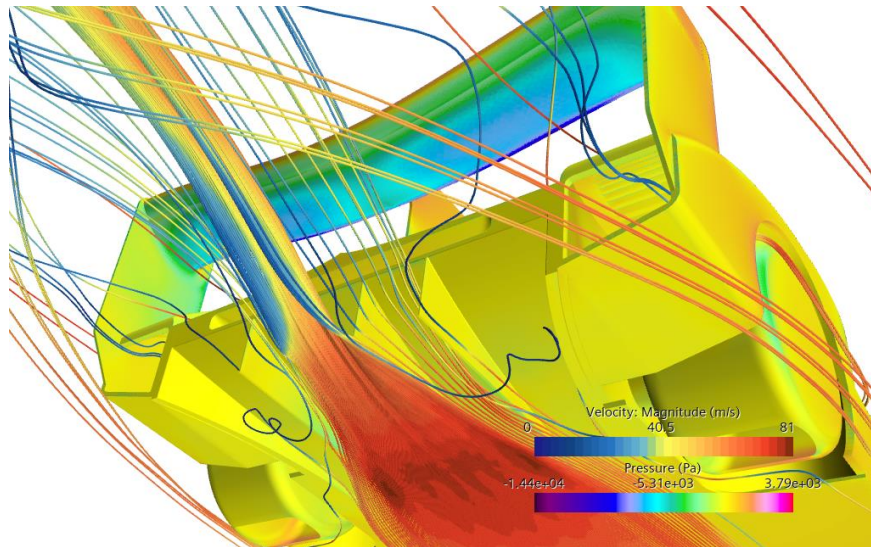


Figure 168: Flow under the rear diffuser. Notice the flow being directed towards the middle section.

On the front part of the car, the newly designed front wing is not optimized, although there is downforce being generated by these surfaces. The main reason as to why the front wing cannot generate as much downforce as expected is the high-pressure area created in front of the car, that reduces the air foil effect by a great amount. The front wing generates most of the downforce near the centre area, where the high-pressure area in front of the car is nowhere near as strong as in front of the wheel fenders:

Simcenter STAR-CCM+

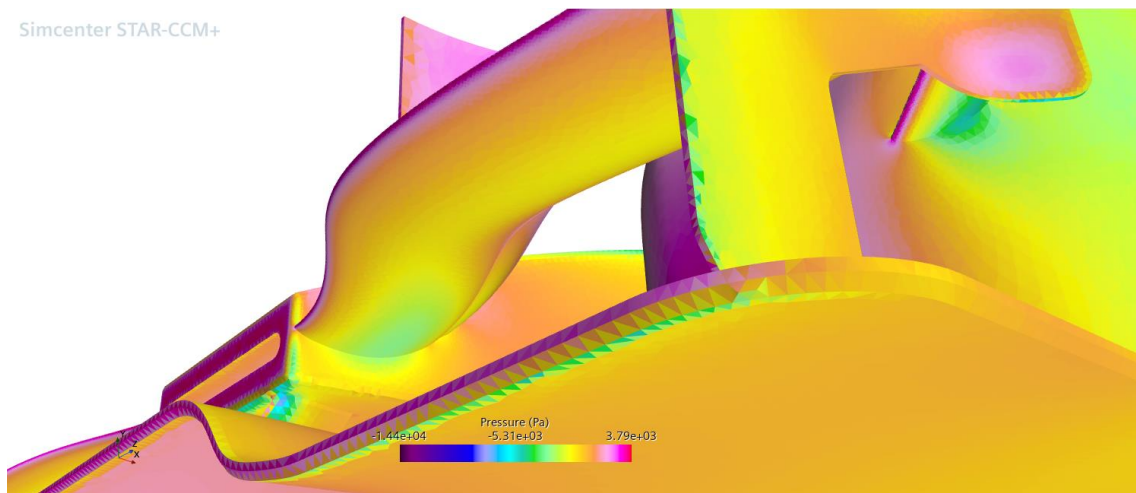


Figure 169: Pressure field under the front wing. Notice the lowest pressure created near the middle section.

The aerodynamic performance of the front wing can be improved by upscaling the air foil profile near the front crash structure of the car, where the flow is not as restricted as near the front wheel fenders. This improvement is further explained on the final geometry iteration.

As explained multiple times before, the main reason as to why the car does not aerodynamically perform as desired is the positive lift generated on the neutral aerodynamic surfaces, like the cockpit, wheel fenders and engine cover. In this case, this problem persists, and is especially present on the upper surface of the front wheel fenders:

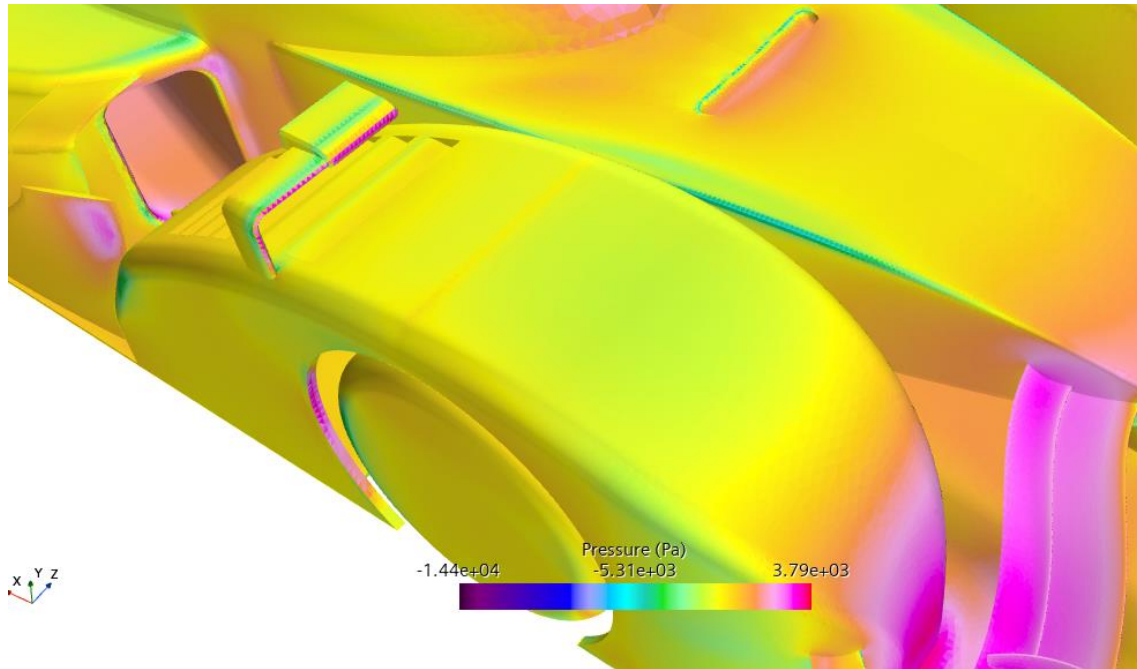


Figure 170: Low pressure on the front wheel fender's surface.

This causes lift that counter effects the overall generated downforce, therefore reducing the aerodynamic performance. There are different approaches to minimize this positive lift, especially on the wheel fenders, that are explained on the final design iteration.

7 Geometry iteration 3. Final design.

For the final geometry iteration, there are changes that imply a different concept compared to the previous design iterations, especially on the front of the car

7.1 Geometry changes

The final elements, and their expected performance, that form the final aerodynamic concept of the car are explained in here.

7.1.1 Front splitter

From the previous simulations, it was obvious that, although the general aerodynamic concept is heading on the right direction, the front section of the car does not produce the necessary amount of downforce to compensate the overall aerodynamic balance of the car.

Previously, the front splitter was modelled into the car as a continuous reduction in section area, connecting the raised front lip and the floor surface. This geometry caused an excessive high pressure area on the front of the splitter that resulted in very low downforce being generated by this aerodynamic surface. For this geometry iteration, the front of the car is completely redesigned, with a new front splitter concept that resembles a rear diffuser:

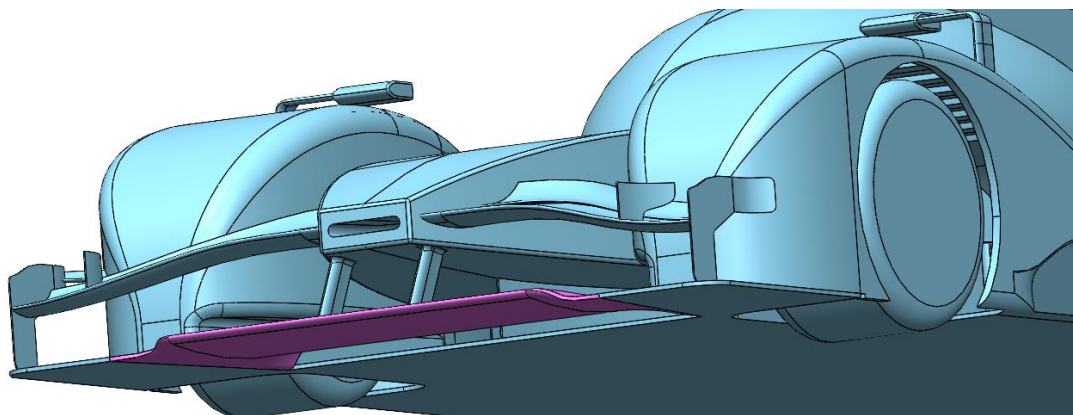


Figure 171: Redesigned front splitter highlighted in pink.

This new front splitter works by expanding the air that flows between the lower surface and the ground, using the same principle as the rear diffuser. The profile used is a regular wing profile:

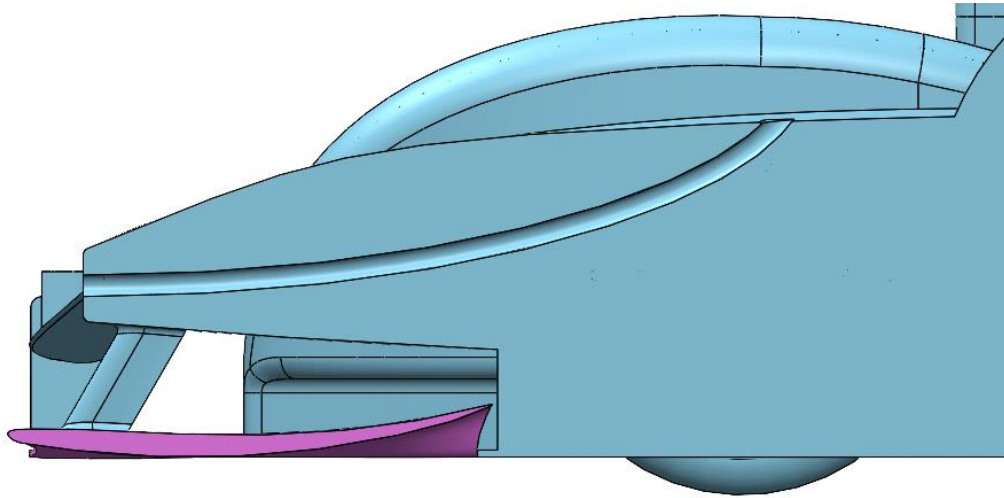


Figure 172: Front splitter profile.

One of the possible issues derived from this new splitter may be the reduced mass flow between the floor and the ground that may decrease the overall generated downforce. The effect of the new splitter is discussed on the simulation chapter.

7.1.2 Front wing

The front wing has been slightly modified to exploit all the available room on the middle section of the car by scaling the wing profile near the center section:

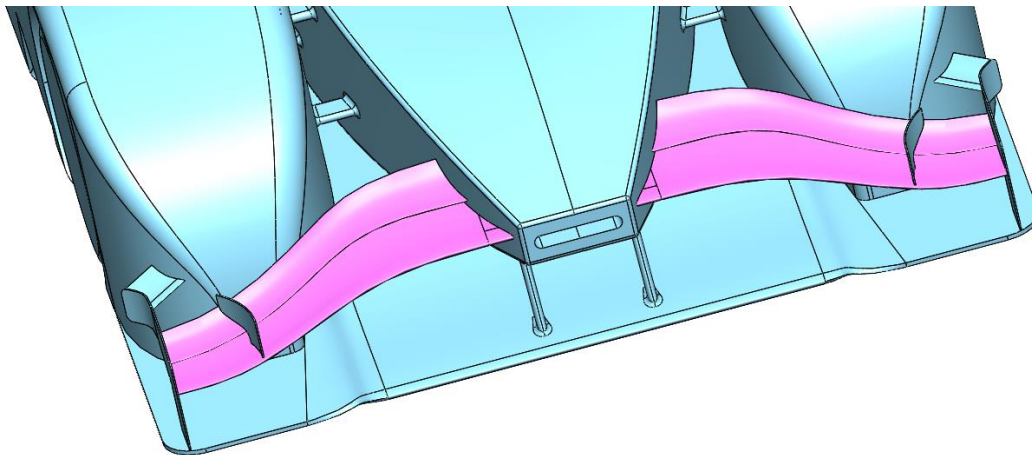


Figure 173: Larger front wing area near the middle section of the car.

7.1.3 Engine air intake

On the previous iteration, the air intake was redesigned with a reduction in negative pressure above the cockpit in mind but the previous design created a higher level of positive lift by itself. For this simulation, the intake design is reverted back to a standard duct design:

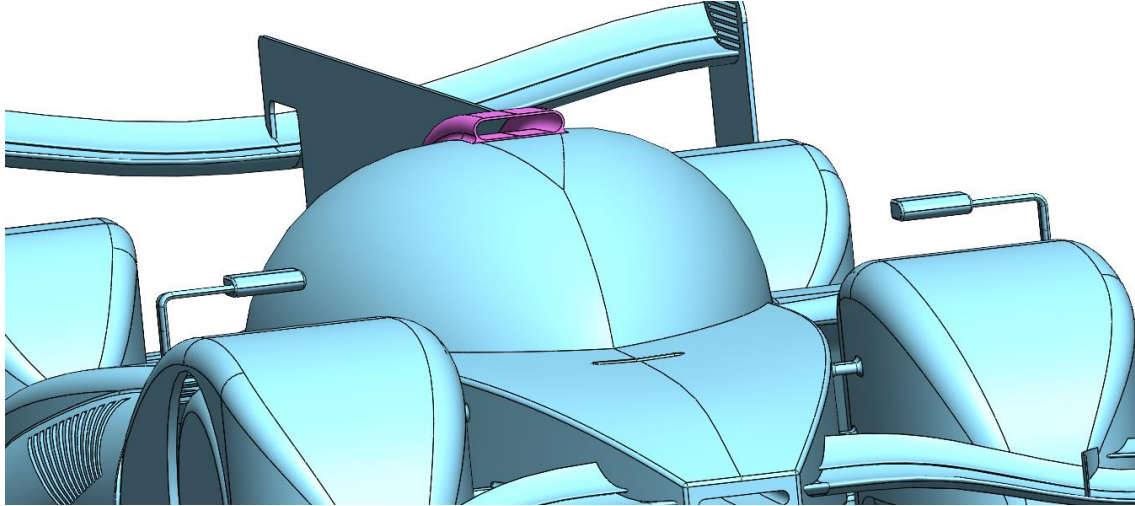


Figure 174: Engine air duct for the final geometry iteration highlighted in pink.

This new engine air duct also reduces the turbulences that collide with the rear wing downstream, creating a more structured flow on the middle section of the rear wing.

7.1.4 Front splitter wake management

The new front splitter geometry generates a high-pressure wake stream around the cooling ducts that must be cared for. This is done by conducting the air stream outwards between the front and rear wheels using a number of geometrical features. The most important of these features are the side panels modelled behind the front wheels:

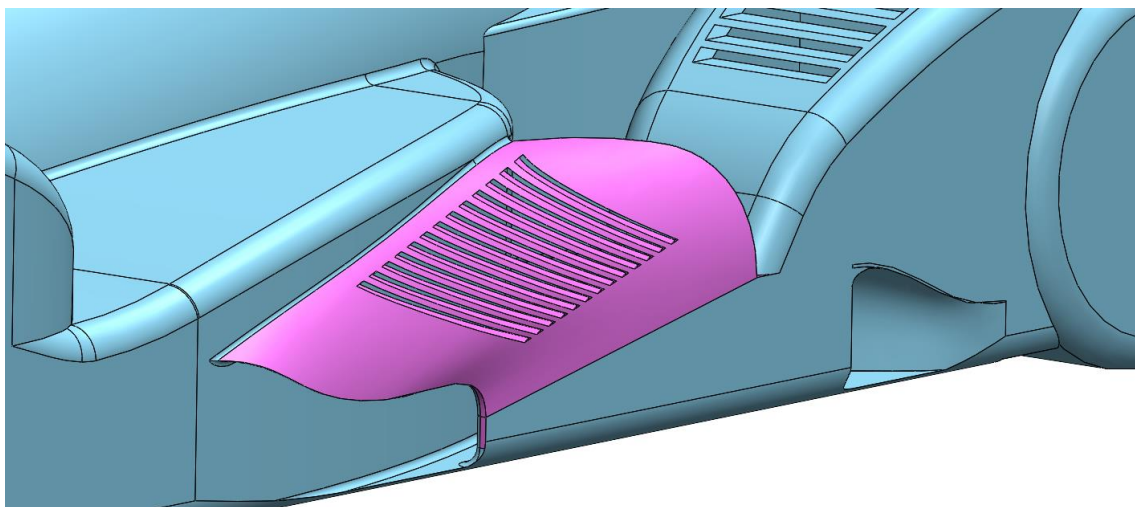


Figure 175: Side panels.

The air exiting the front splitter would otherwise cause stagnation inside the front wheel fender. This low energy air is extracted by a duct placed behind the front wheel. The duct acts as a high velocity air intake that helps extracting all the turbulent air in this area:

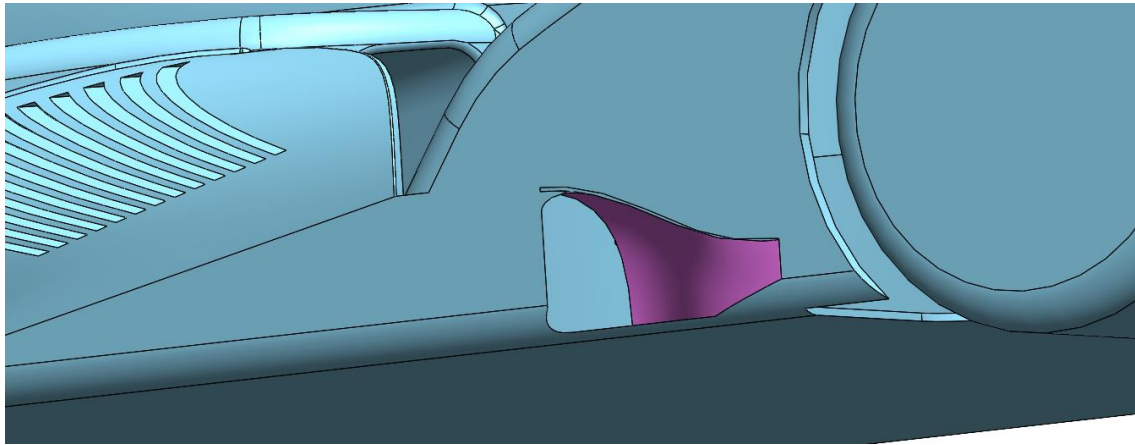


Figure 176: Air duct highlighted in pink.

7.1.5 Floor edges

The last modification for this geometry iteration consists of a radius created along the floor edges that helps transitioning the air that enters or exits the flow. This transition reduces the turbulence between the floor and the ground near the edges:

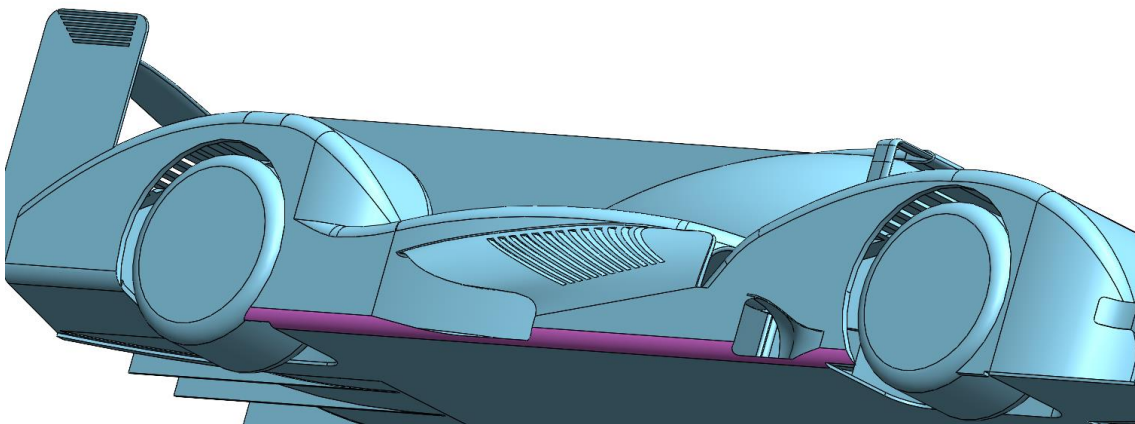


Figure 177: Filleted floor edge highlighted in pink.

7.1.6 Other modifications

There are a number of modifications that are not as important as the ones explained previously.

The ride height has been increased by 15mm and the rake angle has been set to 0.2°

On the previous simulation it was explained that the bodywork of the car generates excessive amounts of positive lift that counteracts the downforce generated by the different aerodynamic surfaces. One solution could be to cut an opening on the upper area of the wheel fender, but this disturbs the air flow near the rear wing. For the final design iteration, the wheel

fenders are kept closed, as the downforce generated by the consistent flow on the rear wing is more important.

7.2 Simulation 4

The pre-processing is carried out using the same parameters as in the previous 3 simulations.

The simulation is fully converged after 2900 iterations, a higher number than in previous simulations. This is mainly caused by the more complex flow structures that need to be computed. This is the residuals plot of the fourth simulation:

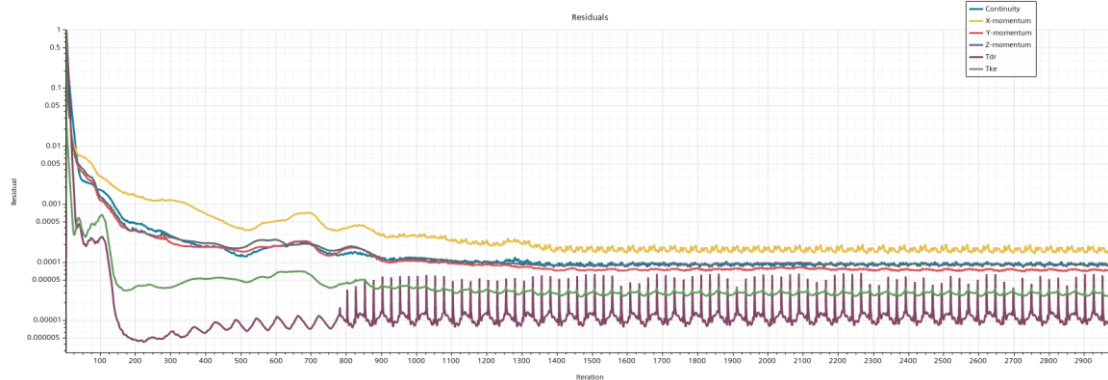


Figure 178: Residuals plot. Simulation 4.

There is a high level of oscillation on the Turbulent Dissipation Rate (Tdr) that indicates that there is a region where the turbulence does oscillate similar to a non-transient flow simulation. Without analyzing any further, it is quite possible that the turbulence oscillation comes from the front wheel wake turbulence. Although the Tdr parameter oscillates, the solution is valid, as the rest of the residuals and data retrieved from the simulation is coherent with the previous simulations.

The global force report indicates that the solution is converged:

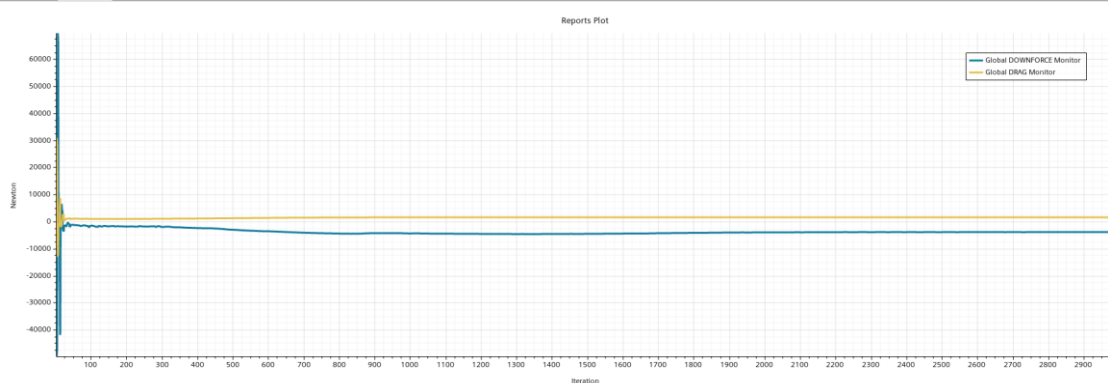


Figure 179: Global force report. Simulation 4.

Both the individual downforce and drag reports are also converged:

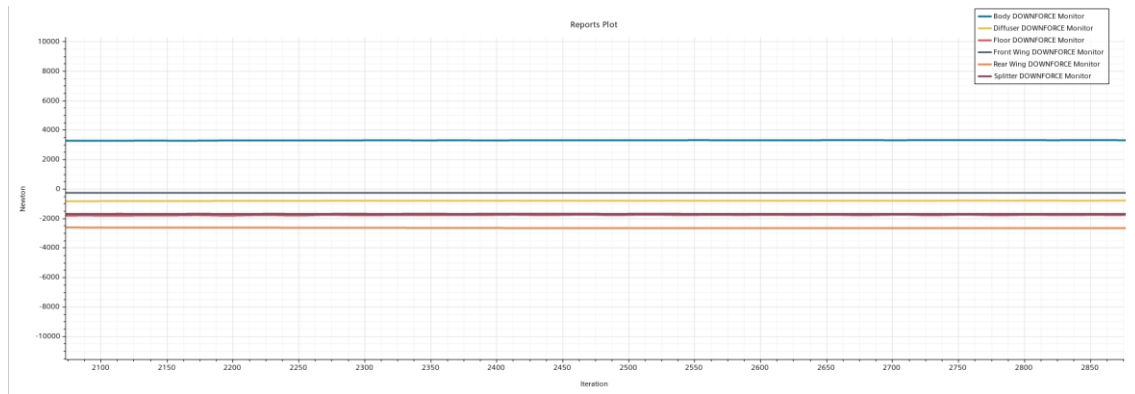


Figure 180: Individual downforce report. Simulation 4.

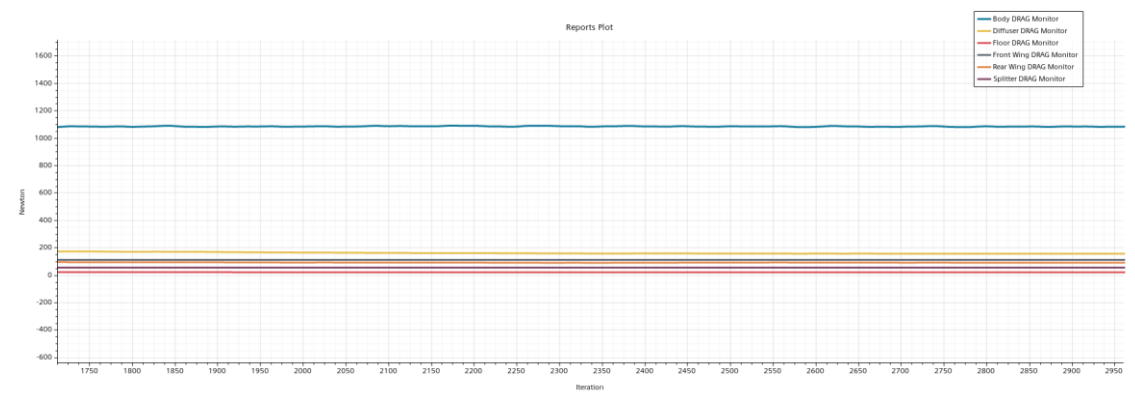


Figure 181: Individual drag report. Simulation 4.

The Centre of Pressure coordinates are also fully converged, although the X coordinate has a small oscillation which is negligible compared to the whole dimension:

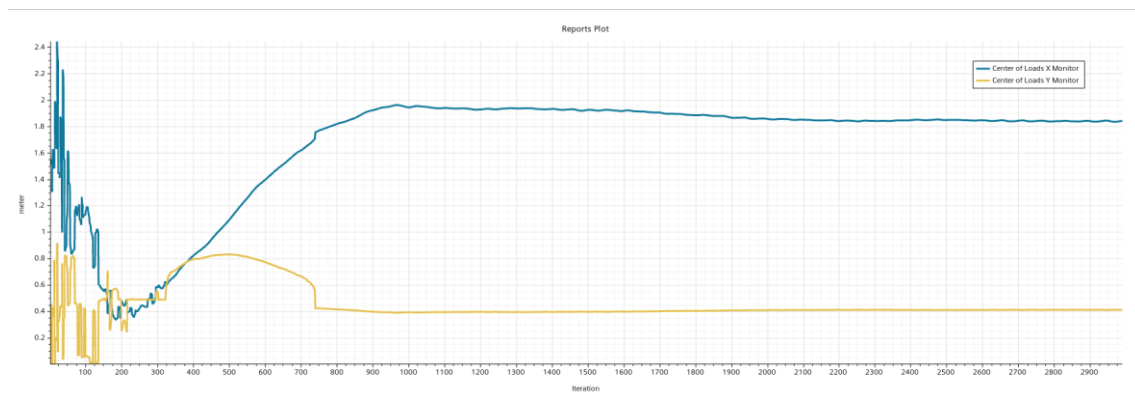


Figure 182: CoP Coordinates. Simulation 4.

The data gathered from this simulation shows that there is an improvement from the previous simulations, mainly due to the new front splitter concept implemented for this geometry iteration. These are the aerodynamic forces of half the car computed for this geometry iteration:

Region	Drag [N]	Downforce [N]
Diffuser	176,77	-1007,93
Floor	21,57	-2044,17
Front wing	111,21	-268,20
Rear wing	94,82	-2605,84
Splitter	54,68	-1698,45
Sum	459,05	-7624,59
Body	1077,78	3201,22
Global	1536,83	-4423,37

Table 41: Aerodynamic forces of half the car. Simulation 4.

The overall forces acting on the whole car are calculated by multiplying the above values by a factor of 2:

Region	Drag [N]	Downforce [N]
Diffuser	353,54	-2155,86
Floor	43,14	-4088,34
Front wing	222,42	-536,40
Rear wing	189,64	-5211,68
Splitter	109,36	-3378,90
Sum	918,10	-15249,18
Body	2155,56	6402,44
Global	3073,66	-8846,74

Table 42: Aerodynamic forces acting on the whole car. Simulation 4.

The CoP coordinates calculated show that the aerodynamic load is rear-biased like in previous simulations, although the bias is not as pronounced:

Coordinate direction	Value [m]
X axis	1,910
Y axis	0,397

Table 43: CoP coordinates. Simulation 4.

By looking just at the coordinates, especially the X axis coordinate, it is quite obvious that the rear axle bears the majority of the aerodynamic loads. This is confirmed by running the dedicated Python script that calculates the aerodynamic load on each axle:

```
Downforce value [N]: 8846.74
Drag value[N]: 3073.66
COP X coordinate [m]: 1.91
COP Y coordinate [m]: 0.397
Rear axle aerodynamic load [N]: 6247.419455172414
Front axle aerodynamic load [N]: 2599.320544827586
Front: 29.38167669477781 % Rear: 70.61832330522219 %
```

Figure 183: Aerodynamic load distribution on each axle. Simulation 4.

As explained in the previous paragraph, the aerodynamic load distribution is extremely rear-biased. By looking at the individual downforce values, the rear wing causes the majority of this bias because of the increased downforce generated on this element as a result of a cleaner air flow stream after the engine air intake.

Ideally, the aerodynamic pressure distribution should be 50% front – 50% rear to have a neutral car in terms of cornering behaviour. In this case, the load distribution can be altered by either reducing the rear wing or diffuser downforce or by increasing the downforce created by the front aerodynamic elements, ideally the latter. An example can be seen below, where an increase in front splitter downforce (+1500 [N]) is simulated (the X coordinate of the CoP is shifted frontwards by 250mm):

```
Downforce value [N]: 10346.74
Drag value[N]: 3073.66
COP X coordinate [m]: 1.66
COP Y coordinate [m]: 0.397
Rear axle aerodynamic load [N]: 6343.390144827587
Front axle aerodynamic load [N]: 4003.3498551724138
Front: 38.69189575820416 % Rear: 61.30810424179584 %
```

Figure 184: Example of how the aerodynamic loads can be evened.

The drag and lift coefficient are calculated following the same method as in previous iterations:

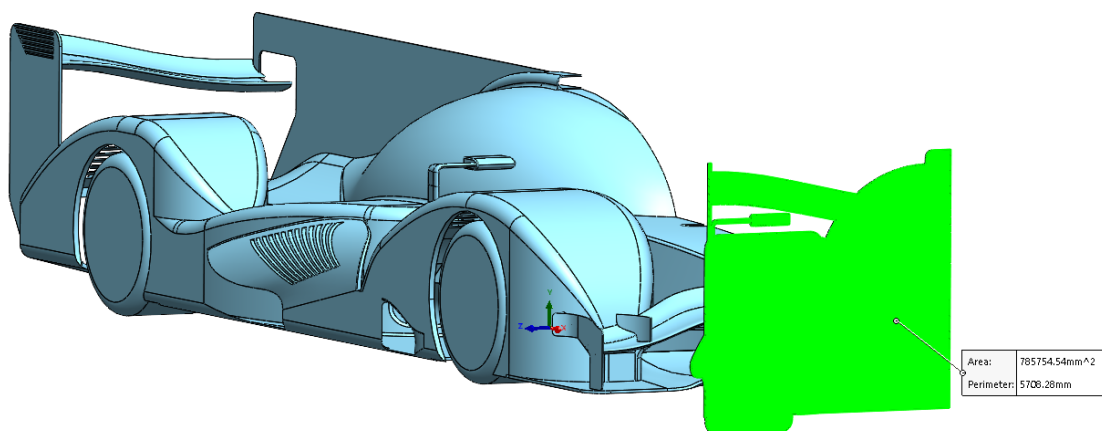


Figure 185: Frontal area. Geometry iteration 3.

The measured frontal area has the following values:

Type	Half car [m ²]	Whole car [m ²]
Frontal area	0,785	1,571

Table 44: Measured frontal area. Geometry iteration 3.

The lift and drag coefficients are calculated using the same equations as in previous occasions:

Coefficient	Value
Cd	0,62
Cl	-1,78

Table 45: Lift and drag coefficients. Simulation 4.

The general aerodynamic data is grouped on the following table:

Simulation 4	Value
Drag force	3073,66 [N]
Downforce	-8846,74 [N]
Cd	0,62
Cl	-1,78
Downforce distribution	29,38 % Front – 70,62 % Rear
L/D	-2,88:1
Frontal area	1,571 [m ²]
Flow velocity	75 [m/s]

Table 46: General aerodynamic data. Simulation 4.

Overall, there is a huge improvement from all the previous design iterations mainly due to the new front splitter concept that generates a great amount of downforce with very little drag in exchange. The load distribution is far from ideal, but once the definitive aerodynamic package has been established, like in this case, the future aerodynamic development can be directed towards optimizing the downforce generated by the car.

Compared to the Audi R18 aerodynamic data that has been obtained, the last geometry iteration has an aerodynamic performance similar to that of the Audi. Although the modelled car does not have an aerodynamic performance as good as the Audi R18, the simulation shows that the performance obtained falls within a reasonable margin:

	Audi R18 (adjusted)	LMP Iteration 3
Drag force	2823,53 [N]	3073,66 [N]
Downforce	-11268,95 [N]	-8846,74 [N]
Cd	0,471	0,62
Cl	-1,8798	-1,78
Downforce distribution	53% Front - 47% Rear	29,38% Front – 70,62% Rear
L/D	-3,99:1	-2,88:1
Frontal area	1,8 [m ²]	1,571 [m ²]
Flow velocity	75 [m/s]	75 [m/s]

Table 47: Comparison between the Audi R18 and the LMP Iteration 3 aerodynamic data.
Simulation 4.

It is important to explain that the aerodynamic data of the Audi R18 may not be completely accurate, as the source may not be 100% accurate, but the velocity adjusted data is coherent with the forces generated by a regular Le Mans prototype car.

7.3 Visual analysis

The main difference in this iteration has to do with the different front splitter concept that generates a lot more downforce. Apart from creating a bigger negative pressure region, the front lip does not generate positive pressure, as opposed to the previous designs of the front splitter:

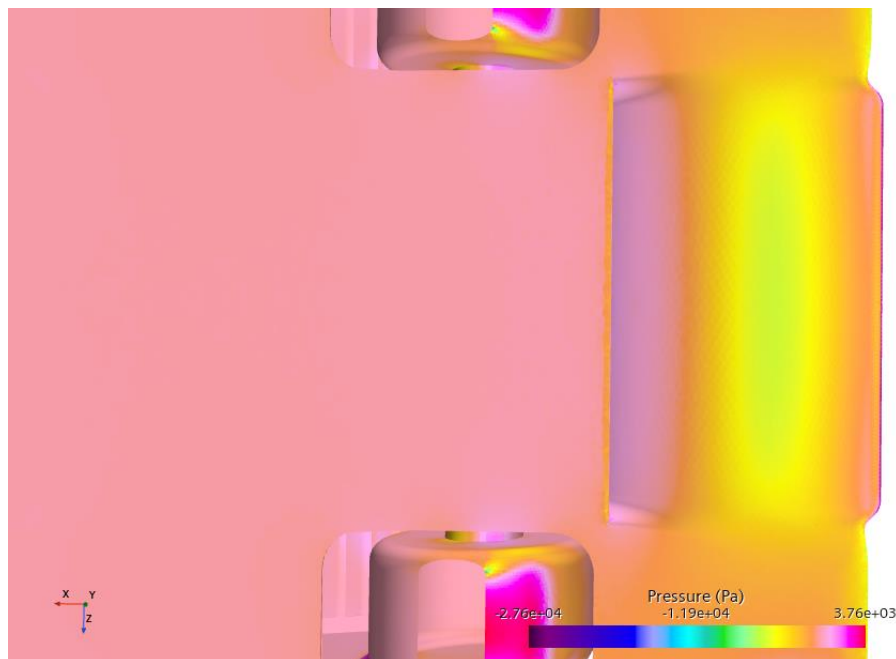


Figure 186: Low pressure region on the front splitter. Simulation 4.

Although the performance of the splitter has improved greatly, the diffuser effect on the exit section is not maximized due to flow separation near the surface, resulting in a higher pressure region that can be seen above. The flow separation can be seen by using streamlines near this area:

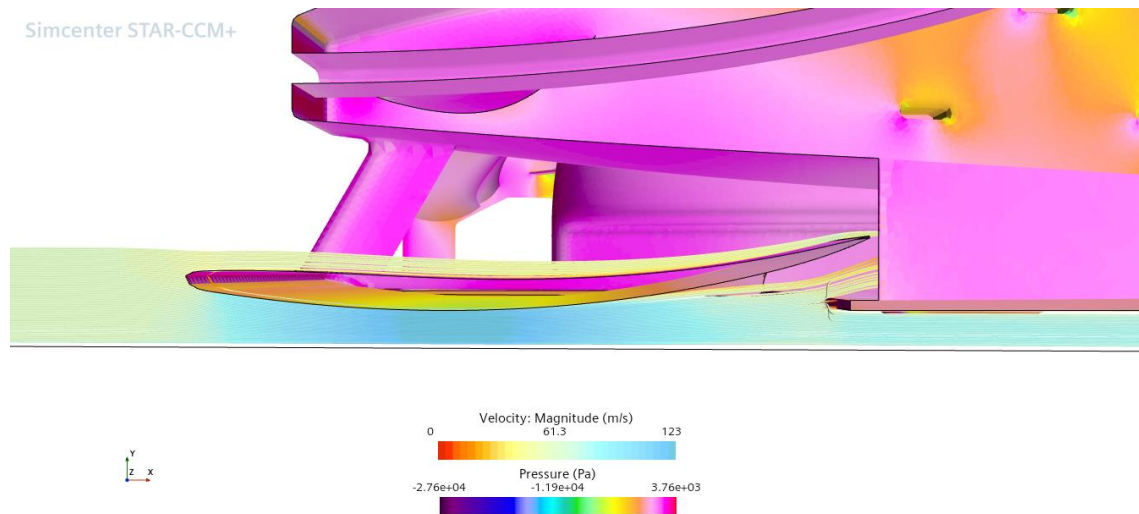


Figure 187: Streamlines around the front splitter. Notice the flow separation near the exit.
Simulation 4.

This flow separation can be easily solved by changing the front splitter profile on the finer development stage of the aerodynamic package, but as a proof of concept, the new splitter concept has the potential to be improved even further.

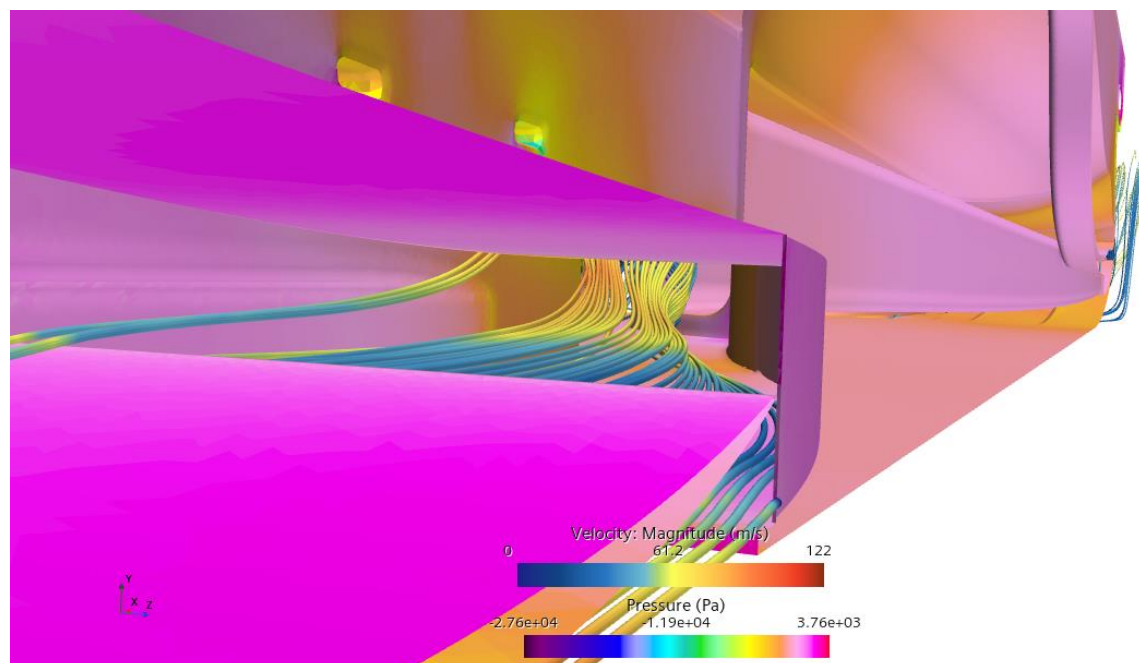


Figure 188: Air flow exiting the front splitter region. Simulation 4.

The new splitter changes the flow structures near the cooling ducts and front wheel fenders, with a higher air mass flow around this area that needs to be managed properly. The added side panels and intake duct help extracting this trapped air:

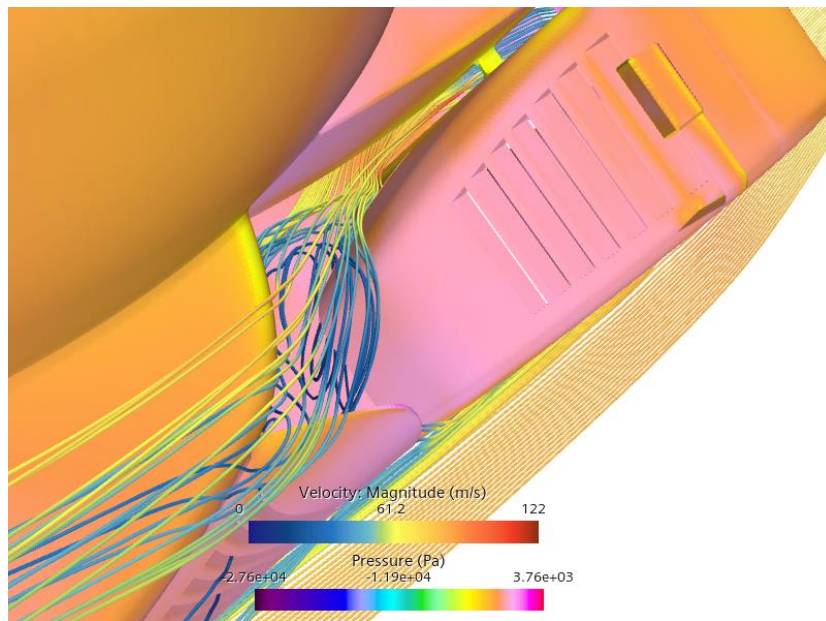


Figure 189: Stagnation region near the cooling ducts. Simulation 4.

On the front wheel wake area inside the wheel fenders, the turbulence is lower thanks to the increased air flow produced by the side intake duct and the vent louvers that help extract the stalled flow:

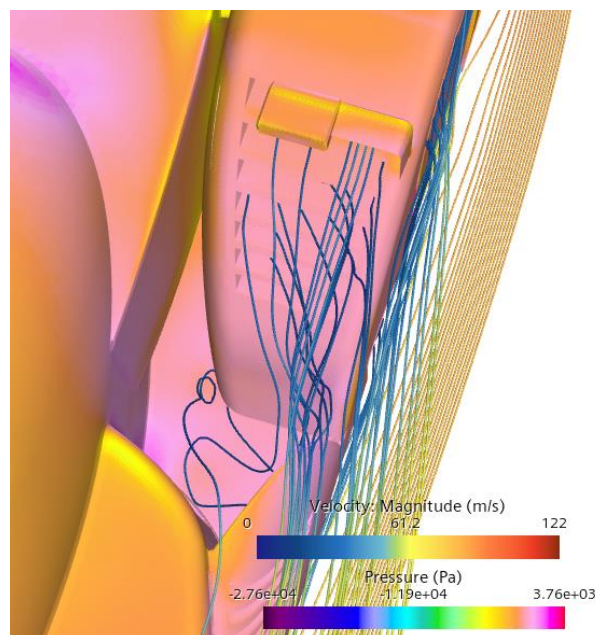


Figure 190: Turbulent flow extraction. Simulation 4.

The side panels fitted to the cooling pontoons do not work to the extent that is desired due to the louvres cut into the surface. These vents counter effect the stream effect that helps extract the trapped air inside between the cooling ducts and front wheel fenders:

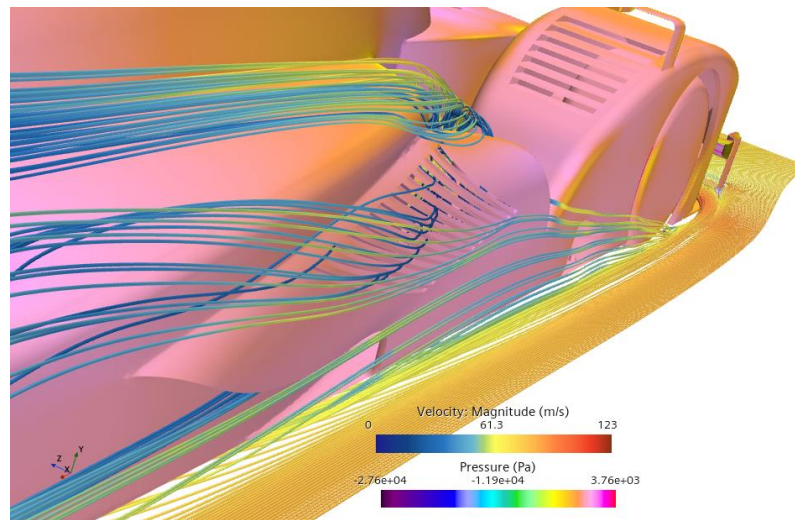


Figure 191: Air flow exiting the side panels through the vent louvres. Simulation 4.

These vent louvres do not work as expected, and should be removed on the next development stage. They are not a critical aerodynamic feature, so the general aerodynamic concept changes very little.

The aerodynamic performance on the rear wing has increased more than expected thanks to the new engine air intake duct for this geometry iteration. The wake turbulence behind the intake duct is much smaller, which creates a constant low-pressure region under the rear wing, unlike in the previous simulation:

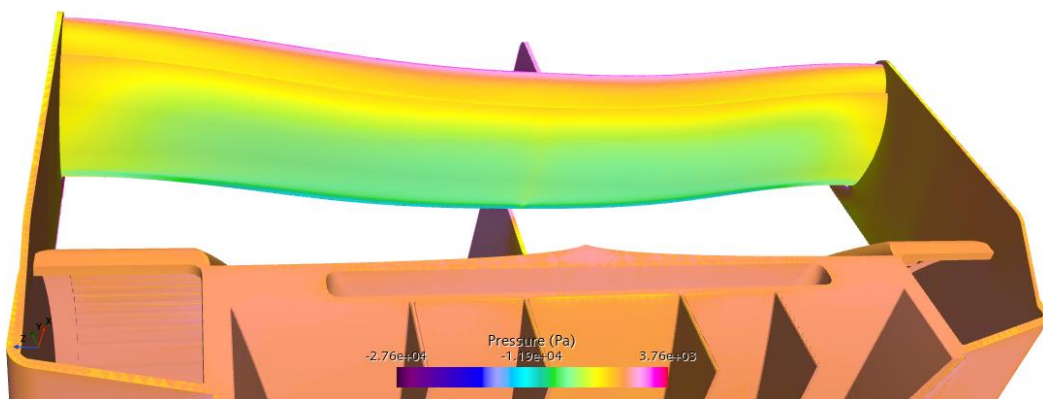


Figure 192: Low pressure region under the rear wing. Notice the constant low-pressure area along the wing. Simulation 4.

This is the main cause as to why the aerodynamic balance is so rear-biased. One solution to solve this issue could be to decrease the rear wing attack angle (less downforce), but this would affect the overall downforce in the car. The preferred solution would be to increase the downforce

generated by the front aerodynamic elements, especially the front splitter (new profile that does not allow the air flow to separate from the surface).

Even though the relative attack angle of the middle section has increased due to a less turbulent flow, there is no flow separation on the middle section of the rear wing:

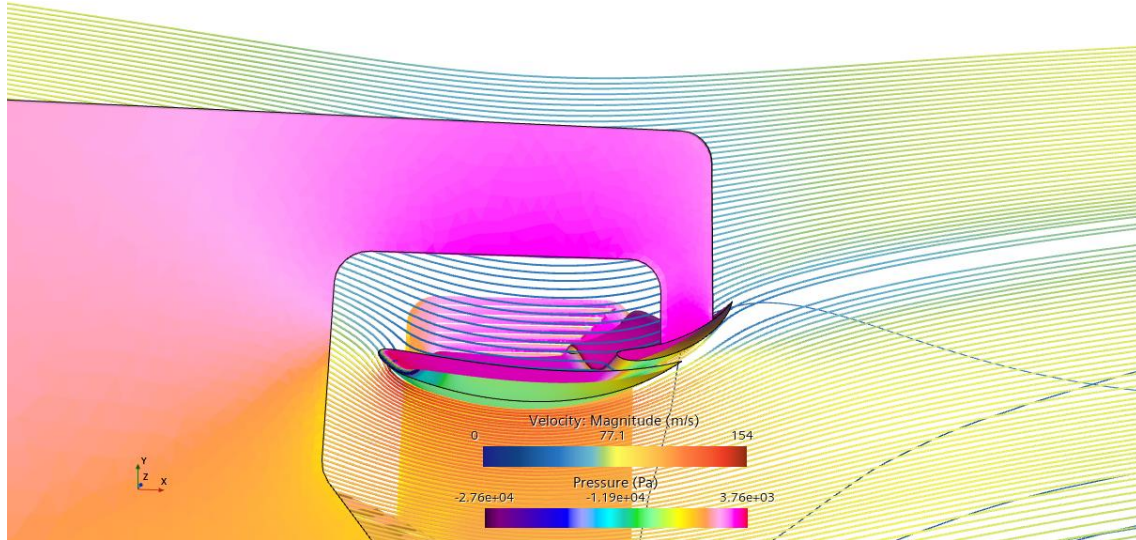


Figure 193: Flow around the rear wing middle section. Simulation 4.

8 Conclusions

8.1 Technical review

There are multiple changes and modifications that have been made during the different design iterations. To understand the different features that compose the final aerodynamic concept, the following list explains the effect of each major aerodynamic element on the final design iteration:

- **Rear wing:** Validated by a number of 2D simulations on the first design iteration, the final design takes advantage from the curved longitudinal profile that reduces the relative angle of attack on the middle section and the twist angle of 20° along the wing to compensate for the increased angle of attack on the centre of the wing.
- **Front splitter:** After testing a continuous splitter profile, the results were far from what was needed to compensate for most of the downforce generated by the rear elements. For the final design iteration, the splitter was designed mimicking the functioning principles of a rear diffuser. The results were much better with almost no disturbance on the air flow that enters the floor.
- **Front wing:** Does not work as good as the rear wing due to the high-pressure region created in front of the car, but there is little room for improvement on this area.
- **Floor:** The main modifications done in this area only manage the front wheel wake to improve the flow characteristics between the floor and ground. The floor edges are filleted to decrease the turbulence in the flow that goes into the floor section from the sides.
- **Diffuser:** The final diffuser design has a longer expansion tunnel than in previous design iterations, with an optimized expansion profile that avoids flow separation on the surface. The spacing between the vertical strakes is also optimized to avoid flow turbulence on the centre section.
- **Engine air intake duct:** After testing alternative duct concepts, the chosen duct geometry is very similar to that of the initial design analyzed in this thesis. In this case, the duct designed for the final design iteration increases the downforce generated by the rear wing.
- **Wheel fender louvres:** The louvres cut on the back of each wheel fender extracts the turbulent air trapped inside the fender and also helps reducing drag by reducing the low pressure behind these fenders.

- **Flow management elements:** To compensate for the increased air mass flow around the cooling ducts introduced by the new front splitter, a number of elements and panels have been fitted to the final concept to manage this increased air mass flow. Ideally, the flow should be directed sideways to avoid low pressure regions that would cause positive lift in the car, but this cannot be fully achieved. In this case, the results are decent, but could be improved by removing the louvres on the side panels

8.2 Final conclusions

The last aerodynamic concept is quite advanced in terms of generated downforce and aerodynamic performance compared to the initial design of the car. The general aerodynamic data shows that the aerodynamic package from the last design iteration has the potential to be developed to a standard that can rival any Le Mans Prototype car. This is the evolution in terms of aerodynamic performance throughout the concept development phase:

	LMP base geometry	LMP Iteration 3	Audi R18 (adjusted)
Drag force	2242,00 [N]	3073,66 [N]	2823,53 [N]
Downforce	-1930,18 [N]	-8846,74 [N]	-11268,95 [N]
Cd	0,210	0,62	0,471
Cl	-0,181	-1,78	-1,8798
Downforce distribution	42,75% F – 57,25% R	29,38% F – 70,62% R	53% F - 47% R
L/D	0,86:1	-2,88:1	-3,99:1
Frontal area	1,6054 [m ²]	1,571 [m ²]	1,8 [m ²]
Flow velocity	75 [m/s]	75 [m/s]	75 [m/s]

Table 48: Comparison between the initial car geometry, final car geometry and Audi R18.

There is still room for improvement if the data is compared to that of a real Le Mans prototype car (Audi R18), but as an initial concept, the results are pretty decent. The finer details of the aerodynamic package are developed in a secondary stage where the general dimensions and component distribution of the car are already established.

The front splitter has been the most important improvement in terms of downforce, even though there is still room for improvement. Prior to designing the open splitter analysed in the last design iteration, there have been multiple designs that, although worked to a certain extent, did not generate the expected downforce needed to compensate the aerodynamic loads between the front and rear axles. The air foil profile that composes the front splitter has to be changed, as there is flow separation near the profile exit. This can be done using a 2D CFD simulation of the car profile to save time and validate multiple profiles at the same time.

On the rest of the car, the aerodynamic properties have also improved greatly mainly due to the addition of a validated diffuser and rear wing, especially the latter. The rear wing has little room for improvement left due to the extremely good pressure field on the underside thanks to the revised engine air intake designed for the last design iteration.

8.3 Future improvements

As explained before, the aerodynamic development studied only represents the general concept of how the aerodynamic package of the car is expected to perform. The next development stage takes care of the finer details of the aerodynamic side of car development. There are a number of smaller improvements that can improve the generated downforce and reduce the overall generated drag:

- **Side cuts on the rear wing pillars:** This is a common feature on formula cars. The side cut resembles the shape of a triangle and is placed under the rear wing lower element to help the formation of the wake vortex while reducing the low pressure behind the wing.
- **Blown diffuser:** The exhaust gases are blown into the rear diffuser to accelerate the air flow and create an additional amount of downforce in the diffuser. This is a concept that has been used in many motorsport series, most notably in Formula 1 during the 2011 season:

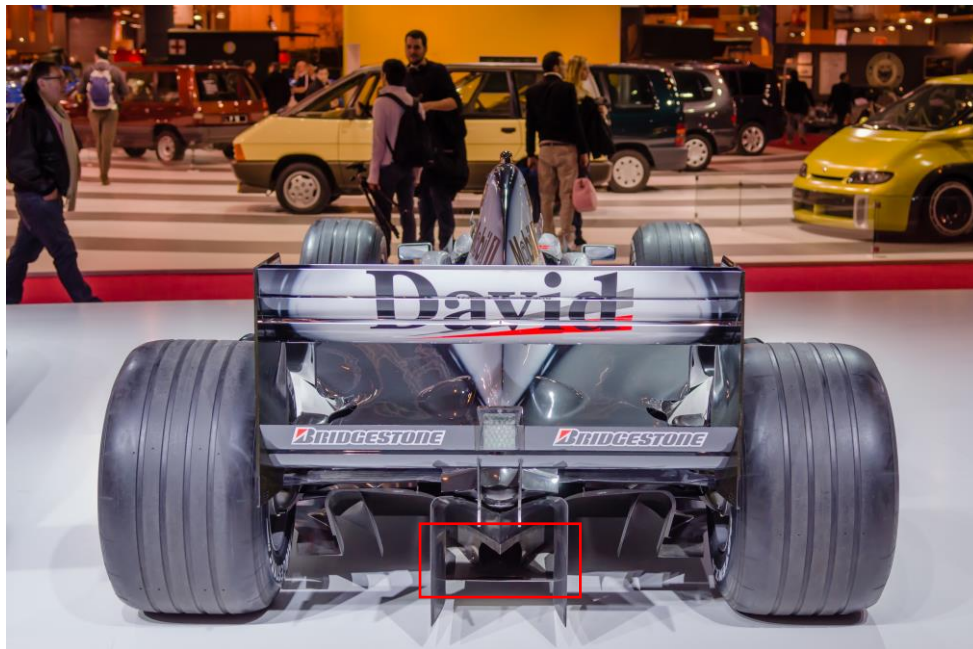


Figure 194: Exhaust exit to increase the flow energy on the rear diffuser . McLaren MP4/15.

On endurance prototypes this concept is easy to implement due to the wide diffusers and extensive bodywork panels that allow for an easy routing of the exhaust pipes.

- **Better flow management near the splitter:** Although the improvements made on the last design iteration to solve this problem do work to some extent, it would be advisable to improve the flow management characteristics around the sidepods and cooling ducts. The design explained in the last design iteration does work, but should be refined in future development stages.

9 Bibliography

- [1] A. Warey, «Investigation of Numerical Diffusion in Aerodynamic Flow Simulations with,» General Motors Global Research and Development, Warren, MI 48090, 2014.
- [2] «thermal-engineering,» [En línea]. Available: <https://thermal-engineering.org/wp-content/uploads/2019/05/Navier-Stokes-Equations-definition.png>.
- [3] «Reynold's Number,» [En línea]. Available: https://en.wikipedia.org/wiki/Reynolds_number#Definition.
- [4] UPV, «UPV RANS equations,» [En línea]. Available: <https://cfd.blogs.upv.es/turbulence/rans/>.
- [5] «SIMSCALE,» 5 May 2021. [En línea]. Available: <https://www.simscale.com/docs/simulation-setup/global-settings/k-omega-sst/>. [Último acceso: 26 October 2022].
- [6] J. FM, «SIMSCALE,» May 2018. [En línea]. Available: <https://www.simscale.com/forum/t/what-is-y-plus/82394>. [Último acceso: 27 October 2022].
- [7] D. R. R. Pijush K. Kundu, «Boundary Layers and Related Topics,» 2016. [En línea]. Available: <https://www.sciencedirect.com/topics/engineering/skin-friction-coefficient#:~:text=The%20skin%20friction%20coefficient%20is,shear%20stress%20on%20the%20surface..> [Último acceso: 27 October 2022].
- [8] «Hmong prototipo de Le Mans,» 2022. [En línea]. Available: https://hmong.es/wiki/Le_Mans_Prototype.
- [9] M. Kuron, «Engineering.com,» 6 January 2015. [En línea]. Available: <https://www.engineering.com/story/3-criteria-for-assessing-cfd-convergence>. [Último acceso: 24 October 2022].
- [10] P. (Siemens), «Simcenter Forum,» 29 April 2021. [En línea]. Available: <https://community.sw.siemens.com/s/question/0D54O00006tntLVSAY/does-symmetryplane-double-downforce-in-report>. [Último acceso: 5 November 2022].
- [11] M. J. Fuller, «Mulsanne's Corner News,» 15 December 2010. [En línea]. Available: <http://www.mulsannescorner.com/newsnov10.html>. [Último acceso: 5 November 2022].
- [12] S. Montes, «Freeflight,» [En línea]. Available: <https://freeflight.org/Library/TechLibrary/GurneyFlap.pdf>. [Último acceso: 9 November 2022].
- [13] C. CFD, «Cadence system analysis,» [En línea]. Available: <https://resources.system-analysis.cadence.com/blog/msa2021-what-is-the-spalart-allmaras-turbulence-model>. [Último acceso: October 2022].

[14 Unknown, «SIMSCALE,» 25 May 2021. [En línea]. Available:
] <https://www.simscale.com/docs/simulation-setup/global-settings/k-omega-sst/>. [Último
acceso: 3 November 2022].